Scale-dependent fracture in gradient elastic materials

Richardson P. Joseph

Doctor of Philosophy

Centre for Infrastructure Engineering

WESTERN SYDNEY
UNIVERSITY

2018

For the Mighty One has done great things for me-- holy is his name

Luke 1:49

To my beloved Parents,
Patrick and Anita Joseph

ACKNOWLEDGEMENT

Firstly, I would like to express my immense indebtedness and gratitude to my supervisor ***Associate Professor Baolin Wang*** and ***Professor Bijan Samali*** who accepted me as their Ph.D. student and offered me their mentorship. I would like to thank them for their continuous support, patience, motivation and immense knowledge. Under their guidance, I successfully overcame many difficulties and learned a lot. Their guidance helped me in all the time of research, writing of research papers and this thesis as well.

I would like to extend my gratitude to Professor Emeritus ***Kendall E. Atkinson***, from the University of Iowa for his valuable and intuitive comments during the execution of this study. I owe my thanks to my colleagues at the Centre for Infrastructure Engineering for their care, assistance, support and friendship when I lived among them in and out of the office. I appreciate the support from the technical and administrative staff throughout my Ph.D. studies, in particular at the beginning of my candidature.

Finally, it would be understated to say thanks to my parents, ***Patrick Joseph*** and ***Anita Joseph***, as I consider it beyond myself to express such feelings for them in always being there as a source of encouragement and inspiration. It is a great honor for me to be called as their son. My forever interested, encouraging and always enthusiastic grandmother ***Laviza Ismail Joseph***: she is always keen to know what I am doing and how I am proceeding, although it is likely that she has never grasped what it is all about! I am grateful to other members of my family ***Austin Joseph***, ***Jasmin Joseph***, ***Dr. Thomson Joseph***, ***Kendrick Joseph***, ***Edrick Joseph*** and ***Adrianna Joseph*** who have provided me through moral and emotional support in my life and have supported me along the way. I consider myself blessed in the world to have such a lovely and caring family, standing beside me with their love and unconditional support. May God bless them always.

Lastly, I would like to express my gratitude to my friend and fiancé ***Ms Jessica Judissa Thomas*** for her love, utmost care and presence which is no less than a comfort for me. Thanks love!

STATEMENT OF AUTHENTICATION

The work presented in this thesis is to the best of my knowledge and belief, original except as acknowledged in the text. I hereby declare that I have not submitted this material, either in full or part, for a degree at this or any other institution.

Candidate's Signature Date: 7th Nov 2018

TABLE OF CONTENTS

LIST OF FIGURES

ABSTRACT

Micro-electromechanical systems (MEMS) and Nano-electromechanical systems (NEMS) have a wide range of applications in aerospace, power industry, automation & robotics, chemical & medical treatment analysis, information technology and in the infrastructure health monitoring equipments. To ensure the reliability of such small devices, the mechanical and hence fracture behaviour of their common building blocks such as beams, tubes, and plates should be carefully evaluated. However, on a smaller scale, the microstructural effects such as size effects, load-induced and geometrically prompted stress singularities are more noticeable, particularly at the micro/nano scale.

Classical continuum elasticity theories are inadequate to accurately describe the situations controlled by the microstructure effects since the influence of these effects are not properly accounted for. On the other hand, the higher order gradient theories such as strain gradient theory may effectively describe the effects of microstructure through the solution of properly formulated boundary value problems. Moreover, when dealing with piezoelectric micro/nano materials, due to the presence of massive strain gradient, the electric field-strain gradient coupling (flexoelectricity) should also be considered. The objective of this research is to evaluate the scale-dependent fracture behaviour of gradient elastic materials using strain gradient theory. In particular, two most widely studied geometrical configurations i.e. double cantilever beam (DCB) and centrally cracked material layer are employed in this work.

For double cantilever beam, the governing equation with respective boundary conditions is obtained through a variational principle, in which the cumulative effects of large deformation, strain gradient, surface elasticity, surface residual stress, uncracked part of DCB and surface piezoelectricity (in case of piezoelectric materials) are considered. The study is then extended to cater for the strain gradient-electromechanical coupling, known as a flexoelectric effect. The size effects are found to be significant when the height of the beam is comparable to the microstructural material's characteristics length. The volumetric strain gradient, negative surface residual stress and positive surface elasticity increase the crack stiffness. On the other hand, the incorporation of the uncracked part of DCB is important at smaller scale even when the length to height ratio of the beam is higher. This observation is completely opposite to the DCB analysis at the macroscale.

In the cracked material layer, the anti-plane strain gradient fracture analysis is carried out in which both volumetric and surface strain gradients are considered. The Fourier transform technique is applied to reduce the solution of a boundary value problem into dual integral equations. The Kernel of the resulting Fredholm integral equation is solved by means of Gauss-Laguerre quadrature method to evaluate the crack tip stress intensity factors. The crack stiffening behaviour, due to volumetric strain gradient for two different boundary conditions i.e. stress-free and clamped boundaries are presented and compared. The positive surface gradient effect increases crack stiffness while negative surface gradient leads to a more compliant crack. The study is then implemented to obtain the governing equations for a scale-dependent piezoelectric cracked material layer under the Mode III loading configuration.

The findings presented in this thesis are expected to give useful insights to those working in the structural integrity analysis at the micro/nano scale. They are anticipated to help in the design of micro/nano structural components and serve as a benchmark for future theoretical and empirical studies.

ANTHOLOGY OF DISSEMINATION

PEER-REVIEWED PUBLICATIONS

1. **Joseph, R. P**., Wang, B. L, & Samali, B., 2017. Size effects on double cantilever beam fracture mechanics specimen based on strain gradient theory. *Engineering Fracture Mechanics*, 169, 309-320. Doi: https://doi.org/10.1016/j.engfracmech.2016.10.013

2. **Joseph, R. P**., Wang, B. L, & Samali, B., 2018. Size-dependent stress intensity factors in a gradient elastic double cantilever beam with surface effects, *Archive of Applied Mechanics*, 88(10),1815-1828. Doi:https://doi.org/10.1007/s00419-018-1406-6

3. **Joseph, R. P**., Wang, B. L, & Samali, B., 2018. Large-deformation and strain gradient fracture analysis of double cantilever beam with piezoelectric effect, *Journal of Engineering Mechanics*, 144(8), 04018071. Doi: https://doi.org/10.1061/(ASCE)EM.1943-7889.0001497

4. **Joseph, R. P**., Chunwei Zhang, Wang, B. L, & Samali, B., 2018. Fracture analysis of flexoelectric double cantilever beams based on the strain gradient theory, *Composite Structures*, 202, 1322-1329. Doi: https://doi.org/10.1016/j.compstruct.2018.06.067

5. **Joseph, R. P**., Wang, B. L, & Samali, B., 2018. Strain gradient fracture in an anti-plane cracked material layer, *International Journal of Solids and Structures*, 146, 214-223. Doi: https://doi.org/10.1016/j.ijsolstr.2018.04.002

CONFERENCES

1. **Joseph, R. P**., Wang, B. Large deformation of the double cantilever beam fracture mechanics specimen with surface effects based on strain gradient theory. Part (a), 3rd*International Conference on Smart Materials and Structures*, 20-22 March 2017, Orlando, USA. Doi: 10.4172/2169-0022.C1.062

2. **Joseph, R. P**., Wang, B., & Samali, B. Large deformation of the double cantilever beam fracture mechanics specimen with surface effects based on strain gradient theory. Part (b), 14th*International Conference of Fracture*, 18-23 June 2017, Rhodes, Greece.

3. **Joseph, R. P**., Wang, B., & Samali, B. Strain gradient fracture in a flexoelectric double cantilever beam, 7th*International Conference on Advanced Materials and Engineering Materials*, 17-18 May 2018, Bangkok, Thailand.

Evidence of peer-reviewed journal papers can be found in Appendix A

CHAPTER 1

INTRODUCTION

1.1 Introduction

Micro and nano structures such as beams, tubes, and plates are the building blocks in many Micro-electromechanical systems (MEMS) and Nano-electromechanical systems (NEMS), for instance, capacitors, sensors, switches, actuators, accelerometers and recently in energy harvesting devices. Their wide applications present significant challenges for the researchers in the field of micro and nano-mechanics. It has been widely recognized that the small-scale components demonstrate superior properties due to the size effect. In order to investigate the exact structural behaviour of the nanostructures, their mechanical, as well as the electromechanical properties (e.g. piezoelectricity and flexoelectricity), should properly be considered in the mathematical framework. Experimental methods to determine the mechanical, as well as the electromechanical behaviour of the small-scale devices, are technically complex and financially expensive. Therefore, theoretical modelling is usually preferred as it can easily be implemented across different length scales.

Continuum methods, being less computationally intensive, have extensively been used to analyze the macro-structural behaviour on theoretical as well as the empirical grounds. Classical continuum elasticity theories assume that the stresses in a material point depend only on the strain components at that point. It does not account for the contributions of strain gradients. However, according to the nonlocal theory of elasticity, the stress at a particular point depends on the strain (first derivative of

displacements) associated with not only that point but also all the other points in the body (higher order derivatives of displacements) (Wang et al., 2012). This phenomenon is more evident when the dimensions of the structure are scale down to the micro (micro-electromechanical systems (MEMS)) and nano-domains (Nano-electromechanical systems (NEMS)). In that case, the material microstructural length scales become comparable to the length scale of the deformation field that tends to cause non-homogenous and scale/size-dependent mechanical behaviour (Giannakopoulos and Stamoulis, 2007).

Size-dependent mechanical behaviour in micro-scale elements have extensively been observed in experiments (Fleck and Hutchinson, 1997; Lam et al., 2003; Ma and Clarke, 1995; McFarland and Colton, 2005) and it has been understood that the non-classical continuum theories such as the higher-order gradient theories and couple stress theory can interpret this scale-dependent behaviour. Mindlin and Tiersten (1962), Toupin (1962) and Koiter (1964) introduced the couple stress elasticity theory, incorporating two higher order material constants to predict the size effects. In their theory, along with the classical stress, the higher order stresses (the couple stress components) are included to cater for the element's rotation. Alongside, the higher-order strain gradient theory was introduced by Mindlin (1965) that includes the effect of the first and second derivatives of the strain tensor on the strain energy density. Later Lam et al. (2003) introduced three higher-order material constants in the constitutive equations of the modified strain gradient theory. In several modern theories, the response at a certain scale is influenced by a characteristic length at the lowest level (Benvenuti and Simone, 2013). This is very evident in the case of the lattice system potential energy that depends on the inter-atomic distance (Kiang et al., 1998). In such cases, the description based on classical continuum theory is inadequate. In order to cater for the underlying microstructure into the continuum theory, the higher order

strain gradient theories and continuum non-local elasticity theories were presented by Mindlin and Eshel (1968) and Eringen (1972) respectively. Comparison between non-local (stress gradient) and strain gradient elasticity theories is made in the next chapter and it is briefly explained why the strain gradient theory is preferable and employed in this work.

On the other hand, as far as the electromechanical behaviour of solids is concerned, numerous studies have been conducted to understand the fundamental physics behind the phenomenon of material polarization under the application of external mechanical stress. The classical relation between applied strain and electric polarization, known as piezoelectricity, is thoroughly defined (Cady, 1946) and has been widely used to investigate the fracture behaviour of the piezoelectric materials at the macro scale. However, a number of experimental studies have demonstrated the size-dependent linear electro-mechanical coupling at micro/nanoscale (Baskaran et al., 2011; Catalan et al., 2011). This occurs when the structural dimensions become comparable to the material length scale and the state of stress at a point is dependent not only on the strain but also on the strain gradient. The electromechanical coupling between polarization and strain gradient is termed flexoelectricity (Mao and Purohit, 2014; Sladek et al., 2017). Contrary to the piezoelectric effect, flexoelectricity is not just limited to non-centrosymmetric materials but it may induce electric polarization in the centrosymmetric material by breaking the material's symmetry (Yan and Jiang, 2013a). Therefore, due to the flexoelectric effect, non-piezoelectric materials may also be used to produce piezoelectric composites (Sharma et al., 2010) and thus call out new challenges to researchers in the field of nanotechnology.

Nanoscale devices and structures demand accurate design and development. Therefore, it is vital to explore their characteristics thoroughly. The experimental investigation of the mechanical response (Chen et al., 2007; Cheng et al., 2008; Jing et

al., 2006; Kang and Xie, 2010; Lagowski et al., 1975; Pharr et al., 1992; Voyiadjis et al., 2010; Wong et al., 1997; Yu et al., 2000) as well as for electromechanical response (Abdollahi et al., 2014; Baskaran et al., 2012; Chu and Salem, 2012; Lu et al., 2016; Poddar and Ducharme, 2013), using modern scientific manipulations and employing atomic/molecular modelling (Behzadi and Rafii-Tabar, 2008; Fermeglia, 2008; Popescu, 2007) are effective methods to determine the size-dependent behaviour of the structure at micro/nano scale. However, the application of theoretical approaches for modelling nano structures is considered more attractive because of their lesser complexity and capability to implement at all the possible length scales.

1.2 Problem Statements

The mechanical behaviour of macro sized specimens using classical continuum elasticity models has been actively analyzed and documented. However, at the micro/nano scale, in practical applications, the continuum models are found inadequate to accurately predict their mechanical as well as the electromechanical (e.g. piezoelectric and flexoelectric effect) behaviour. Essentially, to cater for the size effect, higher order gradient theories were formulated and thoroughly implemented. In particular, the potentials of strain gradient theory to explicate size effect, stress/strain field singularities at dislocations/cracks, surface effects and electromechanical phenomena are rigorously explored by researchers. Relevant works for micro/nano materials are found to be more prevalent and hence are always sought. It solely exhibits that the findings remain open for innovations and new updates. Therefore, it is essential to evaluate the scale-dependent fracture analysis of the micro/nano materials. Due to complexities associated with the experimental setup, analytical and numerical studies are always pursued to reduce the experimental works.

1.3 Research Objectives

Scale-dependent fracture of micro/nano materials, based on strain gradient theory, has not been thoroughly assessed in literature. To update the relevant findings in the respective fields, fracture analysis of double cantilever beam (DCB) and a cracked material layer made up of isotropic and piezoelectric materials shall be carried out. The selection of these two specimens is done based on their wide application on the determination of fracture toughness. The specific objectives of this research are stated as follows;

1. To evaluate the non-linear large deformation of a scale-dependent cantilever beam and to employ this study to analyze the fracture behaviour of DCB.
2. To study the influence of surface effects (predominantly residual surface stresses) on the fracture mechanics of DCB.
3. To investigate the influence of strain gradients on the piezoelectric material.
4. To incorporate the electric field-strain gradient coupling effect (Flexoelectric effect) in studying the fracture associated with the piezoelectric material.
5. To study the cracking behaviour of a boundary value finite material layer problem under Mode III loading configuration. The study shall be conducted for two different boundary value problems i.e. stress-free boundaries and fixed boundaries.
6. To incorporate the influence of surface strain gradient parameter in determining the Mode III fracture of material layer subjected to stress-free and fixed boundaries.
7. To set up a theoretical (mathematical) framework to determine the mode III fracture of a piezoelectric material layer incorporating the electric field-strain gradient coupling effect (Flexoelectric effect).

1.4 Research Scope/Outline

Scale-dependent fracture analysis of a double cantilever beam (1-dimensional problem) and the finite cracked material layer (2-dimensional problem) is carried out based on strain gradient theory. For accurate outcomes, in the case of DCB, surface effects are incorporated for both isotropic and piezoelectric DCBs. The study is further extended to incorporate the electric field-strain gradient coupling effect (Flexoelectric effect). In the case of the finite cracked material layer, a through-crack is assumed under the Mode III loading configuration, and fracture study is conducted under two different boundary conditions i.e. stress-free boundaries and clamped boundaries. Analysis of the piezoelectric (and flexoelectric) material layer is limited to the mathematical frame work. Our research scope is limited to analytical and numerical studies. Due to the complexities of the experimental setup, analytical and numerical studies are always pursued to reduce the experimental works.

1.5 Significance of the outcomes

Presently, the methodologies underpinning the design of the building blocks for MEMS and NEMS are not adequately defined and in some cases are outdated. Due to which the devices are either over-designed or in some cases, are under-designed. Therefore, in order to optimize the investigation of the mechanical and electromechanical behaviour of these devices, accurate methods are essential. The findings from this work are expected to give some insights to those who are working in the small-scale structural integrity analysis and involved in the design process of micro/nano structures. In particular, the accurate understanding of fracture behaviour of micro/nano structures is crucial in the damage tolerance analyses.

1.6 Thesis Outline

This thesis consists of eight chapters as follows:

Chapter 1 - Introduction. This chapter presents the introduction to the topic, problem statement, research objectives, research scope/outline, the significance of the outcomes and overall thesis outline.

Chapter 2 – Literature Review. This chapter reviews some of the relevant literature explaining the theoretical background and the potential research gaps pertaining to the work presented in this thesis.

Chapter 3 – Analysis of a double cantilever beam: The size effect. This chapter investigates the large deformation of a cantilever beam which is further employed to study the fracture behaviour of double cantilever beam (DCB), based on strain gradient elasticity theory. Results of the strain gradient model (with/without surface effects) are compared with the non-gradient as well as the classical results. Root effect of the DCB is also included in this study to make some interesting conclusions.

Chapter 4 – Scale-dependent piezoelectric effect. This chapter examines the scale-dependent fracture of a piezoelectric double cantilever beam (DCB) specimen subjected to large deformation. The governing equations with relevant boundary conditions for a piezoelectric cantilever beam with simultaneous consideration of surface piezoelectricity, surface elasticity, surface residual stress and large deformation are obtained and solved numerically. These results are further utilized to investigate the fracture behaviour of a DCB to study different electrical boundary conditions i.e. short circuit and open circuit boundary condition.

Chapter 5 – Piezoelectric gradient material with flexoelectricity. Following chapter 4, the incorporation of an electric field-strain gradient coupling, known as flexoelectricity, in the constitutive equations of a 1D cantilever beam is studied in this chapter. Along with the material length scale parameter, the effect of the piezoelectric coefficient

scaling parameter is thoroughly studied and fracture mechanics results of DCB are evaluated accordingly.

Chapter 6 – Anti-plane cracked material layer. In this chapter, the fracture mechanics analysis in terms of evaluating stress intensity factors of an anti-plane isotropic cracked layer is carried out. The crack plane is assumed parallel to the layer edges. Both volumetric and surface strain gradient material characteristic lengths are considered in formulations and numerical solutions. Surface strain gradient can be negative or positive, therefore, crack stiffness in both cases is evaluated and compared with the model incorporating only the volumetric strain gradient. Similarly, the analysis is carried out for the stress-free as well as the clamped boundaries to draw conclusions.

Chapter 7 – Scale-dependent piezoelectric anti-plane cracked material layer: A theoretical framework. This chapter establishes the theoretical and mathematical framework to cater for the size-dependent fracture of a piezoelectric material layer under Mode III loading configurations. The constitutive equations and derived and governing equations are obtained analytically.

Chapter 8 – Conclusions and Future work. Finally, conclusions are made in this chapter and an outline of potential future studies is briefly given.

CHAPTER 2

LITERATURE REVIEW

2.1 Introduction

The rapid growth of micro and nano scale structures in current engineering applications is unquestionable. Most of the commonly used small-scale components such as beams and plates in MEMS and NEMS are often used to carry loads and hence deformed elastically. In order to establish their further applications, the fracture analysis of elastic materials at small scale is important. Numerous researchers in the past showed the significant strengthening of the structure when its size is reduced to micro and nanoscale (which in literature is usually termed as small scale). It is also noted that the fracture and damage mechanics models, based on classical continuum theories, are inadequate to completely describe the fracture behaviour of materials at small scale, primarily due to the absence of microstructure effects. Due to this reason and ever-increasing inclination towards the miniaturization of devices, fracture of the small-scale structures has gained tremendous interest among several researchers in the last three decades.

This chapter provides the general literature review of various topics defining the scope of the research presented in this thesis. In particular, some relevant literature specific to the theme of the proceeding chapters is reviewed therein. This chapter commences with the review of classical theory in the field of fracture and damage mechanics, followed by an overview of the various non-classical models developed over the years. Subsequently, the review of the electromechanical effect, known as

piezoelectricity at macroscale and enhanced piezoelectricity at the micro/nanoscale, known as flexoelectricity is made. The review continues with the literature related to the two most commonly used geometrical configurations in the determination of fracture properties i.e. double cantilever beam and the material layer of finite thickness. Finally, some of the fracture mechanics studies prompted by the pure mechanical load, as well as the electromechanical loadings are reviewed so that research gaps and the potential of further research in this field could be clearly stated.

2.2 Classical Continuum Fracture-A brief review

The ductile fracture of a material is generally associated with the nucleation and growth of the inherent micro cracks and their coalescence into the macro cracks. These micro cracks or voids may appear due to material impurities, manufacturing processes metallurgical defects or service handling. The concept of material continuum media in the fracture and damage studies was first introduced by Kachanov (1974) and later by (Rabotnov, 1987) to introduce a damage parameter. The damage parameter/variable was considered to represent the average material degradation on a macro level even though the degradation of material under any load is dominated by the microstructure effects. A brief review of the models describing the damage accumulation in the materials, based on continuum mechanics approach, is presented by Zhang (2010). In their work, a thorough and systematic development in the field of continuum damage theories in isotropic as well as the anisotropic materials is presented. Special emphasis is placed on theoretical formulations and mathematical derivations in case of brittle as well as the ductile fracture.

In general, fracture mechanics can be described briefly as “It aims to describe a material’s resistance to failure i.e. determination of material’s toughness” (Fischer-Cripps, 2007). It is well known that applied stress tends to concentrate around geometric discontinuities within the structure, i.e. pinholes, slots, keyways, sharp corners, notches

or macro cracks. Griffith (1921) proposed his pioneering approach which is widely known as the energy-based approach defining the fracture mechanism. He stated two necessary conditions for the propagation of crack to occur which are; Firstly, the stress due to stress concentration at the crack tip must reach a level that can cause the failure at that point. Secondly, the release of strain energy must be at a minimum value that equates the surface energy for crack extension (Fischer-Cripps, 2007). The stress field around a crack will define three failure modes called Mode I, II and III. The most dominant mode of failure is Mode I, which involves the opening of a crack under the influence of an in-plane stress perpendicular to crack line. In Mode II, a crack grows under an in-plane shear stress in the direction of crack, whereas Mode III which is a tearing mode involves the shearing load out of the plane of material (Trevelyan, 1992). Mode I is the most common case in fatigue/fracture analysis in which the opening of a crack takes place in the plane of maximum tensile stress. Therefore, stress field function is usually written in terms of the strain energy release rate or stress intensity factor. Since crack growth depends on the stress intensity factor (or strain energy release rate), therefore its estimation is vital to predict structural service life. Based on the loading modes, the K_I, K_{II} and K_{III} are used as symbols for Mode I, Mode II and Mode III SIFs.

On the other hand, the development of the macro phenomenological theories related to fracture and damage mechanism is reviewed by Besson (2010). Apart from the general micromechanical modelling of void nucleation, growth and coalescence, the review highlights some of the recent advancements in constitutive material modellings and computational tools are provided in great detail. Some of the recent findings in the field of classical continuum theories on fracture and damage are reported by Volegov et al. (2017) along with the description of finite element techniques to adequately describe the fracture phenomenon. The framework depicting possible incorporation of non-

classical constitutive material's equation in finite element modelling is provided to describe the scale-dependent fracture characteristics at small scale.

In general, for classical continuum elasticity, the principle of virtual work states that the work done by the external forces acting on the body occupying the domain Ω is equal to the total internal energy, which mathematically is written as;

$$\int_{\Omega} \sigma_{ij} \delta \varepsilon_{ij} d\Omega = F_k \delta u_k + \int_{\Gamma} t_k \delta u_k d\Gamma + \int_{\Omega} b_k \delta u_k d\Omega \qquad (2.1)$$

Where $\sigma, \varepsilon, \delta u$ are the stress, strain and virtual displacement respectively. F is the external point force and t and b are the surface load and body forces respectively. Equation (2.1) shows that classical theories are independent of the internal material's characteristic length.

2.3 Non-classical theories

In the case of micro and nano scale fracture investigations, the scale of stress (or strain) induced by the external structure becomes comparable to one of its internal structure (atomic arrangement). Therefore, the internal structure directly influenced the fracture behaviour of the whole component (Kitamura et al., 2016). Classical continuum elasticity theory is independent of scale and hence cannot describe the phenomenon dominated by the material's microstructure. Meanwhile, two prominent effects at the small scale are surface effects and non-local effects (long-range interaction effects). Based on these two effects, the modified continuum theories are introduced by the researchers, i.e. the non-local theory of elasticity (stress gradient theory) and strain gradient theory. These non-classical higher order gradient theories are capable to adequately describe the role of material's microstructure, provided the boundary value problem is correctly formulated.

2.3.1 Non-local theory of elasticity (Stress gradient theory)

Unlike Hooke's law, Eringen (1983) postulates non-local elasticity theory which states that the stress at any reference point *x* in the body depends on the strain not only at *x* but also on the other points of the body. In most of the models proposed by Eringen, the stress is assumed as a weighted average function of the strain field. In this way, this theory may not only avoid the singularity at the dislocations but also successfully illustrates some atomic and molecule level phenomenon such as high-frequency vibration and wave dispersion (Li et al., 2008). The fundamental integral type constitutive equations for an isotropic, homogenous and non-elastic body are given as (Eringen 1983, 1972);

$$\sigma_{ij}(\mathrm{x}) = \int_V \alpha(\left|\mathrm{x}' - \mathrm{x}\right|) t_{ij}(\mathrm{x}') \mathrm{d}V(\mathrm{x}') \tag{2.2}$$

$$t_{ij}(\mathrm{x}') = \lambda \varepsilon_{kk}(\mathrm{x}') \delta_{ij} + 2\mu \varepsilon_{ij}(\mathrm{x}') \tag{2.3}$$

where *V* is the volume occupied by the body, μ and λ are the lame constants, ϵ_{ij} are the strain components, t_{ij} and σ_{ij} are the classical and non-local stress components respectively. The spatial position of a point is defined by *x*, while $\alpha(x)$ denotes the nonlocal attenuation modulus of dimension (length)$^{-3}$. The term $\alpha(\left|\mathrm{x}' - \mathrm{x}\right|)$ is also known as the influence function, that is considered as a positive function between the field point *x* and the source point x'. It has a maximum value when $x' = x$ and decay rapidly with the increasing distance $\left|\mathrm{x}' - \mathrm{x}\right|$ (Eringen, 2002). On the other hand, the differential form, which is also known as the stress gradient form of the constitutive equation is written as;

$$\sigma_{ij} - l^2 \nabla^2 \sigma_{ij} = \lambda \varepsilon_{kk} \delta_{ij} + 2\mu \varepsilon_{ij} \tag{2.4}$$

where l is a material constant with the meaning of the internal length scale parameter. It describes the effect of micro and nanoscale on elastic behaviour and is approximately defined as; $l = e_o a$, here e_o is a non-dimensional material constant that can be determined experimentally or through numerical simulations from lattices dynamics (Wang et al., 2012), a is the internal characteristics length (e.g. lattice parameter, C-C bond length, granular distance, etc.) (Lim and Wang, 2007) and ∇^2 is the Laplacian operator. The intrinsic wavelength l, taken as cell wall spacing by the authors in the references (Mughrabi, 1987) and (Stamoulis and Giannakopoulos, 2012), as depicted in Fig. 2.1, in the case of strain gradient effects, will be a characteristics microstructural length (Stamoulis and Giannakopoulos, 2012). For a one-dimensional structure, from Eq. (2.3), the non-local stress-strain relation can be written as;

$$\varepsilon_{xx} = \frac{1}{E}\left(\sigma_{xx} - l^2 \frac{\partial^2 \sigma_{xx}}{\partial x^2} \right) \tag{2.5}$$

$$\gamma_{xz} = \frac{1}{G}\left(\sigma_{xz} - l^2 \frac{\partial^2 \sigma_{xz}}{\partial x^2} \right) \tag{2.6}$$

Here $\sigma_{yy} = \sigma_{zz} = \sigma_{yz} = \sigma_{xz} = 0$ and lame's constants are replaced by the Young's Modulus and the shear modulus, denoted by E and G respectively.

2.3.2 Strain gradient theory

Strain gradient models are widely recognized in the literature as capable to predict the experimentally identified material behaviour characterized by microstructure internal length scale. Some of these include size effect, surface effect, wave dispersion and stress/strain singularities at crack tips and dislocation cores (Polizzotto, 2015). In parallel with stress gradient theory, strain gradient theory is founded on the idea that the material response on a reference point depends not only on the local strain but also on the strain gradients of various order. Some of the early work in this field is credited to

the researchers such as Mindlin (1965), Toupin (1962) and Koiter (1964) in the early 1960s. They introduced the couple stress elasticity theory to predict the size effects with two higher order material constants in the constitutive equations. In those theories, besides the classical stress components, the higher order stresses are also included to cater for the effect of element rotation. In particular, Mindlin proposed three simplified versions of his theory i.e. Form I, II and III. In Form I, the strain energy density is taken as quadratic function of classical strains and second gradient of displacement; in Form II the gradient of strains is used in place of second gradient displacement and in Form III the strain energy is taken as a function of strain, the rotation gradient, and the fully symmetric part of strain gradient. Among these three Forms, which all result in the same equation of motion, Form II is the one in which the total stresses are symmetric and therefore the problems of non-symmetric stress tensor (in case of couple stresses theories) are avoided. Thus, Form II is the only form with symmetric stresses as in classical elasticity theory. Furthermore, Fleck and Hutchinson (1997, 2001) employed the Mindlin theory by only considering the first derivative of strain tensor and five higher-order material constants in the constitutive equation and termed their theory as strain gradient theory. In comparison with couple stress theory, strain gradient theory has some additional higher order stress components, which if neglected will degenerate the strain gradient theory to the typical couple stress theory (Kahrobaiyan et al., 2011). The simple gradient theory employed by Vardoulakis et al. (1996), combines the concepts of Form II of Mindlin theory, though it has a fewer number of elastic constants comparatively. Consequently, the theory presented by Vardoulakis et al. (1996) is much more convenient in applications (Giannakopoulos and Stamoulis, 2007) and therefore employed in this work. For one-dimensional case, the Cauchy (τ_x), double (μ_x) and total stresses (σ_x) are given for the beam bending in the following constitutive relations; Cauchy stresses; $\tau_x = Ee_x + l^{'}E\dfrac{\mathrm{d}e_x}{\mathrm{d}x}$, double stresses $\mu_x = l^{'}Ee_x + l^{2}E\dfrac{\mathrm{d}e_x}{\mathrm{d}x}$ and

Total stresses; $\sigma_x = \tau_x - \frac{\mathrm{d}\mu_x}{\mathrm{d}x} = E\left(e_x - l^2 \frac{\mathrm{d}^2 e_x}{\mathrm{d}x^2}\right)$. Here, E is the Young's Modulus; e_x is the axial strain in the beam due to bending, l and l' are the material characteristic lengths related to volumetric and surface elastic strain energy. The use of simpler, engineering-type gradient theories (Vardoulakis and Sulem, 1995; Vardoulakis et al., 1996) is much more convenient and valid as shown by Giannakopoulos et al. (2006).

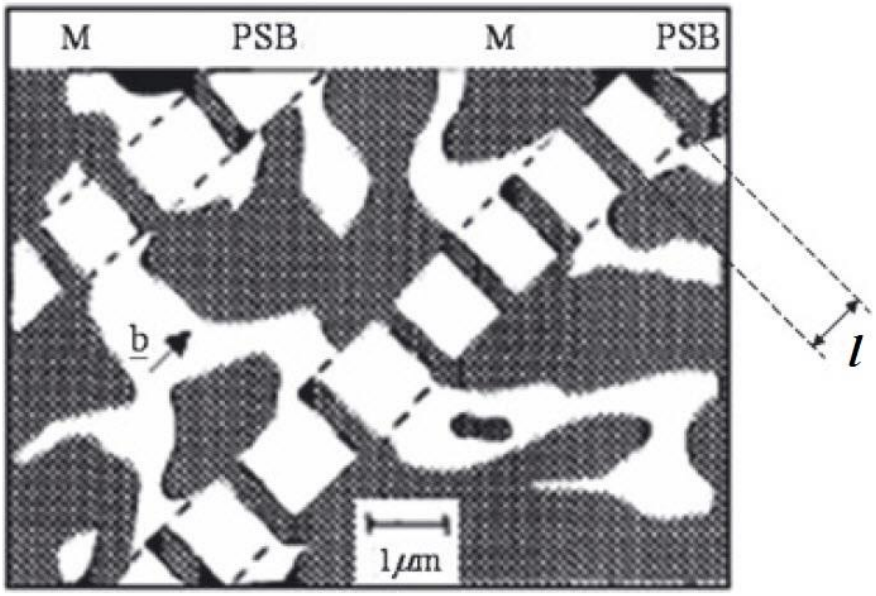

Figure 2.1A characteristics ladder-like microstructure of persistent slip bands (PSBs) which is composed of an alternating succession of rich and poor dislocation regions characterized by an intrinsic wavelength *l* (Mughrabi, 1987)

2.3.3 Stress gradient and strain gradient beam model-A comparison

For illustration, a Euler-Bernoulli beam is considered in both cases of stress gradient and strain gradient constitutive behaviour by Polizzotto (2014). It was shown that the strain gradient beam model manifests itself through the beam deflection independent of the external loads. These effects may also emerge from the bending moment and stress fields provided the beam is statically indeterminate. The comparison between the two theories may be stated in the following points (Polizzotto, 2014).

1. Stress gradient beam behaves as a classical beam when subjected to a linearly distributed load. However, if the load is piecewise non-linear, then the stress gradient effect is evident through the beam deflection. This also holds true in the case of bending and stress fields, provided that the beam is statically indeterminate.
2. In contrast, the manifestation of the strain gradient beam through the deflection curve is independent of the external load conditions. Meanwhile, like the stress gradient beam, the effects are also evident in bending and stress filed, provided that the beam is statically indeterminate.
3. It was concluded that the stress gradient effects enter into play through an enhanced load, while the strain gradient effects enter into play though the strain gradients, independent of the acted loads.

2.4 Electromechanical effects in solids

Materials exhibit electro-mechanical coupling have wide applications in many devices such as sensors, actuators, transistors, resonators and energy harvesting devices. These devices are widely used in smart structures and modern industrial equipments. The materials that show the electro-mechanical coupling at macro scale are known as the piezoelectric materials. On the other hand, at micro/nano scale the size-dependent electro-mechanical coupling is termed as flexoelectricity. In this section, a brief literature related to piezoelectricity, flexoelectricity and their combined effect is reviewed.

2.4.1 Piezoelectricity

Certain crystals such as tourmaline crystals when mechanically stressed show electric potential across their ends. This property is termed as piezoelectricity and is widely explained in the literature. It is further elaborated by Maranganti et al. (2006) in the following words, “Upon application of a uniform strain, internal sub-lattice shifts within

the unit cell of a non-centrosymmetric dielectric crystal result in the appearance of a net dipole moment". On the other hand, if the material induced stress/strain upon the application of external electric-field, then this phenomenon is known as inverse piezoelectricity. The stress-strain constitutive relation with the incorporation piezoelectric effect is given as;

$$\sigma_{ij} = c_{ijkl}\varepsilon_{kl} - e_{kij}E_k \tag{2.8}$$

where c is the fourth order elastic constant tensor, e is the piezoelectric coefficient, σ is the Cauchy stress, ε is the strain and E is the electric field vector. The electric displacement D is given by the following relation;

$$D_k = a_{kl}E_l + e_{kij}\varepsilon_{ij} \tag{2.9}$$

where a is the material's permittivity second order tensor. The electric field vector E is given as;

$$E_k = -\frac{d\psi}{d\mathrm{k}} \tag{2.10}$$

where ψ is the electric potential and k is the axis notation.

2.4.2 Flexoelectricity

A number of experimental studies have demonstrated the size-dependent linear electro-mechanical coupling at micro/nanoscale(Baskaran et al., 2011; Catalan et al., 2011). This occurs when the structure dimensions become comparable to the material length scale and the state of stress at a point is not only depended on the strain but also on the strain gradient. The electromechanical coupling between polarization and strain gradient is termed as flexoelectricity (Mao and Purohit, 2014; Sladek et al., 2017). Contrary to the piezoelectric effect, flexoelectricity is not just limited to non-centrosymmetric materials but it may induce electric polarization in the centrosymmetric material by breaking the material's symmetry (Yan and Jiang, 2013b). Therefore, due to the flexoelectric effect, non-piezoelectric materials may also be used to produce

piezoelectric composites (Sharma et al., 2010) and thus call out new challenges for researchers in the field of nanotechnology. The relation between polarization and strain gradient is given as;

$$P_l = f_{ijkl} \frac{\partial \varepsilon_{ij}}{\partial x_k} \tag{2.11}$$

where f is the electric-field strain gradient coupling coefficient or flexoelectricity tensor and P is the resultant polarization component and x is the direction of the gradient.

2.4.3 Piezoelectricity with flexoelectricity

In order to deal with the coupling of the strain gradient and polarization, higher order gradient theories such as strain gradient theories must be employed. The pioneer work, extending the linear piezoelectric theory by incorporating the effect of polarization gradient was presented by Mindlin (1969). On the other hand, Maranganti et al. (2006) included the polarization gradient as well as the strain gradient effect in their theoretical framework based on the variational principle. Hu and Shen (2010) constructed a comprehensive model incorporating flexoelectricity, an electrostatic force as well as surface effects. Mao and Purohit (2014) presented a detailed analysis for flexoelectric solids using strain theory which is eventually used to derive the governing Navier equation for the isotropic materials. Recently Sladek et al. (2017) developed a finite element method (FEM) formulation to analyze the general 2D boundary value problem incorporating the electric-field strain gradient coupling in the constitutive equations. The constitutive equations with the consideration of electric field-strain gradient coupling and pure non-local effect are given as (Hu and Shen, 2010);

$$\tau_{ij} = c_{ijkl}\varepsilon_{kl} - e_{kij}E_k \tag{2.12}$$

$$\mu_{jkl} = -f_{ijkl}E_i + g_{jklmni}\kappa_{nmi} \tag{2.13}$$

$$D_k = a_{kl}E_l + e_{kij}\varepsilon_{ij} + f_{klmn}\kappa_{lmn} \tag{2.14}$$

where c is the fourth order elastic constant tensor, e is the piezoelectric coefficient, f is the electric-field strain gradient coupling coefficient tensor, the tensor g represent the strain gradient elasticity effect and a is the material's permittivity second order tensor. The symbols τ_{ij}, μ_{ijk} and D_i represent the Cauchy stress, higher order stress, and electric displacement component respectively. The indicial notation is employed in which the repeated indices represent summation and comma indicates differentiation with respect to the spatial variable. The strain ε_{ij} and strain gradient η_{ijk} are related to the displacement u_i as; $\varepsilon_{ij} = (u_{i,j} + u_{j,i})/2$ and $\eta_{ijk} = \varepsilon_{ij,k} = (u_{i,jk} + u_{j,ik})/2$ respectively.

2.5 Surface effects

There are certain molecular effects that are fascinatingly obvious when structural dimensions are in micro and nanometer range. Effect of the surface stresses is one of those effects that have thoroughly been explained (Dingreville et al., 2005; Streitz et al., 1994). The atoms on or near the free surface have different equilibrium requirements as compared to the ones in bulk. This difference causes an excess energy at the surface which is understood as a layer to which that energy is attached (Fischer et al., 2008). Accordingly, the thermodynamic theory of solid surface revealed that the relationship between the surface stress and surface free energy is obtainable (Cahn, 1998; Cammarata, 1997; Cammarata, 1994; Fried and Gurtin, 2003). Meanwhile, when the size of the structure is reduced to the micro/nanoscale, the ratio of the surface area to bulk volume may become enormous. Therefore, the influence of the surface effect on the mechanical behaviour of micro/nanomaterials becomes prominent and hence cannot be neglected (Wang and Wang, 2013). Surface effects on micro/nanostructures may be characterized by two major types i.e. the surface elasticity and the surface residual stress (He and Lilley, 2008). Gurtin and Murdoch (1978) firstly considered the effect of

surface stress in their theoretical framework based on continuum elasticity. In their work, the surface is considered as a mathematical layer of zero thickness with different material properties as compared to an underlying bulk. This theory has shown an excellent capability to successfully cater the surface effect on the mechanical behaviour of micro/nanostructures and is widely employed by the researchers throughout (Jammes et al., 2009; Luo and Wang, 2009; Luo and Xiao, 2009). The general expression for surface stress-strain relation is given as;

$$\sigma^{S}_{\alpha\beta} = \tau_{o}\delta_{\alpha\beta} + (\tau_{o} + \lambda^{S})\varepsilon_{yy}\delta_{\alpha\beta} + 2(\mu^{S} - \tau^{S})\varepsilon_{\alpha\beta} + \tau_{o}u^{S}_{\alpha,\beta} \tag{2.15}$$

whereλ^{S} and μ^{S} are the surface Lame constants, δ is Kronecker delta and τ_{o} is the surface residual stress in the unconstrained condition. In general, the surface properties usually have anisotropic stress (Gurtin and Murdoch, 1978; Shenoy, 2005; Weissmüller and Cahn, 1997) depending upon the crystallographic direction of the surface. However, it is shown in the literature that a surface may assume anisotropic nature and it is still meaningful to use an appropriate average of surface stresses (Duan et al., 2005; Sharma and Ganti, 2004; Sharma et al., 2003). Moreover, for piezoelectric micro/nanomaterials, such elasticity model may not accurately predict the size-dependent fracture properties due to the negligence of surface piezoelectricity (Zhang and Jiang, 2014). The pioneering work for the development of the piezoelectric model with simultaneous incorporation of surface piezoelectricity, surface residual stress, and surface elasticity has been shown by Huang and Yu (2006). Some of the relevant findings may be seen in the works of (Yue et al., 2015). The Cauchy surface stress with the incorporation of surface piezoelectricity is given as;

$$\sigma^{S}_{ij} = c^{S}_{ijkl}\varepsilon^{S}_{kl} - e^{S}_{kij}E^{S}_{k} \tag{2.16}$$

Where c_{11}^{s} is the surface Young's Modulus, e_{kij}^{s} is the piezoelectric constants of the surface and E_{k}^{s} is the surface electric-field. Electric energy and hence electric displacement of the surface is neglecting since its value is negligible as compared to the bulk.

2.6 Double cantilever beam

The Double cantilever beam (DCB) specimen is widely used to determine the critical stress intensity factors (or strain energy release rate) of homogenous, as well as non-homogenous materials under Mode I loading configuration (Whitney, 1985). The ASTM standard, ASTM D 5528 recommends the use of DCB specimen to measure the mode I fracture toughness of fiber reinforced polymer composites (Prasad et al., 2011). The classical approach to conduct stress analysis in DCB is to consider it as a pair of two cantilever beams, in which the uncracked part (also known as the root part) ahead of the crack tip is usually ignored. The approximate solution of a DCB specimen was presented by (Chang et al., 1976) in which the DCB is divided into two parts i.e. cracked and uncracked part. Moreover, the complete stress analysis of a typical DCB is presented by (Whitney, 1985). It is necessary to mention that most of the stress and fracture analysis of a DCB is with the assumption of small deformation theory. However, in practice particularly at the smaller scale, structural elements usually undergo large deformation and hence the subsequent fracture analysis is important. In the preceding section, the brief description of the bending of the cantilever under small and large deformation is presented and compared, followed by the analysis of the uncracked part of DCB.

2.6.1 Cantilever beam bending

The schematic diagram of a double cantilever beam under large deformation is shown in Fig. 2.2. However, it is firstly necessary to briefly describe the small and large deformation formulation as following;

2.6.1.1 Classical small deformation theory

The classical problem of a cantilever beam subjected to bending under the assumption of small strain and small deformation using Euler Bernoulli's beam theory is expressed as;

$$\frac{M}{EI} = \frac{\mathrm{d}^2 y}{\mathrm{d}x^2} = \frac{\mathrm{d}\varphi}{\mathrm{d}x} \tag{2.17}$$

Where M is the bending moment, I is the moment of inertia and $\varphi = \mathrm{d}y / \mathrm{d}x$ is the slope of the beam at a particular point. Above equation (2.17) is usually solved by the method of integration, while the beam is supposed to be acted upon by a concentrated force F at the free end, to give;

$$y = \frac{Fx^2}{6EI}(3L - x) \tag{2.18}$$

The maximum deflection y at $x = L$ is found to be;

$$y = \frac{FL^3}{3EI} \tag{2.19}$$

and the corresponding rotation φ is given as;

$$\varphi = \frac{FL^2}{2EI} \tag{2.20}$$

Moreover, the method of elliptical integrals has been employed by (Beléndez et al., 2002) to analytically approximate the rotation φ at all the points on the cantilever beam by the following relation;

$$\int_0^{\varphi_o} \frac{d\varphi}{\sqrt{\varphi_o - \varphi}} - 2\sqrt{\alpha} = 0 \qquad (2.21)$$

Where $\alpha = FL^2/2EI$ is defined as the load factor and φ_o is the maximum rotation at the free end of the beam. Interestingly, for small deformation, the load factor and α and $\varphi_o$were found to be equal.

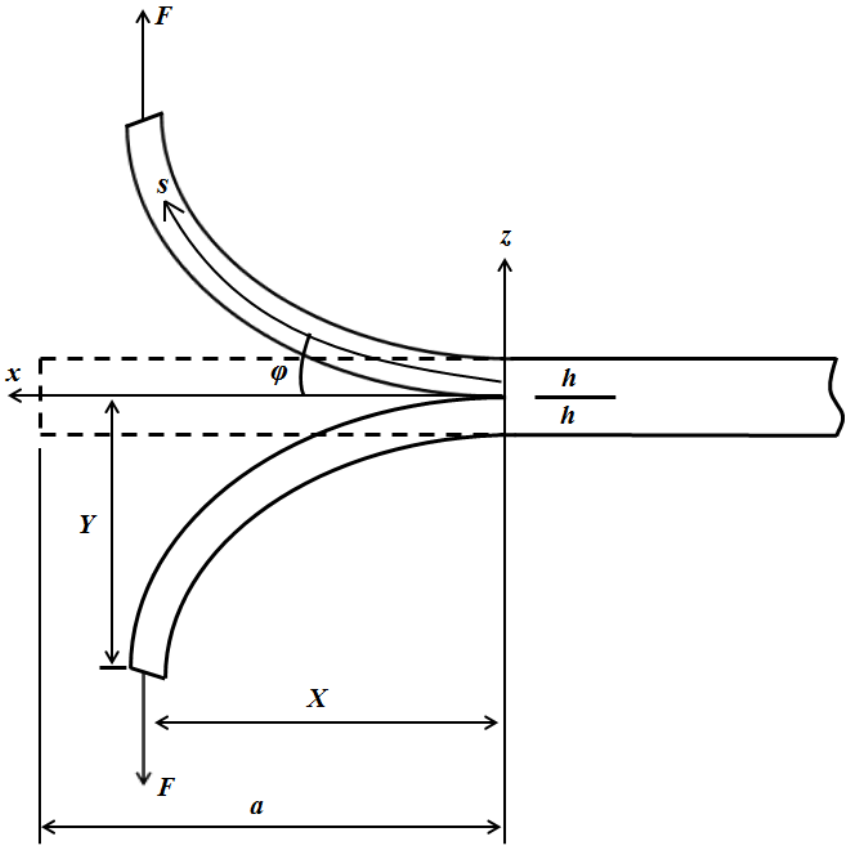

Figure 2.2 Schematic diagrams of double cantilever beam model

2.6.1.2 Large deformation theory

It is important to note in case of a thin beam if the elastic deformation is on the order of beam thickness, linear (small deformation) theory is often inadequate to produce

accurate results (Wang and Wang, 2015). It is also evident that the cantilever beams used in micro and nano-electromechanical often undergo non-linear deformations, particularly those that are actuated electrostatically, due to a phenomenon commonly referred to as "pull-in stability" (Batra et al., 2008; Hsu, 2008; Jia et al., 2010; Wang and Wang, 2015). It is also important to mention that the effect of non-linear strain (von Karman nonlinearity) on the bending behaviour of the cantilever beam is insignificant and can be neglected. However, the effect of non-linear curvature (large deformation) is significant and must not be ignored. Moreover, numerous experimental evidence of the cantilever undergoing large deflection is also provided by the researchers (Heidelberg et al., 2006; Nilsson et al., 2003; Sapsathiarn and Rajapakse, 2012; Wu et al., 2006). Therefore, in order to study the mode I fracture toughness of the DCB at the nanoscale, it is vital to assume the large deformation assumption to accurately estimate the strain energy release rate and hence stress intensity factors. The formulation is based on Euler-Bernoulli theorem, for which the moment–curvature relation of the beam along the *x*-axis is given as $EI\dfrac{\mathrm{d}\varphi}{\mathrm{d}s}=M$. The moment at any point $X_{(s)}$ along the beam may be written as $M = F.\ X_{(s)}$, upon differentiation and using $\mathrm{d}X_{(s)}/\mathrm{d}s = \cos\varphi$, we get;

$$EI\frac{\mathrm{d}^2\varphi}{\mathrm{d}s^2}+F\cos\varphi=0 \tag{2.22}$$

Above equation is the non-linear differential equation that governs the deflection of a cantilever beam made of a linear elastic material subjected to a vertical concentrated load at the free end. Eventually, the arc length *s* (along with the beam) and vertical deflection *Y* can be found as follows;

$$s=\sqrt{\frac{EI}{2F}}\int_0^{\varphi}\frac{\mathrm{d}\varphi}{\sqrt{\sin\varphi_o-\sin\varphi}}, \tag{2.23}$$

$$\frac{Y}{a}=\frac{1}{\sqrt{2}\alpha}\int_0^{\varphi_o}\frac{\sin\varphi \mathrm{d}\varphi}{\sqrt{\sin\varphi_o-\sin\varphi}}, \tag{2.24}$$

here $\alpha=\sqrt{\frac{Fa^2}{EI}}$, a = length of the beam and φ_o is the unknown slope at the free end of the beam.

2.6.1.3 Uncracked part of the double cantilever beam

The schematic diagram of the uncracked crack of DCB is shown in Fig. 2.3. Here, the shear stress may not be neglected, therefore it is necessary to consider the Timoshenko beam model here. Thus, the governing equation and respective boundary conditions of the uncracked of the DCB due to its root effect can be expressed as (Wang and Wang, 2013);

$$\frac{\mathrm{d}N}{\mathrm{d}x}=q, \qquad \frac{\mathrm{d}M}{\mathrm{d}x}=Q+q\frac{h}{2}, \qquad \frac{\mathrm{d}Q}{\mathrm{d}x}=p, \tag{2.25}$$

$$\frac{\mathrm{d}^2u_0}{\mathrm{d}x^2}=0,\ \frac{\mathrm{d}^2\varphi}{\mathrm{d}x^2}-\alpha^2\varphi=0,\ p=G^sA\frac{\mathrm{d}\varphi}{\mathrm{d}x} \qquad \text{here} \qquad \alpha^2=\frac{G^sA}{EI} \tag{2.26}$$

and the boundary Conditions are;

1. At $x = 0$, $N = 0$ and $M_{(0)}=FX_{(\varphi_0)}$ (2.27)
2. At $N=-\infty, N=0, M=0$ (2.28)

where p and q are, respectively the normal stress and the shear stress on the $z = 0$ plane, N is the resultant force along the x-direction, M is the bending moment, Q is the shear force on the beam cross-section, G^s is the effective shear stress and u_o is the displacement of the beam along the x-direction. Using boundary conditions and Eq. (2.26), we obtain;

$$N=0,\ M(x)=M_{(0)}e^{\alpha x},\ Q(x)=\alpha M_{(0)}e^{\alpha x} \tag{2.29}$$

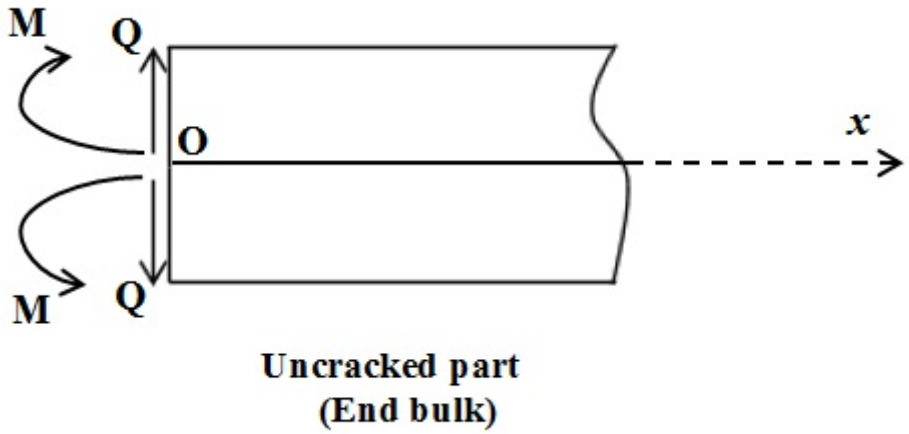

Figure 2.3 Schematic diagram of the root part of the DCB

2.6.2 Fracture of a double cantilever beam

Theoretically, the strain energy release rate G of a double cantilever beam using Euler-Bernoulli beam model and small deformation consideration is estimated as (Wang and Wang, 2016);

$$G = \frac{12F^2a^2}{Eh^3b^2} \tag{2.30}$$

where F is the concentrated endpoint force, a is the crack length, E is the material Young's modulus, h and b are the height and width of the beam respectively. The corresponding strain energy release rate using the Timoshenko beam model is given as (Wang and Wang, 2016);

$$G = \frac{12F^2a^2}{Eh^3b^2}\left[1+\sqrt{\frac{E\left(\frac{h}{a}\right)^2}{12G^s}}\right]^2 \tag{2.31}$$

With G^s as the effective shear modulus. Empirically the Mode I critical strain energy release rate is determined from the load and deflection data associated with the onset of

crack growth. Mathematically, taking the crack length to be the length of the beam as a and width b, the strain energy release rate of the double cantilever beam is given by (Stamoulis and Giannakopoulos, 2012);

$$G = F\frac{dY_{\max}}{bda} \tag{2.32}$$

Here, $Y_{\max}$ is the maximum end point vertical deflection of the cantilever beam.

2.7 2-D elasticity problem

In two-dimensional elasticity problems, most of the crack analyses are conducted in an infinite elastic medium and the material's boundaries do not interact with the crack. However, in many engineering applications, the crack analysis of finite elastic medium is of more interest. In particular, the elastic media of finite thickness/height is of much importance and has better practical relevance. In this section, some of the literature related to the mode III crack analysis in a 2D material layer is reviewed. The schematic diagram of an isotropic material layer of finite height and loading configuration is shown in Fig. 2.4. Consider a crack of length 2a placed at the mid plane of an isotropic layer with thickness (height) 2h. The boundaries of the layer are at $y = \pm h$ and reference axes are shown in Fig. 1a. The crack surfaces are subjected to the applied anti-plane shear stress (τ_1) as shown in Fig. 1b. For mode III crack the displacements are given as;

$$u_x = v_y = 0,\ w_z \neq 0 \tag{2.33}$$

where u_x, v_y and w_z are the displacements along x, y and z direction respectively. Two different boundary conditions are considered i.e. stress-free and clamped boundaries. The classical formulations as shown in this section are primarily reviewed in the following references (Sih and Chen, 1981; Li, 2001; Singh and Moodie, 1981). The conditions at the crack line ($y = 0$) are given as;

$$\tau_{yz}(x,0) = -\tau_1 \quad |x| < a \tag{2.34}$$

$$w_z(x,0) = 0 \quad |x| \geq a \tag{2.35}$$

The application of integral transform technique on the displacement solution that satisfies the non-trivial equilibrium equation in the *z*-direction $\left(\partial^2 w_z / \partial x^2 + \partial^2 w_z / \partial y^2 = 0\right)$is written as;

$$w_z(x,y) = \frac{2}{\pi}\int_0^\infty \left[A(s)e^{-sy} + B(s)e^{sy}\right]\cos(sx)\mathrm{d}s \qquad y \geq 0 \tag{2.36}$$

with the aid of (2.36), $\tau_{yz} = G^s\left(\partial w_z / \partial y\right)$may be expanded as;

$$\tau_{yz}(x,y) = -\frac{2}{\pi}G^s\int_0^\infty s\left[A(s)e^{-sy} - B(s)e^{sy}\right]\cos(sx)\mathrm{d}s \qquad y \geq 0 \tag{2.37}$$

Here G^s is the shear modulus of the material, $A(s)$ and $B(s)$ are constants to be determined from the boundary conditions.

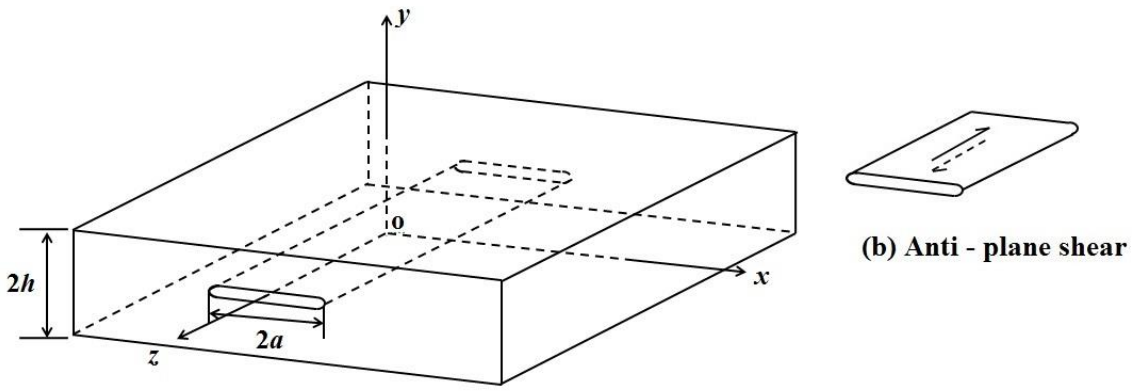

(a) Isotropic layer

Figure 2.4Schematic diagrams of an anti-plane cracked material layer

2.7.1 Stress-free boundaries

For stress-free boundaries, the shear stresses at the upper and lower edge (i.e. $y = \pm h$) of the layer for all values of x would be zero. Mathematically, it may be written as (Sih and Chen, 1981);

$$\tau_{yz}(x,\pm h) = 0, \quad |x| < \infty \tag{2.38}$$

Due to geometrical symmetry, only the upper half of the layer is considered. From Eqs. (2.37) and (2.38), it may be shown that $B(s) = e^{-2sh}A(s)$, so if $A(s) = E(s)/(1+e^{-2sh})$ then $B(s) = e^{-2sh}E(s)/(1+e^{-2sh})$, where $E(s)$ is an unknown function to be determined and sh is the product of s and h. The conditions in Eqs. (2.34) and (2.35) are satisfied if $E(s)$ is the solution of dual integral equations given as (Sih and Chen, 1981);

$$\int_0^\infty E(s)\cos(sx)ds = 0, \qquad x \geq a \tag{2.39}$$

$$\int_0^\infty sF_{sc}(s)E(s)\cos(sx)ds = \frac{\tau_1 \pi}{2G^s}, \qquad x < a \tag{2.40}$$

With $F_{sc}(s) = (1-e^{-2sh})/(1+e^{-2sh})$, here "$sc$" in subscript represents the "stress-free boundaries & classical" case.

2.7.2 Clamped Boundaries

The other practical situation that may be considered for analysis is the condition of clamped boundaries. For fixed boundaries the displacement in Eq. (2.36) must be zero at $y = \pm h$;

$$w_z(x,\pm h) = 0, \quad |x| < \infty \tag{2.41}$$

With the assumption of symmetry (only upper half is considered) and using Eqs. (2.36) and (2.41) we get $B(s) = -e^{-2sh}A(s)$, so if $A(s) = E(s)/(1-e^{-2sh})$, then $B(s) = -e^{-2sh}E(s)/(1-e^{-2sh})$ and corresponding dual integral equations (2.39) and (2.40)

may be obtained with $F_{cc}(s) = (1+e^{-2sh})/(1-e^{-2sh})$, here "*cc*" in subscript represents the "clamped boundaries & classical" case. It is evident that $F_{sc}(s)$ and $F_{cc}(s)$ are the inverses of each other.

2.8 Size-dependent fracture problems –Some recent advancements

Non-classical elasticity theories presented in section 2.2 i.e. non-local theory and strain gradient theory have been widely used to solve some of the size-dependent fracture problems. Applications of non-local elasticity theory are provided by Nejad and Hadi (2016) and the references therein. Since strain gradient theory is preferable as compared with non-local elasticity theory (stress gradient theory) as explained thoroughly in section 2.2, therefore some of the prominent applications of strain gradient theory for one and two-dimensional cases are reviewed here. On the other hand, more relevant research papers specific to the theme of the proceeding chapters are reviewed therein. The simplest strain gradient theory provided by Vardoulakis and Sulem (1995) is effectively employed by Papargyri-Beskou et al. (2003) and Giannakopoulos et al. (2006) to solve the boundary value beam bending problems. This theory has been successfully employed to observe size effects (Aifantis, 2011) in various engineering problems such as in twisted micro-wires and bent micro-cantilever beams (Aifantis, 1999). Some interesting information related to dislocation based-gradient elastic fracture mechanics for the anti-plane crack problem is discussed by Mousavi and Aifantis (2015). A comprehensive review of this gradient theory and applications of an internal length gradient across various scales is recently provided by Aifantis (2016).

Moreover, the emergence of flexoelectricity in modern era demands the application of higher order gradient theories such as strain gradient theory to adequately define the scale-dependent electro-mechanical coupling at a small scale. The pioneer work, extending the linear piezoelectric theory by incorporating the effect of

polarization gradient was presented by Mindlin (1969). On the other hand, Maranganti et al. (2006) included the polarization gradient as well as the strain gradient effect in their theoretical framework based on the variational principle. Their work established the mathematical framework of the non-uniform strain breaking the inversion symmetry and induced polarization in non-piezoelectric materials. Recently, Hu and Shen constructed a comprehensive model incorporating flexoelectricity, an electrostatic force (Hu and Shen, 2010) as well as surface effects (Shen and Hu, 2010). The theory proposed by Hu and Shen is actively sought by researchers to predict the mechanical behaviour of flexoelectric nano structures (Yan and Jiang, 2011; Yan and Jiang, 2013a; Zhang et al., 2014).

2.9 Summary

Past few decades have seen a tremendous advancement in the miniaturization of devices due to which the size of their structural components is greatly reduced. When the size of the structure is reduced to the micro and nano domain, its external dimensions become comparable to its internal ones for which the classical continuum theories are incapable to accurately determine its mechanical behaviour. Moreover, the strain gradients not only enhanced the electro-mechanical coupling effect in case of piezoelectric material but also induced it in case of non-piezoelectric materials. In order to establish the applications of micro/nano materials, it is necessary to evaluate their fracture characteristics based on strain gradient theory. In literature, most of the research works related to one-dimensional micro/nano structures, such as beams, are confined to small deformation. However, as shown in section 2.5, that small-scale structures are more prone to large deformation. Therefore, this work is intended to fill the research gap in analyzing the fracture behaviour of the double cantilever beam fracture mechanics specimen with the simultaneous incorporation of size and surface effects in piezoelectric (and hence flexoelectric) as well as the nonpiezoelectric materials.

For two dimensional structures, most of the models in the literature may be divided into two groups; The first group relates to the evaluation of closed form solution of an anti-plane crack in an infinite medium based on gradient elasticity theories and the second group comprises those classical studies which are conducted to evaluate the closed form solution of cracked elastic strip/layer (finite boundaries). Therefore, in this thesis the simplest strain gradient theory comprising two material parameters, related to volumetric and surface strain gradients, respectively, is applied to solve the mode III crack problem in an elastic isotropic layer. Finally, the study is extended to obtain the constitutive and governing equations in case of scale-dependent anti-plane cracked piezoelectric material layer.

CHAPTER 3

ANALYSIS OF DOUBLE CANTILEVER BEAM: THE SIZE EFFECT

Publications

Paper 1:

Joseph, R. P., Wang, B. L, & Samali, B., 2017. Size effects on double cantilever beam fracture mechanics specimen based on strain gradient theory. *Engineering Fracture Mechanics*, 169, 309-320. Doi: https://doi.org/10.1016/j.engfracmech.2016.10.013

Paper 2:

Joseph, R. P., Wang, B. L, & Samali, B., 2018. Size-dependent stress intensity factors in a gradient elastic double cantilever beam with surface effects, *Archive of Applied Mechanics*, 88(10), 1815-1828. Doi:https://doi.org/10.1007/s00419-018-1406-6

Relevance to the thesis

The papers included in this chapter stem the fundamental aspects associated with materials at the micro/nano scale i.e. the size effects and surface effects. In the first paper, the scale-dependent fracture analysis of a double cantilever beam made up of epoxy is carried out based on the strain gradient theory, as described in chapter 2. Due to the prominent surface effects i.e. surface elasticity and surface residual effect, the second paper, continues the research work incorporating the surface effects and makes relevant conclusions.

Paper 1: Size effects on double cantilever beam fracture mechanics specimen based on strain gradient theory

3.1 Abstract

This paper investigates large deformation of a cantilever beam which is further employed to study the fracture behaviour of double cantilever beam (DCB), based on strain gradient elasticity theory. Root effect of the DCB is also included for modelling and analyses. The numerical solutions of maximum tip deflection and strain energy release rate are presented. Results demonstrate that the consideration of large deformation is crucial at small scale, especially for more slender beams, as the bending behaviour of the beam, in that case, is different from the classical results. The strain gradients and root effect of the DCB are more prominent when the thickness of the beam is less than the material length scale parameter. The strain gradient model demonstrates significant stiffening behaviour at a smaller scale. In general, the root effect may not be neglected if the length to thickness ratio of the beam is smaller. Overall, the strain energy release rate of the gradient model, even with the incorporation of the root part, remains less than that of the non-gradient model. This conclusion is entirely different from the classical method that neglects the uncracked part of the DCB.

3.2 Introduction

Mechanical structures, such as beams are often subjected to large deformation which tends to induce geometrical nonlinearity, such that the relation between applied force and the curvature becomes non-linear. This non-linear behaviour will effectively change the stiffness of the structure. This response is shown to be dominant in literature for the case of clamped-clamped and simply supported beams. In contrast, the non-linear response of cantilever beam has received less attention comparatively (Villanueva et al., 2013). Cantilever beams used in micro and nanoelectromechanical (MEMS & NEMS) switches often undergo geometrical non-linearity. Using linear theory, the error in strain

energy release rate is found to be larger than 30%, as shown by mixed mode bending (MMB) tests. However, with the consideration of geometric nonlinearity, the redesigned MMB apparatus demonstrate the error to be less than 3% (Reeder and Crews Jr., 1991; Wang and Wang, 2016). The conventional mathematical treatment of analyzing a cantilever beam that assumes small deformation does not hold many complexities and hence exact solution can be derived quite comfortably. Nevertheless, with the addition of large deformation (geometrical nonlinearity), the problem involves the non-linear term that is difficult to solve analytically. In the past, several efforts have been devoted to addressing this issue, for instance, the analysis of large deformation of cantilever beams may be found in work of Belendez et al. (2002) and Landau and Lifshitz (1986). It was shown that the results, with the consideration of large deformation, were in better agreement with the experimental data upon comparison with the classical theory. Meanwhile different numerical techniques are also used to obtain large-deformation solutions for cantilever beam (Rao and Raju, 1977).

The bending behaviour of a cantilever beam in literature is often employed to study the fracture behaviour of the double cantilever beam (DCB) (Giannakopoulos and Stamoulis 2007; Stamoulis and Giannakopoulos, 2012). The DCB is typically considered to consist of two cantilevers beams attached to the root part (uncracked part) and is used broadly in experiments to determine the Mode I fracture toughness of the materials. In the tests of DCB, Devitt et al. (1980) found that the effect of geometric nonlinearity on the mode I fracture toughness of composite materials is sufficed for long cracks; similar findings are also mentioned in another reference (Williams, 1987). Furthermore, DCB is the most widely used test configuration for the study of crack propagation and arrest for composite materials and adhesives. Either in theoretical studies or experimental investigations, the DCB specimen has been found to be quite convenient to determine the mode I fracture toughness of homogenous, composite

laminates and adhesively bonded materials. Sebaey et al. (2011) used numerical methods to investigate the asymmetric crack growth in double cantilever beam tests of multidirectional composite laminates. The solution was the extension of the work previously conducted by Kanninen (1973). De Moura et al. (2008) employed numerical and experimental methods to investigate the fracture characteristics of the double cantilever wood beam specimen. De Morais (2011) developed a new analytical method to compute mode I critical strain energy release rates unaffected by fiber bridging. Wang and Wang (2013) derived the closed-form solutions of the strain energy release rate and stress intensity factors, incorporating the effect of surface residual stresses at a smaller scale, using Timoshenko beam theory for double cantilever beam specimen. Zhang et al. (2013) presented the stress intensity factors of double cantilever nanobeams via gradient elasticity theory.

Classical continuum elasticity theories assume that the stresses in a material point depend only on the strain components at the same point. It does not account for contributions from the strain gradients. However, according to the nonlocal theory of elasticity, the stress at a particular point depends on the strain not only at the same point but also on all the other points of the body (Togun, 2016; Wang et al., 2012). This phenomenon is more evident when the dimensions of the structure are scaled down to the micro (MEMS) and nano-domains (NEMS). In this case, the material microstructural length scales become comparable to the length scale of the deformation field which tends to cause non-homogenous and size-dependent mechanical behaviour (Giannakopoulos and Stamoulis, 2007). Size-dependent mechanical behaviour in micro-scale elements have extensively been observed in experiments (Fleck and Hutchinson, 1997; Lam et al., 2003; Li and Wang, 2009; Li et al., 2009; Ma and Clarke, 1995; McFarland and Colton, 2005) and it has been understood that the non-classical continuum theories such as the higher-order gradient theories and couple stress theory

can interpret this size depended on behaviour. The higher-order strain gradient theory was introduced by Mindlin (1965) that includes the effect of the first and second derivatives of the strain tensor on the strain energy density. The physical interpretation of higher order strain tensor, employed in gradient elasticity theories are recently provided by Polizzotto (2016). The simple gradient theory employed by Vardoulakis and Sulem (1995), combines the concepts of Form II of Mindlin theory, though it has a fewer number of elastic constants comparatively. Consequently, the theory presented by Vardoulakis and Sulem (1995) is much more convenient in applications (Giannakopoulos and Stamoulis, 2007) and therefore employed in this work. For one-dimensional case, the Cauchy (τ_x), double (μ_x) and total stresses (σ_x) are given for the beam bending in the following constitutive relations; Cauchy stresses; $\tau_x = E\varepsilon_x + l' E \frac{\mathrm{d}e_x}{\mathrm{d}x}$,double stresses $\mu_x = l' E\varepsilon_x + l^2 E \frac{\mathrm{d}e_x}{\mathrm{d}x}$ and total stresses; $\sigma_x = \tau_x - \frac{\mathrm{d}\mu_x}{\mathrm{d}x} = E\left(\varepsilon_x - l^2 \frac{\mathrm{d}^2\varepsilon_x}{\mathrm{d}x^2}\right)$. Here E is the Young's Modulus; ε_x is the axial strain in the beam due to bending, l and l' are the material characteristic length related to volumetric and surface elastic strain energy. The use of simpler, engineering-type gradient theories (Vardoulakis and Sulem, 1995) is much more convenient and valid as shown by Giannakopoulos et al. (2006).

Nanoscale devices and structure demand accurate design and development. For this, it is vital to explore their characteristics thoroughly. The experimental investigation of the mechanical response, using modern scientific manipulations (Cheng et al., 2008; Jing et al., 2006; Kang and Xie, 2010; Voyiadjis et al., 2010) and atomic/molecular modelling (Behzadi and Rafii, 2008; Fermeglia, 2008; Popescu, 2007) are effective method to determine the size-dependent behaviour of the structure at micro/nano scale. However, the application of theoretical approaches for modelling nano structures is considered more attractive because of their lesser complexity and their capability to be

implemented at all the possible length scales. Meanwhile, according to the author's knowledge, most of the works on micro and nano beam, based on nonlocal elasticity theories are limited to small deformation of the structures. In particular, the nonlinear analyses (large deformation) of micro and nano beams based on strain gradient theories still demand updates. Therefore, in this article, the influence of strain gradients, in terms of material length scale parameters, is introduced in Euler's model to investigate the non-linear deformation of the cantilever beam. Next, the study is extended to explore the fracture behaviour of a double cantilever beam. The material properties of epoxy are used as an example. The schematic diagram of the DCB is shown in Fig. 2.2. Numerical results are obtained and presented for strain energy release rate for various beam configurations. Finally, the effect of the root part (uncracked part) of a double cantilever beam on the strain energy release rate is further estimated to conclude the study.

3.3 Theoretical formulations

The formulation is based on Euler-Bernoulli theorem, for which the moment–curvature relation of the beam along the *x*-axis is given as $EI\dfrac{\mathrm{d}\varphi}{\mathrm{d}s}=M$. The moment at any point $X_{(s)}$ along the beam may be written as $M = F.X_{(s)}$, upon differentiation and using $\mathrm{d}X_{(s)}/\mathrm{d}s = \cos\varphi$, we get;

$$EI\frac{\mathrm{d}^2\varphi}{\mathrm{d}s^2}+F\cos\varphi=0 \qquad (3.1)$$

Above equation is the non-linear differential equation that governs the deflection of a cantilever beam made of a linear elastic material subjected to a vertical concentrated load at the free end. Eventually, the arc length *s* (along with the beam) and vertical deflection *Y* can be found as follows;

$$s=\sqrt{\frac{EI}{2F}}\int_0^{\varphi}\frac{\mathrm{d}\varphi}{\sqrt{\sin\varphi_o-\sin\varphi}}, \qquad (3.2)$$

$$\frac{Y}{a}=\frac{1}{\sqrt{2}\alpha}\int_0^{\varphi_o}\frac{\sin\varphi \mathrm{d}\varphi}{\sqrt{\sin\varphi_o-\sin\varphi}},\quad \text{here}\,\alpha=\sqrt{\frac{Fa^2}{EI}}\text{, } a \text{ = length of the beam} \qquad (3.3)$$

Here $\varphi_o$is the unknown slope at the free end of the beam. Eqs. (3.2) and (3.3) can be split into complete and incomplete elliptic integrals of the first and second kinds that can be solved numerically. Alternatively Eq. (3.1) may be solved numerically to get φ, that may be used to get deflection by the following relation;

$$Y=\int_0^a \sin(\varphi)\mathrm{d}s \qquad (3.4)$$

Primarily, due to the aforementioned size effect at the micro/nano scale, the strain gradients must be incorporated in the formulations to accurately predict the structural behaviour. In general, the higher order strain-gradient models, available in the literature, are majorly concerned with second-order strain gradients. These models have been used in elasticity, plasticity and damage tolerance. As explained in the introduction, the theory presented by Vardoulakis and Sulem (1995) is much more convenient in applications (Giannakopoulos and Stamoulis, 2007) and therefore employed in this work. For one-dimensional case, combined with linear elastic material behaviour the constitutive equation can be written as (Aifantis, 1999; Askes et al., 2002);

$$\sigma=E(\varepsilon-l^2\nabla^2\varepsilon) \qquad (3.5)$$

whereσ is the axial stress, ε is the axial strain, E is the Young's modulus, l is the material parameter with the dimension of length that reflects the micromechanical properties of the material and $\nabla^2=\partial^2/\partial x^2+\partial^2/\partial y^2+\partial^2/\partial z^2$ is the Laplacian operator. Eq. (3.5) is usually taken as a mean of smoothing of heterogeneity. On the other hand, strain gradient theory may also be employed to introduce heterogeneity into the continuum. For the latter case, the second order gradient model is of the type;

$\sigma = E(\varepsilon + l^2\nabla^2\varepsilon)$ .The sign of the higher-gradient term determines the character of the higher-gradient model. The gradient model with the negative sign has the better properties from the point of view of stability and uniqueness (Askes et al., 2002) and, therefore used in this study. The expression of strain for Euler-Bernoulli beam is given as, $\varepsilon = zk = z\dfrac{\mathrm{d}\varphi}{\mathrm{d}s}$, where *k* is the radius of curvature, φ is the deformed angle. Though a beam is defined in a 2D geometrical space, the *xy*-plane, the problem still remains in 1D as the resulting deflection is solely the function of "*s*" or "*x*". Therefore, the ∇^2 operator is reduced to cater only 1D gradient. The constitutive equation for a cantilever beam (provided length to height ratio $\geq$ 10 (Christensen and Bastien, 2015)) for 1D cases i.e. $\sigma_{yy} = \sigma_{zz} = \sigma_{yz} = \sigma_{xz} = \sigma_{xy} = 0$ according to Eq. (3.5) may be written as;

$$\sigma_{xx} = Ez\left[\frac{\mathrm{d}\varphi}{\mathrm{d}s} - l^2\frac{\mathrm{d}^3\varphi}{\mathrm{d}s^3}\right] \tag{3.6}$$

Bending moment at *x* is given as, $M = \int_A \sigma_{xx} z\mathrm{d}A$. Using Eq. (3.6) in bending moment equation and upon integration over the cross-section area *A*, one gets;

$$M = EI\left[\frac{\mathrm{d}\varphi}{\mathrm{d}s} - l^2\frac{\mathrm{d}^3\varphi}{\mathrm{d}s^3}\right] \tag{3.7}$$

Equation (3.7) gives the higher order, non-classical moment incorporating the effects of strain gradients. Here $I = \int_A z^2\mathrm{d}A$ is the second moment of cross-sectional area. Differentiating the above equation with respect to *s*, we get; $\dfrac{\mathrm{d}M}{\mathrm{d}s} = EI\left[\dfrac{\mathrm{d}^2\varphi}{\mathrm{d}s^2} - l^2\dfrac{\mathrm{d}^4\varphi}{\mathrm{d}s^4}\right]$.

From Fig. 3.1, one can obtain;

$$EI\left[\frac{\mathrm{d}^2\varphi}{\mathrm{d}s^2} - l^2\frac{\mathrm{d}^4\varphi}{\mathrm{d}s^4}\right] = -F\cos\varphi \tag{3.8}$$

Here we did not consider the dependence of *E* on size. In order to simplify the strain gradient model, *EI* was assumed to be constant as done by some other researches as well (Kahrobaiyan et al., 2011; Kong et al., 2009), our model applies to these materials without significant dependence of *E* on size. Now, the boundary conditions of the DCB can be described as follows; At clamped end i.e. $s = 0$, the slope or the boundary classical moments of the beam have to be specified (Kong et al., 2009) i.e. the rotation of the beam is zero $\varphi = 0$, and the trivial natural boundary conditions for the non-classical terms may be written as i.e. $\frac{\mathrm{d}^3 w}{\mathrm{d}x^3} = 0$, where *w* is the deflection of the beam. However, for large deformation, it may estimate to be $\frac{\mathrm{d}^2 \varphi}{\mathrm{d}s^2} = 0$ (since $\varphi = \mathrm{d}w/\mathrm{d}s$). Meanwhile, at the free end i.e. $s = a$, $\frac{\mathrm{d}\varphi}{\mathrm{d}s} = 0$ (Belendez et. al, 2002) and the non-classical or higher order moment as depicted in Eq. (3.7) would also be zero at the free end that gives $\frac{\mathrm{d}\varphi}{\mathrm{d}s} - l^2 \frac{\mathrm{d}^3 \varphi}{\mathrm{d}s^3} = 0$. Overall, the boundary conditions may fairly be written as;

At $s = 0$: $\varphi = 0$, $\frac{\mathrm{d}^2 \varphi}{\mathrm{d}s^2} = 0$

At $s = a$: $\frac{\mathrm{d}\varphi}{\mathrm{d}s} = 0$, $\frac{\mathrm{d}\varphi}{\mathrm{d}s} - l^2 \frac{\mathrm{d}^3 \varphi}{\mathrm{d}s^3}$ or $\frac{\mathrm{d}\varphi}{\mathrm{d}s} = 0, \frac{\mathrm{d}^3 \varphi}{\mathrm{d}s^3} = 0$

The nonlinear boundary value problem as presented in Eq. (3.8) and respective boundary conditions is numerically solved using a finite difference method that implements a three-stage Lobatto IIIa collocation formula. Lobatto methods are the numerical integration methods to get the approximate solution of differential equations at the two end points t_n and t_{n+1} of each interval of integration $[t_n, t_{n+1}]$. These methods are based on trapezoidal quadrature rule. There are several types of Lobatto methods

i.e. Lobatto IIIA, IIIB, IIIC and IIIC* that are usually characterized by coefficients being used in the approximated solution. Lobatto IIIA method is usually considered for boundary value problem due to their good stability properties. The Matlab code bvp4c for boundary value problems that have been used in this work is based on the 3 stage Lobatto IIIA method. Further details of this and other relevant methods are provided by Shampine et al. (2000).

3.4 Results and Discussion

To illustrate the bending behaviour of a cantilever beam under large deformation, the material characteristic length (l) is taken to be 17.6 μm (Kong et al., 2009). The values of force F (concentrated vertical force) and height h are chosen in such a way that the beam remains elastic everywhere. The static rotation of a cantilever beam, normalized by the classical result at the free end of the beam i.e. $Fa^2/(2EI)$ is presented in Fig. 3.1. The curves are depicted for $b/h = 2$, here b is the width of the beam. The normalized deformation curves are obtained for different h/l ratios ($a/h = 20$). It can be seen that, for smaller h/l ratios, the strain gradient beam models are stiffer than the classical models. The normalized deformations are shown to be increasing with increasing h/l, with the maximum deformation becoming almost comparable when $h/l \approx 1$. In order to further establish the negligence of strain gradient effects when $h >> l$ and the effect of geometrical non-linearity with increased load factor F_o ($F_o = Fa^2/2(EI)$), the normalized maximum deflections for beams with various h/l ratios ($a/h = 20$) are numerically obtained using Eq. (3.4) and are shown in Fig. 3.2. Here Y_g and Y represent the deflection obtained with strain gradient and non-gradient model. Fig. 3.2 shows that the normalized tip deflection increases with the increasing load factor F_o, signifying greater effect of geometrical non-linearity (larger non-gradient deflection) at enhanced loads. Meanwhile, it may be seen that with a higher h/l ratio, as high as 10, the maximum deflection of the gradient and non-gradient model are equal, demonstrating negligible

strain gradient effects. The comparison of Y_g with Y and Y_g with classical formulation (small deformation & without strain gradient effect) Y_o ($Y_o = Fa^3/(3EI)$) for various beam configurations is established in Fig. 3.3. The non-dimensional parameter as abscissa is defined for convenience, given as $3Fa^2/(Eh^4)$, also for comparison, the h/l ratio is considered to be less than or equal to 1. This was done to precisely illustrate the effect of beam geometry on its mechanical behaviour, particularly on a smaller scale ($h \leq l$). The normalized maximum deflection Y_g/Y versus the non-dimensional parameter $3Fa^2/(Eh^4)$ is plotted in Fig. 3.3a. It is clear from Fig. 3.3a that the effects of strain gradient are more evident when the length to thickness ratio a/h is small, demonstrating small deflections for gradient structure and hence depicting stiffer response. The maximum deflection for strain gradient beam would approach as that of the non-gradient beam when the length of the beam is very large.

It can also be seen that the difference between the results predicted by the model with & without strain gradients effects (large deformation) are significant when h/l is low while the difference diminishes when h/l approaches1(for the presented gradient model). The strain gradients effects are shown to be more prominent when $h/l \leq 0.2$. For instance when $h/l = 0.05$ and $3Fa^2/(Eh^4) = 1$, the strain gradient formulation predicts almost one-third of the deflection obtained from non-gradient formulation. Fig. 3.3b illustrates the comparison of results obtained from strain gradient model with the classical model (small deformation & without strain gradient effect). It is shown that for smaller beam lengths, the Y_g/Y and Y_g/Y_o are identical, indicating that the large deformation and classical model predict the same results. However, with the increase of beam length (hence a/h ratio), the beam will undergo large deformation and hence the classical theory would overestimate the end point deflection. For each curve, the peak point is evident in Fig. 3.3b, which demonstrates the onset of a point at which deficiency of the classical model to accurately predict the large deformation becomes

noticeable. Furthermore, it may fairly be concluded that when $h/l \geq 0.2$, the factor with which the classical model would overestimate the deflection converge to the same point. Next, the accurate tip deflections of a cantilever beam will be used to estimate the fracture behaviour of a double cantilever beam in the following section.

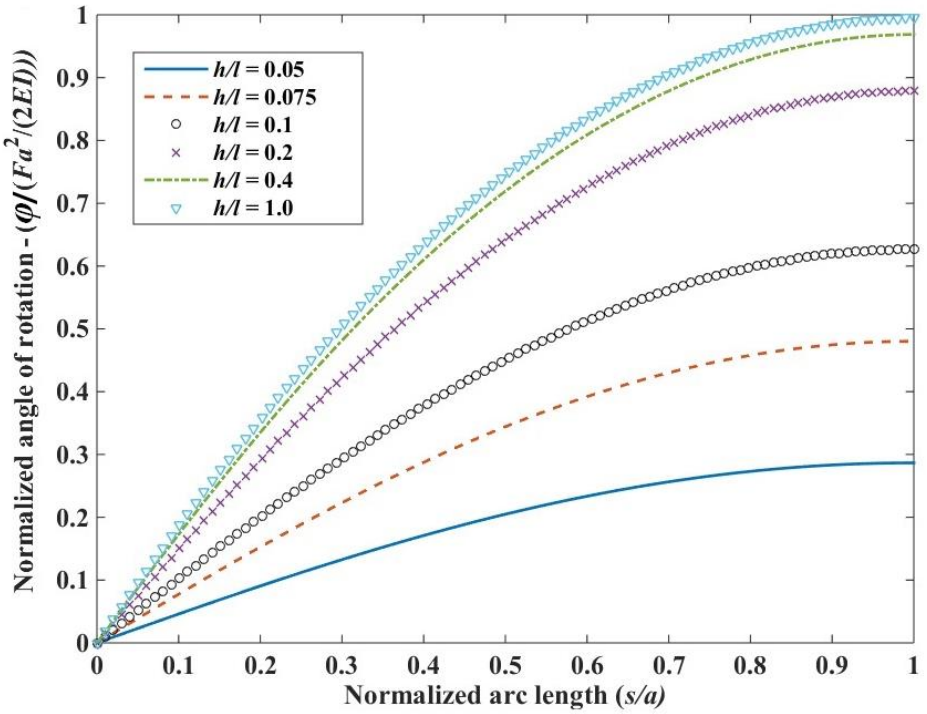

Figure 3.1 Normalized angle of rotation along the beam for strain gradient model

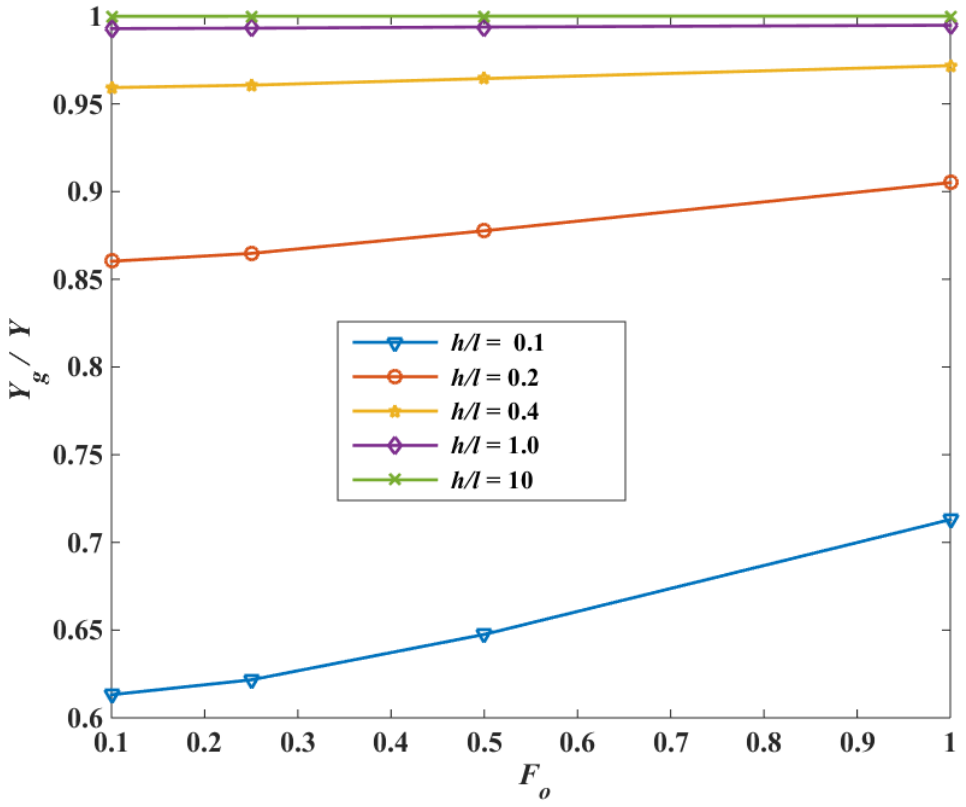

Figure 3.2 Normalized tip deflection against the load factor F_o

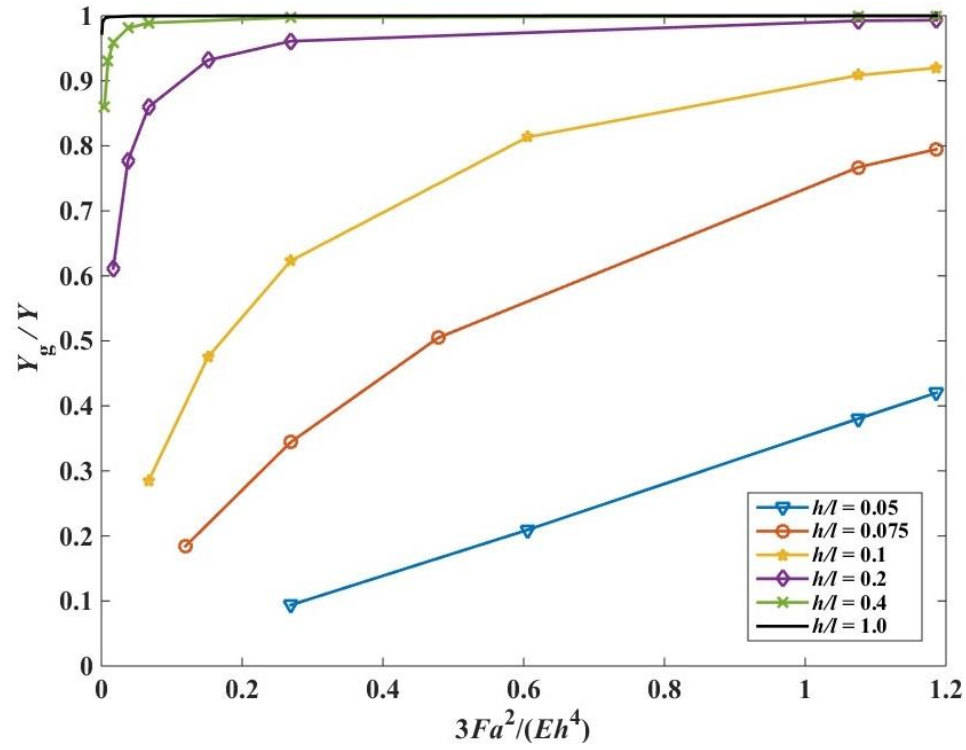

Figure 3.3a Maximum tip deflection (large deformation) versus the parameter $3Fa^2/(Eh^4)$of gradient model, normalized with the non-gradient results (large deformation)

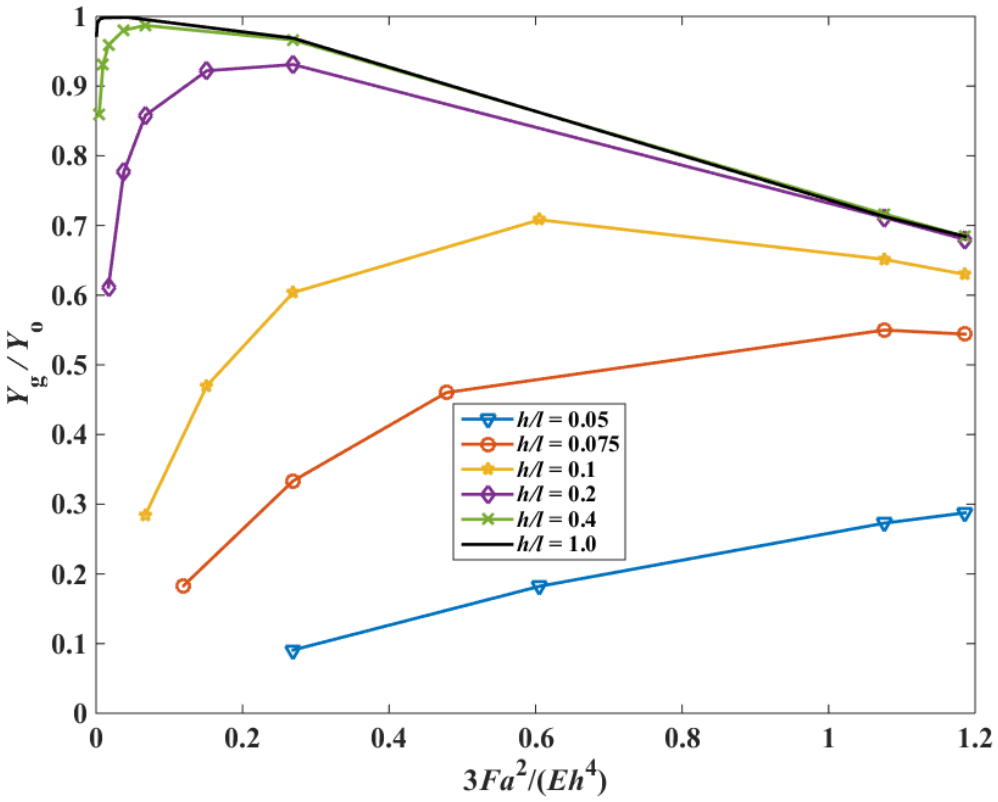

Figure 3.3b Maximum tip deflection (large deformation) versus the parameter $3Fa^2/(Eh^4)$of gradient model, normalized with the classical results

3.5 Fracture analysis of a double cantilever beam

As illustrated in the previous section the size effect on the mechanical behaviour of micro beam, the same influences may also be witnessed in fatigue and fracture properties as well. Since it has been demonstrated, in comparison with classical theories, the strain gradient theory predicts smaller strains (Giannakopoulos and Stamoulis, 2007) and hence longer life for small-scale components according to the approach introduced by Basquin(1910). Zhang et al. (2006) experiments demonstrated a pronounced strengthening in the fatigue strength of small-scale metallic components. The results were credited to the fine grain size and small geometrical dimensions. Stamoulis and Giannakopoulos (2012) adopted strain gradient elasticity formulations to study the size effect and length scale in fracture and fatigue of metals. They also employed Strain gradient theory to analytically investigate the microstructural size

effects in analyzing cantilever bending and cracked bar uniaxial tension (Giannakopoulos and Stamoulis, 2007). In recent times several attempts have been made to evaluate fracture analysis of complex geometries using advance numerical techniques (Fleming et al., 1997; Joseph et al., 2014) and to cater the size effect on the fracture properties at small scale as investigated by Giannakopoulos and Stamoulis (2007), Stamoulis and Giannakopoulos(2012) and Guha et al. (2013), it is evident that this subject is still open for innovation and updates.

3.5.1 Numerical results and discussion

Strain energy release rate may be evaluated using $G = dU_1/bda$, where $U_1 = \frac{1}{2}\int_0^a U\mathrm{d}x$ with U as the specific intrinsic energy (Askes et al., 2002). Alternatively, taking the crack length to be the length of the beam as a and width b, the strain energy release rate of the double cantilever beam is given by $G = F\,(\mathrm{d}Y_{max}/b\mathrm{d}a)$ (Stamoulis and Giannakopoulos, 2012). Meanwhile, the classical Euler beam theory solution is given by $G_o = 12F^2a^2/(Eh^3b^2)$ (Wang and Wang, 2013)**.** The method adopted is based on the notion that the external work done (F^*Y_{max}) will be stored in the body as potential energy.

Double cantilever beam may be assumed to consist of two cantilever beams with the configuration and loading as shown in the previous chapter (Fig. 2.2). Figure 3.4 displays, the normalized energy release with respect to the non-dimensional parameter $3Fa^2/(Eh^4)$. For comparison, as in the previous section, the results for strain gradient & non-gradient model (large deformation) and classical theory are given. Here the notations G_g, G and G_o are used to represent the energy release rate (G) for large deformation strain gradient model, large deformation non-gradient model and classical model (small deformation & without strain gradient effect) respectively. Evidently from Fig. 3.4a, the influence of strain gradients on the strain energy release becomes more

prominent when *h/l* is low i.e. for thinner beams. In particular, the strain gradients effect cannot be neglected when $h/l \leq 0.2$, even when the ratio between the length to the height of the beam is higher. Also, for $h/l \geq 0.2$, the strain gradients effect tends to diminish rapidly and eventually the strain energy release rate would be the same as predicted by large deformation formulation (without strain gradients). Meanwhile, the strain gradients effect diminishes when $h/l \approx 1$ (for the presented gradient model). Such observation is considerably different when the strain gradients results are compared with the classical ones for comparatively larger beams. From Fig. 3.4b, for larger *a/h*, the classical theory will tend to overestimate the strain energy release rate. This can be seen quite clearly as a peak point on each curve. For $h/l \leq 1$, this peak appeared quite early in the curve, depicting a particular *a/h* ratio, beyond which the classical model tends to overestimate the mechanical behaviour.

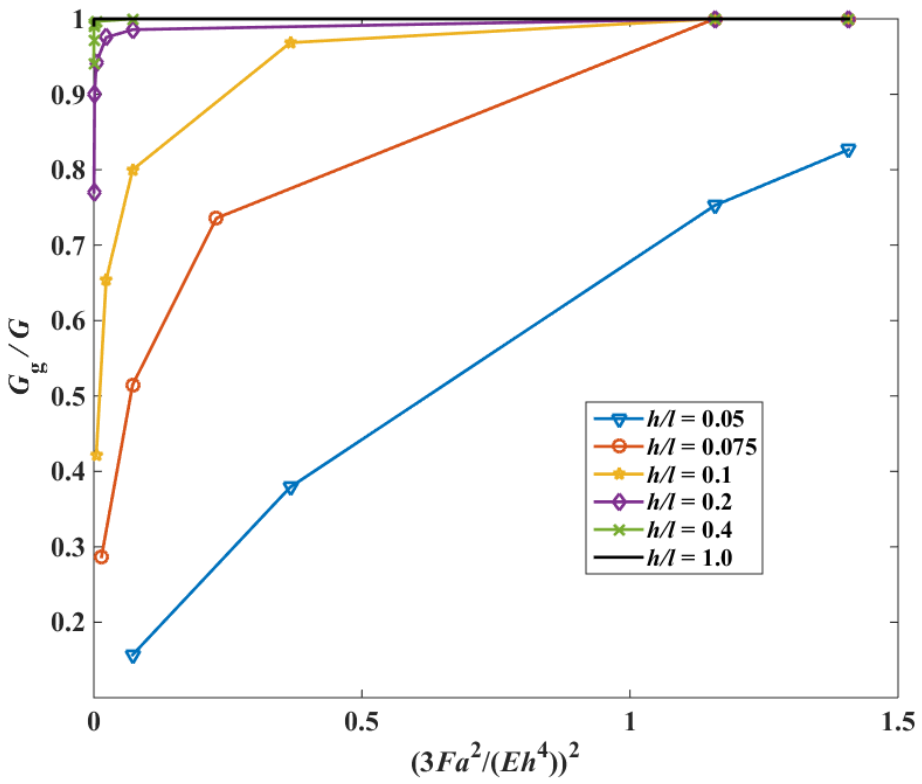

Figure 3.4a Strain energy release rate (large deformation) versus the parameter $(3Fa^2/(Eh^4))^2$of gradient model, normalized with non-gradient results (large deformation)

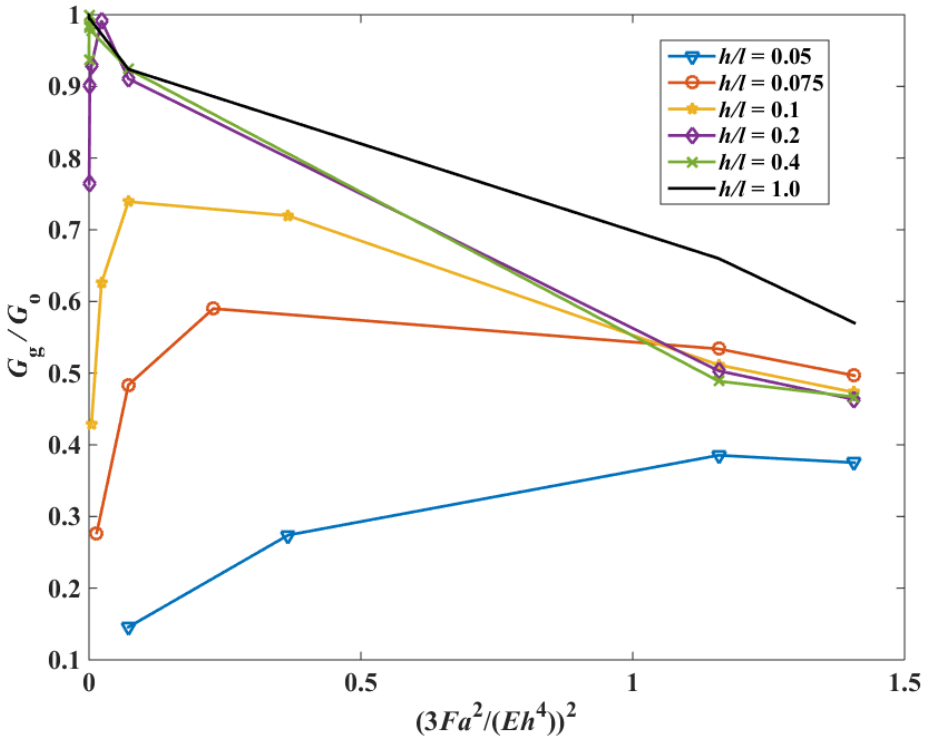

Figure 3.4b Strain energy release rate (large deformation) versus the parameter $(3Fa^2/(Eh^4))^2$ of gradient model, normalized with the classical results

3.5.2 Root Effect of the DCB

For the uncracked part of the DCB (Fig. 2.3), the strain gradient effect is much smaller as compared to that of the cracked part of DCB; therefore the strain gradient effect is neglected here. Thus, the governing equation and respective boundary conditions of the uncracked of the DCB due to its root effect, based on Timoshenko beam theory are shown in section 2.6.1.3. The potential energy of the root part can be expressed as;

$$U_2 = 2\int_{-\infty}^{0} \frac{M^2}{2EI}\mathrm{d}x + 2\int_{-\infty}^{0} \frac{Q^2}{2G^s A}\mathrm{d}x \qquad (3.9)$$

Here E is the Young's Modulus, G^s is the shear modulus, A is the area of cross section and I is the moment of inertia of the beam. It is interesting to note that, for the root part, the integral varies from negative infinity to zero as per the coordinate system. From Eq. (2.29) and using $M_{(o)} = F.X$ we get;

$$U_2 = \frac{F^2 X_{(\varphi_o)}^2}{\sqrt{EIG^s A}}, \text{ here } X_{(\varphi_o)} = \int_0^a \frac{dX}{ds} ds = \int_0^a \cos\varphi(s) ds \tag{3.10}$$

Here $X_{(\varphi_o)}$is the horizontal tip position at deflection φ_o.

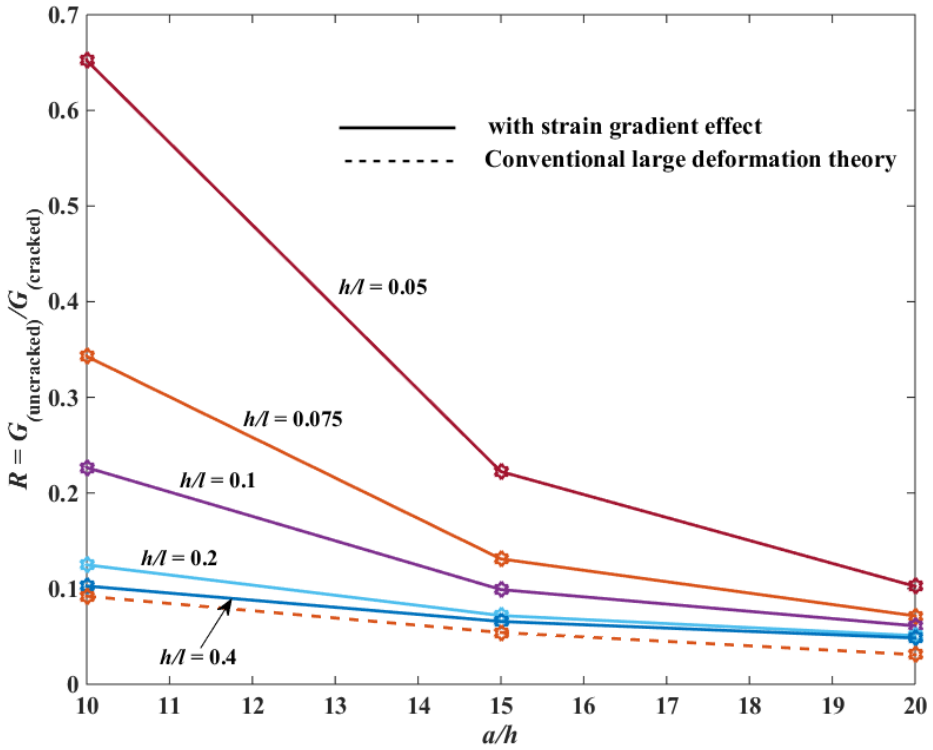

Figure 3.5 Variation of *R* versus *a*/*h*

Now the effect of uncracked part of the DCB on its fracture behaviour is numerically investigated. The ratio of the strain energy release rate contributed by the uncracked part to the strain energy release rate contributed by the cracked part of DCB is defined as *R*. Variations of *R* versus *a/h* for different *h/l* ratios are plotted in Fig. 3.5. It may be seen that for the non-gradient model, *R* approaches 0.05 approximately, when the beam length to thickness ratio approaches 20, demonstrating a neglecting root effect of the DCB. However, when the dimensions of the DCB are very small i.e. for $h/l \leq 0.2$ &$a/h \leq 20$, the value of *R* may not be neglected even though the beam length to thickness ratio is higher. Interestingly, when $h/l \leq 0.1$ and the smaller *a/h*, the

contribution of the root part is shown to be quite prominent and hence should be incorporated in the formulations when dealing with the strain gradient theory. For smaller h/l and a/h ratios, for instance h/l = 0.05 and a/h = 10, it can be seen that the energy release rate of uncracked part is 0.65 (approx.) times as that of cracked part but the overall response of the gradient model will remain stiffer. The comparison of gradient model with and without root effect with the non-gradient (large deformation) model is shown in Fig. 3.6. This observation clearly demonstrates the stiffening response of a structure at a smaller scale (whether root effect is included or not) and is completely different from the classical results. Similarly, it has been observed that for h/l> 0.2 when the length to thickness ratio of the beam exceeds 20 the energy release rate of the uncracked part is small as compared to that of the cracked part and hence may be neglected for the sake for model's simplicity.

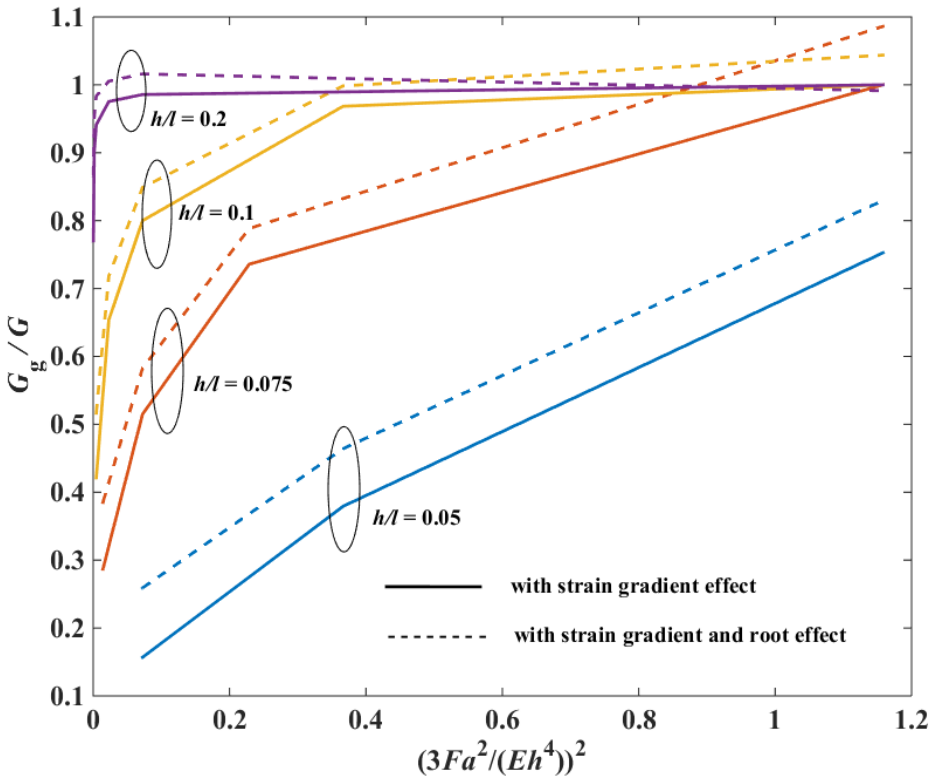

Figure 3.6 Ratio of strain energy release rate with/without root effect with $(3Fa^2/(Eh^4))^2$

3.6 Summary

Strain gradients contribution on the large deformation of the cantilever beam is investigated and compared with the conventional large deformation (without strain gradients) and classical models. The gradient model is shown to enhance the stiffness of the beam. This size effect of the cantilever beam is later employed to investigate the fracture behaviour of a double cantilever beam. The effect of strain gradients on the strain energy release rate is evaluated. Both the cracked and uncracked portions of the DCB are included. The strain energy release rate is numerically estimated by using Euler beam model. Due to small strains, the gradients effect is ignored for the uncracked part of the DCB. Results show that the strain gradients effects are prominent when $h/l \leq 0.2$, however, the effects tend to diminish when the length to thickness ratio of the DCB increases. In particular, the strain gradients effect cannot be neglected when $h/l \leq 0.2$. Moreover, it is shown that the consideration of large deformation is essential for longer beams. The root effect also enhances the normalized strain energy release rate. It is observed that for $h/l \leq 0.2$, uncracked part plays a dominant role in the fracture behaviour of the DCB and it must not be ignored. However, for $h/l > 0.2$, root effect may only be ignored provided $a/h \geq 20$. This observation is completely different from the classical result, which suggests that the root effect can be neglected if beam length to thickness ratio is higher (Wang and Wang, 2013). The results of this paper are useful for the determination of the fracture toughness of micro/nanoscale materials and an explanation of the test data of the DCBs.

Reference

Aifantis, E.C., 1999. Strain gradient interpretation of size effects. *International Journal of Fracture*, 95, 299-314.

Anderson, T.J., Nayfeh, A. H. & Balachandran, B., 1996. Experimental verification of the importance of the nonlinear curvature in the response of a cantilever beam. *Journal of Vibration and Acoustics*, 118, 21-27.

Askes, H, Suiker, A.S. J. & Sluys, L.J., 2002. A classification of higher-order strain-gradient models–linear analysis. *Archive of Applied Mechanics*, 72, 171-188.

Basquin, O.H., 1910. The exponential law of endurance tests. Paper presented at the proc. *ASTM*.

Behzadi, S. H. & Rafii-Tabar, H., 2008. Atomistic modelling of crack propagation in a randomly rough nano-scale metallic surface. *Journal of Molecular Graphics and Modelling*, 27, 356-363.

Beléndez, T., Neipp, C. & Beléndez, A., 2002. Large and small deflections of a cantilever beam. *European Journal of Physics*, 23, 371.

Cheng, M.N., Cheung, C.F., Lee, W. B., To, S. & Kong, L.B., 2008. Theoretical and experimental analysis of nano-surface generation in ultra-precision raster milling. *International Journal of Machine Tools and Manufacture*, 48, 1090-1102.

Christensen, J. & Bastien, C., 2015. Nonlinear Optimization of Vehicle Safety Structures: Modeling of Structures Subjected to Large Deformations. Butterworth-Heinemann USA.

De Morais, A.B., 2011. A new fibre bridging based analysis of the Double Cantilever Beam (DCB) test. *Composites Part A: Applied Science and Manufacturing*, 42, 1361-1368.

De Moura, M.F.S.F., Morais, J.J. L. & Dourado, N., 2008. A new data reduction scheme for mode I wood fracture characterization using the double cantilever beam test. *Engineering Fracture Mechanics*, 75, 3852-3865.

Devitt, D.F., Schapery, R. A. & Bradley, W.L., 1980. A method for determining the mode I delamination fracture toughness of elastic and viscoelastic composite materials. *Journal of Composite Materials*, 14, 270-285.

Fermeglia, M., 2008. Multiscale molecular modeling: a tool for the design of nano structured materials. *Computer Aided Chemical Engineering*, 25, 725.

Fleck, N. A. & Hutchinson, J.W., 1997. Strain gradient plasticity. *Advances in Applied Mechanics*, 33, 296-361.

Fleming, M., Chu, Y.A., Moran, B., Belytschko, T., Lu, Y. Y. & Gu, L., 1997. Enriched element-free Galerkin methods for crack tip fields. *International Journal for Numerical Methods in Engineering*, 40, 1483-1504.

Giannakopoulos, A. E., Amanatidou, E. & Aravas, N., 2006. A reciprocity theorem in linear gradient elasticity and the corresponding Saint-Venant principle. *International Journal of Solids and Structures*, 43, 3875-3894.

Giannakopoulos, A. E. & Stamoulis, K., 2007. Structural analysis of gradient elastic components. *International Journal of Solids and Structures*, 44, 3440-3451.

Guha, S., Sangal, S. & Basu, S., 2013. Finite Element studies on indentation size effect using a higher order strain gradient theory. *International Journal of Solids and Structures*, 50, 863-875.

Jia, X.L., Yang, J. & Kitipornchai, S., 2011. Pull-in instability of geometrically nonlinear micro-switches under electrostatic and Casimir forces. *Acta Mechanica*, 218, 161-174.

Jia, X. L., Yang, J., Kitipornchai, S. & Lim, C.W., 2010. Free vibration of geometrically nonlinear micro-switches under electrostatic and Casimir forces. *Smart Materials and Structures*, 19, 115028.

Jing, G.Y., Duan, H.L., Sun, X.M., Zhang, Z.S., Xu, J., Li, Y. D. & Yu, D.P., 2006. Surface effects on elastic properties of silver nanowires: contact atomic-force microscopy. *Physical Review B*, 73, 235409.

Joseph, R.P., Purbolaksono, J., Liew, H. L., Ramesh, S. & Hamdi, M., 2014. Stress intensity factors of a corner crack emanating from a pinhole of a solid cylinder. *Engineering Fracture Mechanics*, 128, 1-7.

Kahrobaiyan, M. H., Asghari, M., Rahaeifard, M. & Ahmadian, M.T., 2011. A nonlinear strain gradient beam formulation. *International Journal of Engineering Science*, 49, 1256-1267.

Kang, Y., Xie, H., 2010. Micro and nano metrology in experimental mechanics. *Optics and Lasers in Engineering*, 48, 1045.

Kanninen, M.F., 1973. An augmented double cantilever beam model for studying crack propagation and arrest. *International Journal of Fracture*, 9, 83-92.

Kong, S., Zhou, S., Nie, Z., Wang, K., 2009. Static and dynamic analysis of micro beams based on strain gradient elasticity theory. *International Journal of Engineering Science*, 47, 487-498.

Lam, D.C.C., Yang, F., Chong, A.C. M., Wang, J. & Tong, P., 2003. Experiments and theory in strain gradient elasticity. *Journal of the Mechanics and Physics of Solids*, 51, 1477-1508.

Li, X. F. &Wang, B.L., 2009. Vibrational modes of Timoshenko beams at small scales. *Applied Physics Letters*. 94, 101903

Li, X.F., Wang, B. L. & Lee, K.Y., 2009. Size effects of the bending stiffness of nanowires. *Journal of Applied Physics*. 105, 074306

Landau, L. D. & Lifshitz, E.M., 1986. Theory of Elasticity, vol. 7. *Course of Theoretical Physics*, 3, 109.

Ma, Q. & Clarke, D.R., 1995. Size dependent hardness of silver single crystals. *Journal of Materials Research*, 10, 853-863.

McFarland, A. W. & Colton, J.S., 2005. Role of material microstructure in plate stiffness with relevance to microcantilever sensors. *Journal of Micromechanics and Microengineering*, 15, 1060.

Mindlin, R.D., 1965. Second gradient of strain and surface-tension in linear elasticity. *International Journal of Solids and Structures*, 1, 417-438.

Polizzotto, C., 2016. A note on the higher order strain and stress tensors within deformation gradient elasticity theories: physical interpretations and comparisons. *International Journal of Solids and Structures*, 90, 116-121

Popescu, M., 2007. The atomic scale modelling of nanomaterials. *Journal of Physics and Chemistry of Solids*, 68, 687-694.

Rao, G. V. & Raju, K.K., 1977. Variational formulation for the finite deflection analysis of slender cantilever beams and columns. *Aeronautical Society of India, Journal*, 29, 133-135.

Reeder, J.R., & Crews Jr, J., 1991. Nonlinear analysis and redesign of the mixed-mode bending delamination test.

Sebaey, T.A., Blanco, N., Lopes, C. S. & Costa, J., 2011. Numerical investigation to prevent crack jumping in Double Cantilever Beam tests of multidirectional composite laminates. *Composites Science and Technology*, 71, 1587-1592.

Shampine, L. F., Kierzenka, J. & Reichelt, M.W., 2000. Solving boundary value problems for ordinary differential equations in MATLAB with bvp4c. Tutorial notes.

Stamoulis, K., &Giannakopoulos, A.E., 2012. A study of size effects and length scales in fracture and fatigue of metals by second gradient modelling*. *Fatigue and Fracture of Engineering Materials and Structures*, 35, 852-860.

Togun, N., 2016. Nonlocal beam theory for nonlinear vibrations of a nanobeam resting on elastic foundation. *Boundary Value Problems*,

Vardoulakis, I. & Sulem, J., 1995. Bifurcation Analysis in Geomechanics. London: Blackie/Chapman and Hall.

Villanueva, L.G., Karabalin, R. B., Matheny, M.H., Chi, D., Sader, J. E. & Roukes, M.L., 2013. Nonlinearity in nanomechanical cantilevers. *Physical Review B*, 87, 024304.

Voyiadjis, G.Z, Almasri, A. H. & Park, T., 2010. Experimental nanoindentation of BCC metals. *Mechanics Research Communications*, 37, 307-314.

Wang, B. L., Hoffman, M. & Yu, A.B., 2012. Buckling analysis of embedded nanotubes using gradient continuum theory. *Mechanics of Materials*, 45, 52-60.

Wang, B. L. & Wang, K.F., 2013. Effect of surface residual stress on the fracture of double cantilever beam fracture toughness specimen. *Journal of Applied Physics*, 113, 153502.

Wang, K.F. & Wang, B.L., 2016. Nonlinear fracture mechanics analysis of nano-scale piezoelectric double cantilever beam specimens with surface effect. *European Journal of Mechanics-A/Solids*, 56, 12-18.

Williams, J.G., 1987. Large displacement and end block effects in the 'DCB' interlaminar test in modes I and II. *Journal of Composite Materials*, 21, 330-347.

Zhang, G.P., Takashima, K., Higo, Y., 2006. Fatigue strength of small-scale type 304 stainless steel thin films. Materials Science and Engineering: A, 426, 95-100.

Zhang, H., Li, X.B., Tang, G.J., Shen, Z.B., 2013. Stress intensity factors of double cantilever nanobeams via gradient elasticity theory. *Engineering Fracture Mechanics*, 105, 58–64.

Paper 2: Size-dependent stress intensity factors in a gradient elastic double cantilever beam with surface effects

3.7 Abstract

In this article, the size dependent-stress intensity factors in an elastic double cantilever beam (DCB) are obtained using the strain gradient theory. The surface effects are included while the DCB is assumed to undergo large deformation. Both cracked and uncracked parts (root effect) of the DCB are incorporated in modelling and analyses. The Variational principle is employed to obtain the governing equation and the corresponding boundary conditions. The deflections along the beam axis and stress intensity factors are obtained and plotted. Results exhibit large deformation to be influential for slender beams at small scale. Strain gradient effect tends to increase beam stiffness though reverse holds true for the root effect of the DCB. These effects on structure stiffness are conspicuous when the beam thickness is less than the material characteristic length. Due to positive surface residual stress, beam exhibits less stiff behaviour in comparison with the negative surface residual stress. This softening behaviour may be credited to the sign of curvature that causes an additional distributed load and alters beam stiffness. It is shown that even with the root effect, negative surface residual stress causes the DCB to display stiffer response by lowering the stress intensity factors and vice versa.

3.8 Introduction

Redesigned mixed mode bending (MMB) apparatus, based on geometrical non-linearity, reduces the error from 30% to 3% in determining its bending behaviour (Reeder and Crews Jr, 1991; Wang and Wang, 2016). The cantilever beam is one of the essential building blocks used in micro and nanoelectromechanical (MEMS & NEMS) devices and often undergoes geometrical non-linearity. Generally, the geometrical

nonlinearity associated with cantilever beam is the nonlinear curvature, effect of which is highly substantial (Anderson et al., 1996) (due to the insignificance of Von Karman strain (Jia et al., 2010; Jia et al., 2011)). The DCB specimen is widely used to determine the critical stress intensity factors (or strain energy release rate) of homogenous, as well as non-homogenous materials under Mode I loading configuration. Furthermore, a double cantilever beam is generally analyzed by examining the bending behaviour of a cantilever beam (Giannakopoulos and Stamoulis, 2007; Stamoulis and Giannakopoulos, 2012) since it is considered to be made of two cantilevers attached with an uncracked part. Moreover, the consideration of geometric nonlinearity in the mode I fracture toughness of non-homogenous materials is sufficed for long cracks as shown by Devitt et al. (1980) and Williams (1987).

Contrary to the classical continuum elasticity theories, the non-classical theories assume that stress at a material point is not entirely depended on the strain at that point but also on all other points in the body (Togun, 2016; Wang et al., 2012). This process in literature is referred as the strain gradient effect and it is more evident when the external and the internal dimensions of the structure become comparable such as in Micro-electromechanical systems (MEMS) and Nano-electromechanical systems (NEMS). In that case, microstructural length scales of a particular material become comparable to the length scale of the deformation field that eventually leads to a non-homogenous and size-dependent structural behaviour (Giannakopoulos and Stamoulis, 2007). The strain gradient model employed in this work was introduced by Aifantis (1992), Ru and Aifantis (1993) and Vardoulakis and Sulem (1995)which is considered more convenient in applications (Giannakopoulos and Stamoulis, 2007; Joseph et al., 2017). The Cauchy stress (τ_{xx}) and double stress (μ_{xxx}) for the 1-D case are given as; $\tau_{xx} = E\varepsilon_{xx}$ and $\mu_{xxx} = l^2 E \frac{\mathrm{d}\varepsilon_{xx}}{\mathrm{d}x}$ respectively (Stamoulis and Giannakopoulos, 2012). Here,

E is Young's Modulus; ε_{xx} is the axial strain in the beam due to bending, l is the material microstructural length constant related to the bulk strain energy. The total stresses (σ_{xx}) for the beam bending can be evaluated as; $\sigma_{xx} = \tau_{xx} - \frac{\mathrm{d}\mu_{xxx}}{\mathrm{d}x} = E\left(\varepsilon_{xx} - l^2 \frac{\mathrm{d}^2\varepsilon_{xx}}{\mathrm{d}x^2}\right)$. The application and validation of this simpler strain gradient theory are presented by Vardoulakis and Sulem (1995) and Giannakopoulos and Stamoulis (2007) respectively. A comprehensive review of this gradient theory along with the applications of internal length gradient across various scales is provided by Aifantis (2003, 2016)

There are certain molecular effects that are fascinatingly obvious when the structural dimensions are in micro and nanometer range. Effect of the surface stresses is one of those effects that have thoroughly been explained (Dingreville et al., 2005; Streitz et al., 1994). The atoms on or near the free surface have different equilibrium requirements as compared to the ones in bulk. This difference causes an excess energy at the surface which is understood as a layer to which that energy is attached (Fischer et al., 2008). Accordingly, the thermodynamic theory of solid surface revealed that the relationship between the surface stress and surface free energy is obtainable (Cahn, 1998; Cammarata, 1997; Cammarata, 1994; Fried and Gurtin, 2003). Meanwhile, when the size of the structure is reduced to the micro/nanoscale, the ratio of the surface area to bulk volume may become enormous. Therefore, the influence of the surface effect on the mechanical behaviour of the micro/nanomaterials becomes prominent and hence cannot be neglected (Wang and Wang, 2013). Surface effects on micro/nanostructures may be characterized by two major types i.e. the surface elasticity and the surface residual stress (He and Lilley, 2008b). Gurtin and Murdoch (1978) firstly considered the effect of surface stress in their theoretical framework based on continuum elasticity. In their work, the surface is considered as a mathematical layer of zero thickness with

different material properties as compared to an underlying bulk. This theory has shown an excellent capability to successfully cater the surface effect on the mechanical behaviour of the micro/nanostructures and is widely employed by the researchers throughout (Jammes et al., 2009; Lu et al., 2016; Luo and Wang, 2009; On et al., 2010; Wang and Feng, 2007; Wang and Feng, 2010). The general expression for the surface stress-strain relation is given as; $\sigma^s_{\alpha\beta} = \tau_0\delta_{\alpha\beta} + (\tau_0 + \lambda^s)\varepsilon_{yy}\delta_{\alpha\beta} + 2(\mu^s - \tau^s)\varepsilon_{\alpha\beta} + \tau_0 u^s_{\alpha,\beta}$, where λ^s and μ^s are the surface Lame constants, δ is Kronecker delta and τ_0 is the surface residual stress in the unconstrained condition. In general, the surface properties usually have anisotropic stress (Gurtin et al., 1998; Shenoy, 2005; Weissmüller and Cahn, 1997) depending upon the crystallographic direction of the surface. However, it is shown in the literature that a surface may assume anisotropic nature and it is still meaningful to use an appropriate average of the surface stresses (Duan et al., 2005; Sharma and Ganti, 2004; Sharma et al., 2003).

The surface elastic model is effectively employed by the researchers with both surface residual stress and surface elasticity effects in the continuum model (Chen et al., 2006; Gurtin et al., 1998). Moreover, the surface elastic model along with the generalized Young-Laplace equation has also been used widely to investigate the influence of surface effects on the mechanical response of nanostructures such as nanobeams/wires(Ansari and Sahmani, 2011; He and Lilley, 2008a, 2008b), nanoplates (Assadi and Farshi, 2010; Assadi et al., 2010; Zhang et al., 2014) and electrostatically actuated nanobeams (Fu and Zhang, 2011; Koochi et al., 2012; Ma et al., 2010; Yang et al., 2013). However, the contribution of surface residual stress to the total surface stresses is considerably more noticeable than the surface elasticity (Wang and Feng, 2010; Yan and Jiang, 2011). As mentioned before that the DCB is a widely used specimen for the determination of fracture toughness of a particular material. However, very few efforts have been devoted to study its fracture behaviour with the

consideration of surface effect (Wang and Wang, 2013). For precise fracture analysis, future application of micro/nanomaterials demands an inclusion of surface effects in the crack tip field quantities such as strain energy release rate or stress intensity factor. This paper establishes the numerical analysis of a DCB specimen, subjected to large deformation, for the characterization of micro/nanomaterials, with the simultaneous consideration of surface effects and strain gradients. The schematic diagram of a DCB with surface residual stress is shown in Fig. 3.9a. Size-dependent fracture analysis of a DCB in terms of stress intensity factors with various beam configurations is presented. Finally, the role of uncracked part of the DCB (root effect) is elaborated to conclude this study.

3.9 Theoretical formulations of the size-dependent bending of a cantilever beam

Classical beam theory is inadequate to correctly evaluate the solution of a cantilever beam under large deformation (at enhanced loads in particular) primarily as it ignores the shortening of moment arm as the free end of the beam deflects. Due to this reason, the classical results deviate from the actual observations at elevated loads. The correction for this shortening of moment arm plays a key role in solving large deformation problems. For one dimension structure, the stress-strain relation for the bulk material (in case of large deformation) is given as; $Ez\frac{\mathrm{d}\varphi}{\mathrm{d}s}=\sigma_{xx}$, where φ is the slope of beam and E is the Young's Modulus. For the surface layer, stress (τ^{s}) can be expressed as (Wang and Wang, 2015);

$$\tau^{\mathrm{s}}=\tau_{\mathrm{o}}+E_{\mathrm{s}}\varepsilon_{xx}^{\mathrm{s}} \tag{3.11}$$

where τ_{o} is the surface is residual stress, E_{s} and $\varepsilon_{xx}^{\mathrm{s}}$ are Young's modulus and surface strain respectively. Accordingly, the bending moment of a beam is given as;

$$M = \int_b z\sigma_{xx} \mathrm{d}A + \int_C E_s \varepsilon_{xx}^s dC = EI_{\text{eff}} \frac{\mathrm{d}\varphi}{\mathrm{d}s} \tag{3.12}$$

where z is the axis along beam thickness as shown in Fig 3.7, C is the perimeter of the beam's cross-section, $EI_{\text{eff}} = \frac{Ebh^3}{12} + \frac{E_s h^3}{6} + \frac{E_s bh^2}{2}$ (He and Lilley, 2008a, 2008b). At any specified point $P(x,y)$ along a curved beam, moment is given as; $M = F.(a - \delta x - x)$ (where a is the length of a beam and δx is the horizontal deflection), which if differentiated ($\mathrm{d}(a - \delta x - x)/\mathrm{d}s = -\cos\varphi$) gives;

$$EI_{\text{eff}} \frac{\mathrm{d}^2\varphi}{\mathrm{d}s^2} + F\cos\varphi = 0 \tag{3.13}$$

Vertical deflection Y and arc length s (along with the beam axis) may be evaluated as;

$$s = \sqrt{\frac{EI_{\text{eff}}}{2F}} \int_0^{\varphi} \frac{\mathrm{d}\varphi}{\sqrt{\sin\varphi_{\text{o}} - \sin\varphi}}, \tag{3.14}$$

$$\frac{Y}{a} = \frac{1}{\sqrt{2}\alpha} \int_0^{\varphi_{\text{o}}} \frac{\sin\varphi \mathrm{d}\varphi}{\sqrt{\sin\varphi_{\text{o}} - \sin\varphi}}, \qquad \text{here } \alpha = \sqrt{\frac{Fa^2}{EI_{\text{eff}}}} \text{ and } a = \text{length of the beam} \tag{3.15}$$

Here φ_{o} depicts an unknown slope at the free end. Eq. (3.14) and (3.15) are usually solved numerically to evaluate Y. Alternatively, numerical techniques are applied to Eq. (3.13) to get φ and deflection Y by the following relation;

$$Y = \int_0^a \sin(\varphi)\mathrm{d}s \tag{3.16}$$

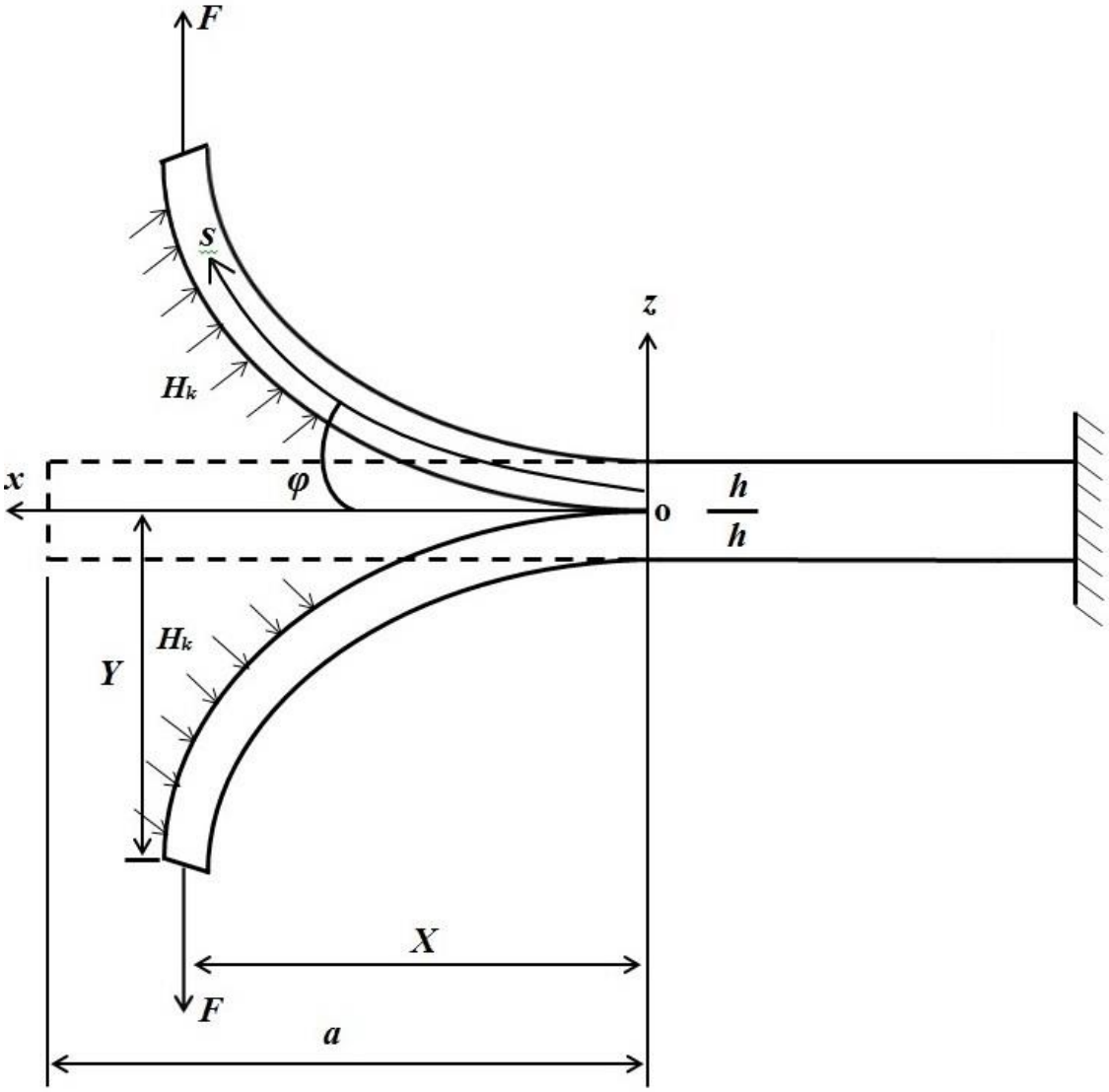

Figure 3.7Schematic diagram of a double cantilever beam with surface residual stress

These straightforward formulations may not be precisely applied at micro/nano scale due to the predominant size effect. In order to cater for this, several strain gradient theories are available in the literature (mostly dealing with second-order strain gradients). The constitutive equation for the one-dimensional case in combination with the linear elastic material behaviour is written as (Aifantis, 1999; Askes et al., 2002; Joseph et al., 2017);

$$\sigma = E(\varepsilon - l^2\nabla^2\varepsilon) \tag{3.17}$$

whereσ and ε are the axial stress and strain respectively, E is Young's modulus, l is the material characteristic length and $\nabla^2 = \partial^2/\partial x^2 + \partial^2/\partial y^2 + \partial^2/\partial z^2$ is the Laplacian operator. Strain for Euler-Bernoulli beam is given as, $\varepsilon = zk = z\dfrac{\mathrm{d}\varphi}{\mathrm{d}s}$, where$\kappa$ is the curvature andφ is the deformed angle. The∇^2operator is reduced to cater only 1D gradient since the deformation is entirely the function of "s" (although a beam is defined in 2D geometrical space i.e. *xy*-plane). For 1D cantilever beam i.e. $\sigma_{yy} = \sigma_{zz} = \sigma_{yz} = \sigma_{xz} = \sigma_{xy} = 0$ (the beam length should at least 10 times of its height (Christensen and Bastien, 2015)), the total stress (σ_{xx}) according to Eq. (3.17) may be written as;

$$\sigma_{xx} = Ez\left[\frac{\mathrm{d}\varphi}{\mathrm{d}s} - l^2\frac{\mathrm{d}^3\varphi}{\mathrm{d}s^3}\right] \tag{3.18}$$

Bending moment at x is given as, $M = \int_A \sigma_{xx} z\mathrm{d}A$. Using Eq. (3.18) in bending moment (for the bulk) equation and upon integration over the cross-section area A, one gets;

$$M = EI\left[\frac{\mathrm{d}\varphi}{\mathrm{d}s} - l^2\frac{\mathrm{d}^3\varphi}{\mathrm{d}s^3}\right] \tag{3.19}$$

here l is the material characteristics length. Here $I = \int_A z^2\mathrm{d}A$ is the second moment of cross-sectional area. Now the governing equation and the corresponding boundary conditions of a strain gradient elastic cantilever beam are evaluated through a variational principle given as; $\delta(U_\mathrm{b} + U_\mathrm{s}) - \delta W = 0$, where W is the work done by the external forces, U_b and U_s are the strain energy of the bulk and surface respectively. For one-dimensional case, the bulk strain energy U_b may be written as;

$$U_b = \frac{1}{2}\int_A \int_0^a [\tau_{xx}\varepsilon_{xx} + \mu_{xxx}.\nabla\varepsilon_{xx}]\mathrm{d}s\mathrm{d}A \tag{3.20}$$

where $\tau_{xx} = E\varepsilon_{xx}$ and $\mu_{xxx} = l^2 E(\mathrm{d}\varepsilon_{xx}/\mathrm{d}s)$ are the Cauchy and double stress respectively, ε_{xx} is the axial strain and $\nabla\varepsilon_{xx} = \mathrm{d}\varepsilon_{xx}/\mathrm{d}s$ denotes the strain gradient. Accordingly Eq. (3.20) may be written as; $U_b = (EI/2)\int[(\mathrm{d}\varphi/\mathrm{d}s)^2 + l^2(\mathrm{d}^2\varphi/\mathrm{d}s^2)^2]\mathrm{d}s$, where I = bh^3/12is the moment of inertia. The variation of the integral of the type $U = \int_0^a F(\varphi', \varphi'')\mathrm{d}s$ (where $\varphi' = \mathrm{d}\varphi/\mathrm{d}s$ and $\varphi'' = \mathrm{d}^2\varphi/\mathrm{d}s^2$), is given as;

$$\delta U = \int_0^a \left[\left\{ -\frac{\mathrm{d}}{\mathrm{d}s}\left(\frac{\partial F}{\partial \varphi'}\right) + \frac{\mathrm{d}^2}{\mathrm{d}s^2}\left(\frac{\partial F}{\partial \varphi''}\right) \right\}\delta\varphi \right]\mathrm{d}s + \left[\left\{ \left(\frac{\partial F}{\partial \varphi'}\right) - \frac{\mathrm{d}}{\mathrm{d}s}\left(\frac{\partial F}{\partial \varphi''}\right) \right\}\delta\varphi' \right]_0^a + \left[\left\{ \left(\frac{\partial F}{\partial \varphi''}\right) \right\}\delta\varphi'' \right]_0^a \tag{3.21}$$

From Eqs. (3.20) and (3.21) one gets;

$$\delta U_b = \int_0^a \left[-EI\left\{ \left(\frac{\partial^2\varphi}{\partial s^2} - l^2\frac{\partial^4\varphi}{\partial s^4} \right) \right\}\delta\varphi \right]\mathrm{d}s + \left[\left\{ EI\left\{ \left(\frac{\partial\varphi}{\partial s} - l^2\frac{\partial^3\varphi}{\partial s^3} \right) \right\}\delta\varphi \right\}\delta\varphi' \right]_0^a + \left[EIl^2\left\{ \frac{\partial^2\varphi}{\partial s^2} \right\}\delta\varphi'' \right]_0^a \tag{3.22}$$

Similarly, the surface strain energy is written as;

$$U_s = \frac{1}{2}\int_A [\tau_{xx}^s\varepsilon_{xx}^s + \mu_{xxx}^s.\nabla\varepsilon_{xx}^s + \tau_o\varepsilon_{xx}^s]\mathrm{d}A \tag{3.23}$$

From Eqs. (3.21) and (3.23) one gets;

$$\begin{aligned}\delta U_s = &\int_0^a \left[\left[-EI_s\left\{ \left(\frac{\partial^2\varphi}{\partial s^2} - l^2\frac{\partial^4\varphi}{\partial s^4} \right) \right\} \right]\delta\varphi \right]\mathrm{d}s + \left[\left[EI_s\left\{ \left(\frac{\partial\varphi}{\partial s} - l^2\frac{\partial^3\varphi}{\partial s^3} \right) \right\} \right]\delta\varphi' \right]_0^a \\ &+ \left[\left[EI_s l^2\left\{ \frac{\partial^2\varphi}{\partial s^2} \right\} \right]\delta\varphi'' \right]_0^a - \int_0^a T^s\delta\varphi\mathrm{d}s\end{aligned} \tag{3.24}$$

where$I_s=(bh^2/2+h^3/6)$ and $T^s=\int_0^a q\mathrm{d}s$, with $q(s)$ is the vertical load induced by the residual stress. According to the Young-Laplace equation (Chen et al., 2006; Gurtin et al., 1998), stress jump across each surface depends on the surface curvature that can be expressed as (Chen et al., 2006; Gurtin et al., 1998); $\left\langle \sigma_{ij}^{+}-\sigma_{ij}^{-}\right\rangle n_i n_j=\tau_{\alpha\beta}^{s}\kappa_{\alpha\beta}$, where n_i denotes the unit vector normal to the surface, σ_{ij}^{+} and σ_{ij}^{-} are respectively the stresses above and below the surface, $\kappa_{\alpha\beta}$ is the surface curvature. Therefore, equivalent vertical load *q(x)* induced by the residual stress is expressed as (He and Lilley, 2008a, 2008b);

$$q=H\kappa=H\frac{\mathrm{d}\varphi}{\mathrm{d}s} \tag{3.25}$$

with $H=2\tau_o b$ (He and Lilley, 2008a, 2008b; Wang and Feng, 2009); where b is the width of the beam. The total force along the beam axis "s" is given as; $T^s=\int_0^a H\frac{\partial\varphi}{\partial s}\mathrm{d}s$.

The variation of the work done by the external forces is written as; $\delta W=\int_0^a F\cos\varphi(s)\delta\varphi\mathrm{d}s$.

So, the variational principle $\delta(U_\mathrm{b}+U_\mathrm{s})-\delta W=0$ gives;

$$\begin{aligned}&\int_0^a\left[\left[-EI_{\mathrm{eff}}\left\{\left(\frac{\partial^2\varphi}{\partial s^2}-l^2\frac{\partial^4\varphi}{\partial s^4}\right)\right\}+H\varphi-H\varphi_{(a)}-F\cos\varphi\right]\delta\varphi\right]\mathrm{d}s-\\&\left[\left[EI_{\mathrm{eff}}\left\{\left(\frac{\partial\varphi}{\partial s}-l^2\frac{\partial^3\varphi}{\partial s^3}\right)\right\}\right]\delta\varphi'\right]_0^a+\left[\left[EI_{\mathrm{eff}}\left\{\left(\frac{\partial^2\varphi}{\partial s^2}\right)\right\}\right]\delta\varphi''\right]_0^a=0\end{aligned} \tag{3.26}$$

The governing equation can be written as;

$$EI_{\mathrm{eff}}\left[\frac{\mathrm{d}^2\varphi}{\mathrm{d}s^2}-l^2\frac{\mathrm{d}^4\varphi}{\mathrm{d}s^4}\right]=-F\cos\varphi+H\varphi-H\varphi_{(a)} \tag{3.27}$$

where $EI_{\text{eff}} = E\frac{bh^3}{12} + E_s\left(\frac{h^3}{6} + \frac{bh^2}{2}\right)$ is necessary to mention for simplification that the size dependence of *E* is not considered, as previously done in these references (Kahrobaiyan et al., 2012; Kong et al., 2009). Our model applies to those materials that do not show the significant dependence of *E* on size. The boundary conditions evaluated from the variational principle require $EI_{\text{eff}}[(\partial\varphi/\partial s) - l^2(\partial^3\varphi/\partial s^3)]$ (moment) and $EI_{\text{eff}}(\partial^2\varphi/\partial s^2)$ (higher order moment) to be specified at $s = 0$ and $s = a$. So, one of the possible set of boundary conditions considered in this work is as follows; At clamped end i.e. $s = 0$, slope i.e. rotation of the beam is zero $\varphi = 0$, and the non-classical terms (from variational principle) is written as; $\frac{\mathrm{d}^2\varphi}{\mathrm{d}s^2} = 0$. Meanwhile, at the free end i.e. $s = a$, the classical moment (without strain gradient) would be zero which eventually gives; $\frac{\mathrm{d}\varphi}{\mathrm{d}s} = 0$. On the other hand, the moment (with strain gradient effect) would also be zero that further gives; $\frac{\mathrm{d}\varphi}{\mathrm{d}s} - l^2\frac{\mathrm{d}^3\varphi}{\mathrm{d}s^3} = 0$. In a nutshell, the boundary conditions, considered in this work are written as;

At $s = 0$: $\varphi = 0$, $\frac{\mathrm{d}^2\varphi}{\mathrm{d}s^2} = 0$ (3.28a)

At $s = a$: $\frac{\mathrm{d}\varphi}{\mathrm{d}s} = 0$, $\frac{\mathrm{d}\varphi}{\mathrm{d}s} - l^2\frac{\mathrm{d}^3\varphi}{\mathrm{d}s^3} = 0$ or $\frac{\mathrm{d}\varphi}{\mathrm{d}s} = 0, \frac{\mathrm{d}^3\varphi}{\mathrm{d}s^3} = 0$ (3.28b)

The nonlinear fourth order differential equation (Eq. (3.27)) with the respective boundary conditions (Eq. (3.28)) is solved using a three-stage Lobatto IIIa collocation formula. It is one of a widely used finite difference method to solve boundary value problems. Details of this and some other relevant methods are provided by Shampine et al. (2000).

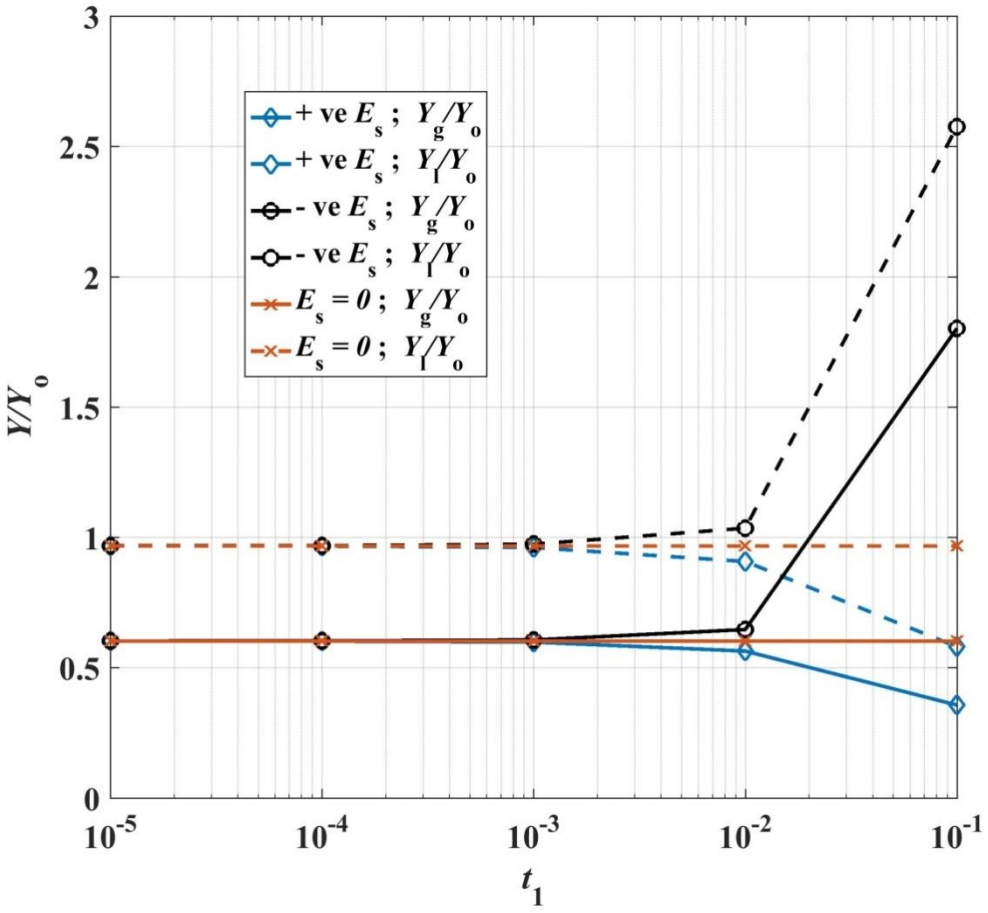

Figure 3.8 Maximum tip deflection of the strain gradient model (Y_g) and non-gradient model (Y_l), normalized with the classical results (Y_o) vs layer thickness to beam's height ratio ($t_1 = t/h$)

3.10 Numerical results for the cantilever beam bending

For results, the material characteristic length (l) of epoxy i.e. 17.6 μm (Kong et al., 2009) is taken to numerically evaluate the large deformation bending behaviour of a cantilever beam. The concentrated vertical force F and height h are chosen in such a way that the beam remains elastic everywhere. In this study, the contribution of the surface residual stress towards the total surface stresses is found more noticeable than the surface elasticity**,** as shown by other researchers (Wang and Feng, 2010; Yan and Jiang, 2011).The end tip deflection for gradient model Y_g, non-gradient (large deformation) model Y_l and the classical model Y_o ($FL^3/3EI$) are plotted in Fig. 3.10. It is shown that when $t_1 << h$, where t_1 is the ratio of the layer's thickness to the height of the

beam, the effect of surface elasticity is negligible and all three models give similar results. Surface elasticity modulus is taken to be as; $E_s = E_1 t_1 \& E_1 = E$ = 1.44 GPa (He and Lilley, 2008a, 2008b). The similar conclusion is drawn in the references (Wang and Feng, 2010; Yan and Jiang, 2011). Therefore for further study, E_s and τ_o are assumed to be zero (Wu et al., 2015) and 0.2 µN/ µm respectively.

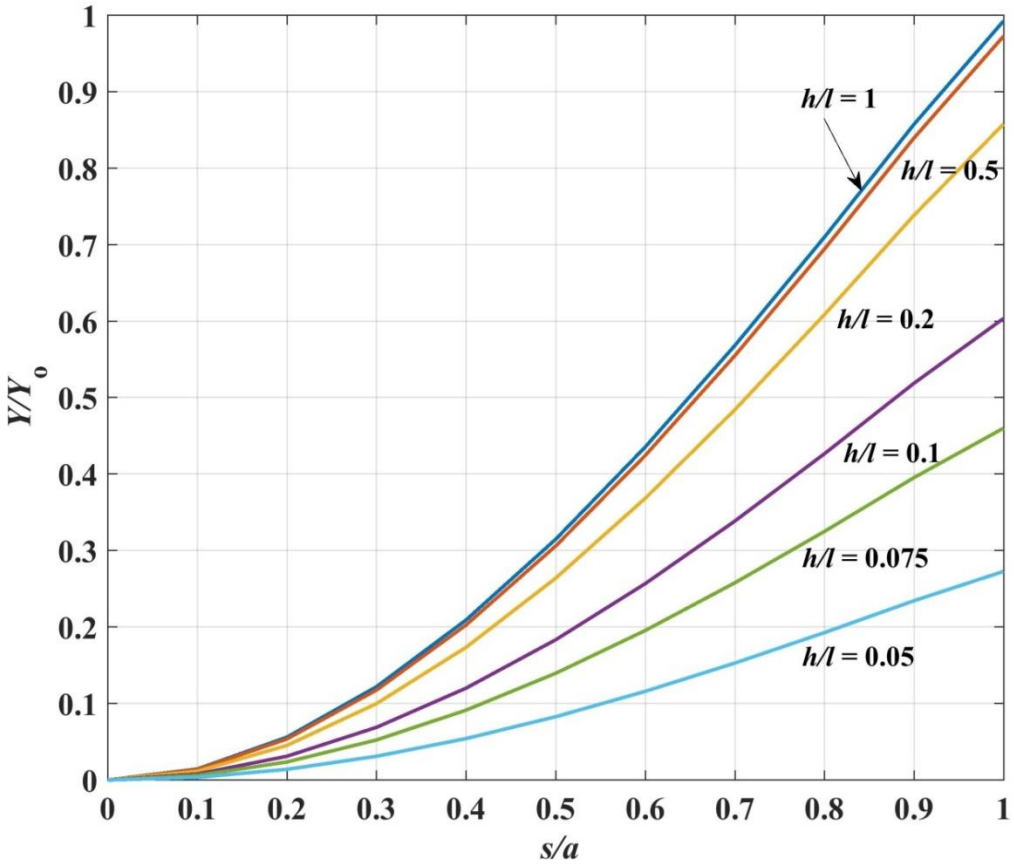

Figure 3.9 The vertical deflection along the beam axis (normalization with the classical result at the tip) for strain gradient models

The effect of the large deformation with increased load factor F_o ($F_o = Fa^2/2(EI)$) is shown by (Joseph et al., 2017) demonstrating its pronounced effect at the enhanced loads. The surface residual stress constant may be positive or negative; therefore results for both positive and negative residual stresses are presented. The vertical deflection of a cantilever beam along its axis, normalized with Y_o ($FL^3/3EI$)

(classical endpoint vertical deflection) is presented in Fig. 3.11. It can be seen, for smaller h/l ratios, that gradient beam models are stiffer than the classical ones. The normalized deflections are shown to increase with increasing h/l while the maximum deflection (at s/a = 1) of the strain gradient and classical model become comparable when $h/l \approx 1$ onwards. It is important to note that the effect of the strain gradient is more prominent when $h/l \leq 0.2$, therefore the subsequent results are primarily presented with $h/l \leq 0.2$. In Fig. 3.12 for $h/l \leq 0.2$, the results are obtained with strain gradient model with no surface effects, strain gradient model with positive surface residual stress and strain gradient model with negative surface residual stress. All effects have shown a significant contribution to the bending behaviour of a cantilever beam. For instance, with the positive surface residual stress, the beam exhibits less stiff behaviour and vice versa. This phenomenon is explained due to the sign of curvature associated with surface residual stress that causes an additional distributed load and change beam stiffness (He and Lilley, 2008a; Wang and Wang, 2015; Wu et al., 2006). In the case of a positive surface residual stress, a positive curvature results in a positive distributed transverse force. This positive force increases the rotation of bending cantilever and thus beam behaves like a softer material. Meanwhile, this behaviour is totally opposite when $\tau_o < 0$ and hence the cantilever beam may exhibit a stiffer response comparatively.

The normalized maximum deflections (maximum tip deflection) for various beams configurations are numerically obtained using Eq. (3.16) and are shown in Fig. 3.13. Here Y_g, $Y_l$andY_o ($Fa^3/(3EI)$) represent the deflection obtained with strain gradient model, non-gradient model and using the classical formulations (small deformation). Additionally, for comparison, maximum tip deflections for positive and negative residual stresses are also included. The non-dimensional parameter ($\alpha = 3Fa^2/(Eh^4)$) as abscissa is defined for convenience.

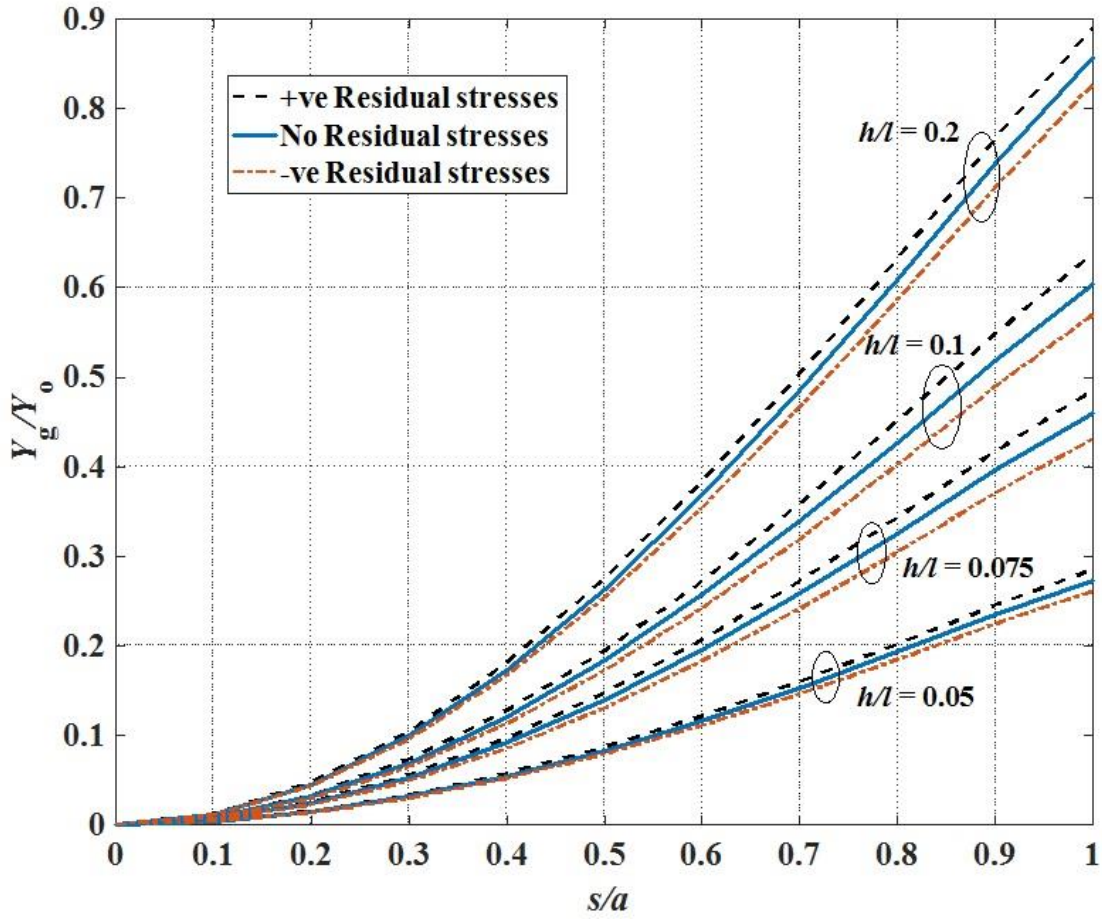

Figure 3.10 The vertical deflection along the beam axis (normalization with the classical result at the tip) for strain gradient models with surface residual effect

The normalized maximum deflection Y_g/Y_l against α is plotted in Fig. 3.13. From Fig. 3.13, the strain gradient effect seems more pronounced for smaller (a/h), presenting smaller deflections and hence exhibiting stiffer response for the gradient beams. The effect of surface residual stress on the tip deflections are shown to be more prominent for slender beams irrespective of any h/l ratio. For a certain beam height, the effect of surface residual stress tends to increase with increasing beam length. Moreover, this behaviour is also evident for increasing h/l ratio. It is clear that positive surface residual stress induces larger tip transverse displacement while the opposite holds true for the negative surface residual stress. Figure 3.14 compares the strain gradient results with the classical model (without strain gradient & small deformation). It is shown for the

smaller beam lengths that Y_g/Y_l and Y_g/Y_o are identical, indicating similar results for large as well as the small deformation theory. However, with an increase in beam slenderness (*a/h* ratio), the beam will undergo large deformation and hence the small deformation theory would over-estimate an endpoint vertical deflection. This is evident from a peak point (in each curve) in Fig. 3.14, indicating the classical model inadequacy to accurately predict the large deformation. Moreover from Fig. 3.14, it is quite evident that the pattern of maximum tip deflections, for the model with cumulative effects of strain gradient and surface residual stress, is similar to that of the model without surface residual stress (only strain gradient effect), apart from the fact that for positive surface residual stress the beam tends to exhibit softer behaviour and vice versa. Nevertheless from Fig. 3.13 and 3.14, it may fairly be concluded that the effect of surface residual stress is more prominent for slender beams.

3.11 Fracture of a double cantilever beam with surface residual effect

Significant developments in the advance numerical methods have been made not only to accurately predict the fracture of various complex geometries (Fleming et al., 1997; Joseph et al., 2014) but also to cater the size effect on the fracture properties at smaller scale (Giannakopoulos and Stamoulis, 2007; Guha et al., 2013; Joseph et al., 2018; Stamoulis and Giannakopoulos, 2012). Adopting one of such numerical methods, in this section, the fracture property of DCB i.e. the stress intensity factor is evaluated numerically by taking the crack length to be the length of a beam as *a* and width *b*, the stress intensity factor (K) of a DCB may be written as $K = \sqrt{EG}$, where $G = F(\mathrm{d}Y_{max}/b\mathrm{d}a)$ and it is defined as the strain energy release rate of a DCB. Meanwhile, the classical result is given by $G_o = 12F^2a^2/(Eh^3b^2)$ (Wang and Wang, 2013). Figure 3.15 and 3.16 display the normalized stress intensity factors versus α. For comparison, as in Fig. 3.13 and 3.14, the results for strain gradient model K_g, non-gradient model $K_l$and classical theory K_o are given. Additionally, for further illustration, the stress intensity

factors for the model with the positive and negative residual stresses are also included. Evidently, from Fig. 3.15 and 3.16, the effect of the surface residual stress is more prominent when $h/l \geq 0.075$ and for slender beams. It is clear that the positive residual stress enhances the stress intensity factors and vice versa. Furthermore, the effect of negative surface residual stress is more noticeable as compared to positive residual stress. For instance, in Fig. 3.15, for $h/l \geq 0.1$ beyond certain peak point the normalized stress intensity factor shows a swift decline, signifying a stiffer beam response. However, this prompt observation is completely absent in the case of positive surface residual stress. Moreover, the normalizations of strain gradient results with the classical ones are shown in Fig. 3.16. From Fig. 3.16, apart from the strain gradient effects, it may clearly be seen that the effect of negative surface residual stress is more noticeable than that of the positive surface residual stress. On the other hand, the overestimation in the fracture characteristics is also evident following the trend as shown in Fig. 3.14.

3.12 Effect of the uncracked part

The strain gradient effect of the uncracked part of DCB is neglected (since strains in the uncracked part would be much lower than that in the cracked part). The schematic of the uncracked part of a DCB is shown in Fig. 2.3. The governing equation and respective boundary conditions of an uncracked part are provided by Wang and Wang (2013) and (Joseph et al., 2017). Here, it is necessary to mention the prominence of shear stresses at the uncracked part that must be incorporated in the constitutive equations. Therefore, the Timoshenko beam model is more suitable to study the uncracked part of the DCB. Accordingly, the potential energy of an uncracked part (U_2) of DCB is given as;

$$U_2 = 2\int_{-\infty}^{0} \frac{M^2}{2EI_{\text{eff}}}\mathrm{d}x + 2\int_{-\infty}^{0} \frac{Q^2}{2G^s A}\mathrm{d}x \tag{3.29}$$

Here E is the Young's Modulus, G^s is the shear modulus, A is the area of cross-section and I_{eff} is the effective moment of inertia. Following the rectangular coordinate system,

the integrals vary from negative infinity to zero. From the references (Joseph et al., 2017; Wang and Wang, 2013) and using $M_{(o)} = F.X_{(\varphi_o)}$ we get,

$$U_2 = \frac{1}{\sqrt{EI_{\text{eff}}\, GA}}\left[F^2 X^2_{(\varphi_o)} + \left[\int_0^a sH \frac{\mathrm{d}\varphi}{\mathrm{d}s}\mathrm{d}s \right]^2 \right] \tag{3.30}$$

Now the influence of the root part of DCB is investigated numerically. Here R_K and R_G are defined, where R_K is the ratio of the stress intensity factor associated with the uncracked part to that of the cracked part of DCB, while R_G is the ratio of the strain energy release rate of an uncracked part to the cracked part. Variations of R_K and R_G versus *a/h* for different *h/l* ratios are plotted in Fig. 3.17. The results are plotted for strain gradient model without surface residual stress, strain gradient model with positive surface residual stress and strain gradient model with negative surface residual stress. It can be seen in Fig. 3.17 that, for a particular *h*/*l*, all models show the identical results. Thus it may be stated that ratios R_K and R_G depend on the DCB geometry and it is independent of the surface residual stress. Moreover, it may equally be concluded that for smaller DCBs i.e. for $h/l \leq 0.2$, the value of R_K and R_G may not be neglected even though the beam length to thickness ratio is higher ($a/h \approx 20$) (which was the case in classical studies).

The comparison of two strain gradient models i.e. with root effect and without root effect in terms of stress intensity factors is shown in Fig. 3.18. The results are plotted for models incorporating strain gradient effect without surface residual stress, strain gradient effect with positive surface residual stress and strain gradient effect with negative surface residual stress. In general, results show that even with the incorporation of root effect, the positive surface residual stress causes DCB to exhibit softer response by enhancing the normalized stress intensity factor and vice versa. Again, this phenomenon may be explained due to the sign of curvature associated with negative

surface residual stress that causes an additional distributed load (opposite to the direction of endpoint force), which in return cause the DCB to exhibit stiffer response. Hence, the influence of the root effect of DCB must be considered in mathematical modelling for accurate prediction of its fracture properties. It seems true even for the slender beams ($a/h > 20$), lest an underestimated fracture behaviour would be expected.

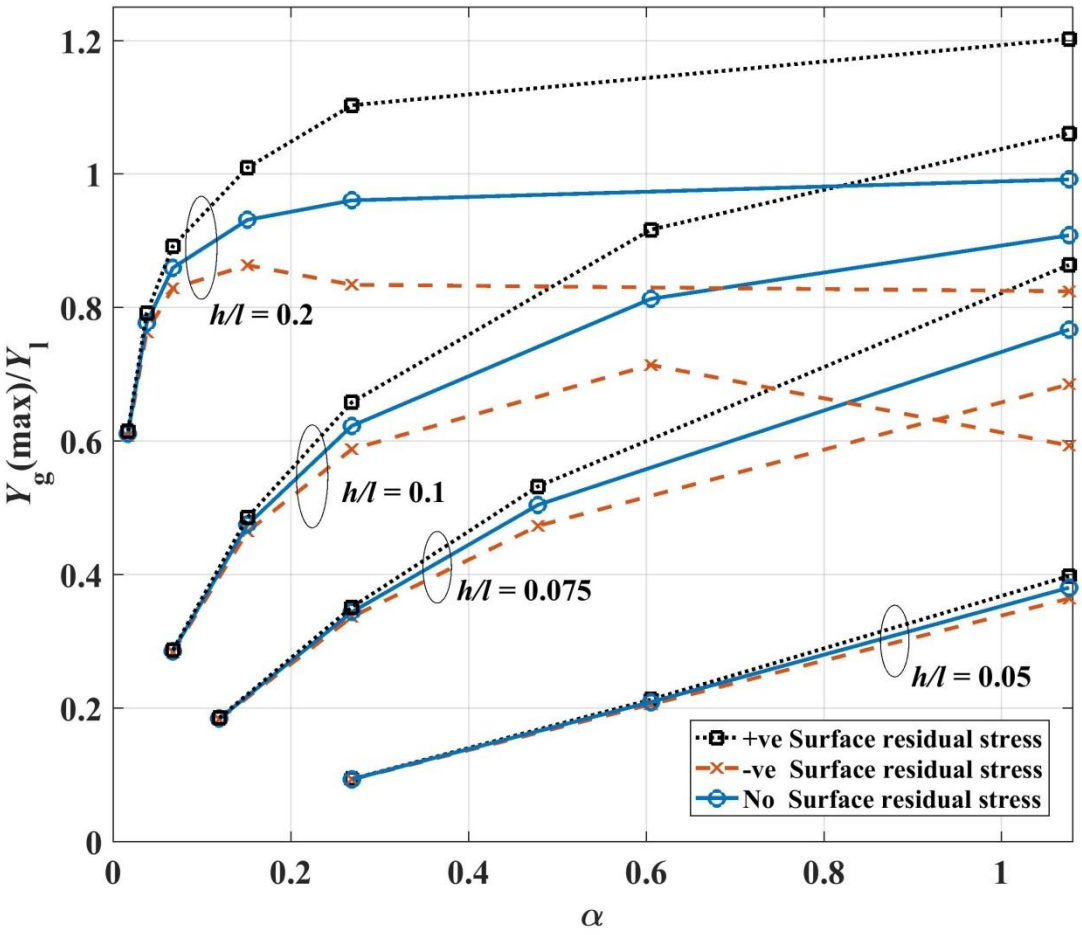

Figure 3.11 End point vertical deflection of the strain gradient model, normalization with the end point non-gradient vertical deflections (large deformation)

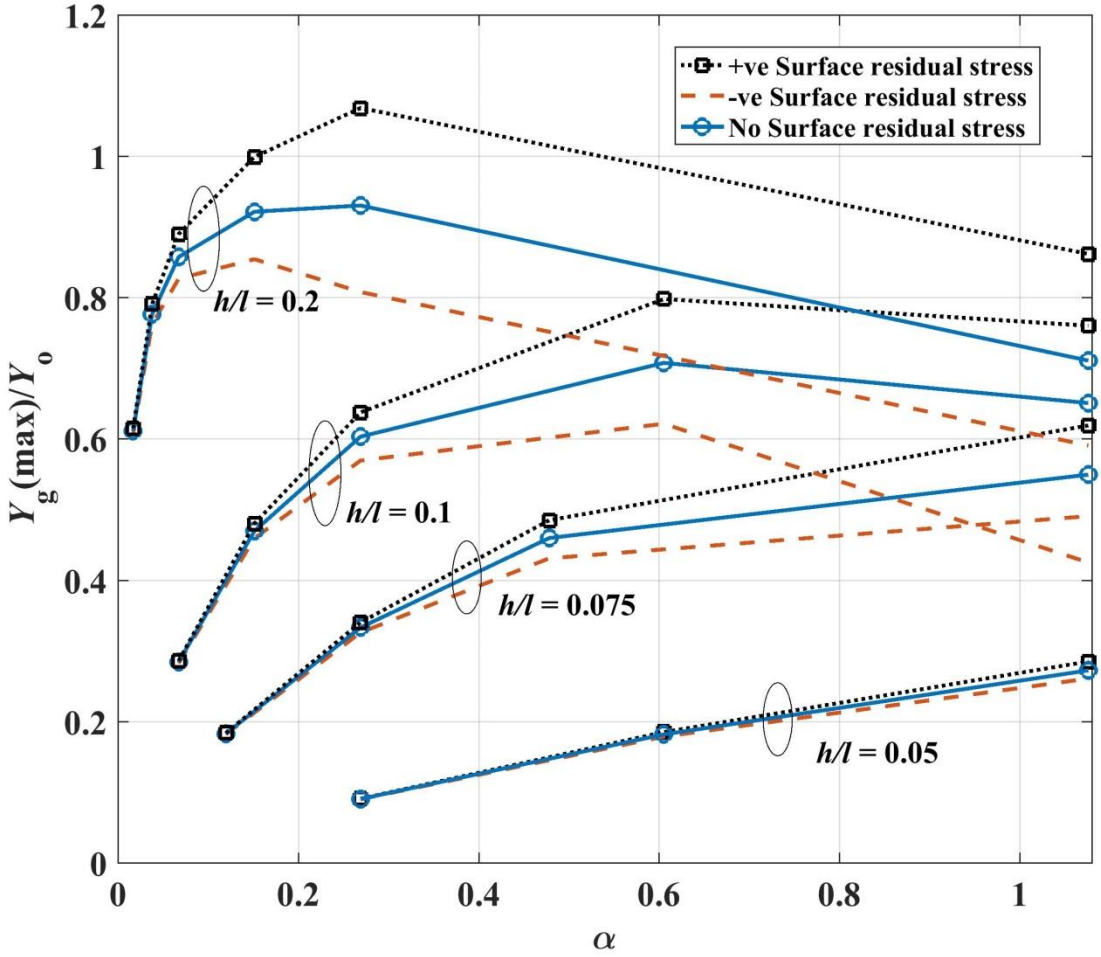

Figure 3.12 End point vertical deflection of the strain gradient model, normalization with the end point classical vertical deflections

3.13 Summary

The cumulative effects of the strain gradient and surface stress on the large deformation bending behaviour of a cantilever beam are investigated. Both surface elasticity and surface residual stress are incorporated in the mathematical modelling. Due to the negligible influence of surface elasticity, most of the results are depicted only with the consideration of surface residual stress. The results are obtained for strain gradient model with no surface effects, strain gradient model with positive surface residual stress and negative surface residual stress individually. Due to the positive surface residual stress, the beam exhibits less stiff behaviour. This softening behaviour may be attributed to the sign of curvature that causes an additional distributed load and change beam

stiffness. Meanwhile, this behaviour is totally opposite in the case when $\tau_o < 0$, hence a cantilever beam may exhibit a stiffer response comparatively. For the fracture property of DCB i.e. stress intensity factor, the effect of the surface residual stress is shown to be increasing with increasing beam dimensions. In general, the influence of surface residual stress is more prominent when $h/l \geq 0.075$ and for slender beams. Moreover, the effect of negative surface residual stress was shown to be more noticeable than the positive surface residual stress. The root effect also enhances the normalized stress intensity factors. It was shown that the root effect on the ratios R_K and R_G for all three models remain same and thus it may be stated that R_K and R_G depend on the DCB geometry and are independent of the surface residual stress. It is observed for $h/l \leq 0.2$, that the significance of the root effect must not be ignored.

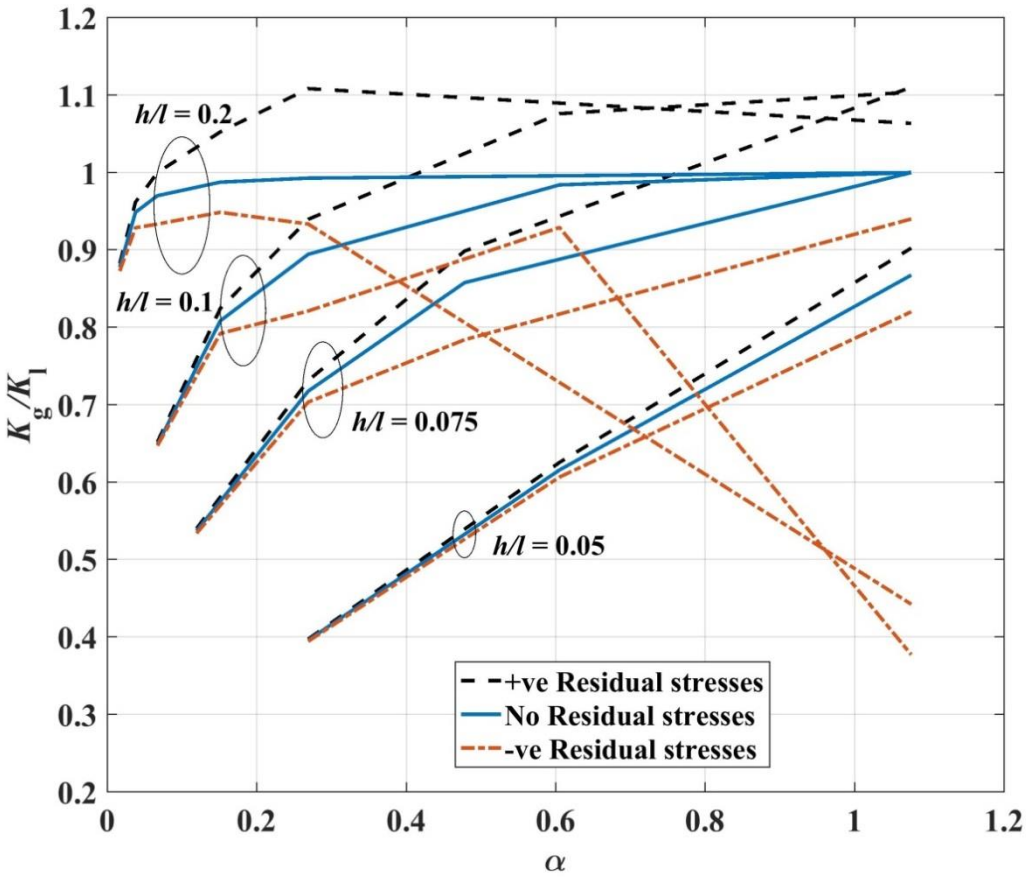

Figure 3.13 Stress intensity factors of the strain gradient model, normalization with the non-gradient stress intensity factors (large deformation)

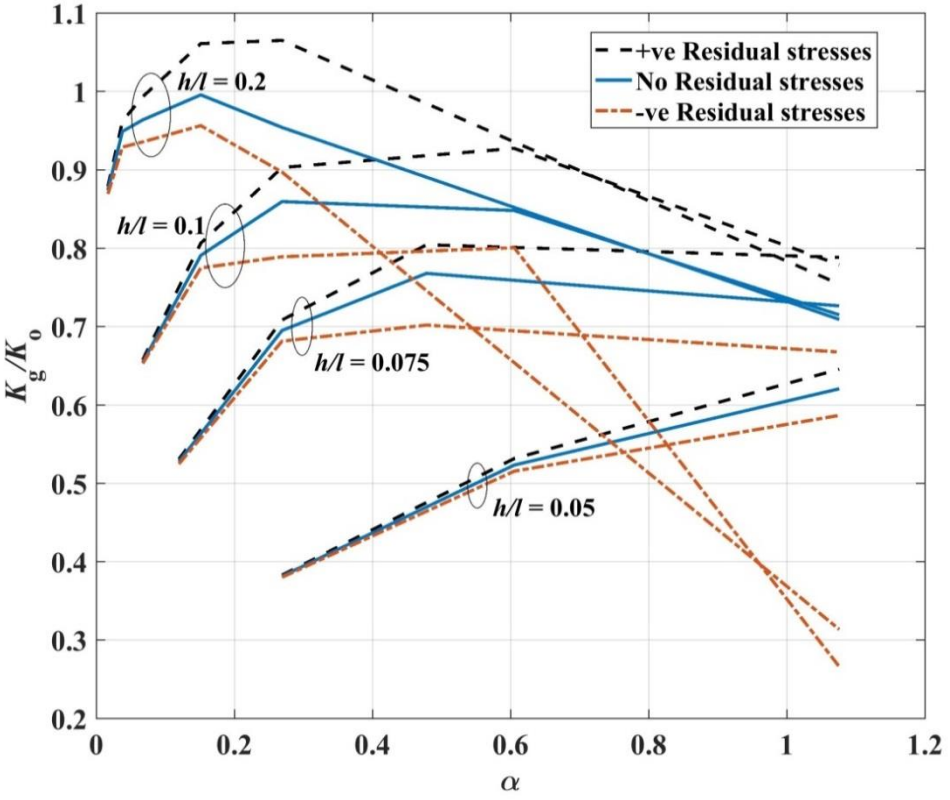

Figure 3.14 Stress intensity factors of the strain gradient model, normalization with the classical stress intensity factors

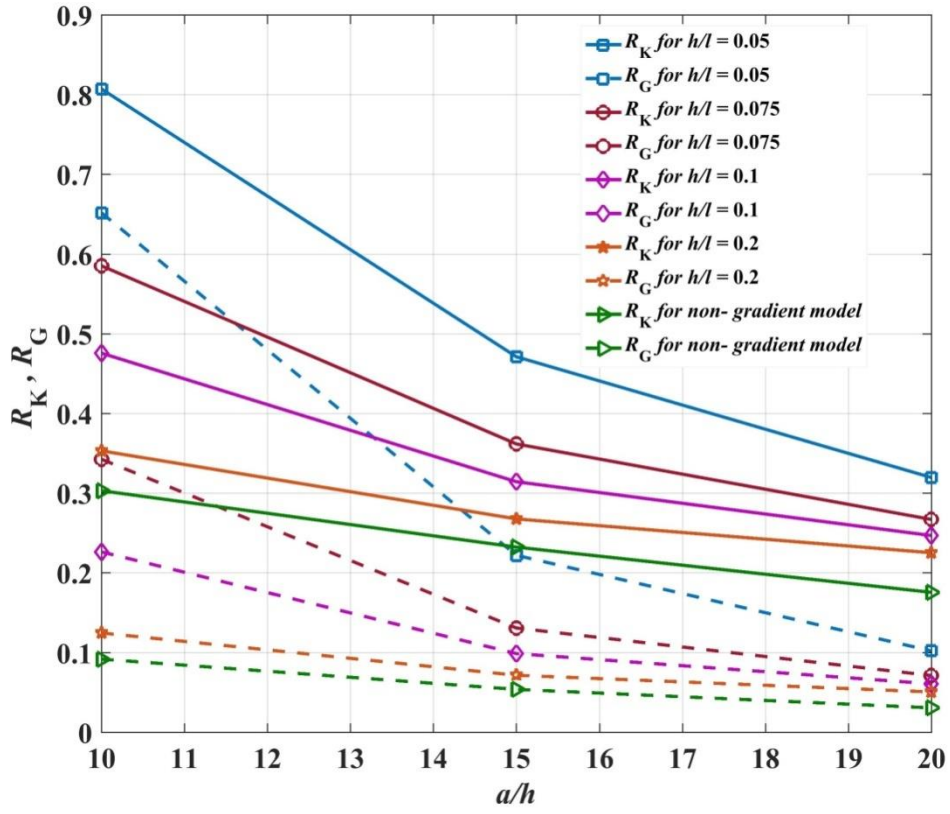

Figure 3.15 Comparison of R_K and R_G plotted against a/h

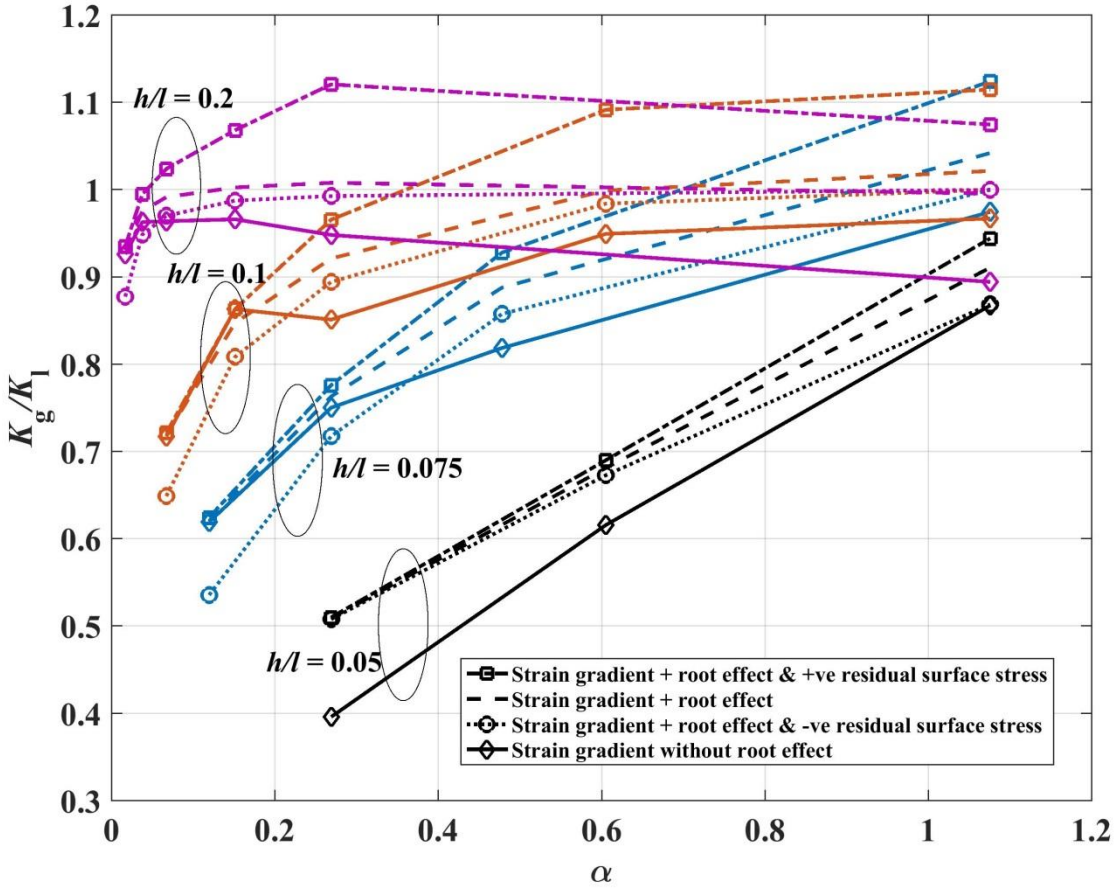

Figure 3.16 Stress intensity factors with the consideration of uncracked part of DCB, normalization with the non-gradient stress intensity factors (large deformation)

The above studies were primarily related to the influence of the strain gradient and surface effects on the bending behaviour of the cantilever beam and hence the fracture analyses of a double cantilever beam. In the next chapter, the strain gradient modelling and analysis

are presented for a double cantilever beam made up of piezoelectric material.

References

Aifantis, E., 2016. Chapter One-Internal Length Gradient (ILG) Material Mechanics Across Scales and Disciplines. *Advances in Applied Mechanics,* 49**,** 1-110.

Aifantis, E. C., 1992. On the role of gradients in the localization of deformation and fracture. *International Journal of Engineering Science,* 30**,** 1279-1299.

Aifantis, E. C., 1999. Strain gradient interpretation of size effects. *International Journal of Fracture,* 95**,** 299-314.

Aifantis, E. C., 2003. Update on a class of gradient theories. *Mechanics of Materials,* 35**,** 259-280.

Anderson, T., Nayfeh, A. & Balachandran, B., 1996. Experimental verification of the importance of the nonlinear curvature in the response of a cantilever beam. *Journal of Vibration and Acoustics,* 118**,** 21-27.

Ansari, R. & Sahmani, S., 2011. Bending behaviour and buckling of nanobeams including surface stress effects corresponding to different beam theories. *International Journal of Engineering Science,* 49**,** 1244-1255.

Askes, H., Suiker, A. & Sluys, L., 2002. A classification of higher-order strain-gradient models–linear analysis. *Archive of Applied Mechanics,* 72**,** 171-188.

Assadi, A. & Farshi, B., 2010. Vibration characteristics of circular nanoplates. *Journal of Applied Physics,* 108**,** 074312.

Assadi, A., Farshi, B. & Alinia-Ziazi, A., 2010. Size dependent dynamic analysis of nanoplates. *Journal of Applied Physics,* 107**,** 124310.

Cahn, J. W., 1998. Thermodynamics of solid and fluid surfaces. *The Selected Works of John W. Cahn***,** 377-378.

Cammarata, R., 1997. Surface and interface stress effects on interfacial and nanostructured materials. *Materials Science and Engineering: A,* 237**,** 180-184.

Cammarata, R. C., 1994. Surface and interface stress effects in thin films. *Progress in surface science,* 46**,** 1-38.

Chen, T., Chiu, M. S. & Weng, C. N., 2006. Derivation of the generalized Young-Laplace equation of curved interfaces in nanoscaled solids. *Journal of Applied Physics,* 100**,** 074308.

Christensen, J. & Bastien, C., 2015. *Nonlinear optimization of vehicle safety structures: Modeling of structures subjected to large deformations*, Butterworth-Heinemann.

Devitt, D., Schapery, R. & Bradley, W., 1980. A method for determining the mode I delamination fracture toughness of elastic and viscoelastic composite materials. *Journal of Composite Materials,* 14**,** 270-285.

Dingreville, R., Qu, J. & Cherkaoui, M., 2005. Surface free energy and its effect on the elastic behaviour of nano-sized particles, wires and films. *Journal of the Mechanics and Physics of Solids,* 53**,** 1827-1854.

Duan, H., Wang, J., Huang, Z. & Karihaloo, B., 2005. Size-dependent effective elastic constants of solids containing nano-inhomogeneities with interface stress. *Journal of the Mechanics and Physics of Solids,* 53**,** 1574-1596.

Fischer, F., Waitz, T., Vollath, D. & Simha, N., 2008. On the role of surface energy and surface stress in phase-transforming nanoparticles. *Progress in Materials Science,* 53**,** 481-527.

Fleming, M., Chu, Y., Moran, B., Belytschko, T., Lu, Y. & Gu, L., 1997. Enriched element-free Galerkin methods for crack tip fields. *International journal for numerical methods in engineering,* 40**,** 1483-1504.

Fried, E. & Gurtin, M. E., 2003. The role of the configurational force balance in the nonequilibrium epitaxy of films. *Journal of the Mechanics and Physics of Solids,* 51**,** 487-517.

Fu, Y. & , J., 2011. Size-dependent pull-in phenomena in electrically actuated nanobeams incorporating surface energies. *Applied Mathematical Modelling,* 35**,** 941-951.

Giannakopoulos, A. & Stamoulis, K., 2007. Structural analysis of gradient elastic components. *International journal of solids and structures,* 44**,** 3440-3451.

Guha, S., Sangal, S. & Basu, S., 2013. Finite Element studies on indentation size effect using a higher order strain gradient theory. *International Journal of Solids and Structures,* 50**,** 863-875.

Gurtin, M., Weissmüller, J. & Larche, F., 1998. A general theory of curved deformable interfaces in solids at equilibrium. *Philosophical Magazine A,* 78**,** 1093-1109.

Gurtin, M. E. & Murdoch, A. I., 1978. Surface stress in solids. *International Journal of Solids and Structures,* 14**,** 431-440.

He, J. & Lilley, C. M., 2008a. Surface effect on the elastic behaviour of static bending nanowires. *Nano Letters,* 8**,** 1798-1802.

He, J. & Lilley, C. M., 2008b. Surface stress effect on bending resonance of nanowires with different boundary conditions. *Applied Physics Letters,* 93**,** 263108.

Jammes, M., Mogilevskaya, S. G. & Crouch, S. L., 2009. Multiple circular nano-inhomogeneities and/or nano-pores in one of two joined isotropic elastic half-planes. *Engineering Analysis with Boundary Elements,* 33**,** 233-248.

Jia, X., Yang, J., Kitipornchai, S. & Lim, C. W., 2010. Free vibration of geometrically nonlinear micro-switches under electrostatic and Casimir forces. *Smart Materials and Structures,* 19**,** 115028.

Jia, X. L., Yang, J. & Kitipornchai, S., 2011. Pull-in instability of geometrically nonlinear micro-switches under electrostatic and Casimir forces. *Acta Mechanica,* 218**,** 161-174.

Joseph, R., Purbolaksono, J., Liew, H., Ramesh, S. & Hamdi, M., 2014. Stress intensity factors of a corner crack emanating from a pinhole of a solid cylinder. *Engineering Fracture Mechanics,* 128**,** 1-7.

Joseph, R. P., Wang, B. & Samali, B., 2017. Size effects on double cantilever beam fracture mechanics specimen based on strain gradient theory. *Engineering Fracture Mechanics,* 169**,** 309-320.

Joseph, R. P., Wang, B. & Samali, B., 2018. Strain gradient fracture in anti-plane cracked material layer. *International Journal of Solid and Structures,*146, 214-223.

Kahrobaiyan, M., Rahaeifard, M., Tajalli, S. & Ahmadian, M., 2012. A strain gradient functionally graded Euler–Bernoulli beam formulation. *International Journal of Engineering Science,* 52**,** 65-76.

Kong, S., Zhou, S., Nie, Z. & Wang, K., 2009. Static and dynamic analysis of micro beams based on strain gradient elasticity theory. *International Journal of Engineering Science,* 47**,** 487-498.

Koochi, A., Kazemi, A., Khandani, F. & Abadyan, M., 2012. Influence of surface effects on size-dependent instability of nano-actuators in the presence of quantum vacuum fluctuations. *Physica Scripta,* 85**,** 035804.

Lu, J., Lv, J., Liang, X., Xu, M. & Shen, S., 2016. Improved approach to measure the direct flexoelectric coefficient of bulk polyvinylidene fluoride. *Journal of Applied Physics,* 119**,** 094104.

Luo, J. & Wang, X., 2009. On the anti-plane shear of an elliptic nano inhomogeneity. *European Journal of Mechanics-A/Solids,* 28**,** 926-934.

Ma, J. B., Jiang, L. & Asokanthan, S. F., 2010. Influence of surface effects on the pull-in instability of NEMS electrostatic switches. *Nanotechnology,* 21**,** 505708.

On, B. B., Altus, E. & Tadmor, E., 2010. Surface effects in non-uniform nanobeams: continuum vs. atomistic modeling. *International Journal of solids and structures,* 47**,** 1243-1252.

Reeder, J. R. & Crews JR, J., 1991. Nonlinear analysis and redesign of the mixed-mode bending delamination test.

Ru, C. & Aifantis, E., 1993. A simple approach to solve boundary-value problems in gradient elasticity. *Acta Mechanica,* 101**,** 59-68.

Shampine, L. F., Kierzenka, J. & Reichelt, M. W., 2000. Solving boundary value problems for ordinary differential equations in MATLAB with bvp4c. *Tutorial notes*.

Sharma, P. & Ganti, S., 2004. Size-dependent Eshelby's tensor for embedded nano-inclusions incorporating surface/interface energies. *Journal of Applied Mechanics,* 71**,** 663-671.

Sharma, P., Ganti, S. & Bhate, N., 2003. Effect of surfaces on the size-dependent elastic state of nano-inhomogeneities. *Applied Physics Letters,* 82**,** 535-537.

Shenoy, V. B., 2005. Atomistic calculations of elastic properties of metallic fcc crystal surfaces. *Physical Review B,* 71**,** 094104.

Stamoulis, K. & Giannakopoulos, A., 2012. A study of size effects and length scales in fracture and fatigue of metals by second gradient modelling*. *Fatigue & Fracture of Engineering Materials & Structures,* 35**,** 852-860.

Streitz, F., Cammarata, R. & Sieradzki, K., 1994. Surface-stress effects on elastic properties. I. Thin metal films. *Physical Review B,* 49**,** 10699.

Togun, N., 2016. Nonlocal beam theory for nonlinear vibrations of a nanobeam resting on elastic foundation. *Boundary Value Problems,* 2016**,** 1-14.

Vardoulakis, I. & Sulem, J., 1995. *Bifurcation Analysis in Geomechanics,* London, Blackie/Chapman and Hall.

Wang, B., Hoffman, M. & Yu, A., 2012. Buckling analysis of embedded nanotubes using gradient continuum theory. *Mechanics of Materials,* 45**,** 52-60.

Wang, B. & Wang, K., 2013. Effect of surface residual stress on the fracture of double cantilever beam fracture toughness specimen. *Journal of Applied Physics,* 113**,** 153502.

Wang, G. F. & Feng, X. Q., 2007. Effects of surface elasticity and residual surface tension on the natural frequency of microbeams. *Applied physics letters,* 90**,** 231904.

Wang, G. F. & Feng, X. Q., 2009. Surface effects on buckling of nanowires under uniaxial compression. *Applied physics letters,* 94**,** 141913.

Wang, G. F. & Feng, X. Q., 2010. Effect of surface stresses on the vibration and buckling of piezoelectric nanowires. *Europhysics Letters,* 91**,** 56007.

Wang, K. & Wang, B., 2015. A general model for nano-cantilever switches with consideration of surface effects and nonlinear curvature. *Physica E: Low-dimensional Systems and Nanostructures,* 66**,** 197-208.

Wang, K. & Wang, B., 2016. Nonlinear fracture mechanics analysis of nano-scale piezoelectric double cantilever beam specimens with surface effect. *European Journal of Mechanics-A/Solids,* 56**,** 12-18.

Weissmüller, J. & Cahn, J., 1997. Mean stresses in microstructures due to interface stresses: A generalization of a capillary equation for solids. *Acta Materialia,* 45**,** 1899-1906.

Williams, J., 1987. Large displacement and end block effects in the'DCB'interlaminar test in modes I and II. *Journal of Composite Materials,* 21**,** 330-347.

Wu, B., Heidelberg, A., Boland, J. J., Sader, J. E., Sun, X. & Li, Y., 2006. Microstructure-hardened silver nanowires. *Nano Letters,* 6**,** 468-472.

Wu, Q., Volinsky, A. A., Qiao, L. & Su, Y., 2015. Surface effects on static bending of nanowires based on non-local elasticity theory. *Progress in Natural Science: Materials International,* 25**,** 520-524.

Yan, Z. & Jiang, L., 2011. The vibrational and buckling behaviours of piezoelectric nanobeams with surface effects. *Nanotechnology,* 22**,** 245703.

Yang, F., Wang, G. F., Long, J. M. & Wang, B. L., 2013. Influence of surface energy on the pull-in instability of electrostatic nano-switches. *Journal of Computational and Theoretical Nanoscience,* 10**,** 1273-1277.

Zhang, L., Liu, J., Fang, X. & Nie, G., 2014. Size-dependent dispersion characteristics in piezoelectric nanoplates with surface effects. *Physica E: Low-dimensional Systems and Nanostructures,* 57**,** 169-174.

CHAPTER 4

SCALE-DEPENDENT PIEZOELECTRIC EFFECT

Publication

Paper 3:

Joseph, R. P., Wang, B. L, & Samali, B., 2018. Large-deformation and strain gradient fracture analysis of double cantilever beam with piezoelectric effect, *Journal of Engineering Mechanics* 144(8), 04018071.
Doi: https://doi.org/10.1061/(ASCE)EM.1943-7889.0001497

Relevance to the thesis

It is important to examine the scale-dependent fracture behaviour of the piezoelectric materials. In this chapter, the strain gradient elasticity is employed to obtain the constitutive and governing equations of a piezoelectric double cantilever beam. Surface effects are also included to fully justify the scale-dependent model requirements.

4.1 Abstract

This paper examines the size-dependent fracture of a piezoelectric double cantilever beam (DCB) specimen based on large deformation-strain gradient theory. The governing equations with relevant boundary conditions for a piezoelectric cantilever beam with simultaneous consideration of surface piezoelectricity, surface elasticity, surface residual stress and large deformation are obtained and solved numerically. These results are further utilized to investigate the fracture behaviour of a DCB. Results show that the strain gradient effect is more eminent when the height of the beam is less than the material length scale parameter. Strain gradient model anticipates significant stiffening behaviour at the micro/nanoscale. Effect of the surface residual stress is more substantial than that of surface elasticity and surface piezoelectricity. The study further established that the strain energy release rate of the short-circuit boundary condition is larger than that of the open-circuit boundary condition. Using strain gradient model, the effect of the uncracked part of DCB is more noticeable on a smaller scale and should not be ignored even for slender beams.

4.2 Introduction

Piezoelectric micro/nanomaterials are extensively used in small-scale devices such as nanoresonators (Gusso, 2010)and nanogenerators (Yang et al., 2009). In order to fully establish their applications, detailed understanding of the fracture behaviour of these micro/nanomaterials is essential. Fracture performance of macro-materials has widely been explored in the literature (Ma et al., 2005a, 2005b; Shi et al., 2014; Zhou et al., 2007, 2005). However, relevant studies related to micro/nanomaterials are uncommon. A comprehensive review of piezoelectric nanostructures and relevant achievements in this field is presented by Fang et al. (2013). Meanwhile, due to the large surface area to volume ratio at the micro/nanoscale, the surface effect has shown to contribute in determining the fracture properties of the structure (Wang and Wang, 2013).

Nevertheless, for piezoelectric micro/nanomaterials, such elasticity model may not accurately predict the size-dependent fracture properties due to the negligence of surface piezoelectricity (Zhang and Jiang, 2014). The pioneering work for the development of the piezoelectric model with simultaneous incorporation of surface piezoelectricity, surface residual stress, and surface elasticity has been shown by Huang and Yu (2006). Some of the relevant findings may be seen in the works of Yue et al. (2015, 2014). Nan and Wang (2013) also found that the strain energy release rate, stress intensity factors and electric field intensity factors are highly influenced by surface effects in nanomaterials. Very recently, Wang and Wang (2016) investigated the fracture toughness of nanoscale piezoelectric DCB specimen incorporating large deformation, shear deformation, uncracked end bulk, surface residual stress, surface elasticity and surface piezoelectricity.

Redesigned mixed mode bending (MMB) apparatus, incorporating geometrical non-linearity, reduces the error from 30% to 3% (Reeder & Crews Jr, 1991; Wang & Wang, 2016). In the context of geometrical non-linearity, Contribution of Von Karman strain (mid-plane extension) in case of the cantilever beam is insignificant and hence can be neglected (Jia et al., 2011, 2010). On the other hand, the effect non-linear force/curvature relation in the static behaviour of micro/nano cantilever beams (particularly in switches) is evident and therefore should be thoroughly assessed (Huang and Yu, 2006; Jia et al., 2011). A typical DCB consists of two cantilever beams attached with an uncracked part, therefore its fracture analysis is often evaluated by studying the cantilever bending behaviour (Joseph et al., 2016; Li and Lee, 2016; Giannakopoulos and Stamoulis, 2007; Stamoulis and Giannakopoulos, 2012). For composite laminates and adhesively bonded materials, DCB specimen has found to be quite suitable for the determination of mode I fracture toughness. Moreover, consideration of geometric

nonlinearity on the mode I fracture toughness of non-homogenous materials is sufficed for long cracks as shown by Devitt et al. (1980) and Williams (1987).

When the external dimensions of the structure become comparable to the material length scale parameter (material microstructural length), it leads to non-homogenous and size-dependent mechanical behaviour (Giannakopoulos and Stamoulis, 2007). Strain gradient theory is one of the non-classical continuum elasticity theories having the capacity to describe the size-dependent behaviour. Mindlin (1965) proposed three simplified versions of his strain gradient framework i.e. Form I, II and III. In Form I, the strain energy density is taken as quadratic function of classical strains and second gradient of displacement; in Form II the gradient of strains is used in place of second gradient displacement and in Form III the strain energy is taken as a function of strain, the rotation gradient, and the fully symmetric part of strain gradient. Among these three forms, the problems of non-symmetric stress tensor (in case of couple stresses theories) may only be avoided in Form II for which the total stresses are symmetric. Polizzotto (2016) recently explained the physical meaning of higher order strain tensor used in gradient elasticity theories. Above mentioned strain gradient theories are primarily postulated to cater the quantitative estimation of size effect, which is important in the design of micro and nano-sized systems such as MEMS and NEMS (Liebold and Müller, 2015).

It is evident that the incorporation of strain gradients in estimating the size effect at micro and nanoscale yields stiffer elastic response to external loads (Liebold and Müller, 2015), such as an increase in bending rigidity of the microbeams made of epoxy is shown by Lam et al. (2003). For piezoelectric materials, Ke et al. (2012) presented the nonlinear vibrations of Timoshenko nanobeams and free vibration of piezoelectric nanoplates (Ke et al., 2015) by using nonlocal elasticity theory. Since DCB is an ideal specimen to determine mode I fracture toughness and it often undergoes large

deformation (Devitt et al., 1980; Williams,1987). Therefore, the accurate design of micro/nanoscale piezoelectric structures demands thorough investigations of the fracture behaviour of piezoelectric DCB specimen under large deformation. Moreover, theoretical modelling of micro/nanostructures is considered more relevant because of their capability to be implemented at all the possible length scales.

In this article, size-dependent fracture mechanics analysis of a piezoelectric DCB specimen with simultaneous consideration of large deformation, strain gradient effect, the uncracked bulk end part, surface residual stress, surface elasticity and surface piezoelectricity is studied. According to the author's knowledge, small-scale piezoelectric beams studies are mostly based either on continuum models or nonlocal elasticity theories with small deformation consideration. In this paper, the deformation behaviour of the cantilever is studied first which is then employed to study the fracture behaviour of a piezoelectric DCB specimen. The results of the beam deformations, endpoint vertical deflections, and strain energy release rates are obtained numerically by using a three-stage Lobatto IIIA collocation method.

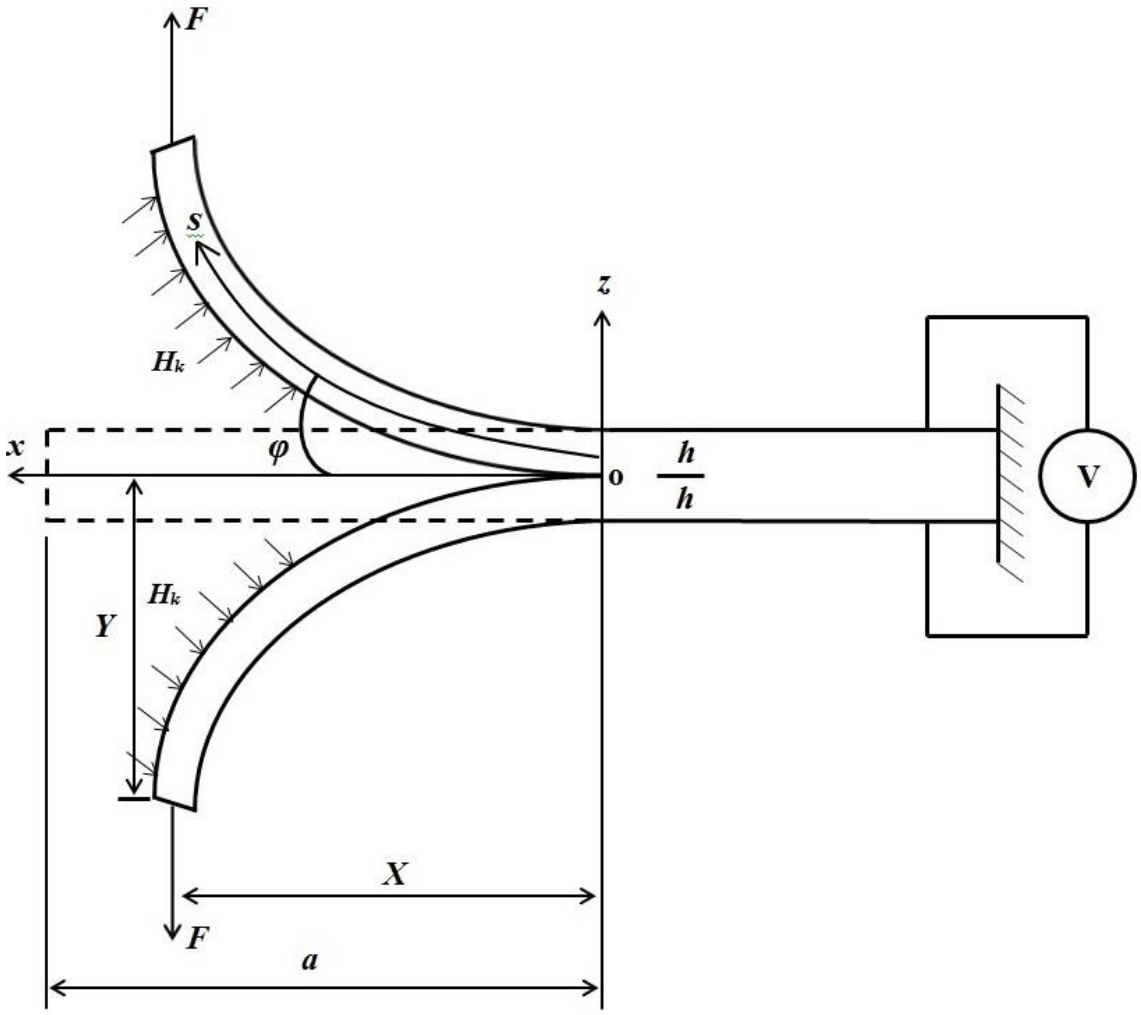

Figure 4.1 Schematic diagram of a piezoelectric double cantilever beam with surface residual stress

4.3 Theoretical background and problem formulation

The strain gradient model employed in this work was introduced by Aifantis (1992) and Ru and Aifantis (1993), which is considered more convenient in practical applications (Giannakopoulos and Stamoulis, 2007; Joseph et al., 2016). The Cauchy stress (τ_{xx}) and double (μ_{xx}) for the 1-D case are given as; $\tau_{xx} = E\varepsilon_{xx}$ and $\mu_{xx} = l^2 E \frac{\mathrm{d}\varepsilon_{xx}}{\mathrm{d}x}$ respectively (Stamoulis and Giannakopoulos, 2012). Here, E is Young's Modulus; ε_{xx} is the axial strain in the beam due to bending, l is the material characteristic lengths related to bulk strain energy. The total stresses (σ_{xx}) for the beam bending can be

evaluated as; $\sigma_{xx} = \tau_{xx} - \frac{\mathrm{d}\mu_{xx}}{\mathrm{d}x} = E\left(\varepsilon_{xx} - l^2 \frac{\mathrm{d}^2\varepsilon_{xx}}{\mathrm{d}x^2}\right)$. The application and validation of this simpler strain gradient theory are presented by Vardoulakis and Sulem (1995) and Giannakopoulos et al. (2006) respectively. A comprehensive review of this gradient theory and applications of internal length gradient across various scales is provided by Aifantis (2003) and Aifantis (2016) respectively. The constitutive equation in the form of the Laplacian operator ($\nabla^2 = \partial^2/\partial x^2 + \partial^2/\partial y^2 + \partial^2/\partial z^2$) is given as (Aifantis 1999a, 1999b);

$$\sigma = E(\varepsilon - l^2\nabla^2\varepsilon) \tag{4.1}$$

where σ, ε, E and l are same as defined earlier. Although the beam is defined in the *xy*-plane (a 2D geometrical space) problem still remains one dimensional since the deflection of the beam is exclusively the function of "*s*" or "*x*". Therefore, ∇^2 the operator is reduced to cater only 1D gradient effect (in the direction of the axis of the beam).

For piezoelectric material, the presence of strain gradient does affect not only the total stress but also electric displacement as well. For illustration, the schematic diagram of piezoelectric DCB specimen with the length of cracked part *a*, width *b*, thickness *h* is shown in Fig. 4.1. The beam configuration is same as that of the following references (Huang and Yu, 2006; Shen and Hu, 2010; Yan and Jiang, 2011; Zhang et al., 2008) and the "bulk + surface" model is used to model the DCB (Huang and Yu, 2006). The constitutive equations of a piezoelectric cantilever beam (provided length to height ratio $\geq$ 10 Christensen and Bastien, 2015) for 1D case i.e. $\sigma_{yy} = \sigma_{zz} = \sigma_{yz} = \sigma_{xz} = \sigma_{xy} = 0$, are written as;

$$\sigma_{xx} = -c_{11} z\left(\frac{\mathrm{d}\varphi}{\mathrm{d}s} - l^2 \frac{\mathrm{d}^3\varphi}{\mathrm{d}s^3}\right) - e_{31} E_Z \tag{4.2}$$

$$D_z = -e_{31} z\left(\frac{\mathrm{d}\varphi}{\mathrm{d}s} - l^2 \frac{\mathrm{d}^3\varphi}{\mathrm{d}s^3}\right) + k_{33} E_Z \tag{4.3}$$

where φ is the slope of the deformed beam, c_{11} is Young's modulus, D_z is the electric displacement, E_z is the electric-field component, l is the material characteristic length, k_{33} and e_{31} are the bulk dielectric and piezoelectric constants respectively.

Moreover, due to the enormous surface area to volume ratio at a smaller scale, the influence of surface effect on the mechanical behaviour of micro/nanomaterials becomes prominent and must be considered (Fang et al., 2013; Wang and Wang, 2013). Surface effects on micro/nanostructures may be divided into two distinct types i.e. the surface elasticity and the surface residual stress (He and Lilley, 2008a). The effect of surface stress, based on continuum elasticity theory, was first considered by Gurtin and Murdoch (1978) in their theoretical framework. In their study, the surface layers of the structures have different material properties as compared to the underlying bulk material. Meanwhile, the surfaces are considered to be as mathematical layers of zero thickness. This theory has shown an excellent capability in successfully addressing the surface effect on the mechanical behaviour of micro/nanostructures and has been thoroughly employed by many researchers. The stress of the surface layer (τ_x^s), using the results presented in reference (Huang and Yu, 2006) along with strain gradient effects may be expressed as;

$$\tau_{xx}^s = \tau_o + c_{11}^s(\varepsilon_{xx} - l^2\nabla^2\varepsilon_{xx}) - e_{31}^s E_z \tag{4.4}$$

where τ_o is the surface residual stress, c_{11}^s and e_{31}^s are the Young's Modulus and piezoelectric constant of the surface respectively. The electric field component can be

expressed as; $E_z = -\psi_{,z}$, here ψ is the electric potential and is taken to be constant along the beam span (*x*-axis) (Yan and Jiang, 2011). It is known that $E_x << E_z$, so that $D_x << D_z$, therefore, only D_z and E_z will be considered for theoretical modelling. The equilibrium equation in the absence of electric charges is $D_{z,z} = 0$ (Wang and Wang, 2016). Using the boundary conditions as follows; $\psi(-h/2) = 0$; $\psi(h/2) = V$, E_z and ψ may be evaluated as follows;

$$\psi = -\frac{e_{31}}{k_{33}}\left(\frac{\mathrm{d}\varphi}{\mathrm{d}s} - l^2\frac{\mathrm{d}^3\varphi}{\mathrm{d}s^3}\right)\left(\frac{z^2 - (h/2)^2}{2}\right) + V\frac{z}{h} + \frac{V}{2} \tag{4.5}$$

$$E_z = -\frac{\partial\psi}{\partial z} = z\frac{e_{31}}{k_{33}}\left(\frac{\mathrm{d}\varphi}{\mathrm{d}s} - l^2\frac{\mathrm{d}^3\varphi}{\mathrm{d}s^3}\right) - \frac{V}{h} \tag{4.6}$$

Therefore, bulk and surface stresses (at the upper (*h*/2) and lower surfaces (-*h*/2)) are;

$$\sigma_{xx} = -z\left(\frac{\mathrm{d}\varphi}{\mathrm{d}s} - l^2\frac{\mathrm{d}^3\varphi}{\mathrm{d}s^3}\right)\left(c_{11} + \frac{e_{31}^2}{k_{33}}\right) + \frac{e_{31}V}{h} \tag{4.7a}$$

$$\tau_{xx}^s = \tau_o - (\frac{h}{2})\left(\frac{\mathrm{d}\varphi}{\mathrm{d}s} - l^2\frac{\mathrm{d}^3\varphi}{\mathrm{d}s^3}\right)\left(c_{11}^s + \frac{e_{31}^s e_{31}}{k_{33}}\right) + \frac{e_{31}^s V}{h} \tag{4.7b}$$

$$\tau_{xx}^s = \tau_o - (-\frac{h}{2})\left(\frac{\mathrm{d}\varphi}{\mathrm{d}s} - l^2\frac{\mathrm{d}^3\varphi}{\mathrm{d}s^3}\right)\left(c_{11}^s + \frac{e_{31}^s e_{31}}{k_{33}}\right) + \frac{e_{31}^s V}{h} \tag{4.7c}$$

Therefore, the moment of the cross section with the consideration of strain gradients, upper surface stress, lower surface stress as well as the surfaces in the thickness direction, is written as;

$$M = EI_{\text{eff}}\left[\frac{\mathrm{d}\varphi}{\mathrm{d}s} - l^2\frac{\mathrm{d}^3\varphi}{\mathrm{d}s^3}\right] \tag{4.8}$$

where $EI_{\text{eff}} = \left(c_{11} + \frac{e_{31}^2}{k_{33}}\right)\frac{bh^3}{12} + \left(c_{11}^s + \frac{e_{31}^s e_{31}}{k_{33}}\right)\frac{h^3}{6} + \left(c_{11}^s + \frac{e_{31}^s e_{31}}{k_{33}}\right)\frac{bh^2}{2}$ (Huang and Yu, 2006).

Here c_{11} is assumed to be size-independent similar to the approach adopted by some other researchers (Joseph et al., 2016; Kahrobaiyan et al., 2011; Kong et al., 2009). Our model applies to those materials for which there isn't any significant size dependence of c_{11}. The electrical force of the cross section induced by the electrical components of σ_{xx} and τ_{xx}^s is given by (Wang and Wang, 2016);

$$T = e_{31}Vb + 2bVe_{31}^s / h \tag{4.9}$$

The equivalent vertical load $q(s)$ induced by the surface residual stress is expressed as (He and Lilley, 2008b; Wang and Feng, 2009);

$$q(s) = H\kappa = H\frac{\mathrm{d}\varphi}{\mathrm{d}s} \tag{4.10}$$

with $H = 2\tau_{\text{o}}b$ is the effective lateral distribution load (He and Lilley, 2008a, 2008b; Wang and Feng, 2009) here b is the beam width. Note that the effects of surface elasticity and surface piezoelectricity have been included in the effective bending stiffness, EI_{eff}. Therefore only τ_{o} is included in H. The equilibrium equations of the DCB give (Wang and Wang 2013); $\frac{\mathrm{d}Q}{\mathrm{d}s} = -H\frac{\mathrm{d}\varphi}{\mathrm{d}s}$, $\frac{\mathrm{d}M}{\mathrm{d}s} = Q$ (shear force). Bending moment at any point "s" induced by the equivalent distributed load $q(s)$, endpoint concentrated vertical force F and the electrical force of the cross-section T may be expressed as;

$$M(s) = \int_0^a (\xi - s)(H + T)\frac{\partial\varphi}{\partial\xi}\mathrm{d}\xi + F[x(a) - x(s)] \tag{4.11}$$

So, the governing equation of a Euler beam with the cumulative consideration of surface effects, piezoelectricity and strain gradient subjected to large deformation is written as;

$$EI_{\text{eff}}\left[\frac{\mathrm{d}^2\varphi}{\mathrm{d}s^2}-l^2\frac{\mathrm{d}^4\varphi}{\mathrm{d}s^4}\right]=-F\cos\varphi+(H+T)\varphi-(H+T)\varphi_a \tag{4.12}$$

Here φ_a is the unknown slope at the free end of the beam. Alternatively, the governing equation and respective boundary conditions may also be evaluated through a variational principle similar to the approach considered by Abdelkefi et al. (2011) for a piezoelectric cantilever beams, Kong et al. (2009), Giannakopoulos and Stamoulis (2007) and Papargyri et al. (2002) for the strain gradient formulations using Euler beam model. The variational principle is given as; $\delta(U_{\text{b}}+U_{\text{s}})-\delta W=0$, where W is the work done by the external forces, U_{b} and U_{s} are the strain energy of the bulk and surface respectively. In the one-dimensional case, the bulk strain energy (U_{b}) is given as; $U_b=\frac{1}{2}\int_A\int_0^a[\tau_{xx}\varepsilon_{xx}+\mu_{xxx}.\nabla\varepsilon_{xx}+D_zE_z]\mathrm{d}s\mathrm{d}A$. On the other hand, the surface strain energy (U_{s}) is given as; $U_s=\frac{1}{2}\int_A[\tau^s_{xx}\varepsilon^s_{xx}+\mu^s_{xxx}.\nabla\varepsilon^s_{xx}+\tau_{\text{o}}\varepsilon^s_{xx}]\mathrm{d}A$. Here ∇ denotes (d/ds) in the case of large deformation. The variation of the work done by the external forces is written as; $\delta W=\int_0^a F\cos\varphi(s)\delta\varphi\mathrm{d}s$. So, the variational principle $\delta(U_{\text{b}}+U_{\text{s}})-\delta W=0$ gives;

$$\begin{aligned}&\int_0^a\left[\left[-EI_{\text{eff}}\left\{\left(\frac{\partial^2\varphi}{\partial s^2}-l^2\frac{\partial^4\varphi}{\partial s^4}\right)\right\}+(H+T)\varphi-(H+T)\varphi_{(a)}-F\cos\varphi\right]\delta\varphi\right]\mathrm{d}s-\\&\left[\left[EI_{\text{eff}}\left\{\left(\frac{\partial\varphi}{\partial s}-l^2\frac{\partial^3\varphi}{\partial s^3}\right)\right\}\right]\delta\varphi'\right]_0^a+\left[\left[EI_{\text{eff}}\left\{\left(\frac{\partial^2\varphi}{\partial s^2}\right)\right\}\right]\delta\varphi''\right]_0^a=0\end{aligned} \tag{4.13}$$

From Eq. (4.13) the governing equation similar to Eq. (4.12) is obtained. In order to solve the governing equation (4.12), we need four boundary conditions, comprised of classical as well as non-classical boundary conditions. The boundary conditions evaluated from the variational principle require $EI_{\text{eff}}[(\partial\varphi/\partial s)-l^2(\partial^3\varphi/\partial s^3)]$ (moment) and $EI_{\text{eff}}(\partial^2\varphi/\partial s^2)$ (higher order moment) to be specified at $s = 0$ and $s = a$. So, one of the possible set of boundary conditions considered in this work is as follows; At clamped end i.e. $s = 0$, the rotation of the beam is zero ($\varphi = 0$). Meanwhile, for the non-classical terms, the trivial natural boundary conditions (higher order moment evaluated from variational principle) is expressed as $\frac{\mathrm{d}^2\varphi}{\mathrm{d}s^2} = 0$. Moreover, at the free end, i.e. $s = a$ the zero classical moment gives $\frac{\mathrm{d}\varphi}{\mathrm{d}s} = 0$ (Beléndez, 2002) and the non-classical or higher order moment (from variational principle) as depicted in Eq. (4.8) would also be zero, that gives $\frac{\mathrm{d}\varphi}{\mathrm{d}s} - l^2\frac{\mathrm{d}^3\varphi}{\mathrm{d}s^3} = 0.$ Overall, the boundary conditions used in this paper are as follows;

At $s = 0$: $\varphi = 0$, $\frac{\mathrm{d}^2\varphi}{\mathrm{d}s^2} = 0$ (4.14a)

At $s = a$: $\frac{\mathrm{d}\varphi}{\mathrm{d}s} = 0$, $\frac{\mathrm{d}\varphi}{\mathrm{d}s} - l^2\frac{\mathrm{d}^3\varphi}{\mathrm{d}s^3}$ or $\frac{\mathrm{d}\varphi}{\mathrm{d}s} = 0$, $\frac{\mathrm{d}^3\varphi}{\mathrm{d}s^3} = 0$ (4.14b)

Eq. (4.12) with the boundary conditions described in Eq. (4.14) is solved numerically by using Matlab code bvp4c. This code is specifically designed for boundary value problems and is based on finite difference method that implements a three-stage Lobatto IIIa collocation formula. Lobatto methods (based on trapezoidal quadrature rule) are widely used in numerical integration for evaluating the approximate solution of differential equations at two endpoints t_n and t_{n+1} of the interval $[t_n, t_{n+1}]$. Out of several

Lobatto methods, Lobatto IIIA is usually preferred for boundary value problems and therefore considered in this work. Further details about these methods are provided by Shampine et al. (2000), while the implementation of other methods such as dual boundary element method for the determination of fracture properties is provided by Joseph et al. (2014). Furthermore, the strain energy release rate G may be found by taking beam length as a (crack length) and width b, the strain energy release rate of the double cantilever beam can be written as; $G = F\,(\mathrm{d}Y_{max}/b\mathrm{d}a)$ (Wang and Wang, 2013; Stamoulis and Giannakopoulos, 2012). For the uncracked part (root part) of DCB, governing equation (using Timoshenko beam theory (Wang & Wang, 2013; Joseph et al., 2016)) is shown in section 2.6.1.3. It is necessary to mention the prominence of shear stresses at the uncracked part that must be incorporated in the constitutive equations. Therefore, the Timoshenko beam model is more suitable to study the uncracked part of the DCB (section 2.6.1.3). Accordingly, the potential energy of the uncracked part (U_r) is expressed as;

$$U_r = 2\int_{-\infty}^{0} \frac{(M(x))^2}{2EI_{\text{eff}}}\mathrm{d}x + 2\int_{-\infty}^{0} \frac{(Q(x))^2}{2G^s A}\mathrm{d}x \tag{4.15}$$

Here, $M(x)$ and $Q(x)$ are the bending moment and shear force on cross-section area A, G^s is an effective shear modulus and EI_{eff} is the effective bending rigidity as defined in Eq. (4.8). As per the coordinate system, the integrals vary from negative infinity to zero. Using Eq. (4.15) and Eq. (2.29), one gets;

$$U_r = \frac{1}{\sqrt{EI_{\text{eff}} G^s A}}\left[F^2 X^2(\varphi_{\text{a}}) + \left[\int_0^a s(H+T)\frac{\mathrm{d}\varphi}{\mathrm{d}s}\mathrm{d}s\right]^2\right] \tag{4.16}$$

where $X(\varphi_a)$ is the endpoint horizontal deflection (as shown in Fig. 4.1), F is the vertical concentrated force, φ_a is the unknown slope at the free end of the beam, $H = 2\tau_o b$ and T is the electrical force of cross-section as given in Eq. (4.9).

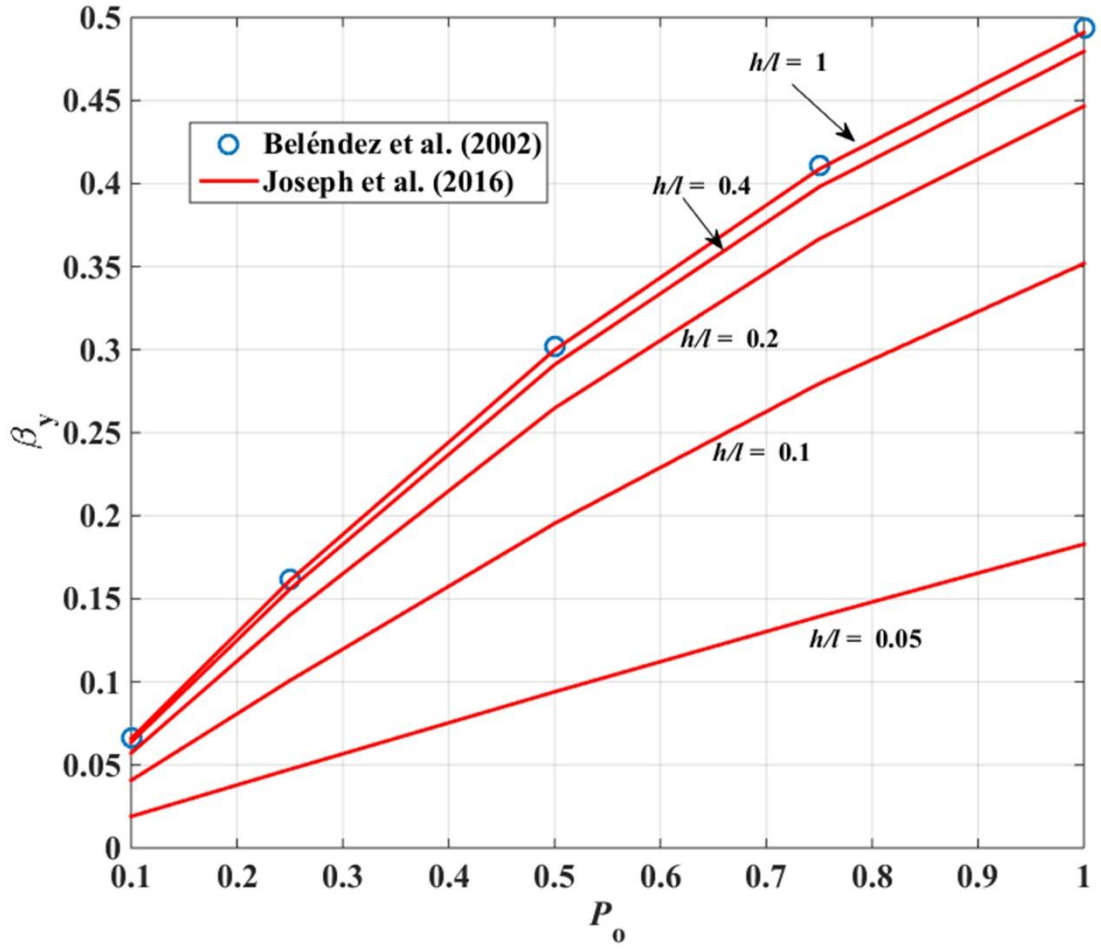

Figure 4.2 Comparison of the results obtained from the current method with the results provided by Beléndez et al. (2002) and Joseph et al. (2016)

4.4 Results and Discussion

In order to numerically solve Eq. (4.12), material bulk properties of PZT-5H (Yan and Jiang, 2012) are taken i.e. c_{11} = 102 GPa, $e_{31} = -17.05\,\mathrm{Cm}^{-2}$, k_{33} = 1.76 x 10^{-8} $\mathrm{CV}^{-1}\mathrm{m}^{-1}$, $G^s = c_{66}$ = 35.5 GPa. For the surface, the properties are taken from (Huang & Yu, 2006; Yan & Jiang, 2011, 2012) i.e. $E^s = 7.56\,\mathrm{Nm}^{-1}$ and $e_{31}^s = -3\times10^{-8}\,\mathrm{Cm}^{-1}$. The

value of surface residual stresses τ_o and material characteristic length (l) are assumed to be $\pm$ 10 Nm^{-1} (since it can be positive or negative) and 17.6 μm (Kong et al., 2009). In order to solve the bending problem of the piezoelectric DCB with strain gradient effects using the numerical method of Lobatto IIIa collocation formula, the accuracy of this method is tested by comparing the large deformation (without strain gradient effect) results presented by Beléndez et al. (2002) and the results with the strain gradient effects (with and without surface effect and large deformation) presented by the authors (Joseph et al., 2017) against the P_o ($P_o = Fa^2/2(EI)$). The results are shown in Fig. 4.2 (here $\beta_y = Y/a$, where Y is the vertical end point deflection and a is the length of the beam) and are shown to be in agreement with Beléndez et al. (2002). Nevertheless, it also vital to further elaborate the effect of large deformation against the load factor P_o. The effect of large deformation for gradient beams with increased load factor is recently shown by Joseph et al. (2016), here the results are replicated for larger normalized endpoint force (gradient models are stiffer but the plot is not a straight line especially for $h/l \leq 0.2$). However, this effect shrinks when the height of the beam equals the material characteristic length. The results are shown in Fig. 4.3. Here, Y_g, Y_l and Y_o are the endpoint vertical deflections for the strain gradient piezoelectric cantilever beam (large deformation theory), non-gradient piezoelectric cantilever beam (large deformation theory) and the classical beam Y_o ($Y_o = Fa^3/(3EI)$) respectively. Meanwhile contrary to the classical theory, which assumes the endpoint deflection to be independent of normalized endpoint force, this result demonstrates large deformation to be more pronounced at larger normalized endpoint force (curve for Y_l/Y_o).

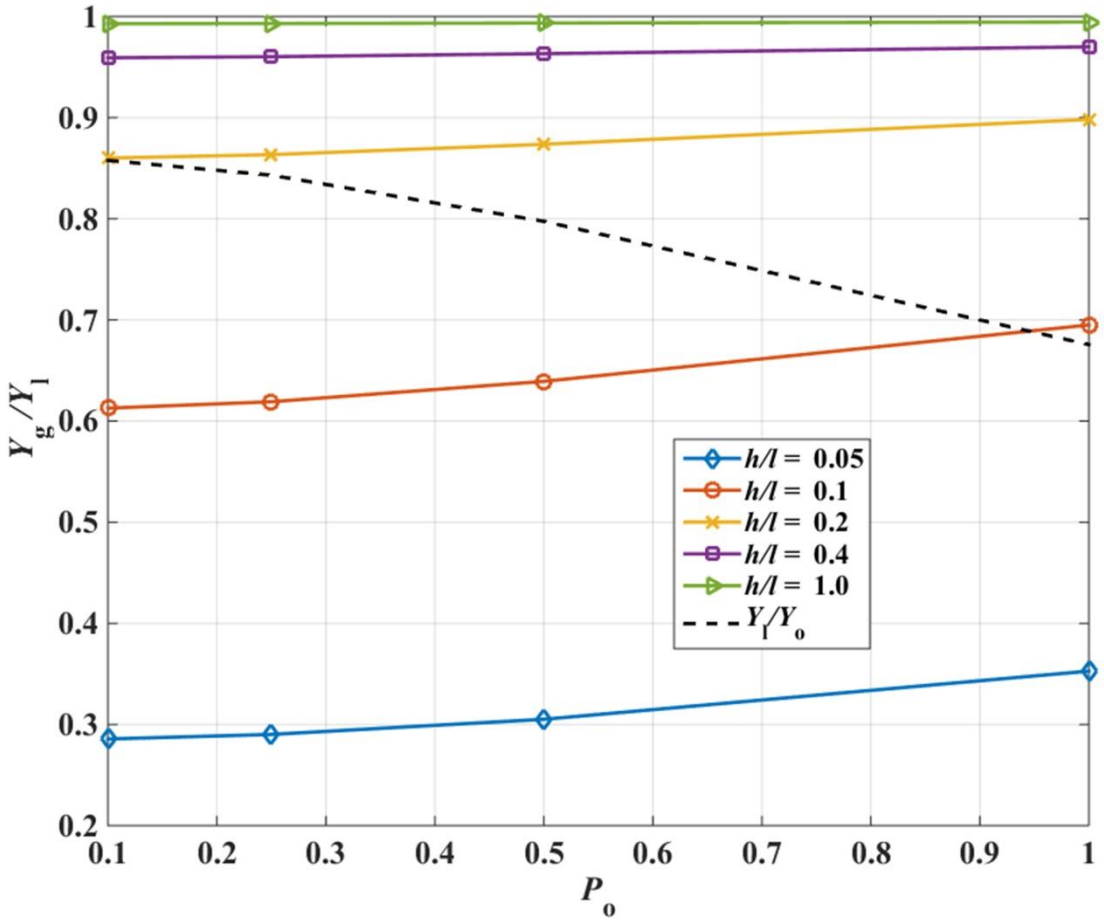

Figure 4.3 Normalized tip deflection against the load factor Po (only bulk piezoelectric effect

For piezoelectric cantilever bending under large deformation, the force F (1 μN) and height h are chosen in a manner such that the beam remains elastic throughout. The static rotation of a cantilever beam (φ), normalized by i.e. $Fa^2/(2EI)$ (classical result at the free end of the beam) is presented in Fig. 4.4. Here a/h is taken as 20 and the only bulk piezoelectric effect is taken into account. It is shown that, for lower h/l ratios, the strain gradient beam models predict stiffer behaviour than the classical ones. The normalized deformations are shown to be increasing with higher h/l ratio. Positive voltage tends to increase the stiffness of beam and vice versa since the negative voltage will induce a compressive force which makes the beam to behave softer (Wang and Wang, 2016). Moreover, the results for the non-piezoelectric beam are also shown

representing relatively softer behaviour. Hence from Fig. 4.4, it is evident that the piezoelectric effect enhances beam stiffness.

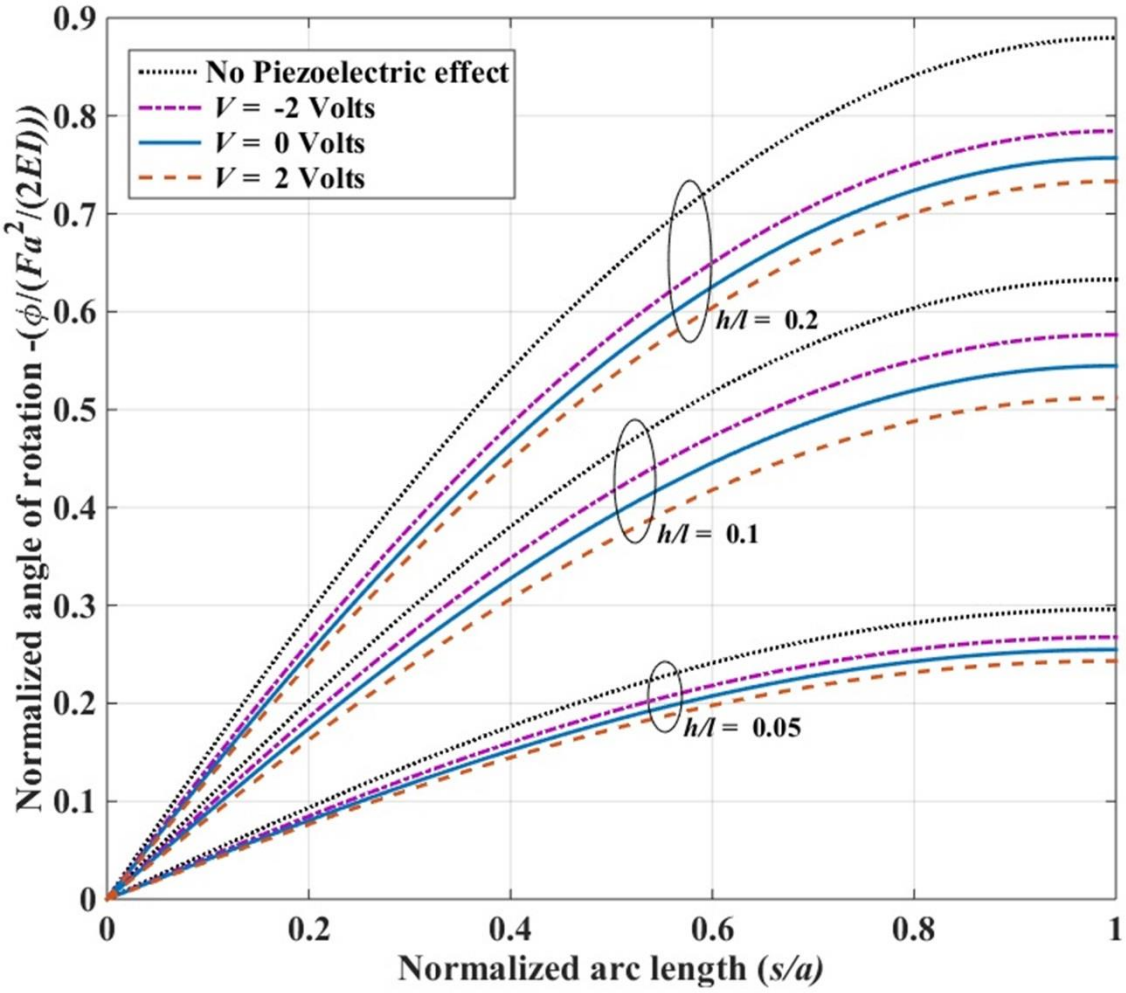

Figure 4.4 Normalized angle of rotation along the piezoelectric beam for strain gradient model

For DCB, rotation of cantilever beam may be used to evaluate its strain energy release rate. It may be done by taking the length of the beam as crack length *a* and width *b*, with that the strain energy release rate of the double cantilever beam is given by $G = F\,(\mathrm{d}Y_{max}/b\mathrm{d}a)$. Here Y_{max} may be found by using the relation; $Y_{max} = \int_0^a \sin(\varphi_a)\mathrm{d}s$, where φ_a is the unknown slope at the free end of the beam (as illustrated in the previous section). The effect of piezoelectricity on the strain energy release rate, normalized with

the classical solution of DCB ($G_o = 12F^2a^2/(c_{11}h^3b^2)$), is plotted in Fig. 4.5. The results are plotted for different a/h and h/l ratios. Figure 4.5 shows that the normalized strain energy release rate of strain gradient piezoelectric DCB model (G_g) is lower for smaller h/l ratios. It is noted that the piezoelectric effect tends to increase the stiffness of the beam irrespective of a/h ratio (but this effect decreases for more slender beams). The results are plotted for different voltage values (zero, positive and negative). It may be seen that negative voltage increases the strain energy release rate and vice versa. The effect of the applied voltage is more significant for slender beams. Moreover, it is necessary to evaluate the relationship between gradient and non-gradient piezoelectric DCB with the consideration of large deformation theory. For this, the ratio of strain energy release rate for the strain gradient models (G_g) to the conventional large deformation (non-gradient) piezoelectric DCB (G_l) is plotted in Fig. 4.6. The ratios are greater for positive voltage and vice versa. Meanwhile, it may clearly be seen that the gradient effect is more prominent for smaller h/l and it decreases as h/l is increased. From Fig. 4.6, similar to Fig. 4.5, it is evident that the effect of the applied voltage is more significant for slender beams. Overall, it may fairly be concluded that the strain gradient effect must be incorporated in the formulation to accurately predict the fracture behaviour of micro/nano piezoelectric DCB.

Next, the influence of surface effects i.e. surface elasticity and surface residual stress on the fracture behaviour of piezoelectric DCB (here surface piezoelectricity is also considered) is evaluated and plotted in Fig. 4.7. Since surface elasticity and surface residual stress can be positive or negative; therefore, it is necessary to demonstrate the influence of both positive and negative surface parameters (surface residual stress and surface elasticity) on the strain energy release rate of the piezoelectric DCB. For this reason, the results are plotted with six different kinds of inputs as shown in Fig. 4.7. Here voltage is taken as zero. The normalized strain energy release rate of the strain

gradient models (different h/l ratios) of piezoelectric DCB is evaluated and plotted. From Fig. 4.7, it is evident that the influence of surface elasticity and surface piezoelectricity is very small as compared to that of surface residual stress i.e. the surface residual stress constitutes a major proportion of all the surface effects on the fracture behaviour of DCB (Wang and Wang, 2013). Moreover, it can be seen that the surface effects are more prominent for higher a/h ratios i.e. for slender beams. The positive surface residual stress and negative surface elasticity enhance the normalized strain energy release rate while the negative surface residual stress and positive surface elasticity reduce the normalized strain energy release rate. Due to the prominent effect of surface residual stress, the results for strain energy release rate are separately plotted with different applied voltages in Fig. 4.8. Here the results are plotted only for h/l = 0.05 (under higher strain gradient effect). Interestingly, under positive applied voltage and negative surface residual stress (V = 2 Volts; $\tau_o = -10\ \mathrm{Nm^{-1}}$), beam tends to behave much stiffer when $a/h \geq 15$. This stiffer behaviour may be explained due to the sign of curvature and surface residual stress (using Young-Laplace equation (Chen et al., 2006; Gurtin et al., 1998)) that cause an additional distributed load and change beam stiffness (He and Lilley, 2008a; Wang and Wang, 2015; Wu et al., 2015). For instance, with a positive surface residual stress, a positive curvature results in a positive distributed transverse force. This positive force increases the rotation of the cantilever and thus beam behaves like a softer material. Meanwhile, this behaviour is totally opposite in the case when $\tau_o < 0$, hence a cantilever beam may exhibit a stiffer response comparatively.

It is necessary to evaluate the fracture behaviour of piezoelectric DCB with different electrical boundary conditions i.e. the open and short circuit condition. For the short-circuit condition boundary condition, the electric field (E_z) would be zero which nullify the role of surface piezoelectricity. Here the following parameters are considered

i.e. V = 0 Volts, $E^s = -7.56\ \mathrm{Nm}^{-1}$ and $\tau_o = -10\ \mathrm{Nm}^{-1}$. Figure 4.9 shows the normalized strain energy release rate of DCB with different electrical boundary conditions. From Fig. 4.9, it is evident that the normalized strain energy rate with short-circuit boundary condition is larger than that of an open-circuit condition. This effect may be explained by comparing the bending rigidities of the beam with different electrical boundary conditions. For instance, in the case of short-circuit (E_z = 0) the bulk stress is given as; $\sigma_{xx} = Ez\mathrm{d}\varphi/\mathrm{d}s$ that gives the effective bending rigidity to be; $EI_{\mathrm{eff}} = c_{11}bh^3/12$. On the other hand, for open-circuit boundary condition, the stress is $\sigma_{xx} = c_{11}z\mathrm{d}\varphi/\mathrm{d}s + e_{31}E_z$ that gives the bending rigidity as; $EI_{\mathrm{eff}} = (c_{11} + e_{31}^2/k_{33})bh^3/12$. It is evident, by comparing two bending rigidities that the one of short-circuit condition is smaller than that of open circuit condition. Therefore, the normalized energy release rate of the short circuit is larger than that of an open circuit condition. This difference in normalized strain energy release rate is more evident when the height of the beam is increased.

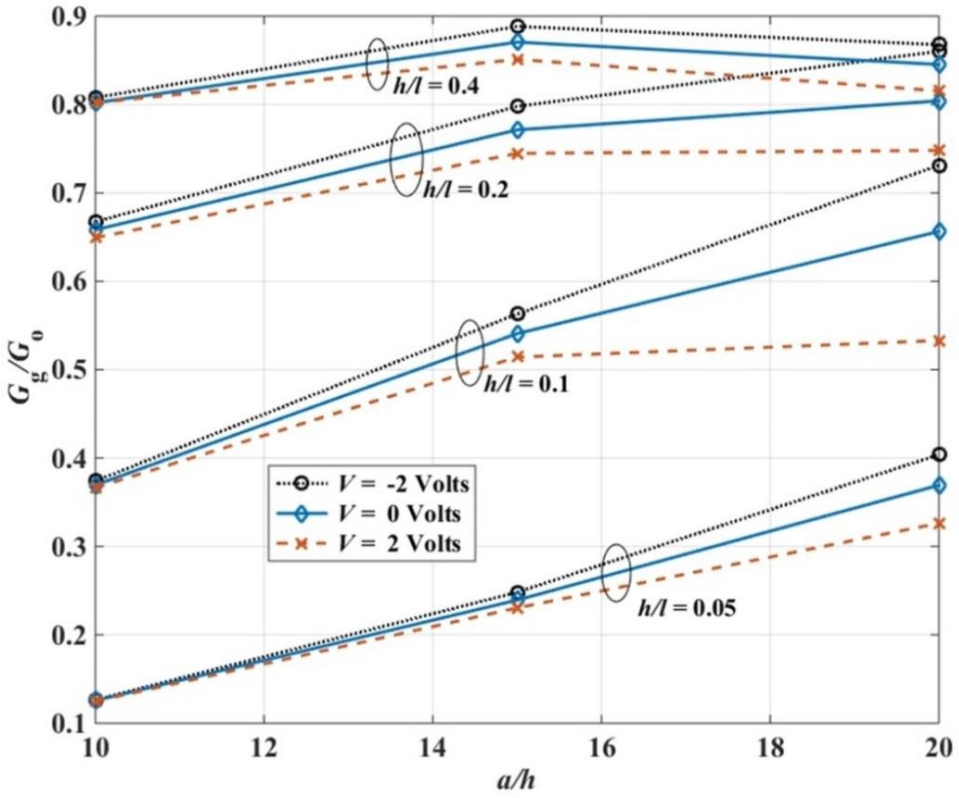

Figure 4.5 Strain energy release rate for piezoelectric strain gradient DCB normalized with the classical result - G_o

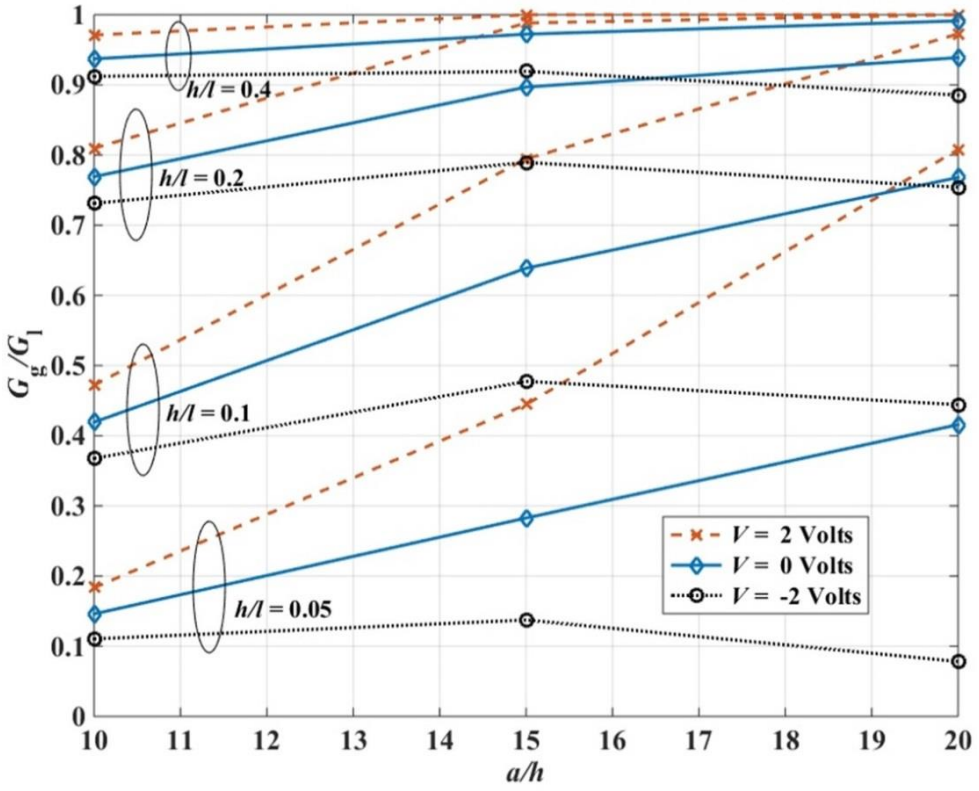

Figure 4.6 Strain energy release rate for strain gradient piezoelectric DCB normalized with non-gradient piezoelectric DCB

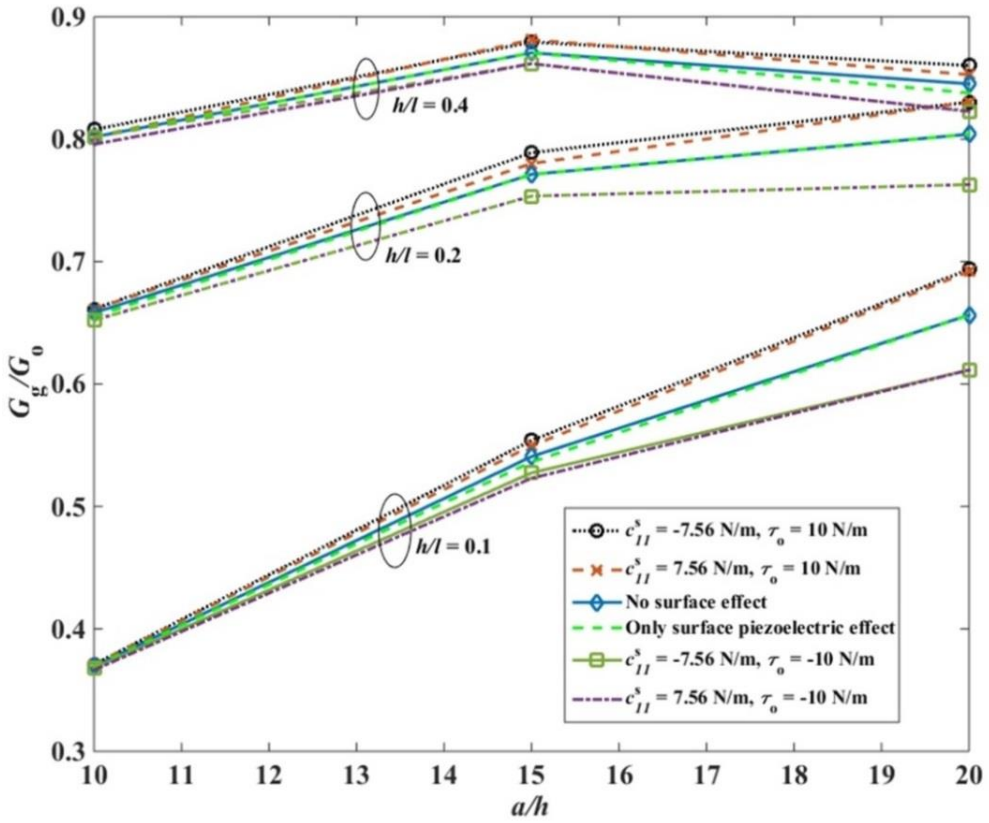

Figure 4.7 Normalized strain energy release rate for piezoelectric strain gradient DCB with and without surface effects (surface elasticity, surface residual stress and surface piezoelectricity, V = 0 Volts)

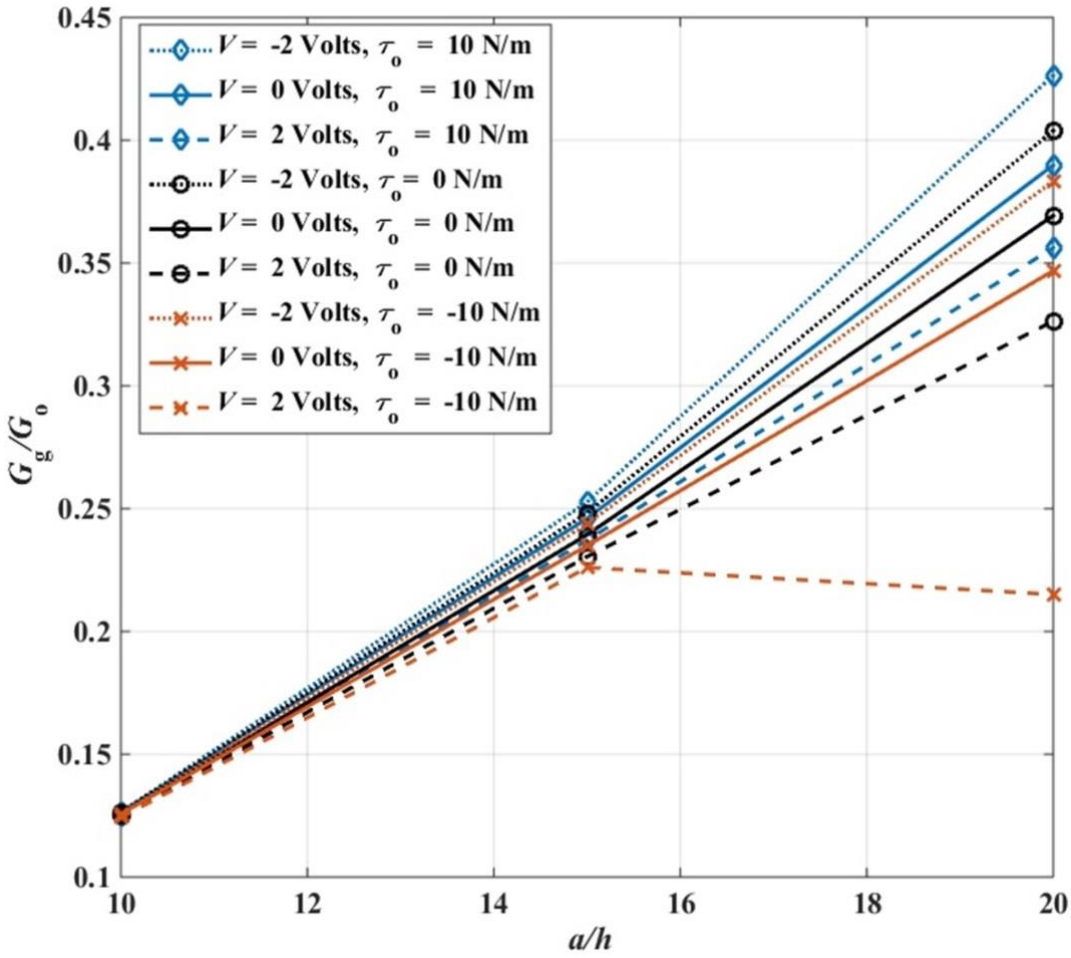

Figure 4.8 Effect of surface residual stress on the normalized strain energy release rate ($E^s = e_{31}^s = 0$)

Now the influence of the uncracked (root) part of DCB is investigated numerically. Here all the surface effects are included i.e. $E^s = 7.56\ \mathrm{Nm}^{-1}$, $e_{31}^s = -3\times10^{-8}\ \mathrm{Nm}^{-1}$ and $\tau_o = -10\ \mathrm{Nm}^{-1}$ (V = 0 Volts). Firstly, the strain energy release rate of the uncracked part (G_2) is evaluated using $G_2 = \mathrm{d}U_r/b\mathrm{da}$ (U_r is defined in Eq. (4.16)). Here R is defined, which is the ratio of the strain energy release rate contributed by the uncracked part to the cracked part of DCB ($R = G_2/G_1$). The variations of R versus a/h for different h/l ratios are plotted in Fig. 4.10. The results are plotted for both piezoelectric DCB models (with strain gradient effect and without strain gradient effect). It can be seen from Fig. 4.10 in case of strain gradient models that, for smaller

DCBs i.e. $h/l \leq 0.2$ and $a/h \leq 20$, the value of R is huge and hence should not be neglected even for slender beams (higher a/h ratios). Also when $h/l = 0.05$ and $a/h = 10$, the value of R is greater than 0.7 that establishes the contribution of the uncracked part of DCB is approximately 70% of the cracked part. The shows the massive root effect at the smaller scale (that further elaborates the argument made by Wang and Wang (2013). The contribution of the uncracked part decreases as a/h is increased. The results presented in Fig. 4.10 further strengthen the argument presented by Wang and Wang (2013). However, for non-gradient models, the contribution of the uncracked part is between 6 to 13 % (depending on the height and a/h ratio).

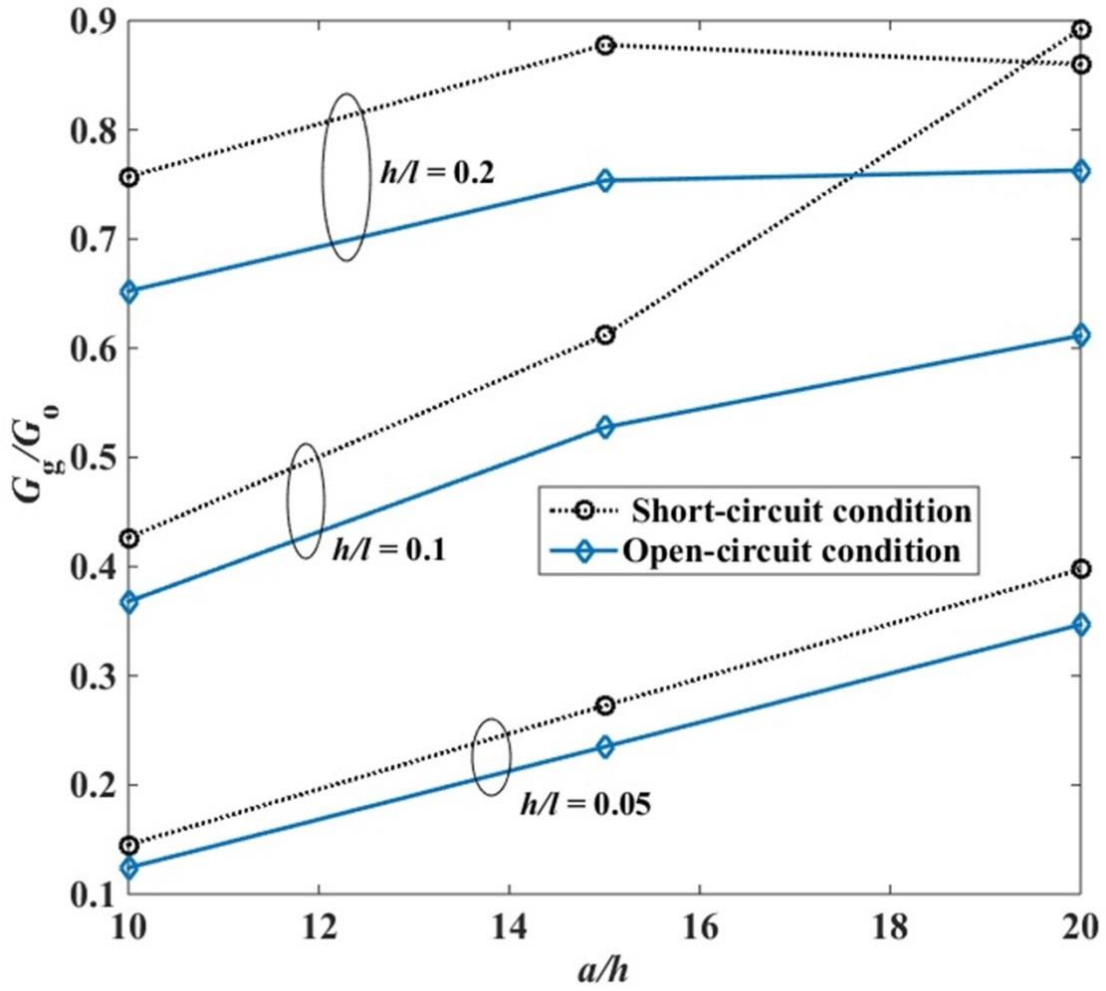

Figure 4.9 Comparison of normalized strain energy release rate under different electrical boundary conditions (E_s = -7.56 N/m, τ_0 = -10 N/m, V = 0 Volts)

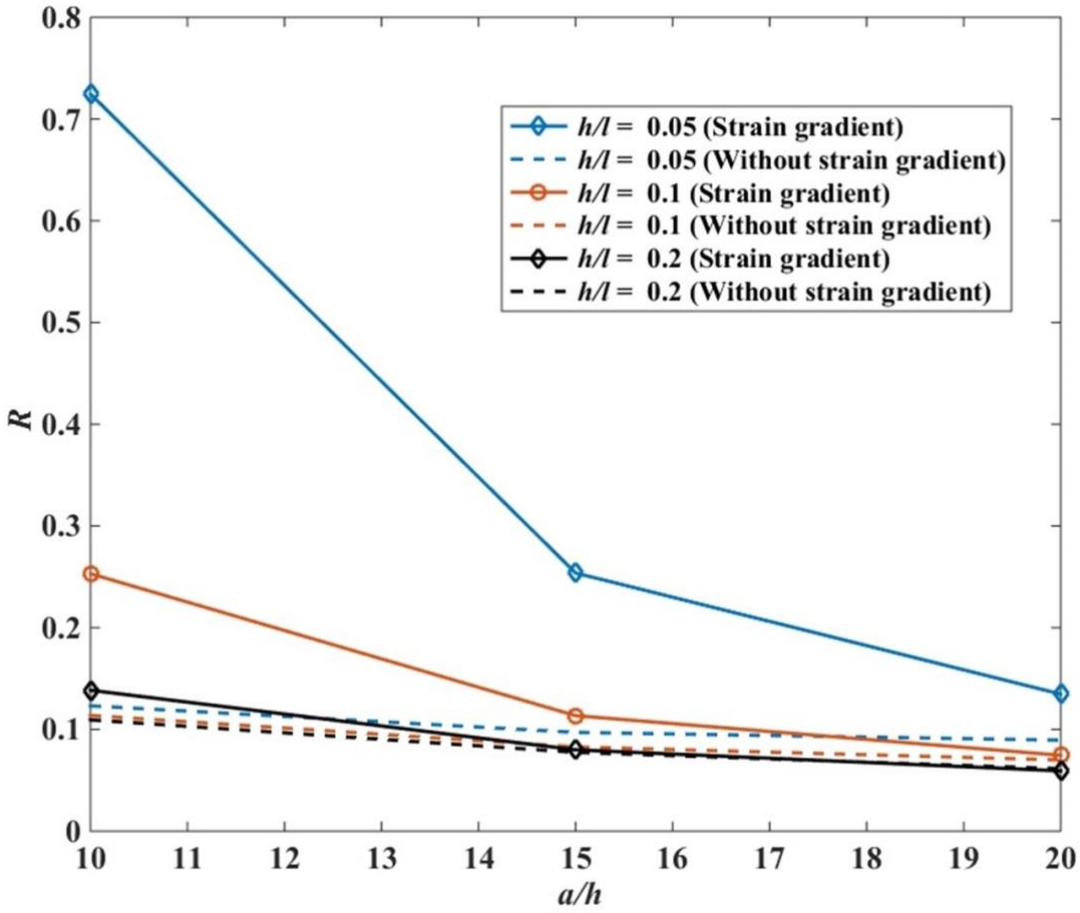

Figure 4.10 Variation of *R* versus *a*/*h*

The comparison of the normalized strain energy release rate for the strain gradient model (with and without root effect) as well as the non-gradient (with and without root effect) is shown in Fig. 4.11. It is evident that the incorporation of un-cracked part enhances the strain energy release rate of the piezoelectric DCBs with different *h*/*l* and *a*/*h* ratios. In particular, for $h/l < 0.1$, it may fairly be stated that even with the fusion of root effect (either in strain gradient or non-gradient (large deformation) model), the normalized strain energy release rate of the gradient model remains lower than that of non-gradient models (this highlights a massive strain gradient effect in lowering the strain energy release rate and hence stiffening the structure). Although the difference between the strain energy release rate of gradient and non-gradient models decreases with higher *a*/*h* ratio but this statement may not be true when $h/l \geq 0.1$, since the strain

energy release rate becomes more sensitive to beam slenderness (at higher h/l). Overall, from Fig. 4.10 and 4.11, it is evident that the incorporation of root (uncracked) part is essential for accurate prediction of fracture behaviour of DCB.

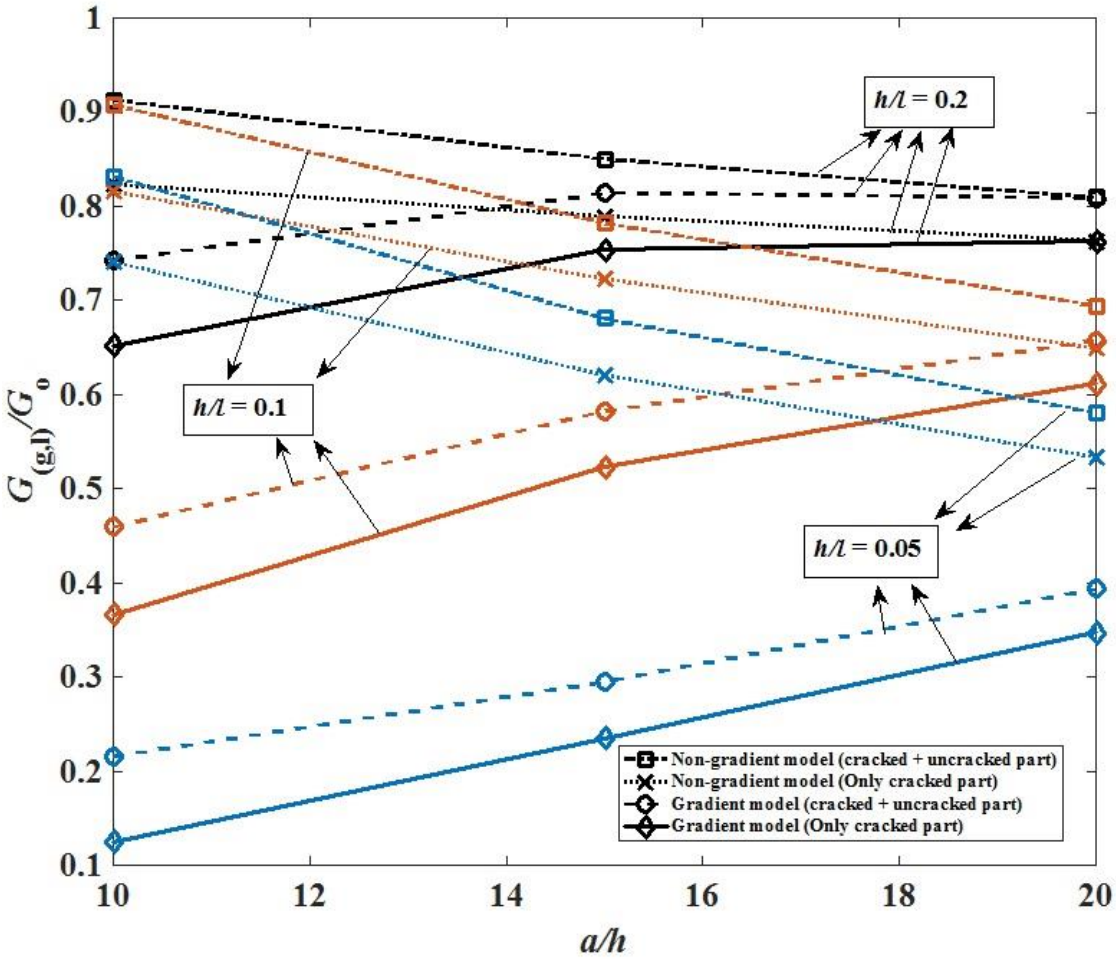

Figure 4.11 Normalized strain energy release rate with/without root effect versus a/h (blue, h/l = 0.05; orange, h/l = 0.1; black, h/l = 0.2)

4.5 Summary

This paper investigates the influence of strain gradient on the fracture of piezoelectric double cantilever beam fracture mechanics specimen subjected to large deformation. The results demonstrate that the effect of large deformation is dependent on the normalized endpoint force. As expected, the strain gradient model is shown to enhance the stiffness of a piezoelectric beam. The effect of strain gradient, surface

piezoelectricity, surface elasticity, surface residual stress, applied voltage and different electrical boundary conditions are thoroughly studied on the fracture behaviour of piezoelectric DCB. Both cracked and uncracked parts of DCB are included in modeling and analysis. Results show that the strain gradient effect tends to decrease the strain energy release rate and this effect is more evident when $h/l < 0.4$. The effect of surface residual stress is more significant than surface elasticity and surface piezoelectricity. Strain energy release rate of short-circuit model is higher than the open-circuit. The root effect also enhances the normalized strain energy release rate it must not be ignored even for slender beams (this observation is completely different from the classical results). The results of this paper are useful not only for determining the fracture toughness of micro/nanoscale piezoelectric materials but also for explaining and validating the relevant test data.

Moreover, this paper studies a homogenous DCB specimen, however in many engineering practices, materials are nonhomogenous and their fracture has generated great interest among the experts in the field of mechanics of material (Ma et al., 2007; Zhou et al., 2005; Guo et al., 2004a, 2004b). Additional investigations are clearly needed in order to gain further knowledge to capture the influence of material inhomogeneity on the large deformation and strain gradient effects on the fracture of DCB.

References

Abdelkefi, A., Najar, F., Nayfeh, A. & Ayed, S. B., 2011. An energy harvester using piezoelectric cantilever beams undergoing coupled bending–torsion vibrations. *Smart Materials and Structures*, 20, 115007

Aifantis, E. C., 1992. On the role of gradients in the localization of deformation and fracture. *International Journal of Engineering Science*, 30, 1279-1299.

Aifantis, E. C., 1999. Gradient deformation models at nano, micro and macro scales. *Journal of Engineering Materials and Technology, ASME*, 121, 189-202

Aifantis, E. C., 1999. Strain gradient interpretation of size effects. *International of Fracture.*, 95, 299-314

Aifantis, E. C., 2003. Update on a class of gradient theories. *Mechanics of Materials*, 35, 259-280.

Aifantis, E. C., 2016. Chapter One-Internal Length Gradient (ILG) Material Mechanics Across Scales and Disciplines. *Advances in Applied Mechanics*, 49, 1-110.

Beléndez, T., Neipp, C. & Beléndez, A., 2002.Large and small deflections of a cantilever beam. *European Journal of Physics*, 23, 371.

Chen, T., Chiu, M. S. &Weng, C. N., 2006. Derivation of the generalized Young-Laplace equation of curved interfaces in nanoscaled solids. *Japanese Journal of Applied Physics*, 100, 074308.

Christensen, J.& Bastien, C., 2015.Nonlinear Optimization of Vehicle Safety Structures: Modelling of Structures Subjected to Large Deformations.Butterworth-Heinemann.USA.

Devitt, D., Schapery, R.& Bradley, W., 1980. A method for determining the mode I delamination fracture toughness of elastic and viscoelastic composite materials. *Journal of Composite Materials*, 14, 270-285.

Fang, X. Q., Liu, J. X.& Gupta, V., 2013.Fundamental formulations and recent achievements in piezoelectric nan-structures: a review. *Nanoscale*, 5, 1716-1726.

Giannakopoulos, A.E., Amanatidou, E.& Aravas, N., 2006. A reciprocity theorem in linear gradient elasticity and the corresponding Saint-Venant principle. *International Journal of Solids and Structures*, 43, 3875-3894.

Giannakopoulos, A.E. & Stamoulis, K., 2007. Structural analysis of gradient elastic components. *International Journal of Solids and Structures*, 44, 3440-3451.

Gurtin, M. E. & Murdoch, A. I. 1978. Surface stress in solids. *International Journal of Solids and Structures*, 14, 431-440.

Gurtin, M., Weissmuller, J.&Larche, F., 1998. A general theory of curved deformable interfaces in solids at equilibrium. *Philos. Mag. A.*, 78, 1093-1109.

Guo, L.C., Wu, L.Z. & Zeng, T., 2004. Mode I crack problem for a functionally

graded orthotropic strip. *European Journal of Mechanics-A/Solids*, 23, 219-234.

Guo, L.C., Wu, L.Z., Zeng, T.& Ma, L., 2004.The dynamic fracture behaviour of a functionally graded coating-substrate system. *Composite Structures*, 64, 433-441.

Gusso, A. 2010. Acoustic electromechanical energy loss mechanism for suspended micro-and nanoelectromechanical resonators. *Applied Physics Letters*, 96, 193504.

He, J. & Lilley, C. M. 2008a. Surface effect on the elastic behaviour of static bending nanowires. *Nano Letters*, 8, 1798-1802.

He, J. & Lilley, C. M. 2008b. Surface stress effect on bending resonance of nanowires with different boundary conditions. *Applied Physics Letters*, 93, 263108.

Huang, G. Y.& Yu, S. W. 2006. Effect of surface piezoelectricity on the electromechanical behaviour of a piezoelectric ring. *Phys. Status. Solidi*. (*b*)., 243(4), R22-R24.

Jia, X., Yang, J., Kitipornchai, S.& Lim, C. W., 2010. Free vibration of geometrically linear micro-switches under electrostatic and Casimir forces. *Smart Materials and Structures*, 19, 115028.

Jia, X. L., Yang, J.& Kitipornchai, S. 2011. Pull-in instability of geometrically nonlinear micro-switches under electrostatic and Casimir forces. *Acta Mechanica*, 218, 161-174.

Joseph, R. P., Purbolaksono, J., Liew, H. L., Ramesh, S. &Hamdi, M., 2014.Stress Intensity factors of a corner crack emanating from a pinhole of a solid cylinder. *Engineering Fracture Mechanics*, 128, 1-7.

Joseph, R. P., Wang, B. L.&Samali, B.,2017. Size effects on double cantilever beam fracture mechanics specimen based on strain gradient theory. *Engineering Fracture Mechanics*, 169, 309-320.

Kahrobaiyan, M. H., Asghari, M. Rahaeifard, M. &Ahmadian, M. T., 2011. A nonlinear strain gradient beam formulation. *International Journal of Engineering Science*, 49, 1256-1267.

Ke, L. L., Wang, Y. S.& Wang, Z. D., 2012. Nonlinear vibration of the piezoelectric nanobeams based on the nonlocal theory**.***Composite Structures*, 94, 2038–2047.

Ke, L. L., Chen, L. & Wang, Y. S., 2015.Free vibration of nonlocal piezoelectric nanoplates under various boundary conditions. *Physica. E*, 66, 93-106.

Kong, S., Zhou, S., Nie, Z. &Wang, K., 2009. Static and dynamic analysis of micro beams based on strain gradient elasticity theory. *International Journal of Engineering Science*, 47, 487-498.

Lam, D.C.C., Yang, F., Chong, A.C.M., Wang, J.. & Tong, P., 2003. Experiments and theory in strain gradient elasticity. *Journal of Mechanics and Physics of Solids*, 51, 1477-1508.

Li, X. F. & Lee, K. Y., 2016. Fracture of a thin power-law nonlinear material with a crack using the DCB model. *International Journal of Fracture*, 201, 119-125.

Liebold, C.& Muller, W. F., 2015. Applications of Strain Gradient Theories to the Size effect in Submicro-Structures incl. Experimental Analysis of Elastic Material Parameters. *Bulletin of TICMI-EMIS*, 19 (1), 45-55.

Ma, L. Li, H., Abdelmoula, R.& Wu, L. Z., 2007. Mode III crack problem in a functionally graded magneto-electro-elastic strip. *International Journal of Solids and Structures*, 44, 5518-5537.

Ma, L., Wu, L.Z., Zhou, Z. G.&Guo L. C., 2005. Fracture analysis of a functionally graded piezoelectric strip. *Journal of Composite Materials*, 69, 294-300

Ma, L., Wu, L.Z., Zhou, Z. G.&Guo L. C., 2005. Scattering of the harmonic anti-plane shear waves by a crack in functionally graded piezoelectric materials. *Journal of Composite Materials*, 69, 436-441

Mindlin, R. D., 1965. Second gradient of strain and surface-tension in linear elasticity. *International Journal of Solids and Structures*, 1, 417-438.

Nan, H. & Wang, B., 2013. Effect of crack face residual surface stress on nanoscale fracture of piezoelectric materials. *Engineering Fracture MEchanics*, 110, 68-80.

Papargyri-Beskou, S., Tsepoura, K., Polyzos, D., & Beskos, D., 2003. Bending and stability analysis of gradient elastic beams. *International Journal of Solids and Structures*, 40, 385-400

Polizzotto, C., 2016. A note on the higher order strain and stress tensors within deformation gradient elasticity theories: physical interpretations and comparisons.*International Journal of Solids and Structures*, 90, 116 -121

Reeder, J. R.& Crews Jr, J., 1991. Nonlinear analysis and redesign of the mixed-mode bending delamination test.

Ru, C. Q.& Aifantis, E. C., 1993. A simple approach to solve boundary-value problems in gradient elasticity. *Acta Mechanica*, 101, 59-68.

Shampine, L. F., Kierzenka, J.& Reichelt, M.W., 2000. Solving boundary value problems for ordinary differential equations in MATLAB with bvp4c. Tutorial notes.

Shi, M., Wu, H. P., Li, L. & Chai, G. H., 2014.Calculation of stress intensity factors for functionally graded materials by using the weight functions derived by the virtual crack extension technique. *International Journal of Mechanics and Materials in Design*, 10, 65-77.

Shen, S.& Hu, S., 2010. A theory of flexoelectricity with surface effect for elastic dielectrics. *Journal of Mechanics and Physics of Solids*, 58, 665-677.

Stamoulis, K.& Giannakopoulos, A.E., 2012. A study of size effects and length scales in fracture and fatigue of metals by second gradient modelling*. *Fatigue and Fracture of Engineering Materials & Structures*, 35, 852-860.

Vardoulakis, I., and Sulem, J., 1995. “Bifurcation Analysis in Geomechanics: Blackie/Chapman and Hall, London.

Wang, B. L.& Wang, K.F., 2013. Effect of surface residual stress on the fracture of double cantilever beam fracture toughness specimen. *Japanese Journal of Applied Physics*, 113, 153502.

Wang, G. F.& Feng, X. Q., 2009. Surface effects on buckling of nanowires under uniaxial compression. *Applied Physics Letters*, 94, 141913.

Wang, K. & Wang, B., 2015. A general model for nano-cantilever switches with consideration of surface effects and nonlinear curvature. *Physica. E*, 66, 197-208.

Wang, K. F. & Wang, B. L., 2016. Nonlinear fracture mechanics analysis of nano-scale piezoelectric double cantilever beam specimens with surface effect. *European Journal of Mechanics-A/Solids*, 56, 12-18.

Williams, J. G., 1987. Large displacement and end block effects in the 'DCB' interlaminar test in modes I and II. *Journal of Composite Materials*, 21, 330-347.

Wu, Q., Volinsky, A. A., Qiao, L.& Su, Y., 2015. Surface effects on static bending of nanowires based on non-local elasticity theory. *Materials International: Progress in Natural Sciences*, 25, 520-524.

Yan, Z. & Jiang, L., 2011. The vibrational and buckling behaviours of piezoelectric nanobeams with surface effects. *Nanotechnology*., 22, 245703.

Yan, Z.& Jiang, L., 2012. Vibration and buckling analysis of a piezoelectric nanoplate considering surface effects and in-plane constraints. Paper presented at the Proc. R. Soc. A.

Yang, R., Qin, Y., Li, C., Dai, L. & Wang, Z. L., 2009. Characteristics of output voltage and current of integrated nanogenerators. *Applied Physics Letters*, 94, 022905.

Yue, Y. M., Xu, K. Y.& Aifantis, E. C., 2014. Microscale size effects on the electromechanical coupling in piezoelectric material for anti-plane problem. *Smart Materials and Structures*, 23, 125043.

Yue, Y. M., Xu, K. Y., Chen, T.& Aifantis, E. C., 2015. Size effects on magnetoelectric response of multiferroic composite with inhomogeneities. *Physica B*, 478, 36-42.

Zhang, W., Wang, T.& Chen, X. 2008. Effect of surface stress on the asymmetric yield strength of nanowires. *Japanese Journal of Applied Physics*, 103, 123527.

Zhang, Z.& Jiang, L. 2014. Size effects on electromechanical coupling fields of a bending piezoelectric nanoplate due to surface effects and flexoelectricity. *Japanese Journal of Applied Physics*, 116, 134308.

Zhou, Z. G., Wu, L. Z. &Wang, B., 2005. The dynamic behaviour of two collinear Interface cracks in magneto-electro-elastic materials. *European Journal of Mechanics-A/Solids*, 24, 253-262.

Zhou, Z. G., Zhang, P. W. & Wu, L.Z., 2005.The dynamic behaviour of two collinear interface cracks in magneto-electro-elastic materials. *European Journal of Mechanics-A/Solids*, 24, 253-262.

Zhou, Z. G., Wu, L. Z.& Wang, B., 2005. The behaviour of a crack in functionally graded Piezoelectric/piezomagnetic materials under anti-plane shear loading. *Archives of Applied Mechanics*, 74, 526-535.

CHAPTER 5

PIEZOELECTRIC GRADIENT ELASTIC MATERIAL WITH FLEXOELECTRICITY

Publication

Paper 4:

Joseph, R. P., Chunwei Zhang, Wang, B. L, & Samali, B., 2018. Fracture analysis of flexoelectric double cantilever beams based on the strain gradient theory, *Composite* Structures. Doi: https://doi.org/10.1016/j.compstruct.2018.06.067

Relevance to the thesis

In the previous chapter, only the electro-mechanical coupling effect was considered to determine the possible size effects based on strain gradient theory. In this chapter, due to the presence of strain gradients, the Electric field-strain gradient coupling known as the flexoelectric effect is also incorporated in the constitutive equations of the piezoelectric beam. The model presented in this chapter is expected to cater the maximum scale-dependent effects, in particular on the micro/nano scale.

5.1 Abstract

In this article, the fracture behaviour of a flexoelectric double cantilever beam (DCB) under large deformation is investigated using strain gradient theory. Incorporation of electric field-strain gradient coupling, known as flexoelectricity, in the constitutive equations of a 1D cantilever beam is studied. Moreover, due to the enormous surface area to volume ratio at the micro/nanoscale, surface effects are also included in the theoretical formulations. The governing equation with the respective boundary conditions is derived and solved numerically by using the Lobatto IIIA collocation method. The solutions of the cantilever beam deflections and strain energy release rates of the DCB with different configurations are numerically evaluated and compared. Numerical results anticipate significant size effect (higher structural stiffness) as the values of the material length scale parameter (l) and piezoelectric coefficient scaling parameter (m) are increased. DCB with the open circuit boundary condition demonstrates higher stiffness than the short circuit boundary condition. At the micro/nanoscale, the effect of uncracked part of the DCB is found to be substantial in determining the strain energy release rate and it must not be ignored even for the slender beams.

5.2 Introduction

Ever increasing demands of piezoelectric micro/nanomaterials in small-scale devices such as Light emitting diodes (LEDs), nanoresonators and nanogenerators are evident as the technological advances toward the miniaturization of devices are being made (Ke et al., 2015). Over the past several decades, numerous studies have been conducted to understand the fundamental physics behind the phenomenon of material polarization under the application of external mechanical stress. The classical relation between applied strain and electric polarization, known as piezoelectricity, is thoroughly defined (Cady, 1946) and has been widely used to investigate the fracture behaviour of the

piezoelectric materials at the macro scale. However, a number of experimental studies have demonstrated the size-dependent linear electro-mechanical coupling at micro/nanoscale (Baskaran et al., 2011; Catalan et al., 2011). This occurs when the structure dimensions become comparable to the material length scale and the state of stress at a point is depended on not only the strain but also the strain gradient. The electromechanical coupling between polarization and strain gradient is termed as flexoelectricity (Mao and Purohit, 2014; Sladek et al., 2017). Contrary to the piezoelectric effect, flexoelectricity is not just limited to non-centrosymmetric materials but it may induce electric polarization in the centrosymmetric material by breaking the material's symmetry (Yan and Jiang, 2013b). Therefore, due to the flexoelectric effect, non-piezoelectric materials may also be used to produce piezoelectric composites (Sharma et al., 2010) and thus call out new challenges for researchers in the field of nanotechnology.

Due to an encounter of flexoelectricity in the modern era, detailed investigations relating to the fracture behaviour of the micro/nano piezoelectric materials are therefore essential in order to ensure their structural reliability for further establishing their applications. Traditionally, the amalgamation of classical continuum mechanics and electrostatics has been employed to study the electromechanical coupling phenomenon in piezoelectricity. However, in order to deal with the coupling of the strain gradient and polarization, higher order gradient theories such as strain gradient theories must be employed. The pioneer work, extending the linear piezoelectric theory by incorporating the effect of polarization gradient was presented by Mindlin (1969). On the other hand, Maranganti et al. (2006) included the polarization gradient as well as the strain gradient effect in their theoretical framework based on the variational principle. Recently, Hu and Shen constructed a comprehensive model incorporating flexoelectricity, an electrostatic force (Hu and Shen, 2010) as well as surface effects (Shen and Hu, 2010).

Mao and Purohit (2014) presented a detailed analysis for flexoelectric solids using strain theory which is eventually used to derive the governing Navier equation for the isotropic materials. In recent times Sladek et al. (2017) developed a finite element method (FEM) formulation to analyze the general 2D boundary value problem incorporating the electric-field strain gradient coupling in the constitutive equations. Some of the above-mentioned pioneer works have been thoroughly employed by researchers to investigate the electromechanical coupling behaviour of piezoelectric nanobeams. For instance, Majdoub et al. (2008) employed a modified Euler beam model and found that the electromechanical coupling coefficient in case of the piezoelectric nanowire is enhanced due to the flexoelectric effect. Liang et al. (2014) presented a modified Euler-Bernoulli beam model and highlighted some of its applications based on strain gradient theory. (Yan and Jiang, 2013a) evaluated the size-dependent electroelastic responses of piezoelectric nanobeams using Euler beam model along with the incorporation of flexoelectric effect. Moreover, this study was further extended to predict the size-dependent bending and vibration behaviour of the Timoshenko beam model as well (Yan and Jiang, 2013b). Li et al. (2014) proposed a size-dependent model for a layered micro beam incorporating the effect of electromechanical coupling. Some of the recent findings in this field can be found in the works of Chu et al. (2018), Qi et al. (2016), Qiu et al. (2018) and Yue et al. (2014).

The problem of evaluating the size-dependent electromechanical behaviour of various beam models is mostly limited to small deformation consideration. However, several studies have shown that the incorporation of geometrical non-linearity can greatly reduce the error i.e. from 30% to 3% (Reeder and Crews Jr, 1991; Wang and Wang, 2016). The geometrical non-linearity in case of the cantilever beam is primarily due to the non-linear force/curvature relation, and it must, therefore, be assessed thoroughly (Huang and Yu, 2006; Jia et al., 2011), particularly when it is associated

with the fracture mechanics analysis of a double cantilever beam (DCB). Since DCB is considered to be made of two cantilever beams attached to the uncracked part, therefore, the bending behaviour of cantilever beam is often employed to study the fracture toughness of DCB (Giannakopoulos and Stamoulis, 2007; Joseph et al., 2017; Li and Lee, 2016; Stamoulis and Giannakopoulos, 2012). Moreover, DCB specimen is an ideal choice for the determination of mode I fracture toughness of composite laminates and adhesively bonded materials in which the geometric non-linearity is sufficed for long cracks (Devitt et al., 1980; Williams, 1987). Furthermore, due to the enormous surface area to volume ratio at the micro/nanoscale, the influence of surface effects becomes prominent and should not be ignored in order to accurately predict the mechanical behaviour of the micro/nanostructures. Surface effects on micro/nanostructures may be characterized by two major types i.e. the surface elasticity and the surface residual stress (He and Lilley, 2008a). Nevertheless, in the case of piezoelectric nanomaterials, the effect of surface piezoelectricity must also be incorporated (Zhang and Jiang, 2014). Huang and Yu (2006) developed the pioneering work for the development of the piezoelectric model with simultaneous consideration of surface piezoelectricity, surface residual stress and surface elasticity.

In this paper, the fracture analysis of a flexoelectric (size-dependent piezoelectric) DCB is evaluated using modified Euler-Bernoulli beam model. In the constitutive equations, the effect of both strain gradient, as well as the electric field-strain gradient coupling, is considered. Moreover, the model also includes the simultaneous incorporation of large deformation, surface residual effects, surface elasticity, surface piezoelectricity and uncracked part of the DCB. The governing equation with respective boundary conditions, obtained through a variational principle, is solved numerically by using the Lobatto IIIA collocation method. The description of the used numerical method and the application of some other numerical techniques are

presented by various researchers (Joseph et al., 2014; Shampine et al., 2000; Wu et al., 2016) and results are presented in terms of strain energy release rates.

5.3 Theoretical formulations

5.3.1 Bending of a flexoelectric cantilever beam

The constitutive equations with the consideration of electric field-strain gradient coupling are given as (Hu and Shen, 2010);

$$\tau_{ij} = c_{ijkl}\varepsilon_{kl} - e_{kij}E_k \tag{5.1}$$

$$\mu_{jkl} = -f_{ijkl}E_i + g_{jklmni}\kappa_{nmi} \tag{5.2}$$

$$D_k = a_{kl}E_l + e_{kij}\varepsilon_{ij} + f_{klmn}\kappa_{lmn} \tag{5.3}$$

Where c is the fourth order elastic constant tensor, e is the piezoelectric coefficient, f is the electric-field strain gradient coupling coefficient tensor, the tensor g represent the strain gradient elasticity effect and a is the material's permittivity second order tensor. The symbols τ_{ij}, μ_{ijk} and D_i represent the Cauchy stress, higher order stress, and electric displacement component respectively. The indicial notation is employed in which the repeated indices represent summation and comma indicates differentiation with respect to the spatial variable. The strain ε_{ij} and strain gradient η_{ijk} are related to the displacement u_i as; $\varepsilon_{ij} = (u_{i,j} + u_{j,i})/2$ and $\eta_{ijk} = \varepsilon_{ij,k} = (u_{i,jk} + u_{j,ik})/2$ respectively. For illustration, the schematic diagram of a flexoelectric DCB specimen with the length of cracked part a, width b, thickness h is shown in Fig. 4.1. The beam configuration is same as that of the following references (Huang and Yu, 2006; Shen and Hu, 2010; Yan and Jiang, 2011) and the "bulk + surface" model (Huang and Yu, 2006) is used to model the DCB. For 1D mode I problem, the Cauchy and higher order stresses with the consideration of large deformation are written as;

$$\tau_{xx} = c_{11} z \frac{\mathrm{d}\varphi}{\mathrm{d}s} - e_{31} E_z \tag{5.4}$$

$$\mu_{xxx} = -f_{31} E_z + g_{11} \kappa_{xxx} = -m^2 e_{31} E_z + l^2 c_{11} z \frac{\mathrm{d}^2 \varphi}{\mathrm{d}s^2} \tag{5.5}$$

whereφ is the slope of the deformed beam, c_{11} is the Young's modulus. The higher order elastic parameter g_{11} is related to the conventional elastic stiffness coefficient c_{11} by a factor *l* which is known as internal length material parameter (Sladek et al., 2017; Xu and Shen, 2013). Similarly, the electric-field strain gradient coupling coefficient f_{31} is proportional to the conventional piezoelectric coefficient e_{31} by a scaling parameter *m* (Huang and Yu, 2006). The total stress is given as;

$$\sigma_{xx} = \tau_{xx} - \frac{\mathrm{d}\mu_{xxx}}{\mathrm{d}s} \tag{5.6}$$

The electric field component can be expressed as; $E_z = -\psi_{,z}$, here ψ is the electric potential and taken to be constant along the beam span (*x*-axis) (Yan and Jiang, 2011). The electrical displacement in the *z*-direction is written as;

$$D_z = a_{33} E_z + e_{31} \varepsilon_{xx} + f_{31} \kappa_{xxx} = -a_{33} \frac{\mathrm{d}\psi}{\mathrm{d}z} + e_{31} z \frac{\mathrm{d}\varphi}{\mathrm{d}s} + m^2 e_{31} z \frac{\mathrm{d}^2 \varphi}{\mathrm{d}s^2} \tag{5.7}$$

Due to the massive surface area to volume ratio at the nanoscale, the influence of surface effects must be considered in the theoretical modeling (Wang and Wang, 2013). As previously mentioned that the surface effects on micro/nanostructures may be divided into two distinct types i.e. the surface elasticity and the surface residual stress (He and Lilley, 2008a). However, the effect of surface residual stress is always prominent (Wang and Wang, 2013). The surface stress σ_{xx}^{s} and electric displacement

D_x^s in *x*-direction including the effects of surface piezoelectricity is given as (Wang and Wang, 2016);

$$\sigma_{xx}^s = \tau_o + c_{11}^s \varepsilon_{xx}^s - e_{31}^s E_z^s \tag{5.8}$$

$$D_x^s = D_x^0 + e_{15}^s \gamma_{xy} + a_{11}^s E_x \tag{5.9}$$

where τ_o in Eq. (5.8) is the surface residual stress, c_{11}^s is the Young's Modulus, e_{31}^s is the and piezoelectric constant of the surface, γ_{xy} is the shear stress, a_{11}^s is the surface material permittivity Electric energy, electric displacement and the strain gradient effect of the surfaces is neglecting since its value is negligible as compared to the bulk. Moreover, it is known that $E_x << E_z$, so that $D_x << D_z$, therefore, only D_z and E_z will be considered for theoretical modeling. The equilibrium equation in the absence of electric charges is $D_{z,z} = 0$ (Wang and Wang, 2016) that gives;

$$\psi(z) = \frac{e_{31}}{a_{33}} \frac{\mathrm{d}}{\mathrm{d}s} \left[\varphi + m^2 \frac{\mathrm{d}\varphi}{\mathrm{d}s} \right] \frac{(z)^2}{2} + C_1 z + C_2 \tag{5.10}$$

Here C_1 and C_2 are the constants to be determined. Using the boundary conditions i.e. $\psi(-h/2) = 0$; $\psi(h/2) = V$, where V is the applied voltage, E_z and ψ may be evaluated as follows;

$$\psi(-h/2) = \frac{e_{31}}{a_{33}} \frac{\mathrm{d}}{\mathrm{d}s} \left[\varphi + m^2 \frac{\mathrm{d}\varphi}{\mathrm{d}s} \right] \frac{(-h/2)^2}{2} - C_1(h/2) + C_2 = 0 \tag{5.11}$$

$$\psi(h/2) = \frac{e_{31}}{a_{33}} \frac{\mathrm{d}}{\mathrm{d}s} \left[\varphi + m^2 \frac{\mathrm{d}\varphi}{\mathrm{d}s} \right] \frac{(h/2)^2}{2} + C_1(h/2) + C_2 = V \tag{5.12}$$

Solving Eqs. (5.11) and (5.12) gives;

$$C_1 = V/h,\ C_2 = \frac{V}{2} - \frac{e_{31}}{a_{33}}\frac{\mathrm{d}}{\mathrm{d}s}\left[\varphi + m^2\frac{\mathrm{d}\varphi}{\mathrm{d}s}\right]\frac{(h/2)^2}{2} \tag{5.13}$$

So, the electric potential from Eq. (5.10) is given as;

$$\psi(z) = \frac{e_{31}}{a_{33}}\frac{\mathrm{d}}{\mathrm{d}s}\left[\varphi + m^2\frac{\mathrm{d}\varphi}{\mathrm{d}s}\right]\frac{(z^2 - (h/2)^2)}{2} + \frac{V}{h}z + \frac{V}{2} \tag{5.14}$$

The corresponding electric field in *z*-direction may be written as;

$$E_z = -\frac{\mathrm{d}\psi}{\mathrm{d}z} = -\frac{e_{31}}{a_{33}}\frac{\mathrm{d}}{\mathrm{d}s}\left[\varphi + m^2\frac{\mathrm{d}\varphi}{\mathrm{d}s}\right]z - \frac{V}{h} \tag{5.15}$$

with the aid of Eq. (5.15), bulk and surface stress from Eqs. (5.6) and (5.8) are written as;

$$\sigma_{xx} = c_{11}z\left[\frac{\mathrm{d}\varphi}{\mathrm{d}s} - l^2\frac{\mathrm{d}^3\varphi}{\mathrm{d}s^3}\right] + \frac{e_{31}^2}{a_{33}}z\left[\frac{\mathrm{d}\varphi}{\mathrm{d}s} - m^4\frac{\mathrm{d}^3\varphi}{\mathrm{d}s^3}\right] + e_{31}\frac{V}{h} \tag{5.16}$$

$$\sigma_{xx}^s = \tau_0 + c_{11}^s\left(\int_C z^2 dC\right)\frac{\mathrm{d}\varphi}{\mathrm{d}s} + \frac{e_{31}e_{31}^s}{a_{33}}\left(\int_C z^2 dC\right)\frac{\mathrm{d}}{\mathrm{d}s}\left[\varphi + m^2\frac{\mathrm{d}\varphi}{\mathrm{d}s}\right] + e_{31}^s\frac{V}{h} \tag{5.17}$$

where C is the perimeter of the cross-section. Therefore, the moment of the cross section ($M = \int_A \sigma_{xx} z dA + \int_S \sigma_s z dS$) with the consideration of strain gradients and flexoelectricity is;

$$M = \overbrace{\frac{\mathrm{d}\varphi}{\mathrm{d}s}\left[\left(c_{11} + \frac{e_{31}^2}{a_{33}}\right)\frac{bh^3}{12} + \left(c_{11}^s + \frac{e_{31}e_{31}^s}{a_{33}}\right)\left(\frac{bh^2}{2} + \frac{h^3}{6}\right)\right]}^{Classical\ \ Piezoelectricity} - \overbrace{l^2\frac{\mathrm{d}^3\varphi}{\mathrm{d}s^3}\left[c_{11}\frac{bh^3}{12}\right]}^{Strain\ \ gradient\ \ effect} + \underbrace{m^2\frac{\mathrm{d}^2\varphi}{\mathrm{d}s^2}\left[\frac{e_{31}e_{31}^s}{a_{33}}\left(\frac{bh^2}{2} + \frac{h^3}{6}\right)\right] - m^4\frac{\mathrm{d}^3\varphi}{\mathrm{d}s^3}\left[\frac{e_{31}^2}{a_{33}}\frac{bh^3}{12}\right]}_{Electric field - Strain\ \ gradient\ \ coupling\ \ effect} \tag{5.18}$$

The electrical force at the cross-section is given as;

$$T = \int_A \sigma_x dA + \int_s \tau_x ds = e_{31} V b + 2 b e_{31}^s \frac{V}{h} \tag{5.19}$$

The equivalent vertical load $q(s)$ induced by the surface residual stress is expressed as [33, 34];

$$q(s) = H\kappa = H \frac{\mathrm{d}\varphi}{\mathrm{d}s} \tag{5.20}$$

With $H = 2\tau_0 b$ is the effective lateral distribution load (He and Lilley, 2008a, 2008b; Wang and Feng, 2009), τ_0 is the surface residual stress and b is the beam width. Note that the effects of surface elasticity and surface piezoelectricity have been included in the effective bending stiffness as expressed in Eq. (5.18), therefore only τ_0 is included in H. The equilibrium equations of the DCB give (Wang and Wang, 2013); $\frac{\mathrm{d}Q}{\mathrm{d}s} = -H \frac{\mathrm{d}\varphi}{\mathrm{d}s}$, $\frac{\mathrm{d}M}{\mathrm{d}s} = Q$ (shear force). Bending moment at any point "s" induced by the equivalent distributed load $q(s)$, endpoint concentrated vertical force F and the electrical force of the cross-section T may be expressed as;

$$M_{(o)} = \int_0^a (\xi - s)(H + T) \frac{\partial \varphi}{\partial \xi} \mathrm{d}\xi + F[x(a) - x(s)] \tag{5.21}$$

It is important to note that at any specified point $P(x, y)$ along a curved beam, bending moment induced by the external force F is given as; $M = F.(a - \delta x - x)$ (where a is the length of a beam and δx is the horizontal deflection), which if differentiated ($\mathrm{d}(a - \delta x - x)/\mathrm{d}s = -\cos\varphi$). So, the following governing equation of a Euler beam with the cumulative effects of surface, piezoelectricity and strain gradient subjected to large deformation is written as;

$$\overbrace{\underbrace{\frac{\mathrm{d}^2\varphi}{\mathrm{d}s^2}\left[\left(c_{11}+\frac{e_{31}^2}{a_{33}}\right)\frac{bh^3}{12}+\left(c_{11}^s+\frac{e_{31}e_{31}^s}{a_{33}}\right)\left(\frac{bh^2}{2}+\frac{h^3}{6}\right)\right]}_{Classical\quad Piezoelectricity}-\overbrace{l^2\frac{\mathrm{d}^4\varphi}{\mathrm{d}s^4}\left[c_{11}\frac{bh^3}{12}\right]}^{Strain\quad gradient\quad effect}+}$$
$$\underbrace{m^2\frac{\mathrm{d}^3\varphi}{\mathrm{d}s^3}\left[\frac{e_{31}e_{31}^s}{a_{33}}\left(\frac{bh^2}{2}+\frac{h^3}{6}\right)\right]-m^4\frac{\mathrm{d}^4\varphi}{\mathrm{d}s^4}\left[\frac{e_{31}^2}{a_{33}}\frac{bh^3}{12}\right]}_{Electricfield-Strain\quad gradient\quad coupling\quad effect} \tag{5.22}$$
$$=-F\cos\varphi+(H+T)\varphi-(H+T)\varphi_a$$

Here φ_a is the unknown slope at the free end of the beam. Alternatively, the governing equation and respective boundary conditions may also be evaluated through a variational principle. The variational principle is given as; $\delta(U_b+U_s)-\delta W=0$, where W is the work done by the external forces, U_b and U_s are the strain energy of the bulk and surface respectively. In the one-dimensional case, the bulk strain energy (U_b) is given as; $U_b=\frac{1}{2}\int_A\int_0^a[\tau_{xx}\varepsilon_{xx}+\mu_{xxx}\nabla.\varepsilon_{xx}+D_zE_z]\mathrm{d}s\mathrm{d}A$. As previously mentioned that the equilibrium equation in the absence of electric charges is $D_{z,z}$ = 0 (by means of the Gaussian theorem (Wang and Wang, 2016). So, the electric Gibbs energy of the bulk is written as; $U_b=\frac{1}{2}\int_A\int_0^a[\tau_{xx}\varepsilon_{xx}+\mu_{xxx}\nabla.\varepsilon_{xx}]\mathrm{d}s\mathrm{d}A$. On the other hand, the surface strain energy (U_s) is given as; $U_s=\frac{1}{2}\int_A[\tau_{xx}^s\varepsilon_{xx}^s+\tau_o\varepsilon_{xx}^s]\mathrm{d}A$. Here ∇ denotes (d/ds) in the case of large deformation. The variation of the work done by the external forces is written as; $\delta W=-\int_0^a F\cos\varphi(s)\delta\varphi\mathrm{d}s$. So, the variational principle $\delta(U_b+U_s)-\delta W=0$ gives;

$$\int_0^a\left[\frac{\mathrm{d}}{\mathrm{d}s}(M-\frac{\mathrm{d}M^h}{\mathrm{d}s}+M^s)+F\cos\varphi-(H+T)\varphi+(H+T)\varphi_a\right]\delta\varphi\mathrm{d}s+$$
$$-\left[(M-\frac{\mathrm{d}M^h}{\mathrm{d}s}+M^s)\delta\varphi'\right]_0^a+\left[M^h\delta\varphi''\right]_0^a=0 \tag{5.23}$$

where M, M^handM^s are the classical bending moment, higher-order bending moment and bending moment due to surface stress respectively, which are defined as;

$$M = \int_A \tau_{xx} z \mathrm{d}A,\ M^h = \int_A \mu_{xxx} z \mathrm{d}A,\ M^s = \int_A \tau^s_{xx} z \mathrm{d}A \tag{5.24}$$

Using the above equations M, M^h and M^s are evaluated as;

$$M = c_{11}\left(\frac{bh^3}{12}\right)\frac{\mathrm{d}\varphi}{\mathrm{d}s} + \frac{e_{31}^2}{a_{33}}\frac{\mathrm{d}}{\mathrm{d}s}\left[\varphi + m^2\frac{\mathrm{d}\varphi}{\mathrm{d}s}\right]\left(\frac{bh^3}{12}\right) \tag{5.25}$$

$$M^s = c_{11}^s\left(\frac{bh^2}{2} + \frac{h^3}{6}\right)\frac{\mathrm{d}\varphi}{\mathrm{d}s} + \frac{e_{31}e_{31}^s}{a_{33}}\frac{\mathrm{d}}{\mathrm{d}s}\left[\varphi + m^2\frac{\mathrm{d}\varphi}{\mathrm{d}s}\right]\left(\frac{bh^2}{2} + \frac{h^3}{6}\right) \tag{5.26}$$

$$M^h = l^2 c_{11}\left(\frac{bh^3}{12}\right)\frac{\mathrm{d}^2\varphi}{\mathrm{d}s^2} + m^2\frac{e_{31}^2}{a_{33}}\frac{\mathrm{d}}{\mathrm{d}s}\left[\varphi + m^2\frac{\mathrm{d}\varphi}{\mathrm{d}s}\right]\left(\frac{bh^3}{12}\right) \tag{5.27}$$

The governing equation from Eq. (5.23) is given as;

$$\frac{\mathrm{d}}{\mathrm{d}s}\left(M - \frac{\mathrm{d}M^h}{\mathrm{d}s} + M^s\right) + F\cos\varphi - (H+T)\varphi + (H+T)\varphi_a = 0 \tag{5.28}$$

with the aid of Eqs. (5.25-5.27) and from Eq. (5.28), one may get the governing equation (Eq. (5.22)). The boundary conditions evaluated from the variational principle require $\left(M - \frac{\mathrm{d}M^h}{\mathrm{d}s} + M^s\right)$ (total moment) and M^h (higher-order moment) to be specified at $s = 0$ and $s = a$.

5.4 Boundary conditions

In order to solve the governing equation (5.22), we need four boundary conditions to be specified at $s = 0$ and $s = a$ (classical as well as non-classical). With the consideration of classical and non-classical boundary conditions evaluated from the variational principle, it is evident that more than one set of boundary conditions may be obtained. However, in our case, the classical boundary condition at the fixed end of the beam i.e. $s = 0$ is

expressed as; $\varphi = 0$ (Kong et al., 2009), which indicates zero rotation. Meanwhile at the free end i.e. *s* = *a*, the classical moment for the piezoelectric beam from Eq. (5.18) gives; $\mathrm{d}\varphi/\mathrm{d}s = 0$. The higher order boundary conditions from the variational principle give;

At *s*= 0, $M^h = 0$ namely;

$$\frac{bh^3}{12}\left(l^2 c_{11} + m^4 \frac{e_{31}^2}{a_{33}}\right)\frac{\mathrm{d}^2\varphi}{\mathrm{d}s^2} + \left(m^2 \frac{e_{31}^2}{a_{33}}\frac{bh^3}{12}\right)\frac{\mathrm{d}\varphi}{\mathrm{d}s} = 0 \qquad (5.29a)$$

At *s* = *a*, with $\mathrm{d}\varphi/\mathrm{d}s = 0$ (classical one) and with zero higher order moment ($\mathrm{d}^2\varphi/\mathrm{d}s^2 = 0$), from $(M - \frac{\mathrm{d}M^h}{\mathrm{d}s} + M^s = 0)$ we get,

$$\frac{\mathrm{d}^3\varphi}{\mathrm{d}s^3}\left[l^2 c_{11} + m^4 c_{11}\frac{e_{31}^2}{a_{33}}\right]\frac{bh^3}{12} = 0, \text{namely}\ \frac{\mathrm{d}^3\varphi}{\mathrm{d}s^3} = 0 \qquad (5.29b)$$

So, the set of boundary conditions considered in this work is given as;

At *s* = 0 $\varphi = 0$ and $\frac{bh^3}{12}\left(l^2 c_{11} + m^4 \frac{e_{31}^2}{a_{33}}\right)\frac{\mathrm{d}^2\varphi}{\mathrm{d}s^2} + \left(m^2 \frac{e_{31}^2}{a_{33}}\frac{bh^3}{12}\right)\frac{\mathrm{d}\varphi}{\mathrm{d}s} = 0$ (5.30a)

At *s* = *a* $\mathrm{d}\varphi/\mathrm{d}s = 0$ and $\frac{\mathrm{d}^3\varphi}{\mathrm{d}s^3} = 0$ (5.30b)

5.5 The strain energy release rate of the cracked and uncracked part of DCB

The strain energy release rate *G* may be found by taking the beam length as *a* (crack length) and width *b*, the strain energy release rate of a double cantilever beam is given as; $G = F\,(\mathrm{d}Y_{max}/b\mathrm{d}a)$. Here $Y_{\max} = \int_0^a \sin(\varphi)\mathrm{d}s$ (Joseph et al., 2017, Wang and Wang, 2013). On the other hand, for the uncracked part of the DCB, the influence of the shear stresses must not be ignored. Therefore the governing equations of the uncracked part of

the DCB are usually evaluated using Timoshenko beam theory (Wang and Wang, 2016). According to which the potential energy of the uncracked or root part (U_r) is expressed as;

$$U_r = 2\int_{-\infty}^{0} \frac{M_{(x)}{}^2}{2EI_{\text{eff}}}\mathrm{d}x + 2\int_{-\infty}^{0} \frac{Q_{(x)}{}^2}{2G^s A}\mathrm{d}x \tag{5.31a}$$

$$EI_{\text{eff}} = \left(c_{11} + \frac{e_{31}^2}{a_{33}}\right)\frac{bh^3}{12} + \left(c_{11}^s + \frac{e_{31}e_{31}^s}{a_{33}}\right)\left(\frac{bh^2}{2} + \frac{h^3}{6}\right) \tag{5.31b}$$

where $M_{(x)}$ and $Q_{(x)}$ are the bending moment and shear force on the cross-section area A respectively, G^s is an effective shear modulus and EI_{eff} is the effective bending rigidity as defined in Eq. (5.31b). As per the coordinate system, the integrals vary from negative infinity to zero. Using Eq. (5.31a) and the results provided by Joseph et al. (2017) one gets;

$$U_r = \frac{1}{\sqrt{EI_{\text{eff}}G^s A}}\left[F^2X^2(\varphi_{\text{a}}) + \left[\int_0^a s(H+T)\frac{\mathrm{d}\varphi}{\mathrm{d}s}\mathrm{d}s\right]^2\right] \tag{5.32a}$$

$$\int_0^a s(H+T)\frac{\mathrm{d}\varphi}{\mathrm{d}s}\mathrm{d}s = (H+T)\left[s.\varphi(s)\Big|_0^a - \int_0^a \varphi \mathrm{d}s\right] \tag{5.32b}$$

where $X(\varphi_{\text{a}})$ is the endpoint horizontal deflection (as shown in Fig. 4.1), F is the vertical concentrated force, φ_{a} is the unknown slope at the free end of the beam, $H = 2\tau_{\text{o}}b$ and T is the electrical force of cross-section (Eq. (5.19)).

5.6 Electrical boundary conditions

5.6.1 Short-circuit Boundary condition

Here the governing equations of two electrical boundary conditions i.e. short circuit and open circuit boundary conditions are evaluated. For short circuit boundary condition,

the electric field would be zero i.e. $E_z = 0$. Therefore the total stress of the bulk and surface are written as;

$$\sigma_{xx} = c_{11} z \left[\frac{\mathrm{d}\varphi}{\mathrm{d}s} - l^2 \frac{\mathrm{d}^3\varphi}{\mathrm{d}s^3} \right] \tag{5.33}$$

$$\sigma_{xx}^s = \tau_0 + c_{11}^s z \frac{\mathrm{d}\varphi}{\mathrm{d}s} \tag{5.34}$$

Equation (5.33) depicts only mechanical gradient to be effective, it may be seen only mechanical gradient is effective, so the piezoelectric material properties and strain field-strain gradient coupling effect would vanish. The moment is found to be;

$$M = \left[\frac{\mathrm{d}\varphi}{\mathrm{d}s} - l^2 \frac{\mathrm{d}^3\varphi}{\mathrm{d}s^3} \right] c_{11} \frac{bh^3}{12} + \frac{\mathrm{d}\varphi}{\mathrm{d}s} \left[c_{11}^s \left(\frac{bh^2}{2} + \frac{h^3}{6} \right) \right] \tag{5.35}$$

Moreover, due to diminishing potential difference across the boundaries, the governing equation (5.22) would reduce to;

$$\left[\frac{\mathrm{d}^2\varphi}{\mathrm{d}s^2} - l^2 \frac{\mathrm{d}^4\varphi}{\mathrm{d}s^4} \right] c_{11} \frac{bh^3}{12} + \frac{\mathrm{d}^2\varphi}{\mathrm{d}s^2} \left[c_{11}^s \left(\frac{bh^2}{2} + \frac{h^3}{6} \right) \right] = -F \cos\varphi + H\varphi - H\varphi_a \tag{5.36}$$

The classical and non-classical boundary conditions (evaluated from variational principle) are as follows;

$$\text{At } s = 0:\ \varphi = 0\,,\ M^h = 0 \text{ gives; } \frac{\mathrm{d}^2\varphi}{\mathrm{d}s^2} = 0 \tag{5.37a}$$

$$\text{At } s = a:\ \left(M - \frac{\mathrm{d}M^h}{\mathrm{d}s} + M^s = 0\right) \text{gives; } \frac{\mathrm{d}\varphi}{\mathrm{d}s} = 0\ ,\ \frac{\mathrm{d}\varphi}{\mathrm{d}s} - l^2 \frac{\mathrm{d}^3\varphi}{\mathrm{d}s^3} = 0$$

$$\text{or } \frac{\mathrm{d}\varphi}{\mathrm{d}s} = 0\,,\ \frac{\mathrm{d}^3\varphi}{\mathrm{d}s^3} = 0 \tag{5.37b}$$

5.6.2 Open-circuit boundary conditions

Similarly, for an open circuit, the electrical displacement would be zero i.e. $D_z = 0$ (Wang and Wang, 2016) that gives;

$$D_z = a_{33}E_z + e_{31}\varepsilon_{xx} + f_{31}\kappa_{xxx} = a_{33}E_z + e_{31}z\frac{\mathrm{d}\varphi}{\mathrm{d}s} + m^2 e_{31}z\frac{\mathrm{d}^2\varphi}{\mathrm{d}s^2} = 0 \tag{5.38}$$

or

$$E_z = -\frac{e_{31}}{a_{33}}z\frac{\mathrm{d}\varphi}{\mathrm{d}s} - m^2\frac{e_{31}}{a_{33}}z\frac{\mathrm{d}^2\varphi}{\mathrm{d}s^2} \tag{5.39}$$

with the aid of Eq. (5.39), the total moment as given in Eq. (5.18) is recovered. Meanwhile, the electrical force T would be zero. So, the resulting governing equation (22) is reduced to;

$$\begin{aligned}&\frac{\mathrm{d}^2\varphi}{\mathrm{d}s^2}\left[\left(c_{11}+\frac{e_{31}^2}{a_{33}}\right)\frac{bh^3}{12}+\left(c_{11}^s+\frac{e_{31}e_{31}^s}{a_{33}}\right)\left(\frac{bh^2}{2}+\frac{h^3}{6}\right)\right]-l^2\frac{\mathrm{d}^4\varphi}{\mathrm{d}s^4}\left[c_{11}\frac{bh^3}{12}\right]\\&+m^2\frac{\mathrm{d}^3\varphi}{\mathrm{d}s^3}\left[\frac{e_{31}^2}{a_{33}}\frac{bh^3}{12}+\frac{e_{31}e_{31}^s}{a_{33}}\left(\frac{bh^2}{2}+\frac{h^3}{6}\right)\right]=-F\cos\varphi+H\varphi-H\varphi_a\end{aligned} \tag{5.40}$$

Apart from the classical boundary conditions, the higher-order boundary conditions are similar to those in Eq. (5.30). The governing equations (5.22), (5.36) and (5.40) with the mechanical boundary conditions are solved numerically using a Matlab function bvp4c. This function solves the boundary value problem with the aid of three-stage Lobatto IIIa collocation formula (which is a preferred method in the case of boundary value problems). Detailed literature about this method and its implement in bvp4c is provided by Shampine et al. (2000).

5.7 Numerical Results

In order to evaluate the numerical solution of Eq. (22), the material bulk properties of $BaTiO_3$ are taken (Giannakopoulos and Suresh, 1999;Zhang and Jiang, 2014; Yue et

al., 2016)) i.e. c_{11} = 131 GPa, e_{31}= -4.4 Cm^{-2}, a_{33} = 1.2658 x 10^{-8} CV^{-1}m^{-1}, G^s = c_{66} = 44.7 GPa. For the surface, the properties are taken as $E^s = 9.72$ Nm^{-1}(Chu et al., 2018; Yue et al., 2016) and e_{31}^s= 0.7 x 10^{-9} Cm^{-1}(Dai et al., 2011). The value of surface residual stresses τ_o is assumed to be $\pm$ 10 Nm^{-1} (since it can be positive or negative) and it may range from 1-10 Nm^{-1} (Cammarata, 1994). In order to investigate the effect of strain gradient, the material length scale parameter (l) and the flexoelectricity coefficient (f_{31})are related to an introduced factor q as;

$$l^2 = q.l_o^2, \quad f_{31} = q.f_{(31)o} \tag{5.41}$$

and the numerical values of l_o^2 and $f_{(31)o}$ are assumed to be 4 x 10^{-9}m^2 and 1x 10^{-6} C/m (as the flexoelectric coefficient may range from 1-10 μC/m (Morozovska et al., 2011)). Since the effect of large deformation is more pronounced at elevated load, therefore, bending behaviour of a cantilever beam is not independent of the normalized endpoint force as elaborated by the authors in their previous article (Joseph et al., 2017). Here, the endpoint vertical force F (1 μN) and height h (10 μm) are chosen in a manner such that the beam remains elastic throughout. The results of the vertical deflections along a flexoelectric cantilever beam (Y_f), normalized by $Y_o = Fa^3/(3EI)$ i.e. classical non-piezoelectric beam deflection (small deflection) at the free end are presented in Fig. 5.1. With the consideration of only bulk piezoelectricity and a/h = 20, the normalized beam deflections are evaluated for different values of q. It is shown that for higher q (greater flexoelectric effect), the strain gradient model predicts stiffer behaviour. Effect of flexoelectricity and beam slenderness on its bending behaviour is further elaborated in Fig. 5.2, where the end-point flexoelectric beam deflection is normalized with the classical piezoelectric cantilever beam Y_p (with large deformation). The results are also obtained for positive as well as the negative voltage. From Fig. 5.2, the stiffening effect is shown to be more prominent for smaller (a/h) (apart from the stiffening effect with

increasing q). Positive voltage tends to increase the stiffness of the beam and vice versa since the negative voltage will induce a compressive force which makes the beam to behave softer (Wang and Wang, 2016). Moreover, the results for the classical piezoelectric beam (with large deformation) may be recovered as the value of q is reduced to zero.

In order to investigate the fracture behaviour of DCB, the endpoint vertical deflection of a cantilever beam is used to evaluate its strain energy release rate given as; $G = F\,(\mathrm{d}Y_{max}/b\mathrm{d}a)$, where b and a are the width and length of the beam respectively. The strain release rate of a flexoelectric DCB G_f normalized with the strain energy release rate of the classical piezoelectric DCB G_p (with large deformation) against different a/h ratios is plotted in Fig. 5.3. Here the applied external voltage is set to 5 volts. As expected, the strain energy release rate of the flexoelectric DCB increases as q is decreased and eventually, the results of classical piezoelectric DCB are recovered as q approaches zero. Next, the effect of surface stresses is evaluated and presented. Since the effect of surface residual stress is found to be more pronounced as compared to the effect of surface elasticity (as shown by Wang and Wang (2013) and Yan and Jiang (2012)) and surface piezoelectricity, therefore only the effect of surface residual stress for $q = 1$ is presented in Fig. 5.4. It is shown that the flexoelectric DCB exhibit stiffer response by lowering the normalized strain energy release rate with negative surface residual stress and vice versa. The stiffer or softer response may be attributed to the signs of curvature during the bending of a cantilever beam as thoroughly explained by He and Lilley (2008a).

Meanwhile, it is also important to present the results with different electrical boundary conditions. Therefore, the strain energy release rate of the flexoelectric DCBs with the short circuit and open circuits boundary conditions are evaluated (as described in section 2.4) and compared in Fig. 5.5. From Fig. 5.5, it is evident that the strain

energy release rate with the short circuit boundary condition is higher than those with the open circuit boundary condition. It is clear from the governing equations of short and open circuit boundary conditions as presented in Eq. (5.36) and (5.40) respectively that the effective bending rigidity components associated with the higher order strain gradient ($d^2\varphi/ds^2$) and ($d^4\varphi/ds^4$) are greater for open circuit boundary condition. Moreover, the piezoelectric (e_{31} and e_{31}^s) and flexoelectric (f_{31}) coefficients also play a significant part in the open circuit model, which on the other hand is absent for the short circuit model. This indicates that larger force is required to deform the beam under open circuit and hence higher stiffness and lower strain release rate is expected. The results shown here are similar to the one shown by Wang and Wang (2016) but those were the results of the classical piezoelectric DCB (with the large deformation consideration).

The effect of uncracked part of the DCB on its fracture analysis is crucial as demonstrated by the authors in their previous article (Joseph et al., 2017). Therefore, the effect of the uncracked/root part is established with the help of a variable $R = G_2/G_1$, which is defined as the ratio of the strain energy release rate of the uncracked part (G_2) to the cracked part (G_1). The plot of R vs a/h is shown in Fig. 5.6. Here all the surface effects are included i.e. E^s = 7.56 Nm^{-1}, $e_{31}^s = -3\times10^{-8}$ Nm^{-1}, $\tau_o = -10$ Nm^{-1} and voltage is taken as zero. It may be seen from Fig. 5.6 that for flexoelectric DCB, the contribution of the uncracked part to characterize its fracture behaviour is more noticeable as q is increased. For instance, at q = 4 and a/h =10, the strain energy release rate of the cracked and the uncracked parts are almost identical demonstrating stronger size effect. However, as q approaches zero, R is usually less than 10% and it may be neglected for the sake of model simplicity. Next, the comparison between the total strain energy release rate G_T (including both the cracked and uncracked part) and the strain energy release rate of the cracked G_c is made for the flexoelectric as well as the classical piezoelectric DCB (q = 0). The results in Fig. 5.7 further established the

argument presented in Fig. 5.6 that for higher q such as q = 4, the contribution of the strain energy release rate of the uncracked part is almost half of the total strain energy release rate of the DCB. The contribution of the uncracked part reduces as q is decreased and as a/h is increased. By examining Fig. 5.6 and 5.7 one may say that the effect of the uncracked part must not be ignored in case of flexoelectric DCB even when the beam is slender (higher a/h).

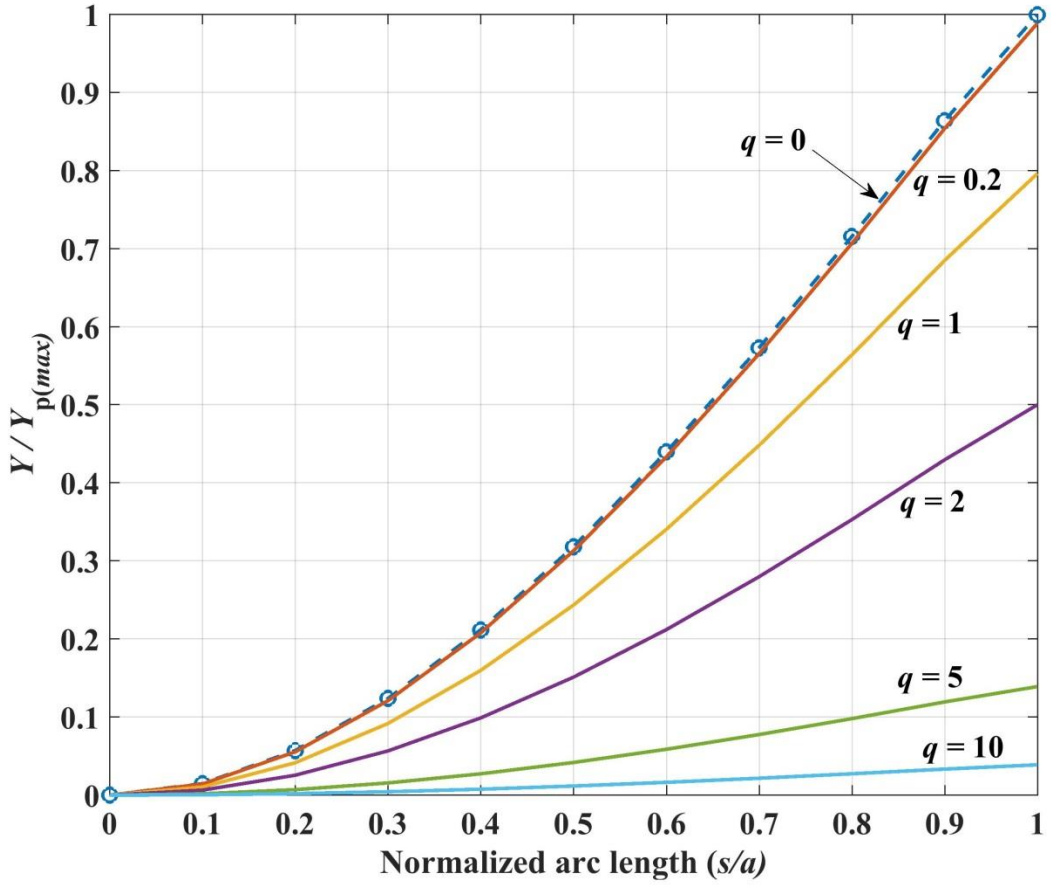

Figure 5.1 Deflection along the beam axis

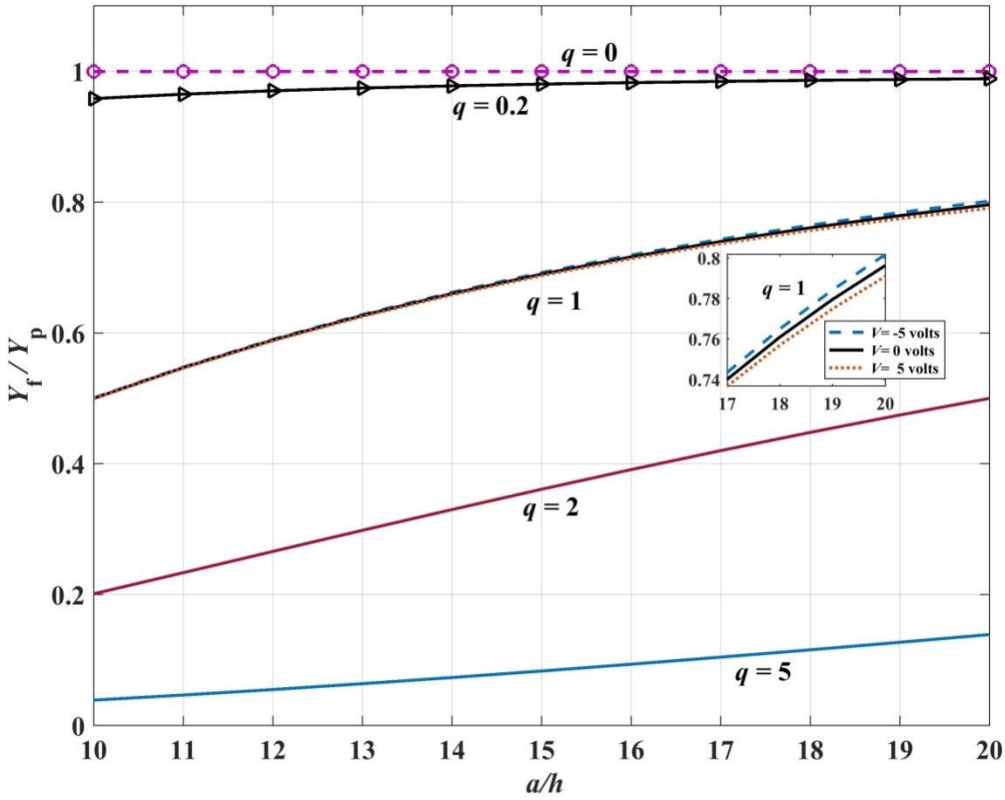

Figure 5.2 Maximum tip deflection of a cantilever beam vs *a*/*h*

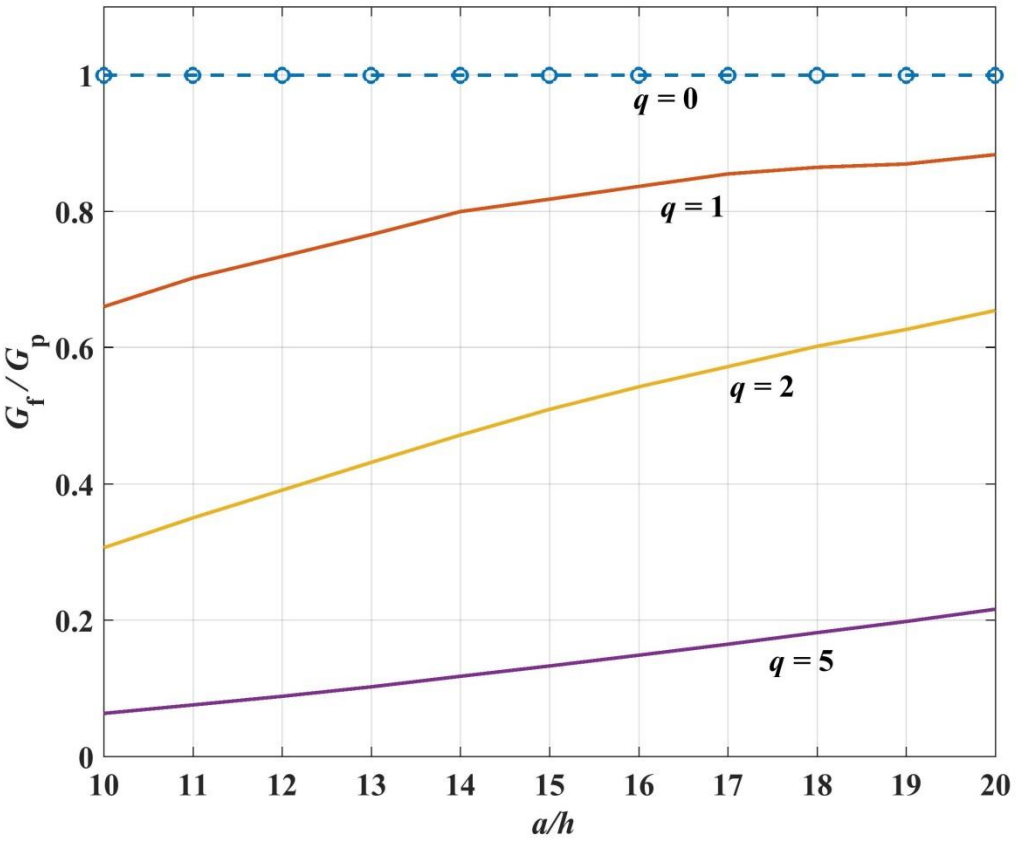

Figure 5.3 Strain energy release rate of the flexoelectric DCB vs *a*/*h*

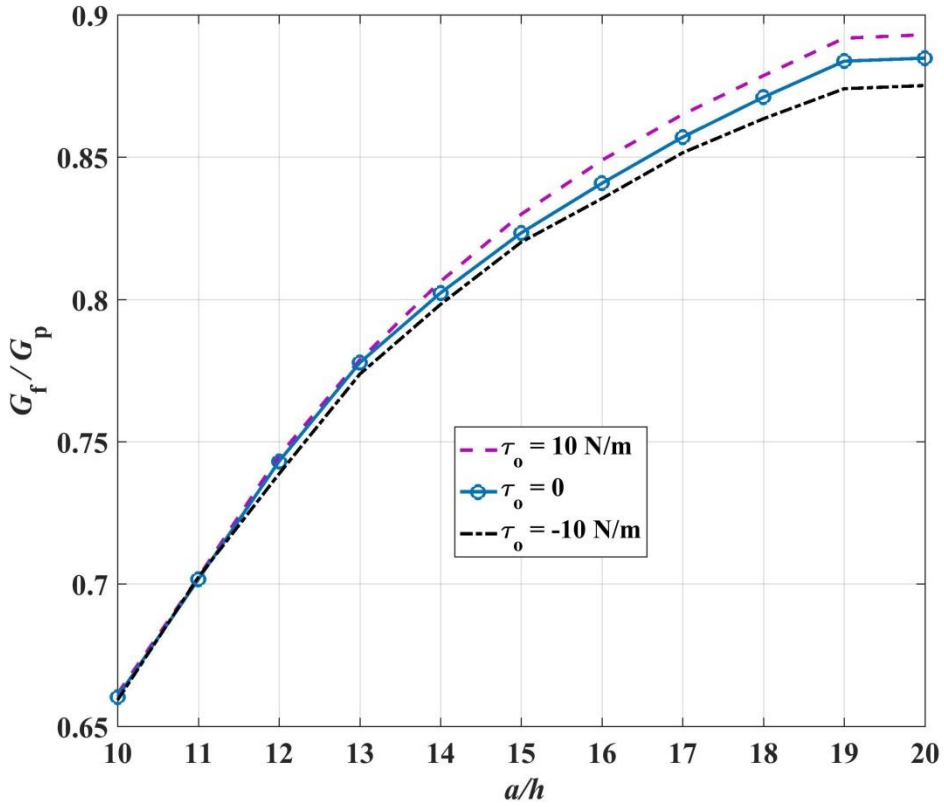

Figure 5.4 Effect of surface residual stress

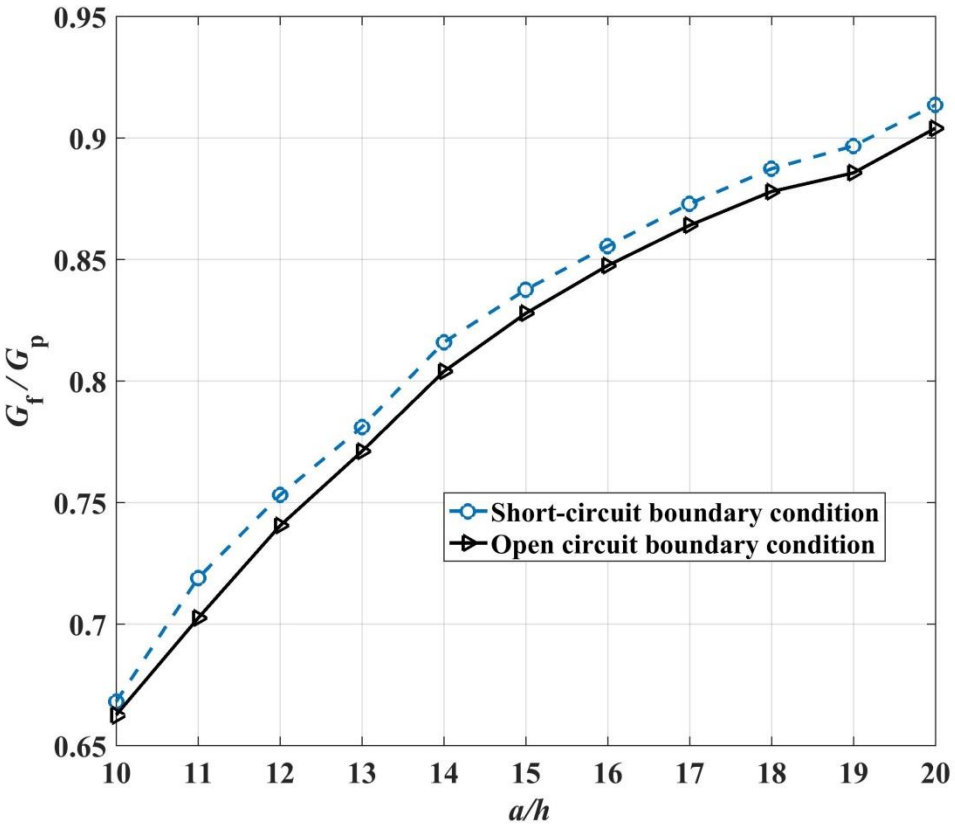

Figure 5.5 Comparison of the strain energy release rate of the short circuit with the open circuit boundary condition

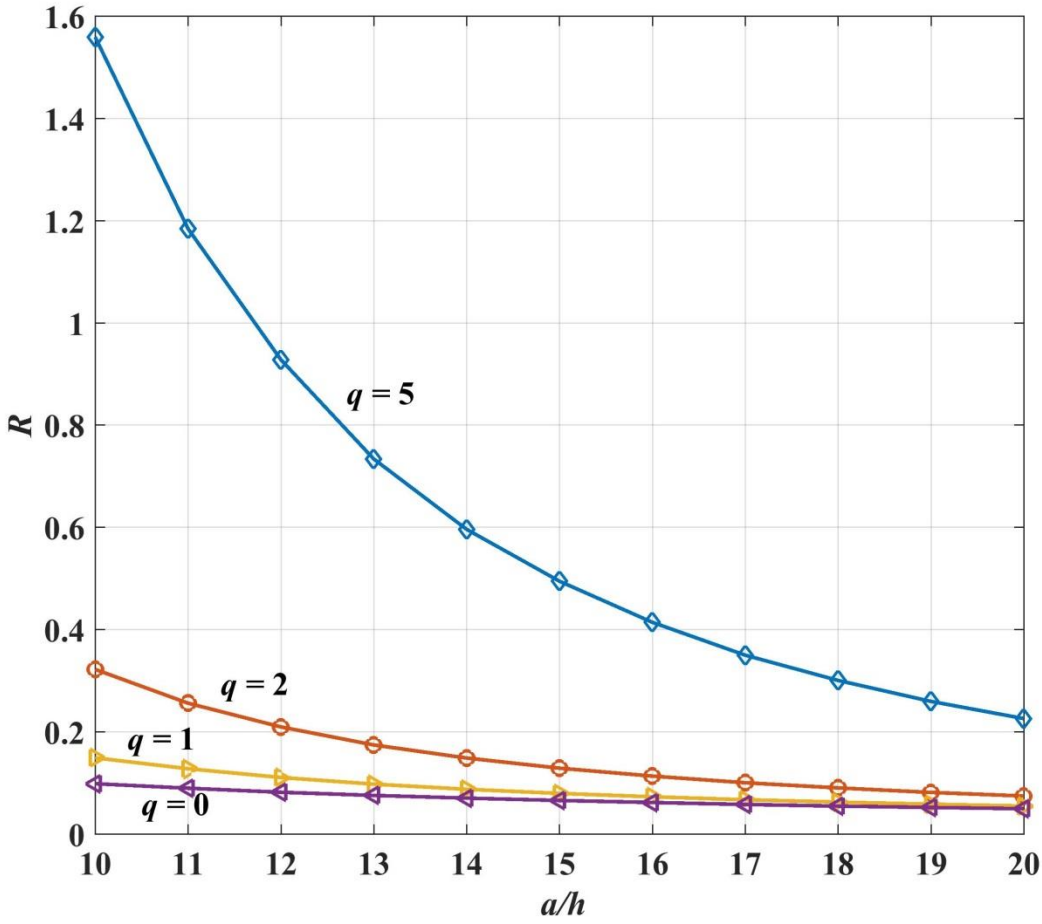

Figure 5.6 Variation of *R* vs *a/h*

5.8 Summary

In this paper, the fracture analysis of a flexoelectric DCB (size dependent piezoelectric DCB) is investigated using the strain gradient elasticity theory. Contrary to the classical approach, this work is based on the consideration of large deformation which is a common phenomenon at the nanoscale. The governing equation and the relevant boundary conditions are obtained by means of a variational principle. The surface effects are also incorporated in the theoretical framework as well as the numerical results. The flexoelectric DCB is shown to exhibit stiffer response than the classical piezoelectric DCB. Meanwhile, the strain energy release rate of the flexoelectric DCBs with different electrical boundary conditions i.e. short circuit and open circuit boundary conditions are evaluated and compared. It is demonstrated that the effect of the

uncracked part of the flexoelectric DCB is very prominent in determining its fracture behaviour and it must not be ignored even for the slender beams. The findings of this research paper are beneficial not only for the relevant experimental design but also in testing the available real time data.

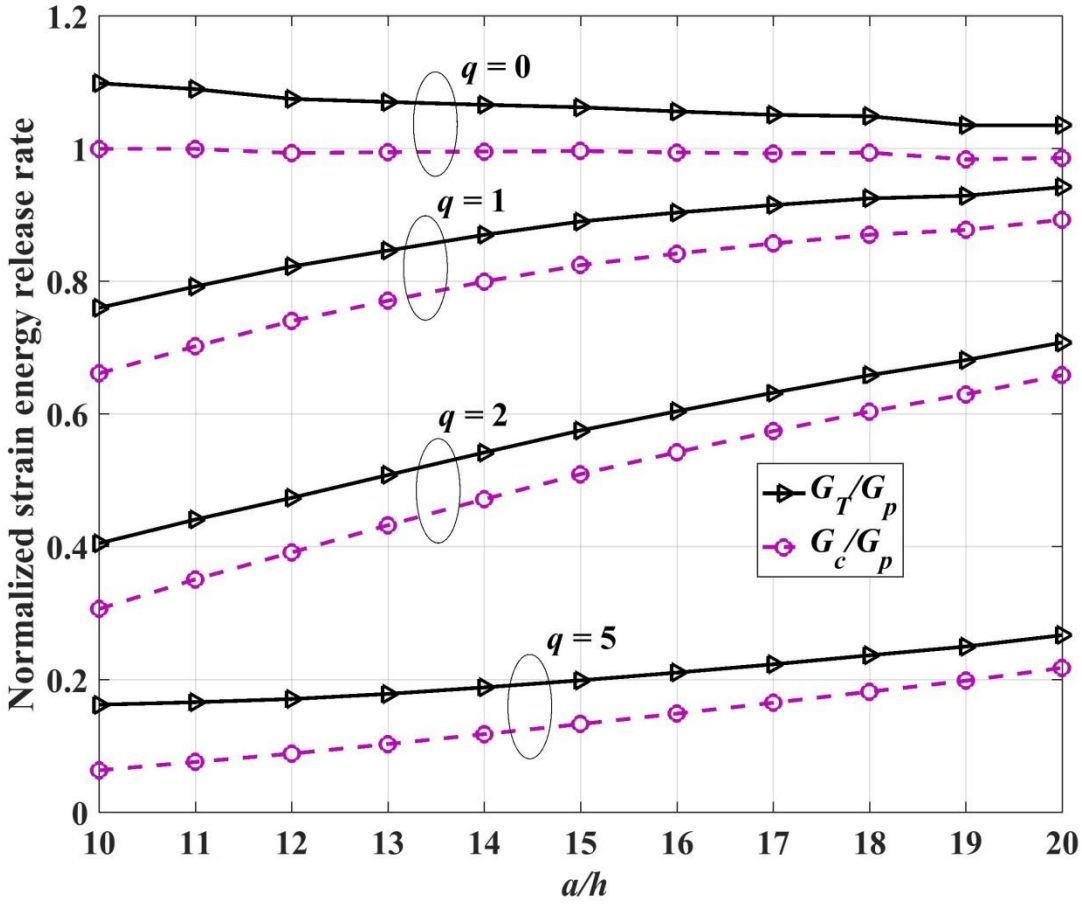

Figure 5.7 Comparison of the strain energy release rate of the DCB with and without the uncracked part

Reference

Baskaran, S., He, X., Chen, Q. & Fu, J. Y., 2011. Experimental studies on the direct flexoelectric effect in α-phase polyvinylidene fluoride films. *Applied Physics Letters*, 98, 242901.

Cady, W. G., 1946. Piezoelectricity: an introduction to the theory and applications of electromechanical phenomena in crystals.

Cammarata, R. C., 1994. Surface and interface stress effects in thin films. *Progress in Surface Science*, 46(1), 1-38.

Catalan, G., Lubk, A., Vlooswijk, A., Snoeck, E., Magen, C., Janssens, A., Rispens, G., Rijnders, G., Blank, D. & Noheda, B., 2011. Flexoelectric rotation of polarization in ferroelectric thin films. *Nature Materials*, 10, 963.

Chu, L., Dui, G. & Ju, C., 2018. Flexoelectric effect on the bending and vibration responses of functionally graded piezoelectric nanobeams based on general modified strain gradient theory. *Composite Structures*, 186, 39-49.

Dai, S., Gharbi, M., Sharma, P., Park, H. S., 2011. Surface piezoelectricity: size effects in nanostructures and the emergence of piezoelectricity in non-piezoelectric materials. *Journal of Applied Physics*, 110(10), 104305.

Devitt, D., Schapery, R. & Bradley, W., 1980. A method for determining the mode I delamination fracture toughness of elastic and viscoelastic composite materials. *Journal of Composite Materials*, 14, 270-285.

Giannakopoulos, A. & Stamoulis, K., 2007. Structural analysis of gradient elastic components. *International Journal of Solids and Structures*, 44, 3440-3451.

Giannakopoulos, A. E., Suresh, S.,1999. Theory of indentation of piezoelectric materials. *Acta Materialia*, 47(7), 2153-2164.

He, J. & Lilley, C. M., 2008a. Surface effect on the elastic behaviour of static bending nanowires. *Nano Letters*, 8, 1798-1802.

He, J. & Lilley, C. M., 2008b. Surface stress effect on bending resonance of nanowires with different boundary conditions. *Applied Physics Letters*, 93, 263108.

Hu, S. & Shen, S., 2010. Variational principles and governing equations in nano-dielectrics with the flexoelectric effect. *Science China Physics, Mechanics and Astronomy*, 53, 1497-1504.

Huang, G. Y. & Yu, S. W., 2006. Effect of surface piezoelectricity on the electromechanical behaviour of a piezoelectric ring. *Physica StatusSolidi (b)*, 243.

Jia, X. L., Yang, J. & Kitipornchai, S., 2011. Pull-in instability of geometrically nonlinear micro-switches under electrostatic and Casimir forces. *Acta Mechanica,* 218, 161-174.

Joseph, R. P., Wang, B. & Samali, B., 2017. Size effects on double cantilever beam fracture mechanics specimen based on strain gradient theory. *Engineering Fracture Mechanics,* 169, 309-320.

Joseph, R. P., Wang, B. L., 2017. Large deformation of the double cantilever beam fracture mechanics specimen with surface effects based on strain gradient theory. In *Journal of Material Sciences & Engineering, Proceedings of the 3rd International Conference on Smart Materials and Structures,* Orlando, USA, 20-22 March 2017. p. 80.

Joseph, R. P, Purbolaksono, J., Liew, H. L., Ramesh, S., Hamdi, M., 2014. Stress intensity factors of a corner crack emanating from a pinhole of a solid cylinder.*Engineering Fracture Mechanics*, 128: 1-7.

Ke, L. L., Liu, C. & Wang, Y. S., 2015. Free vibration of nonlocal piezoelectric nanoplates under various boundary conditions. *Physica E: Low-dimensional Systems and Nanostructures,* 66, 93-106.

Kong, S., Zhou, S., Nie, Z. & Wang, K., 2009. Static and dynamic analysis of micro beams based on strain gradient elasticity theory. *International Journal of Engineering Science,* 47, 487-498.

Li, A., Zhou, S., Zhou, S. & Wang, B., 2014. Size-dependent analysis of a three-layer microbeam including electromechanical coupling. *Composite Structures,* 116, 120-127.

Li, X. F. & Lee, K. Y., 2016. Fracture of a thin power-law nonlinear material with a crack using the DCB model. *International Journal of Fracture,* 201, 119-125.

Liang, X., Hu, S. & Shen, S., 2014. A new Bernoulli–Euler beam model based on a simplified strain gradient elasticity theory and its applications. *Composite Structures,* 111, 317-323.

Majdoub, M., Sharma, P. & Cagin, T., 2008. Enhanced size-dependent piezoelectricity and elasticity in nanostructures due to the flexoelectric effect. *Physical Review B,* 77, 125424.

Mao, S. & Purohit, P. K., 2014. Insights into flexoelectric solids from strain-gradient elasticity. *Journal of Applied Mechanics,* 81, 081004.

Maranganti, R., Sharma, N. & Sharma, P., 2006. Electromechanical coupling in nonpiezoelectric materials due to nanoscale nonlocal size effects: Green's function solutions and embedded inclusions. *Physical Review B,* 74, 014110.

Mindlin, R. D., 1969. Continuum and lattice theories of influence of electromechanical coupling on capacitance of thin dielectric films. *International Journal of Solids and Structures,* 5, 1197-1208.

Morozovska, A. N., Eliseev, E. A., Tagantsev, A. K., Bravina, S. L., Chen, L. Q, Kalinin, S. V., 2011. Thermodynamics of electromechanically coupled mixed ionic-electronic conductors: Deformation potential, Vegard strains, and flexoelectric effect. *Physical Review B*, 83(19), 195313.

Qi, L., Zhou, S. & Li, A., 2016. Size-dependent bending of an electro-elastic bilayer nanobeam due to flexoelectricity and strain gradient elastic effect. *Composite Structures*, 135, 167-175.

Qiu, Y., Wu, H., Wang, J., Lou, J., Zhang, Z., Liu, A. & Chai, G., 2018. The enhanced piezoelectricity in compositionally graded ferroelectric thin films under electric field: A role of flexoelectric effect. *Journal of Applied Physics*, 123(8): 084103.

Reeder, J. R. & Crews Jr, J., 1991. Nonlinear analysis and redesign of the mixed-mode bending delamination test.

Shampine, L. F., Kierzenka, J. & Reichelt, M. W., 2000. Solving boundary value problems for ordinary differential equations in MATLAB with bvp4c. *Tutorial notes*, 2000, 1-27.

Sharma, N., Landis, C. & Sharma, P., 2010. Piezoelectric thin-film superlattices without using piezoelectric materials. *Journal of Applied Physics*, 108, 024304.

Shen, S. & Hu, S., 2010. A theory of flexoelectricity with surface effect for elastic dielectrics. *Journal of the Mechanics and Physics of Solids*, 58, 665-677.

Sladek, J., Sladek, V., Stanak, P., Zhang, C. & Tan, C. L., 2017. Fracture mechanics analysis of size-dependent piezoelectric solids. *International Journal of Solids and Structures*, 113, 1-9.

Stamoulis, K. & Giannakopoulos, A., 2012. A study of size effects and length scales in fracture and fatigue of metals by second gradient modelling. *Fatigue & Fracture of Engineering Materials & Structures*, 35, 852-860.

Wang, B. & Wang, K., 2013. Effect of surface residual stress on the fracture of double cantilever beam fracture toughness specimen. *Journal of Applied Physics*, 113, 153502.

Wang, G. F. & Feng, X. Q., 2009. Surface effects on buckling of nanowires under uniaxial compression. *Applied Physics Letters*, 94, 141913.

Wang, K. & Wang, B., 2016. Nonlinear fracture mechanics analysis of nano-scale piezoelectric double cantilever beam specimens with surface effect. *European Journal of Mechanics-A/Solids*, 56, 12-18.

Williams, J., 1987. Large displacement and end block effects in the'DCB'interlaminar test in modes I and II. *Journal of Composite Materials*, 21, 330-347.

Wu, H., Li, L., Chai, G., Song, F., Kitamura, T., 2016. Three-dimensional thermal weight function method for the interface crack problems in bimaterial structures under a transient thermal loading. *Journal of Thermal Stresses*, 39(4), 371-385.

Xu, L. & Shen, S., 2013. Size-dependent piezoelectricity and elasticity due to the electric field-strain gradient coupling and strain gradient elasticity. *International Journal of Applied Mechanics,* 5, 1350015.

Yan, Z. & Jiang, L., 2011. The vibrational and buckling behaviours of piezoelectric nanobeams with surface effects. *Nanotechnology,* 22, 245703.

Yan, Z. & Jiang, L., 2012. Vibration and buckling analysis of a piezoelectric nanoplate considering surface effects and in-plane constraints. Proc. R. Soc. A,. The Royal Society, rspa20120214.

Yan, Z. & Jiang, L., 2013a. Flexoelectric effect on the electroelastic responses of bending piezoelectric nanobeams. *Journal of Applied Physics,* 113, 194102.

Yan, Z. & Jiang, L., 2013b. Size-dependent bending and vibration behaviour of piezoelectric nanobeams due to flexoelectricity. *Journal of Physics D: Applied Physics,* 46, 355502.

Yue, Y,, Xu, K., Chen, T., 2016. A micro scale Timoshenko beam model for piezoelectricity with flexoelectricity and surface effects. *Composite Structures,* 136, 278-286.

Yue, Y., Xu, K. & Aifantis E., 2014. Microscale size effects on the electromechanical coupling in piezoelectric material for anti-plane problem. *Smart Materials and Structures*, 23(12), 125043.

Zhang, Z. & Jiang, L., 2014. Size effects on electromechanical coupling fields of a bending piezoelectric nanoplate due to surface effects and flexoelectricity. *Journal of Applied Physics,* 116, 134308.

Chapter 6

ANTI-PLANE CRACKED MATERIAL LAYER

Publication

Paper 5:

Joseph, R. P., Wang, B. L, & Samali, B., 2018. Strain gradient fracture in an anti-plane cracked material layer, *International Journal of Solids and Structures*, 146, 214-223. Doi: https://doi.org/10.1016/j.ijsolstr.2018.04.002

Relevance to the thesis

The aim of this chapter is to extend the application of strain gradient theory in modelling two-dimensional crack problem. In this paper, the strain gradient theory is implemented to explore the fracture behaviour of an anti-plane cracked material layer. The layer is assumed to be made of an isotropic material, while the mathematical modelling incorporates both volumetric and surface gradient effect. The study also explored some significant application of advanced numerical methods in solving scale-dependent fracture problems.

6.1 Abstract

Fracture mechanics analysis in terms of evaluating stress intensity factors of an anti-plane isotropic cracked layer is carried out using strain gradient elasticity theory. The crack plane is assumed parallel to the layer edges. Both volumetric and surface strain gradient material characteristic lengths are considered in formulations and numerical solutions. Two boundary value problems corresponding to "stress-free" and "clamped" boundaries are considered in which each solution is reduced to the dual integral equations. The Fredholm integral equation, proceeding from the dual integral equations, is numerically solved to evaluate crack tip stress intensity factor. Stress intensity factors for stress-free boundary conditions are higher with smaller height (or with a longer crack) and vice versa for clamped boundaries. Volumetric strain gradient effect reduces stress intensity factor and demonstrates a strong size effect on a smaller scale. Crack stiffness becomes more pronounced with positive surface strain gradient, while negative surface gradient leads to a more compliant crack. In general, the contribution of volumetric strain gradient is shown to be more dominant than that of surface strain gradient.

6.2 Introduction

Material discontinuities in micro and nanoscale structures promote its mechanical behaviour to be size dependent. This size dependency (size effect) has been thoroughly observed in experimental studies (Fleck & Hutchinson, 1997; Lam et al., 2003; McFarland & Colton, 2005). The discrete nature of the material medium (at a smaller scale) is not considered in classical continuum theories where internal dimensions of the structure are assumed negligible in comparison to the external ones. Hence, material's elastic as well as the plastic behaviour becomes scale-free and independent of an underlying microstructure. Over the years, several theories have been proposed incorporating intrinsic length scale in the continuum model to cater for size effect. Some

of the well-known theories in this regard are non-local elasticity theory (Eringen and Edelen, 1972), couple stress theory (Yang et al., 2002) and strain gradient theory (Aifantis, 2003, 1992; Lam et al., 2003). Pioneer work related to strain gradient theory was first postulated by Mindlin (1964, 1965) and further re-established and updated by Aifantis in (1992) and (2003) respectively. The physical meaning of higher order strain tensor employed in gradient elasticity theories is recently provided by Polizzotto (2016). On the other hand, the strain gradient theory proposed by Vardoulakis et al. (1996), provides the simplest and most practical generalization of corresponding constitutive theory accounting for only two material characteristic lengths (with the units of length). These material constants are responsible for material volumetric and surface strain gradient terms, usually represented as l and l', respectively (Chan et al., 2008; Paulino et al., 2003; Vardoulakis et al., 1996). This theory has been successfully employed to observe size effects (Aifantis, 2011) in various engineering problems such as in twisted micro-wires and bent micro-cantilever beams (Aifantis, 1999). A comprehensive review of this gradient theory and applications of an internal length gradient across various scales is recently provided by Aifantis (2016). Further application and validation of this simpler strain gradient theory are confirmed by Vardoulakis and Sulem (1995) and Giannakopoulos and Stamoulis (2007). Very recently application can be found in the fracture study of double cantilever beam fracture mechanics specimen conducted by the authors (Joseph et al., 2017).

Quite a few studies related to the fracture problem in infinite medium (in which the geometric disturbance is only due to crack), based on gradient elasticity theories, are conducted over the years. For instance, one of the pioneering works in the field of gradient elasticity in Mode-III crack problem was conducted by Vardoulakis et al. (1996), Exadaktylos (1998) and subsequently by Exadaktylos and Vardoulakis (2001). In these papers, two material parameters l and l' related to volumetric and surface strain

gradients were used to solve two boundary value problems i.e. traction boundary value problem and mixed boundary value problem. Paulino et al. (2003) and Chan et al. (2008) employed gradient elasticity theory to solve mode III crack problems in functionally graded materials. In the first case, crack is assumed perpendicular (Paulino et al., 2003), while in second case crack plane is parallel to the material gradation (Chan et al., 2008). Fannjiang et al. (2002) employed a hyper-singular integrodifferential equation approach to solve the anti-plane shear crack problem using strain gradient elasticity theory. Some interesting information related to dislocation based-gradient elastic fracture mechanics for the anti-plane crack problem is discussed by Mousavi and Aifantis (2015). A very comprehensive study related to an anti-plane analysis of an infinite plane with multiple cracks based on strain gradient theory is recently conducted by Karimipour and Fotuhi (2017).

Above studies are strictly related to the bodies whose edges are far away and any disturbance in the material medium is primarily due to crack initiation and propagation. However, in many practical engineering applications, the specimen boundaries are finite and hence contribute significantly to its fracture behaviour. One such case is the crack initiation and propagation in elastic media of the form of layer/strip with finite height. Estimation of fracture properties in this case, such as stress intensity factor at the crack tip, is extremely vital to accurately predict crack growth rates. For classical case, several analytical models have been proposed by researchers using different approaches. For instance, closed-form solutions of a crack at the mid-plane of elastic media subjected to anti-plane shear stress are obtained by (Yang, 1997). Singh et al. (1981) employed Fourier transform technique, while Tait and Moodie (1981) utilized the complex variable method to provide the closed form solution of mode-III crack moving along the center of an elastic strip. On the other hand, the solution of interface crack between two dissimilar materials in a closed form is provided by Li (2001). For an anti-plane

interface crack between two dissimilar magneto-electroelastic layers, Wang and Mai (2006) evaluated closed-form solutions for stress intensity factors. Furthermore, thorough investigations of mode-III crack in multi-layered composites are provided by Sih and Chen (1981).

According to the authors' knowledge, most of the models in the literature may be divided into two groups; The first group relates to the evaluation of closed form solution of an anti-plane crack in an infinite medium based on gradient elasticity theories and the second group comprises those classical studies which are conducted to evaluate the closed form solution of cracked elastic strip/layer (finite boundaries). Therefore, in this article the simplest strain gradient theory (proposed by Vardoulakis et al. (1996), Exadaktylos (1998) and subsequently elaborated by Exadaktylos and Vardoulakis (2001)) comprising two material parameters, related to volumetric and surface strain gradients, respectively, is applied to solve the mode III crack problem in an elastic isotropic layer. The objective here is to numerically estimate the crack tip stress intensity factors of a crack propagated at the middle plane of an elastic isotropic layer having finite height. Two types of boundary value problems are considered i.e. stress-free boundaries and clamped boundaries. The solution of each problem is reduced to dual integral equations. The kernel of the Fredholm integral equation (an improper integral that ranges from 0 to infinity) of the second kind, thus obtained (by applying the method of Copson (1961) on the dual integral equations) is numerically solved by using the collocation method of Gauss-Laguerre quadrature.

6.3 Theoretical formulations

This section introduces the constitutive equations and theoretical formulations of an isotropic elastic layer of finite thickness using strain gradient theory. Firstly, the constitutive equations are derived without incorporating surface strain gradient effect ($l' = 0$) followed by the detailed analysis of the complete strain gradient model (with both

volumetric and surface strain gradient effect). The approach considered in this paper is similar to one adopted by Vardoulakis et al. (1996) and Exadaktylos (1998).

Consider a crack of length 2*a* placed at the mid plane of an isotropic layer with thickness (height) 2*h*. The boundaries of the layer are at $y = \pm h$ and reference axes are shown in Fig. 2.4a. The crack surfaces are subjected to the applied anti-plane shear stress (τ_1) as shown in Fig. 2.4b. The conditions at $y = 0$ are given as: $\tau_{yz}(x,0) = -\tau_1$ for $|x| < a$ and $w_z(x,0) = 0$ for $|x| \geq a$. For the upper half plane i.e. $y \geq 0$, the stresses and double stress derived from the constitutive equations of gradient elasticity with surface energy are given as (Chan et al., 2008; Vardoulakis et al., 1996);

$$\tau_{zx} = G\left[\frac{\partial w_z}{\partial x} - l^2\nabla^2\frac{\partial w_z}{\partial x}\right] \tag{6.1a}$$

$$\tau_{yz} = G\left[\frac{\partial w_z}{\partial y} - l^2\nabla^2\frac{\partial w_z}{\partial y}\right] \tag{6.1b}$$

$$\mu_{xxz} = Gl^2\frac{\partial^2 w_z}{\partial x^2} \tag{6.1c}$$

$$\mu_{xyz} = Gl^2\frac{\partial^2 w_z}{\partial x\partial y} \tag{6.1d}$$

$$\mu_{yxz} = G\left[-l'\frac{\partial w_z}{\partial x} + l^2\frac{\partial^2 w_z}{\partial x\partial y}\right] \tag{6.1e}$$

$$\mu_{yyz} = G\left[-l'\frac{\partial w_z}{\partial y} + l^2\frac{\partial^2 w_z}{\partial y^2}\right] \tag{6.1f}$$

Here $\nabla^2 = \partial^2/\partial x^2 + \partial^2/\partial y^2$, *G* is the shear modulus, *l* and l' are the volumetric and surface material characteristic lengths, respectively. For an anti-plane shear crack problem as depicted in Fig. 6.1, we have $u_x = u_y = 0$, $u_z \neq 0$. Also

$\sigma_{xx} = \sigma_{yy} = \sigma_{zz} = \tau_{xy} = 0$ while $\tau_{yz} \neq 0$ and $\tau_{xz} \neq 0$. The equilibrium equation i.e. $\partial \tau_{yz} / \partial y + \partial \tau_{xz} / \partial x = 0$ with the help of equations (6.1a - 6.1f) may be expanded as;

$$\nabla^2 w_z - l^2 \nabla^4 w_z = 0 \tag{6.2a}$$

Or

$$\left[\frac{\partial^2 w_z}{\partial x^2} + \frac{\partial^2 w_z}{\partial y^2} \right] - l^2 \left[\frac{\partial^4 w_z}{\partial x^4} + \frac{\partial^4 w_z}{\partial y^4} + \frac{2\partial^4 w_z}{\partial x^2 \partial y^2} \right] = 0 \tag{6.2b}$$

The general solution of the fourth order differential equation (6.2) may be represented as; $w_z(x,y) = w_z^c(x,y) + w_z^g(x,y)$ (Vardoulakis et al., 1996), where w_z^c and w_z^g are the solutions of the harmonic $\left(\nabla^2 w_z^g = 0\right)$ and Helmholtz's equation $\left(w_z^g - l^2 \nabla^2 w_z^g = 0\right)$. The application of Fourier transform gives the solution of harmonic function as;

$$w_z^c(x,y) = \frac{2}{\pi} \int_0^\infty \left[A(s) e^{-sy} + C(s) e^{sy} \right] \cos(sx) ds \,, \qquad y \geq 0 \tag{6.3}$$

where *sy* is the product of *s* and *y*, moreover the solution of a Helmholtz's equation is given as;

$$w_z^c(x,y) = \frac{2}{\pi} \int_0^\infty \left[B(s) e^{-y\sqrt{s^2 + (1/l^2)}} + D(s) e^{y\sqrt{s^2 + (1/l^2)}} \right] \cos(sx) ds \,, \; y \geq 0 \tag{6.4}$$

combining Eqs. (6.3) and (6.4) give;

$$w_z(x,y) = \frac{2}{\pi} \int_0^\infty \left[\begin{matrix} A(s) e^{-sy} + B(s) e^{-y\sqrt{s^2 + (1/l^2)}} + \\ C(s) e^{sy} + D(s) e^{y\sqrt{s^2 + (1/l^2)}} \end{matrix} \right] \cos(sx) ds \,, \; y \geq 0 \tag{6.5}$$

A(*s*), *B*(*s*), *C*(*s*) and *D*(*s*) are the constants to be determined from the boundary conditions.

6.4 Stress-free Boundaries without surface gradient effect (l' =0)

The shear stress $\tau_{yz}(x,y)$ from Eqs. (6.1b) and (6.5) is written as;

$$\tau_{yz}(x,y)=G\begin{bmatrix}\frac{2}{\pi}\int_0^{\infty}\begin{bmatrix}A(s)e^{-sy}(-s)+B(s)e^{-y\sqrt{s^2+(1/l^2)}}(-\sqrt{s^2+(1/l^2)})+\\C(s)e^{sy}(s)+D(s)e^{y\sqrt{s^2+(1/l^2)}}(\sqrt{s^2+(1/l^2)})\end{bmatrix}\cos(sx)\mathrm{d}s\\ \frac{-2l^2}{\pi}\begin{bmatrix}-\int_0^{\infty}s^2\begin{bmatrix}A(s)e^{-sy}(-s)+B(s)e^{-y\sqrt{s^2+(1/l^2)}}(-\sqrt{s^2+(1/l^2)})+\\C(s)e^{sy}(s)+D(s)e^{y\sqrt{s^2+(1/l^2)}}(\sqrt{s^2+(1/l^2)})\end{bmatrix}\cos(sx)\mathrm{d}s+\\ \int_0^{\infty}\begin{bmatrix}A(s)e^{-sy}(-s^3)+B(s)e^{-y\sqrt{s^2+(1/l^2)}}(-\sqrt{s^2+(1/l^2)})^3+\\C(s)e^{sy}(s^3)+D(s)e^{y\sqrt{s^2+(1/l^2)}}(\sqrt{s^2+(1/l^2)})^3\end{bmatrix}\cos(sx)\mathrm{d}s\end{bmatrix}\end{bmatrix} \quad (6.6)$$

For stress-free boundaries, similar to the classical case, the shear stress Eq. (6.6) at the upper and lower edge of the layer would be zero i.e. $\tau_{yz}(x,\pm h)=0,\ |x|<\infty$, that may further be reduced to;

$$\tau_{yz}(x,h)=\frac{2G}{\pi}\int_0^{\infty}\left[A(s)e^{-sh}(-s)+C(s)e^{sh}(s)\right]\cos(sx)\mathrm{d}s=0 \quad (6.7)$$

that gives $C(s)=e^{-2sh}A(s)$. The double stress $\mu_{yyz}(x,y)$ (with l' = 0) from Eqs. (6.1f) and (6.5) is written as;

$$\mu_{yyz}(x,y)=G\left[\frac{2l^2}{\pi}\int_0^{\infty}\begin{bmatrix}A(s)e^{-sy}\left(s^2\right)+B(s)e^{-y\sqrt{s^2+(1/l^2)}}\left(s^2+(1/l^2)\right)+\\C(s)e^{sy}\left(s^2\right)+D(s)e^{y\sqrt{s^2+(1/l^2)}}\left(s^2+(1/l^2)\right)\end{bmatrix}\right]\cos(sx)\mathrm{d}s \quad (6.8)$$

The double stress (Eq. (6.8)) at the upper edge is expressed as: $\mu_{yyz}(x,h)=0,|x|<\infty$ that is further reduced to;

$$s^2l^2\left(A(s)e^{-sh}+C(s)e^{sh}\right)+(s^2l^2+1)\left(B(s)e^{-h\sqrt{s^2+(1/l^2)}}+D(s)e^{h\sqrt{s^2+(1/l^2)}}\right)=0 \quad (6.9)$$

By substituting $C(s)=e^{-2sh}A(s)$ in Eq. (6.9) one obtains;

$$\frac{2}{a^{(1)}}A(s)e^{-sh}+\left(D(s)e^{h\sqrt{s^2+(1/l^2)}}\right)=-B(s)e^{-h\sqrt{s^2+(1/l^2)}} \tag{6.10}$$

where $a^{(1)}=1+1/(s^2l^2)$. Similarly, the second non-classical boundary condition at the crack surface is written as $\mu_{yyz}(x,0)=0\ |x|<\infty$ that may further gives;

$$s^2A(s)+(s^2+1/l^2)B(s)+s^2C(s)+(s^2+1/l^2)D(s)=0 \tag{6.11}$$

Again from $C(s)=e^{-2sh}A(s)$ and $a^{(1)}=1+1/(s^2l^2)$, Eq. (6.11) may be written as;

$$D(s)=-\left(B(s)+(1+e^{-2sh})A(s)/a^{(1)}\right) \tag{6.12}$$

To obtain an expression for $B(s)$ in terms of $A(s)$, substituting Eq. (6.12) into Eq. (6.10) and after re-arrangement we get;

$$\frac{2}{a^{(1)}}\left(e^{-sh}-\frac{(1+e^{-2sh})e^{h\sqrt{s^2+(1/l^2)}}}{2a^{(1)}}\right)A(s)=B(s)\left(-e^{-h\sqrt{s^2+(1/l^2)}}+e^{h\sqrt{s^2+(1/l^2)}}\right) \tag{6.13}$$

Or $B(s)=2b^{(1)}A(s)/a^{(1)}$ with;

$$a^{(1)}=1+1/(s^2l^2),\ b^{(1)}=\frac{e^{-sh}-\left(1+e^{-2sh}\right)e^{h\sqrt{s^2+(1/l^2)}}/2a^{(1)}}{-e^{-h\sqrt{s^2+(1/l^2)}}+e^{h\sqrt{s^2+(1/l^2)}}} \tag{6.14}$$

And by substituting $B(s)=2b^{(1)}A(s)/a^{(1)}$ into Eq. (6.12) we get $D(s)$ in terms of $A(s)$;

$$D(s)=-\frac{2}{a^{(1)}}\left(\frac{(1+e^{-2sh})}{2}+b^{(1)}\right)A(s) \tag{6.15}$$

Now in order to obtain the dual integral equations, Let $A(s)=G(s)/(1+e^{-2sh})$ so, $C(s)=e^{-2sh}A(s)$, $B(s)=2b^{(1)}A(s)/a^{(1)}$ and Eq. (6.15) provide expressions for $C(s)=e^{-2sh}G(s)/(1+e^{-2sh})$, $B(s)=2b^{(1)}G(s)/a^{(1)}(1+e^{-2sh})$ and $D(s)=-2((1+e^{-2sh})/2+b^{(1)})G(s)/(a^{(1)}(1+e^{-2sh})$, respectively. Here $G(s)$ is an unknown function. From $w_z(x,0)=0,\ |x|\geq a$, we obtained;

$$w_z = \frac{2}{\pi}\int_0^{\infty}\left[A(s)+B(s)+C(s)+D(s)\right]\cos(sx)ds = 0\,, \quad |x| \geq a \tag{6.16}$$

By expressing $A(s)$, $B(s)$, $C(s)$ and $D(s)$ in terms of an unknown function $G(s)$ in Eq. (6.16) we obtain;

$$\int_0^{\infty} E(s)\cos(sx)ds = 0 \tag{6.17}$$

here $E(s) = P^{(1)}G(s)$ and;

$$P^{(1)} = \frac{1}{1+e^{-2sh}}\left[1+e^{-2sh} - \frac{(1+e^{-2sh})}{a^{(1)}}\right] = 1 - \frac{1}{a^{(1)}} = \frac{1}{1+s^2l^2} \tag{6.18}$$

As l approaches 0, the term $(1+e^{-2sh})/a^{(1)}$ approaches zero as well and hence $P^{(1)}$ will reduce to 1. For the second integral equation we have $\tau_{yz}(x,0) = -\tau_1\,,\ |x| < a$ which is expanded as;

$$\tau_{yz}(x,0) = \frac{2G}{\pi}\left[\begin{array}{l}\int_0^{\infty}\left[\begin{array}{l}A(s)(-s)+B(s)(-\sqrt{s^2+(1/l^2)})+\\ C(s)(s)+D(s)(\sqrt{s^2+(1/l^2)})\end{array}\right]\cos(sx)\mathrm{d}s \\ -l^2\left[\begin{array}{l}-\int_0^{\infty}s^2\left[\begin{array}{l}A(s)(-s)+B(s)(-\sqrt{s^2+(1/l^2)})+\\ C(s)(s)+D(s)(\sqrt{s^2+(1/l^2)})\end{array}\right]\cos(sx)\mathrm{d}s + \\ \int_0^{\infty}\left[\begin{array}{l}A(s)(-s^3)+B(s)(-\sqrt{s^2+(1/l^2)})^3+\\ C(s)(s^3)+D(s)(\sqrt{s^2+(1/l^2)})^3\end{array}\right]\cos(sx)\mathrm{d}s\end{array}\right]\end{array}\right] = -\tau_1 \tag{6.19}$$

Equation (6.19) can be reduced to;

$$\frac{-2G}{\pi}\int_0^{\infty}\left[sA(s)-sC(s)\right]\cos(sx)ds = -\tau_1 \tag{6.20}$$

By substituting $C(s) = e^{-2sh}A(s)$ into Eq. (6.20) and after rearrangement we get;

$\int_0^\infty s\left[1-e^{-2sh}\right]A(s)\cos(sx)ds = \tau_1\pi/2G$ and since $A(s) = G(s)/\left(1+e^{-2sh}\right) = E(s)/P^{(1)}\left(1+e^{-2sh}\right)$

so,

$$\int_0^\infty sF_{sg}(s)E(s)\cos(sx)ds = \frac{\tau_1\pi}{2G} \tag{6.21}$$

$$F_{sg}(s) = \frac{\left(1-e^{-2sh}\right)}{P^{(1)}\left(1+e^{-2sh}\right)} \tag{6.22}$$

here "*sg*" in subscript represents the "stress-free boundaries & gradient (l' =0)" case with $P^{(1)}$ given in Eq. (6.18). Equations (6.17) and (6.21) are the dual integral equations. When l approaches zero, $P^{(1)}$ approaches 1 and, hence, $F_{sg}(s)$ will reduce to the classical case (see section 2.7.1).

6.5 Clamped Boundaries without surface gradient effect (l' =0)

As with classical case (see section 2.7.2) for clamped boundaries i.e. $w_z(x,\pm h) = 0$, $|x| < \infty$ and using Eq. (6.5) we get;

$$A(s)e^{-sh} + B(s)e^{-h\sqrt{s^2+(1/l^2)}} + C(s)e^{sh} + D(s)e^{h\sqrt{s^2+(1/l^2)}} = 0 \tag{6.23}$$

The non-classical trivial boundary condition for double stress at upper edge is $\mu_{yyz}(x,h) = 0$, $|x| < \infty$ that yields (with l' =0);

$$\begin{aligned} &s^2l^2A(s)e^{-sh} + (1+s^2l^2)B(s)e^{-h\sqrt{s^2+(1/l^2)}} + s^2l^2C(s)e^{sh} + \\ &(1+s^2l^2)D(s)e^{h\sqrt{s^2+(1/l^2)}} = 0 \end{aligned} \tag{6.24}$$

Also $\mu_{yyz}(x,0) = 0$, $|x| < \infty$ further gives;

$$A(s) + (1+1/(s^2l^2))B(s) + C(s) + (1+1/(s^2l^2))D(s) = 0 \tag{6.25}$$

Eliminating $A(s)$ and $C(s)$ from Eqs. (6.23) and (6.24) we obtain;

$$D(s) = \frac{-B(s)e^{-h\sqrt{s^2+(1/l^2)}}}{e^{h\sqrt{s^2+(1/l^2)}}} = -B(s)e^{-2h\sqrt{s^2+(1/l^2)}} = -B(s)a^{(2)} \tag{6.26}$$

with $e^{-2h\sqrt{s^2+(1/l^2)}} = a^{(2)}$

Multiplying Eq. (6.25) by e^{sh} and subtracting Eq. (6.23) we get;

$$\begin{aligned}&\left(e^{sh} - e^{-sh}\right)A(s) + \left((1+1/(s^2l^2))e^{sh} - e^{-h\sqrt{s^2+(1/l^2)}}\right)B(s) + \\ &\left((1+1/(s^2l^2))e^{sh} - e^{h\sqrt{s^2+(1/l^2)}}\right)D(s) = 0\end{aligned} \tag{6.27a}$$

or

$$b^{(2)}A(s) + c^{(2)}B(s) + d^{(2)}D(s) = 0 \tag{6.27b}$$

where $b^{(2)} = \left(e^{sh} - e^{-sh}\right)$, $c^{(2)} = \left((1+1/(s^2l^2))e^{sh} - e^{-h\sqrt{s^2+(1/l^2)}}\right)$ and

$d^{(2)} = \left((1+1/(s^2l^2))e^{sh} - e^{h\sqrt{s^2+(1/l^2)}}\right)$. Substituting Eq. (6.26) into Eq. (6.27b) and after rearrangement we obtain;

$$B(s) = \frac{b^{(2)}}{\left(a^{(2)}d^{(2)} - c^{(2)}\right)}A(s) \tag{6.28}$$

And by substituting Eq. (6.28) into Eq. (6.26) we obtain $D(s)$ in terms of $A(s)$;

$$D(s) = \frac{-b^{(2)}a^{(2)}}{\left(a^{(2)}d^{(2)} - c^{(2)}\right)}A(s) \tag{6.29}$$

Now substituting Eqs. (6.28) and (6.29) into Eq. (6.23) we get $C(s)$ in terms of $A(s)$;

$$C(s) = -A(s)\left[e^{-2sh} + \frac{b^{(2)}e^{-sh}}{\left(a^{(2)}d^{(2)} - c^{(2)}\right)}\left(e^{-h\sqrt{s^2+(1/l^2)}} - a^{(2)}e^{h\sqrt{s^2+(1/l^2)}}\right)\right] = -A(s)e^{(2)} \tag{6.30}$$

where

$$\left[e^{-2sh}+\frac{b^{(2)}e^{-sh}}{\left(a^{(2)}d^{(2)}-c^{(2)}\right)}\left(e^{-h\sqrt{s^2+(1/l^2)}}-a^{(2)}e^{h\sqrt{s^2+(1/l^2)}}\right)\right]=e^{(2)} \tag{6.31}$$

Now in order to obtain the dual integral equations, let $A(s)=G(s)/(1-e^{-2sh})$, so from Eqs. (6.28) to (6.30) we get $B(s)=b^{(2)}G(s)/((a^{(2)}d^{(2)}-c^{(2)})(1-e^{-2sh}))$, $D(s)=-b^{(2)}a^{(2)}G(s)/((a^{(2)}d^{(2)}-c^{(2)})(1-e^{-2sh}))$ and $C(s)=-e^{(2)}G(s)/(1-e^{-2sh})$, respectively. Here $G(s)$ is an unknown function. The dual integral equations may be obtained similar to the previous section (& from see section 2.7.2);

$$\int_0^\infty E(s)\cos(sx)ds=0, \tag{6.32}$$

here $E(s)=P^{(2)}G(s)$ and

$$\int_0^\infty sF_{cg}(s)E(s)\cos(sx)ds=\frac{\tau_1\pi}{2G} \tag{6.33}$$

where

$$P^{(2)}=\frac{1}{1-e^{-2sh}}\left[\begin{array}{l}1-e^{-2sh}+\frac{b^{(2)}}{\left(a^{(2)}d^{(2)}-c^{(2)}\right)}\left(1-a^{(2)}\right)- \\ \frac{b^{(2)}e^{-sh}}{\left(a^{(2)}d^{(2)}-c^{(2)}\right)}\left(e^{-h\sqrt{s^2+(1/l^2)}}-a^{(2)}e^{h\sqrt{s^2+(1/l^2)}}\right)\end{array}\right] \tag{6.34}$$

$$F_{cg}(s)=\frac{\left(1+e^{-2sh}+e^{(2)}-e^{-2sh}\right)}{P^{(2)}\left(1-e^{-2sh}\right)} \tag{6.35}$$

As *l* approaches zero, the term

$\frac{b^{(2)}}{\left(a^{(2)}d^{(2)}-c^{(2)}\right)}\left(1-a^{(2)}\right)-\frac{b^{(2)}e^{-sh}}{\left(a^{(2)}d^{(2)}-c^{(2)}\right)}\left(e^{-h\sqrt{s^2+(1/l^2)}}-a^{(2)}e^{h\sqrt{s^2+(1/l^2)}}\right)$ in Eq. (6.34)

approaches zero as well and hence $P^{(2)}$ will reduce to 1. Moreover, "*cg*" in subscript

(Eq. (6.35)) represents the "clamped boundaries & gradient (l' =0)" case. When l approaches zero, $P^{(2)}$ given by Eq. (6.34) and ($e^{(2)}$ - e^{-2sh}) in Eq. (6.35) approach to 1 and zero, respectively. Hence $F_{cg}(s)$ will reduce to the classical case (see section 2.7.2).

6.6 Stress-free Boundaries with surface gradient effect ($l' \neq 0$)

The classical boundary condition, similar to the classical case (section 2.7.1) and strain gradient model ($l' = 0$) gives $C(s) = e^{-2sh}A(s)$. The double stress (with l') from Eqs. (6.1f) and (6.5) is given as;

$$\begin{aligned}&\frac{-2l'}{\pi}\int_0^{\infty}\left[\begin{array}{l}A(s)e^{-sy}(-s)+B(s)e^{-y\sqrt{s^2+(1/l^2)}}(-\sqrt{s^2+(1/l^2)})+\\ C(s)e^{sy}(s)+D(s)e^{y\sqrt{s^2+(1/l^2)}}(\sqrt{s^2+(1/l^2)})\end{array}\right]\cos(sx)ds+\\ &\left[\frac{2l^2}{\pi}\int_0^{\infty}\left[\begin{array}{l}A(s)e^{-sy}\left(s^2\right)+B(s)e^{-y\sqrt{s^2+(1/l^2)}}\left(s^2+(1/l^2)\right)+\\ C(s)e^{sy}\left(s^2\right)+D(s)e^{y\sqrt{s^2+(1/l^2)}}\left(s^2+(1/l^2)\right)\end{array}\right]\right]\cos(sx)ds=\mu_{yyz}(x,y)\end{aligned} \tag{6.36}$$

The non-classical trivial boundary condition for double stress at the upper edge i.e. $\mu_{yyz}(x,h)=0,\ |x|<\infty$ is expanded as;

$$\begin{aligned}&\left(sl'+s^2l^2\right)A(s)e^{-sh}+\left(l'\sqrt{s^2+(1/l^2)}+l^2(s^2+(1/l^2))\right)B(s)e^{-h\sqrt{s^2+(1/l^2)}}\\ &+\left(-sl'+s^2l^2\right)C(s)e^{sh}+\left(-l'\sqrt{s^2+(1/l^2)}+l^2(s^2+(1/l^2))\right)D(s)e^{h\sqrt{s^2+(1/l^2)}}=0\end{aligned} \tag{6.37}$$

Substituting $C(s)=e^{-2sh}A(s)$ in Eq. (6.37) one obtains;

$$\left(a^{(3)}+c^{(3)}\right)e^{-sh}A(s)+\left(d^{(3)}e^{h\sqrt{s^2+(1/l^2)}}\right)D(s)=\left(-b^{(3)}e^{-h\sqrt{s^2+(1/l^2)}}\right)B(s) \tag{6.38a}$$

where

$$a^{(3)}=sl'+s^2l^2,\ c^{(3)}=-sl'+s^2l^2,\ b^{(3)}=l'\sqrt{s^2+(1/l^2)}+l^2(s^2+(1/l^2)),$$

$$d^{(3)}=-l'\sqrt{s^2+(1/l^2)}+l^2(s^2+(1/l^2)) \tag{6.38b}$$

Similarly the second non-classical boundary condition at the crack is written as; $\mu_{yyz}(x,0) = 0, |x| < \infty$ that may further yields;

$$a^{(3)}A(s) + b^{(3)}B(s) + c^{(3)}C(s) + d^{(3)}D(s) = 0, \tag{6.39a}$$

or

$$D(s) = -\left(a^{(3)} + c^{(3)}e^{-2sh}\right)A(s) - b^{(3)}B(s)/d^{(3)}, \tag{6.39b}$$

Since $C(s) = e^{-2sh}A(s)$, also let

$$D(s) = \alpha A(s) + \beta(s) \tag{6.39c}$$

where

$$\alpha = -\left(a^{(3)} + c^{(3)}e^{-2sh}\right)/d^{(3)}, \ \beta = -b^{(3)}/d^{(3)} \tag{6.39d}$$

Substituting Eq. (6.39c) in Eq. (6.38a) we get $B(s)$ in terms of $A(s)$ as follows;

$$\gamma A(s) + \theta\left(\alpha A(s) + \beta B(s)\right) = -\xi B(s) \tag{6.40}$$

where $\gamma = \left(a^{(3)} + c^{(3)}\right)e^{-sh}$, $\theta = d^{(3)}e^{h\sqrt{s^2+(1/l^2)}}$, $\xi = b^{(3)}e^{-h\sqrt{s^2+(1/l^2)}}$ and after simplification we get;

$$B(s) = -\frac{(\gamma + \theta\alpha)A(s)}{(\xi + \theta\beta)} \tag{6.41}$$

Substituting Eq. (6.41) into Eq. (6.39c) one obtains $D(s)$ in terms of $A(s)$;

$$D(s) = \left[\alpha - \beta\frac{(\gamma + \theta\alpha)}{(\xi + \theta\beta)}\right]A(s) \tag{6.42}$$

To obtain dual integral Equations; Let $A(s) = G(s)/(1+e^{-2sh})$, so $C(s) = e^{-2sh}A(s)$, (6.41) and (6.42) give $C(s) = e^{-2sh}G(s)/(1+e^{-2sh})$, $B(s) = -(\gamma + \theta\alpha)G(s)/((\xi + \theta\beta)(1+e^{-2sh}))$ and

$D(s) = [\alpha - \beta(\gamma + \theta\alpha)/(\xi + \theta\beta)]G(s)/(1 + e^{-2sh})$ respectively. Here $G(s)$ is an unknown function. The dual integral equations may be obtained similar to the previous sections as;

$$\int_0^\infty E(s)\cos(sx)ds = 0 \tag{6.43}$$

here $E(s) = P^{(3)}G(s)$, and

$$\int_0^\infty sF_{sg'}(s)E(s)\cos(sx)ds = \frac{\tau_1\pi}{2G} \tag{6.44}$$

$$P^{(3)} = \frac{1}{1+e^{-2sh}}\left[1 + e^{-2sh} - \frac{(\gamma+\theta\alpha)}{(\xi+\theta\beta)} + \alpha - \frac{\beta(\gamma+\theta\alpha)}{(\xi+\theta\beta)}\right] \tag{6.45}$$

$$F_{sg'}(s) = \frac{\left(1-e^{-2sh}\right)}{P^{(3)}\left(1+e^{-2sh}\right)} \tag{6.46}$$

As l and l' approach zero, the term $(\gamma+\theta\alpha)/(\xi+\theta\beta) + \alpha - \beta(\gamma+\theta\alpha)/(\xi+\theta\beta)$ in Eq. (6.45) also approaches zero and hence $P^{(3)}$ will reduce to 1. Moreover, "*sg*'" in subscript represents the "stress-free boundaries & gradient ($l' \neq 0$)" case and $P^{(3)}$ is given in Eq. (6.45). When l and l' approach zero, $P^{(3)}$ approaches 1 and, hence, $F_{sg'}(s)$ will reduce to the classical case (see section 2.7.1).

6.7 Clamped Boundaries with surface gradient effect ($l' \neq 0$)

As done in section 2.7.2 for clamped boundaries i.e. $w_z(x,\pm h) = 0, |x| < \infty$ and using Eq. (6.5) we get;

$$A(s)e^{-sh} + B(s)e^{-h\sqrt{s^2+(1/l^2)}} + C(s)e^{sh} + D(s)e^{h\sqrt{s^2+(1/l^2)}} = 0 \tag{6.47}$$

The non-classical trivial boundary condition for double stress at upper edge is $\mu_{yyz}(x,h) = 0,\ |x| < \infty$ that further gives;

$$a^{(4)}A(s)e^{-sh} + b^{(4)}B(s)e^{-h\sqrt{s^2+(1/l^2)}} + c^{(4)}C(s)e^{sh} + d^{(4)}D(s)e^{h\sqrt{s^2+(1/l^2)}} = 0 \quad (6.48)$$

Also $\mu_{yyz}(x,0) = 0$, $|x| < \infty$ gives;

$$a^{(4)}A(s) + b^{(4)}B(s) + c^{(4)}C(s) + d^{(4)}D(s) = 0 \quad (6.49)$$

Multiplying Eq. (6.49) by e^{sh} and subtracting Eq. (6.48), we get;

$$D(s) = \frac{\left(e^{-sh} - e^{sh}\right)a^{(4)}A(s) + \left(e^{-h\sqrt{s^2+(1/l^2)}} - e^{sh}\right)b^{(4)}B(S)}{\left(e^{sh} - e^{h\sqrt{s^2+(1/l^2)}}\right)d^{(4)}} = \alpha^* A(s) + \beta^* B(s) \quad (6.50a)$$

where

$$\alpha^* = \frac{\left(e^{-sh} - e^{sh}\right)a^{(4)}}{\left(e^{sh} - e^{h\sqrt{s^2+(1/l^2)}}\right)d^{(4)}}, \beta^* = \frac{\left(e^{-h\sqrt{s^2+(1/l^2)}} - e^{sh}\right)b^{(4)}}{\left(e^{sh} - e^{h\sqrt{s^2+(1/l^2)}}\right)d^{(4)}}B(s) \quad (6.50b)$$

Multiplying Eq. (6.49) by $e^{h\sqrt{s^2+(1/l^2)}}$ and subtracting Eq. (6.48) we get;

$$B(s) = \frac{\left(e^{-sh} - e^{h\sqrt{s^2+(1/l^2)}}\right)a^{(4)}A(s) - \left(e^{h\sqrt{s^2+(1/l^2)}} - e^{sh}\right)c^{(4)}C(s)}{\left(e^{h\sqrt{s^2+(1/l^2)}} - e^{-h\sqrt{s^2+(1/l^2)}}\right)b^{(4)}} = \gamma^* A(s) - \theta^* C(s) \quad (6.51a)$$

where

$$\gamma^* = \frac{\left(e^{-sh} - e^{h\sqrt{s^2+(1/l^2)}}\right)a^{(4)}}{\left(e^{h\sqrt{s^2+(1/l^2)}} - e^{-h\sqrt{s^2+(1/l^2)}}\right)b^{(4)}}, \theta^* = \frac{\left(e^{h\sqrt{s^2+(1/l^2)}} - e^{sh}\right)c^{(4)}}{\left(e^{h\sqrt{s^2+(1/l^2)}} - e^{-h\sqrt{s^2+(1/l^2)}}\right)b^{(4)}} \quad (6.51b)$$

Substituting Eq. (6.51a) in (6.50a) we get $D(s)$ in terms of $A(s)$ and $C(s)$;

$$D(s) = \alpha^* A(s) + \beta^* B(s) = \alpha^* A(s) + \beta^*\left(\gamma^* A(s) - \theta^* C(s)\right) \quad (6.52a)$$

$$D(s) = \left(\alpha^* + \beta^*\gamma^*\right)A(s) - \theta^*\beta^* C(s) \quad (6.52b)$$

And substituting Eqs. (6.51a) and (6.52b) into Eq. (6.47) we get $C(s)$ in terms of $A(s)$;

$$\left(e^{-sh}+\gamma^{*}e^{-h\sqrt{s^2+(1/l^2)}}+\left(\alpha^{*}+\beta^{*}\gamma^{*}\right)e^{h\sqrt{s^2+(1/l^2)}}\right)A(s)+\left(e^{sh}-\theta^{*}e^{-h\sqrt{s^2+(1/l^2)}}-\theta^{*}\beta^{*}e^{h\sqrt{s^2+(1/l^2)}}\right)C(s)=0 \qquad (6.53)$$

After simplifying one obtains

$$C(s)=\frac{-\left(e^{-sh}+\gamma^{*}e^{-h\sqrt{s^2+(1/l^2)}}+\left(\alpha^{*}+\beta^{*}\gamma^{*}\right)e^{h\sqrt{s^2+(1/l^2)}}\right)A(s)}{\left(e^{sh}-\theta^{*}e^{-h\sqrt{s^2+(1/l^2)}}-\theta^{*}\beta^{*}e^{h\sqrt{s^2+(1/l^2)}}\right)}=-e^{(4)}A(s) \qquad (6.54a)$$

where

$$\frac{\left(e^{-sh}+\gamma^{*}e^{-h\sqrt{s^2+(1/l^2)}}+\left(\alpha^{*}+\beta^{*}\gamma^{*}\right)e^{h\sqrt{s^2+(1/l^2)}}\right)A(s)}{\left(e^{sh}-\theta^{*}e^{-h\sqrt{s^2+(1/l^2)}}-\theta^{*}\beta^{*}e^{h\sqrt{s^2+(1/l^2)}}\right)}=e^{(4)} \qquad (6.54b)$$

So, $B(s)$ and $D(s)$, in terms of $A(s)$ are written as;

$$B(s)=\left(\gamma^{*}+\theta^{*}e^{(4)}\right)A(s) \qquad (6.55)$$

$$D(s)=\left(\alpha^{*}+\beta^{*}\left(\gamma^{*}+\theta^{*}e^{(4)}\right)\right)A(s) \qquad (6.56)$$

Now in order to get the dual integral equations let $A(s)=G(s)/(1-e^{-2sh})$, so from Eqs. (6.54a), (6.55) and (6.56) we get $C(s)=-e^{(4)}G(s)/(1-e^{-2sh})$, $B(s)=(\gamma^{*}+\theta^{*}e^{(4)})G(s)/(1-e^{-2sh})$ and $D(s)=(\alpha^{*}+\beta^{*}(\gamma^{*}+\theta^{*}e^{(4)}))G(s)/(1-e^{-2sh})$. Here $G(s)$ is an unknown function. The dual integral equations may be obtained similar to the previous sections as;

$$\int_0^{\infty}E(s)\cos(sx)ds=0, \text{ here } E(s)=P^{(4)}G(s) \qquad (6.57)$$

here $E(s)=P^{(4)}G(s)$ and

$$\int_0^\infty sF_{cg'}(s)E(s)\cos(sx)ds = \frac{\tau_1\pi}{2G} \tag{6.58}$$

where

$$P^{(4)} = \frac{1}{1-e^{-2sh}}\left(1-e^{-2sh}+e^{-2sh}+\alpha^*+\left(1+\beta^*\right)\left(\gamma^*+\theta^* e^{(4)}\right)-e^{(4)}\right) \tag{6.59}$$

$$F_{cg'}(s) = \frac{\left(1+e^{-2sh}+e^{(4)}-e^{-2sh}\right)}{P^{(4)}\left(1-e^{-2sh}\right)} \tag{6.60}$$

As l and l' approach zero, the term $e^{-2sh}+\alpha+(1+\beta)\left(\gamma+\theta e^{(4)}\right)-e^{(4)}$ also approaches zero and hence $P^{(4)}$ will reduce to 1. Moreover, "cg'" in subscript represents the "clamped boundaries & gradient ($l' \neq 0$)" case. When l and l' approach zero, $P^{(4)}$ given by Eq. (6.59) and ($e^{(4)}$ - e^{-2sh}) approach to 1 and zero, respectively. Hence, $F_{cg'}(s)$ will reduce to the classical case (see section 2.7.2).

6.8 A solution of the dual integral equation

The dual integral equations presented in the previous section are treated with the method of Copson (1961) to give; $E(s) = (\pi\tau_1 a^2/2G)\int_0^1 \sqrt{\xi}\Omega(\xi)J_o(sa\xi)\mathrm{d}\xi$ (Here J_o is the Bessel function of the first kind of order zero), such that the Fredholm integral equation is obtained;

$$\Omega(\xi) + \int_0^1 \Omega(\eta)L(\xi,\eta)\mathrm{d}\eta = \sqrt{\xi}, \qquad 0 \le \xi \le 1, \tag{6.61}$$

Solving for $\Omega(\xi)$ (unknown function to be determined) and $L(\xi,\eta)$ (kernel) takes the form;

$$L(\xi,\eta) = \sqrt{\xi\eta}\int_0^\infty s\left[F\left(\frac{s}{a}\right)-1\right]J_o(s\xi)J_o(s\eta)\mathrm{d}s, \qquad 0 \le \xi,\eta \le 1, \tag{6.62}$$

The details of this method may be found in the work of Copson (1961) and Sih and Chen (1981). The Fredholm integral equation (Eq. (6.61)) is solved by the Matlab code Fie, in which the kernel is taken to be moderately smooth in [*a*, *b*] x [*a*, *b*] and also smooth on the diagonal. Here *a* and *b* are the lower and upper limits of the integral in Eq. (6.61) i.e. 0 and 1, respectively. More description related to different types of kernels with relevant examples can be seen in the work of Atkinson (2008). For the kernel to be smooth it must be infinitely differentiable with respect to its variables i.e. ξ and η. Moreover, the term $\int_0^\infty s[F(s/a)-1]J_o(s\xi)J_o(s\eta)\mathrm{d}s$ in Eq. (6.62) is a smooth function of ξ and η but the multiplication of the term $\sqrt{\xi\eta}$ means the kernel function $L(\xi,\eta)$ will have a square root singularity. This effects the approximation of the integral at 1. Therefore, the change of variables in the integral equation is done as follows. Let $\xi = x^2$, $\eta = y^2$ such that $0 \leq x, y \leq 1$, introducing the new unknown function $W(x) = \Omega(x^2)$, Eq. (6.61) may be written as;

$$W(x) + \int_0^1 W(y)K(x,y)\mathrm{d}y = x, \qquad 0 \leq x \leq 1 \tag{6.63}$$

The kernel now has the form;

$$K(x,y) = 2yL_3(x^2, y^2), \qquad 0 \leq x, y \leq 1 \tag{6.64}$$

$$L_3(x^2, y^2) = xy\int_0^\infty s\left[F_3(\frac{s}{a}) - 1\right]J_o(sx^2)J_o(sy^2)\mathrm{d}s, \qquad 0 \leq x, y \leq 1 \tag{6.65}$$

The kernel formula Eq. (6.64) is infinitely differentiable in terms of *x* and *y*. The integrand Eq. (6.63) is better behaved than in Eq. (6.61); it can be more easily approximated by numerical integration, which is at the heart of the program Fie. The

evaluation of $W(1) = \Omega(1)$ is obtained, which is the normalized stress intensity factor at crack tip given by the following relation;

$$K_{III} = \Omega(1)\tau_1\sqrt{a} \tag{6.66}$$

where K_{III} is the mode III stress intensity factor at the crack tip, τ_1 and a are the applied stress on crack surface and half crack length respectively. Moreover, the Gauss-Laguerre quadrature method is used to solve the term $\int_0^\infty s[F(s/a)-1]J_o(s\xi)J_o(s\eta)ds$ which is given as;

$$\int_0^\infty f(x)dx = \sum_{i=1}^{n} A_i \exp(x_i) f(x_i) \tag{6.67}$$

where x_i and $A_i\exp(x_i)$ are the nodes and weights, respectively. The parameters x_i and A_i are chosen such that for any n the rule is exact for polynomials up to and including degree $2n$-1. More information on this method and the way it can be implemented in Matlab may be seen in the reference (Lindfield and Penny, 2012).

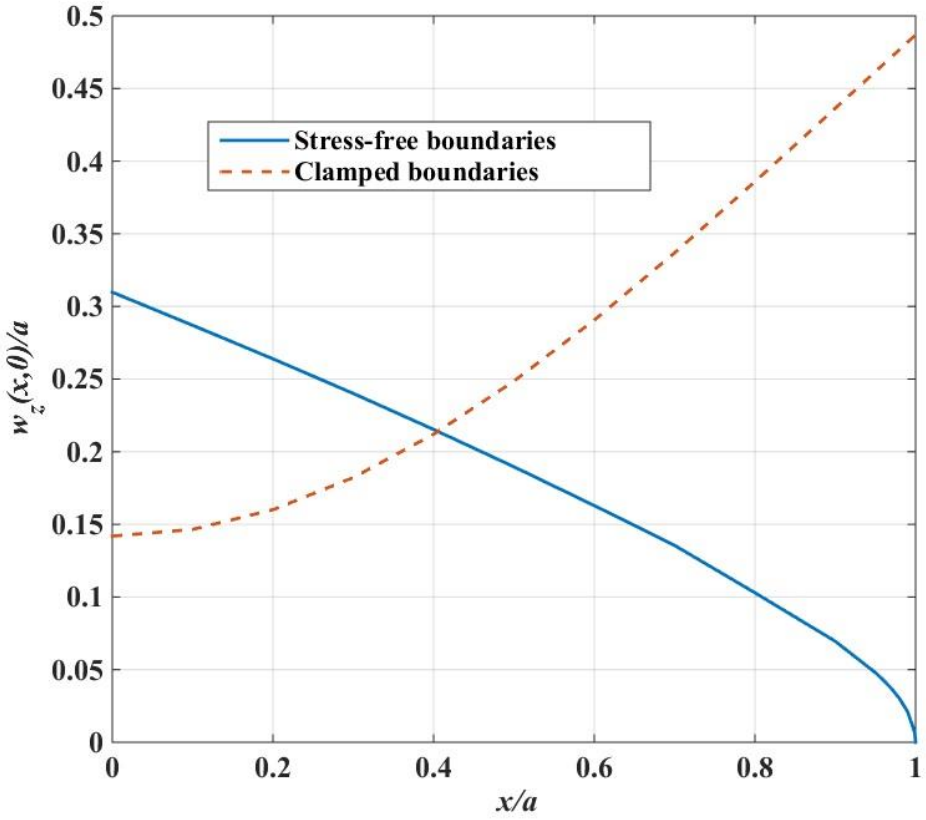

Figure 6.1Normalized quarter crack displacement profile for *h*/*a* = 2

6.9 Results and Discussion

Firstly, the quarter crack displacement profile with different types of boundary conditions i.e. stress-free boundaries and clamped boundaries are evaluated and compared in Fig. 6.1. Here *h*/*a* is taken as 2, where *h* and *a* are the half layer thickness and the half crack length respectively (see Fig. 2.4). With the stress-free boundaries, it may be seen from Fig. 6.1that the displacement decreases along the crack and approaches zero near its tip. On the other hand, with clamped boundaries, the maximum displacement occurs at the crack tip. For further results, the value of *n* in Gauss-Laguerre quadrature method is chosen based on a convergence study conducted for the classical case subjected to stress-free boundaries. The plot of normalized stress intensity factor at the crack tip i.e. $W(1) = \Omega(1) = K_{\text{III}} / \tau_1 \sqrt{a}$ versus *n* is plotted in Fig. 6.2. It is apparent from Fig. 6.2 that the value of $K_{\text{III}} / \tau_1 \sqrt{a}$ is identical from *n* =12 onwards.

These results are compared with the results provided by Sih and Chen (1981) and they are both shown to be in good agreement. Therefore, in accordance with other numerical results n =14 is taken throughout this study. In order to demonstrate the strain gradient effect, it is considered necessary to evaluate the classical results as a benchmark for both types of boundary conditions i.e. stress-free and clamped boundaries. Therefore, in Fig. 6.3, the normalized stress intensity factor at the crack tip is plotted as a function of "layer height to crack length"(h/a) ratio. It is clear from Fig. 6.3 $K_{\mathrm{III}} / \tau_1 \sqrt{a}$ to be decreasing with increasing h/a for stress-free boundaries, while this is completely the opposite in the case of clamped boundaries. This behaviour is expected if one analyzes the $F(s)$ function for both cases (see section 2.7). The difference between the crack tip stress intensity factors for both types of boundary conditions is greater for smaller layer height and it diminishes as the height of the layer is increased. Moreover, the stress intensity factor is shown to approach 1 from h/a = 5 onwards for both types of boundary conditions.

Secondly, the results are evaluated for strain gradient models. Here, only the volumetric strain gradient effect, represented by the material parameter l (volumetric strain gradient material characteristic length), is considered (surface strain gradient is considered as zero i.e. $l' = 0$). The stress intensity factors at the crack tip for different l/a versus h/a are plotted in Fig. 6.4 (for stress-free boundaries) and Fig. 6.5 (for clamped boundaries). It is clear from Figs. 6.4 and 6.5 that stress intensity factors decrease as l/a increases and vice versa. This may alternatively be defined as crack stiffening when compared with the classical case, with increasing l. The stiffening effect is evident for both stress-free and clamped boundary conditions. Moreover, it is apparent that results are closer to the classical ones when l leads to 0. This may also be explained if one examines $P^{(1)}$ given in Eq. (6.18) and $F_{sg}(s)$ given in Eq. (6.22) that if l approaches 0,

$P^{(1)}$ approaches 1 and, hence, $F_{sg}(s)$ will reduce to the classical case. The same explanation applies to clamped boundaries from Eqs.(6.34) and (6.35).

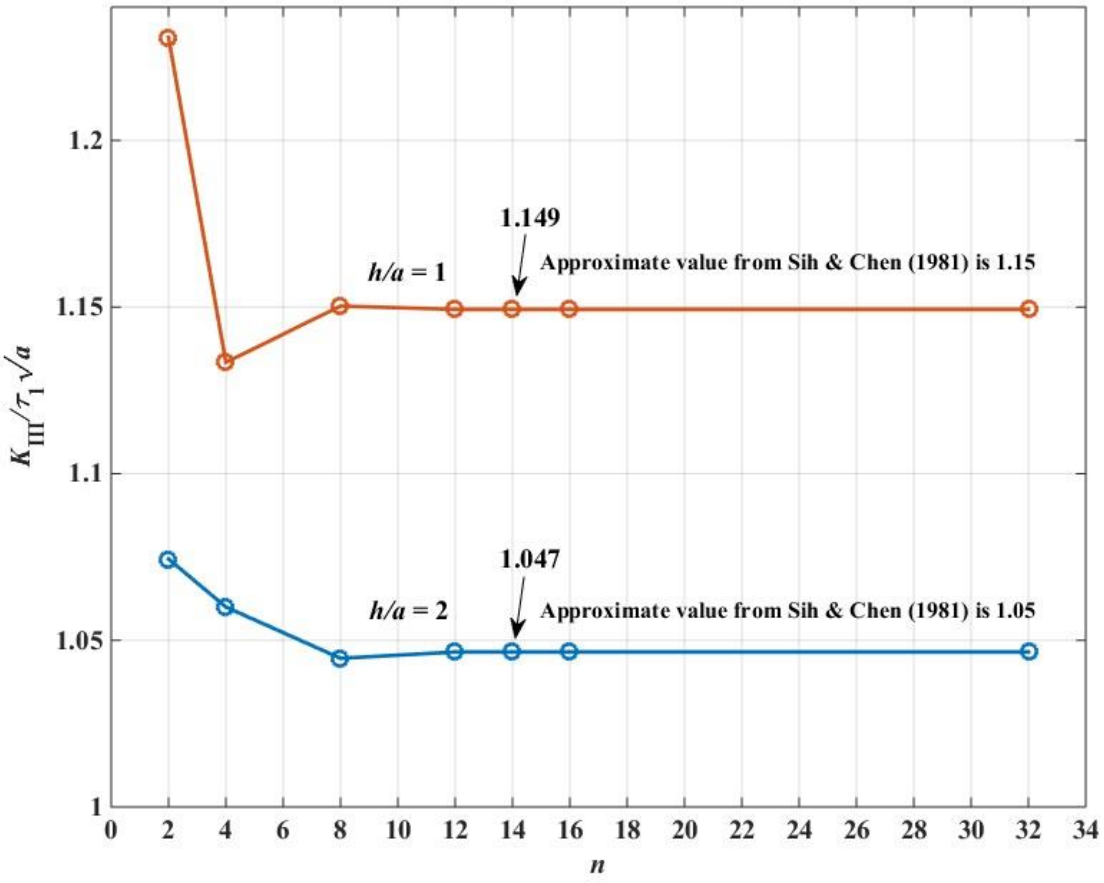

Figure 6.2 Convergence study to get optimum *n* for Gauss- Laguerre quadrature method while comparison with the results provided by Sih and Chen (1981) is made

Finally, stress intensity factors with both volumetric and surface strain gradient (represented as l and$l^{'}$) are presented in Figs. 6.6 and 6.7 for stress-free and clamped boundaries, respectively. It should be mentioned from the energy consideration that the material constant $l^{'}$ may assume positive as well as negative values (Vardoulakis et al., 1996). Therefore, the results are presented for both positive and negative surface strain gradient material parameter $l^{'}$ while maintaining the volumetric strain gradient material parameter l as constant. Results are plotted with h/a = 1 and 2 for comparison purposes. It may be seen from Figs. 6.6 and 6.7 that the crack stiffening effect becomes significant as $l^{'}$ increases in the domain [0, l]. On the other hand, negative $l^{'}$ leads to more

"compliant" crack, which in general, in order to observe experimental data, is a desirable property of the mathematical model (Paulino et al., 2003; Vardoulakis et al., 1996). Overall, it may fairly be concluded that the effect of volumetric strain gradient is more prominent as compared to the surface strain gradient.

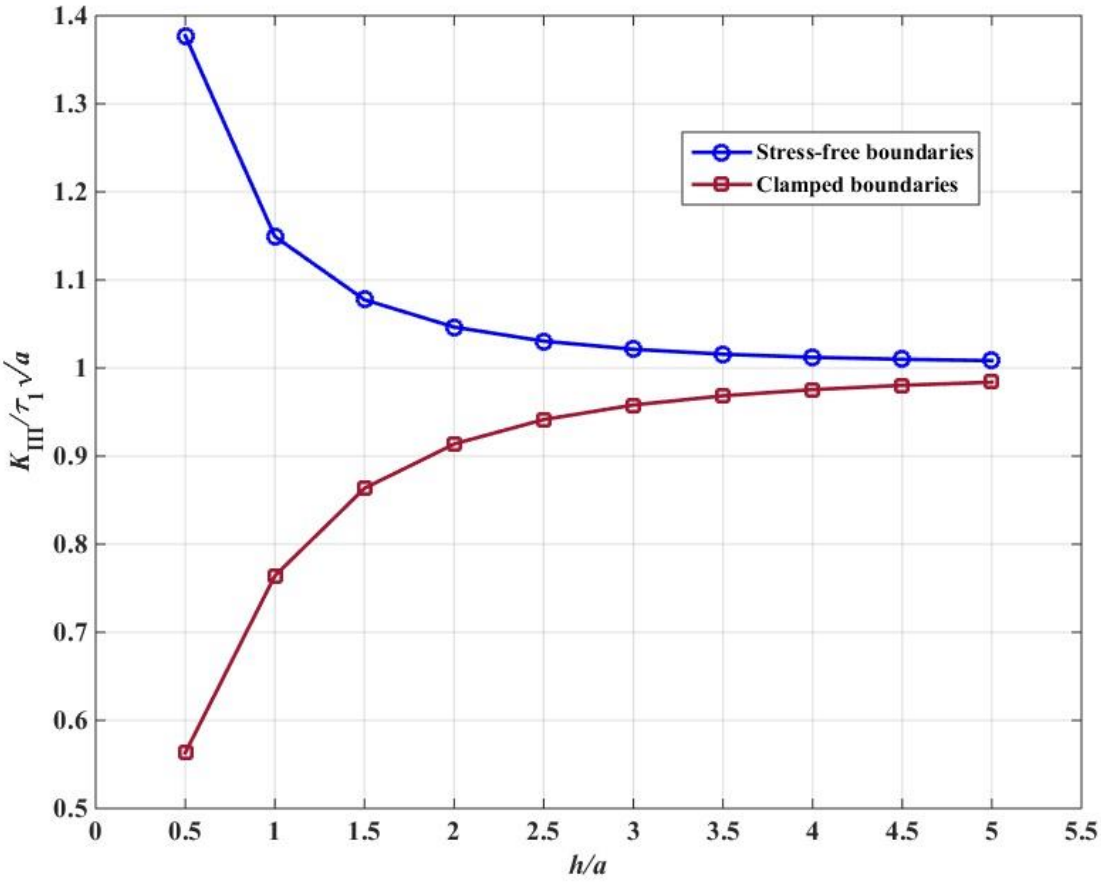

Figure 6.3Normalized stress intensity factor as a function of layer height to crack length for classical models

6.10 Summary

Theoretical framework and corresponding computational strategy to solve anti-plane cracked material layer of finite height using strain gradient elasticity theory are presented in this paper. Both volumetric and surface gradient material parameters i.e. l and l' are considered in this article. Two types of boundary conditions i.e. stress-free and clamped boundaries are studied in this paper. The solution of each problem is discussed separately and reduced to the dual integral equations. Resulting Fredholm integral

equation is solved numerically in which the kernel (an improper integral that ranges from 0 to infinity) of the second kind is solved by using Gauss-Laguerre quadrature to evaluate crack tip stress intensity factors. Classical results under stress-free boundary condition are obtained and compared with the available literature for benchmarking. Next, the results for strain gradient models are evaluated and plotted. Incorporation of volumetric strain gradient effect increases crack stiffness by reducing the stress intensity factor, demonstrating pronounced size effect at a smaller scale. Furthermore, from energy consideration, both positive and negative surface strain effects are considered in the following results by maintaining the volumetric strain gradient material parameter as constant. Positive surface gradient effect stiffened crack while negative surface gradient leads to a more compliant crack. Potential extension of this work is investigating the stress intensity factors for the finite width problem.

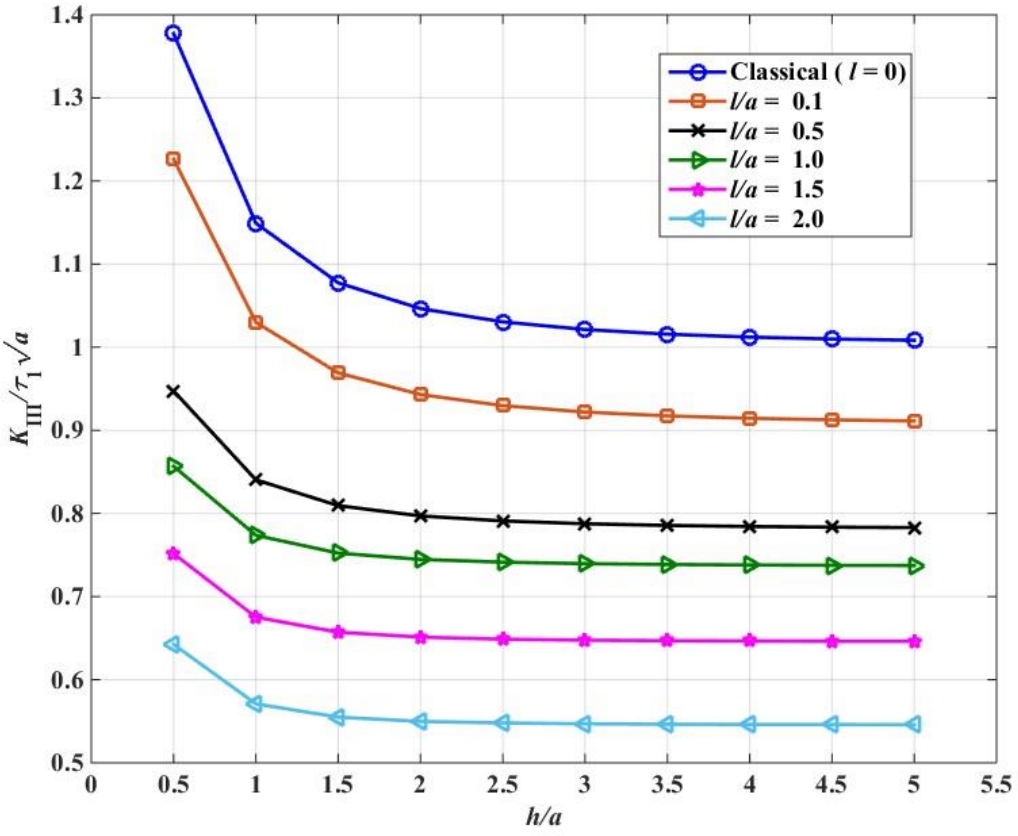

Figure 6.4 Normalized stress intensity factor as a function of layer height to crack length for Strain gradient models (without surface gradient effect) with stress-free boundaries

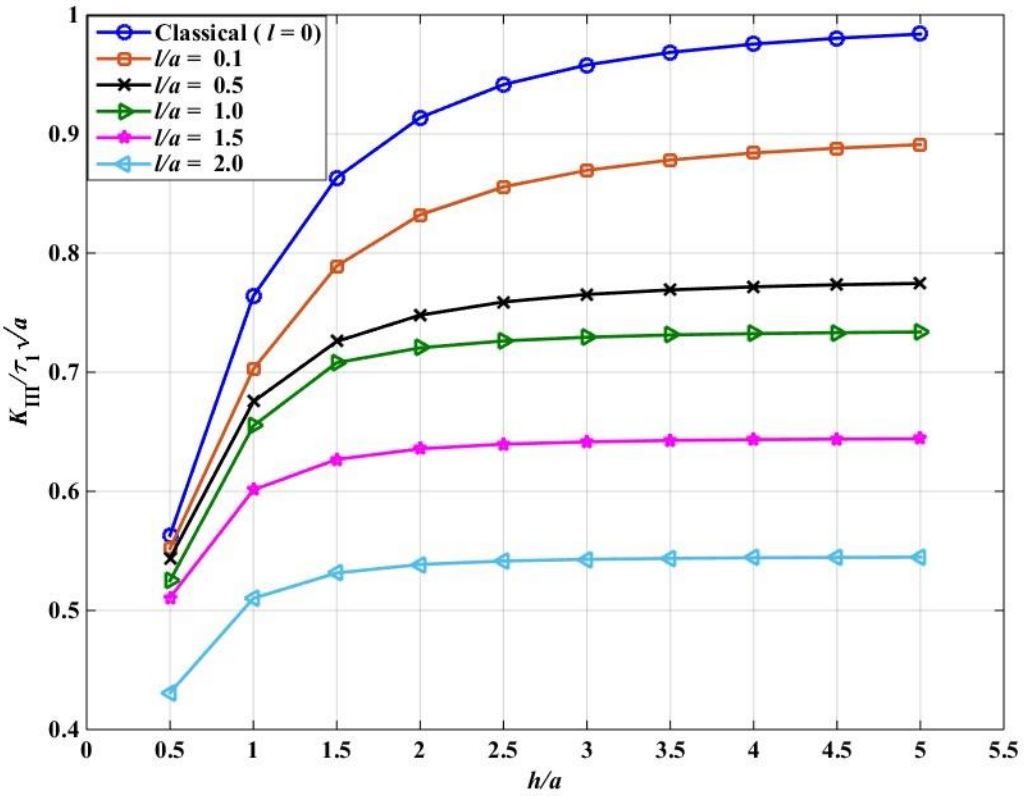

Figure 6.5 Normalized stress intensity factor as a function of layer height to crack length for Strain gradient elastic models (without surface gradient effect) with clamped boundaries

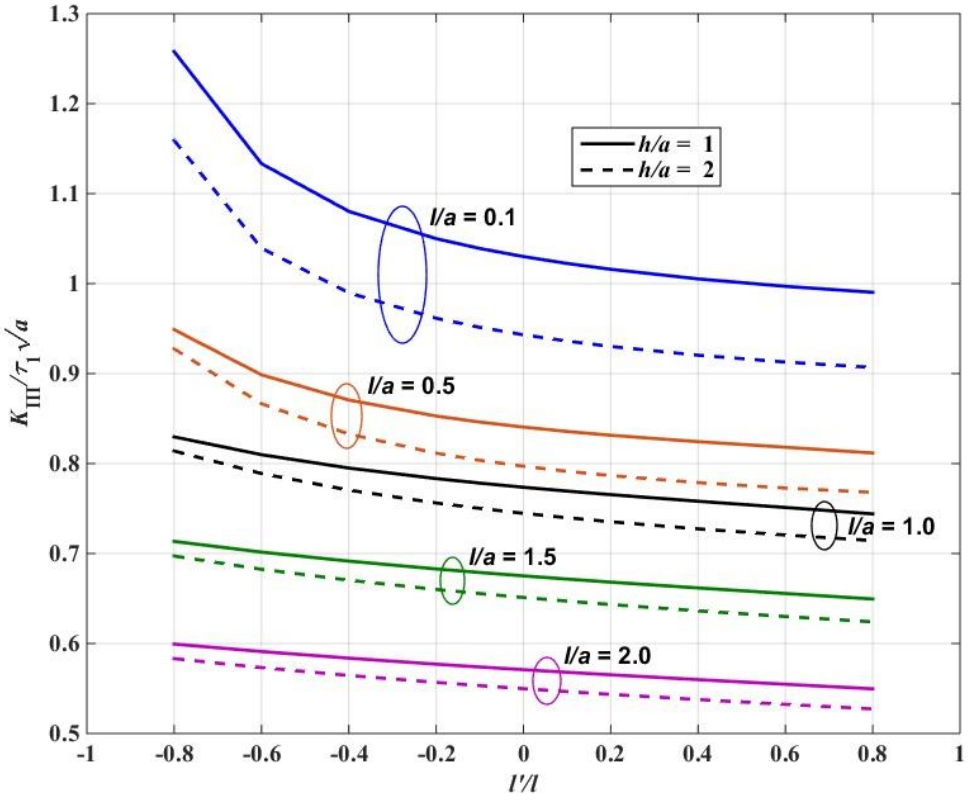

Figure 6.6 Normalized stress intensity factor as a function of layer height to crack length for Strain gradient elastic models (with surface gradient effect) with stress-free boundaries

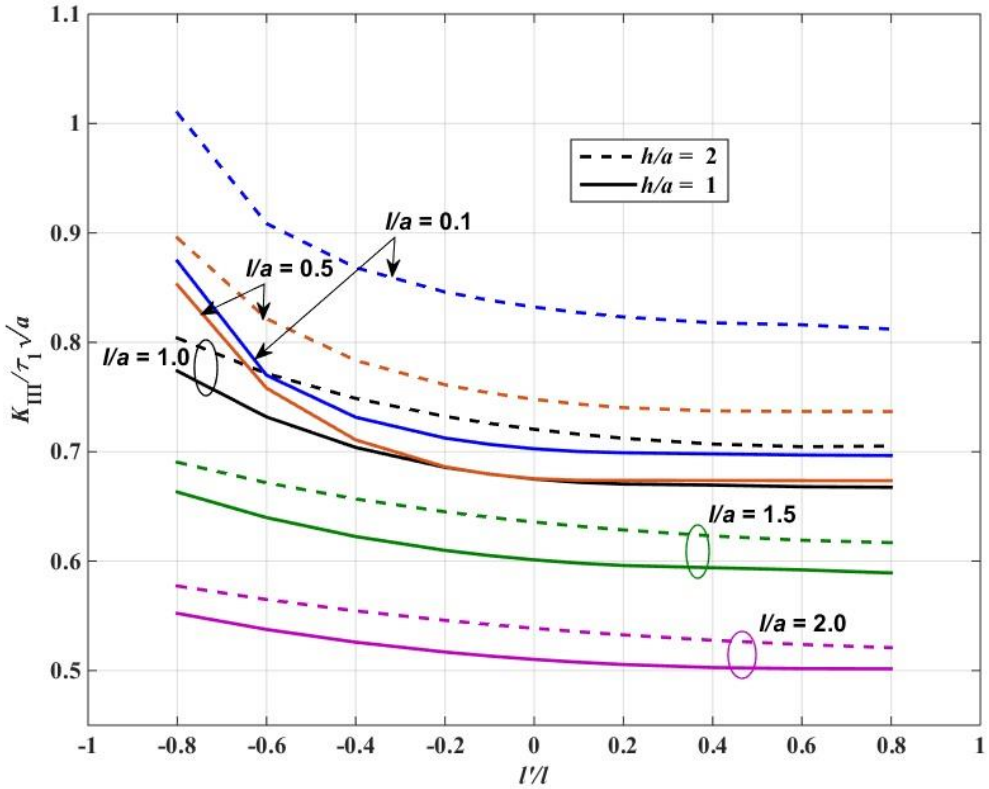

Figure 6.7 Normalized stress intensity factor as a function of layer height to crack length for Strain gradient elastic models (with surface gradient effect) with clamped boundaries

References

Aifantis, E., 2016. Chapter One-Internal Length Gradient (ILG) Material Mechanics Across Scales and Disciplines. *Advances in Applied Mechanics*, 49, 1-110.

Aifantis, E. C., 1992. On the role of gradients in the localization of deformation and fracture. *International Journal of Engineering Science*, 30, 1279-1299.

Aifantis, E. C., 1999. Strain gradient interpretation of size effects. *International Journal of Fracture*, 95, 299-314.

Aifantis, E. C., 2003. Update on a class of gradient theories. *Mechanics of Materials*, 35, 259-280.

Aifantis, E. C., 2011. A note on gradient elasticity and nonsingular crack fields. *Journal of the Mechanical Behaviour of Biomedical Materials*, 20, 103-105.

Atkinson, K., & Shampine, L., 2007. Solving Fredholm integral equations of the second kind in MATLAB. *ACM Transactions on Mathematical Software* 34 (4)

Chan, Y. S., Paulino, G. H., & Fannjiang, A. C., 2008. Gradient elasticity theory for mode III fracture in functionally graded materials-part II: crack parallel to the material gradation. *Journal of Applied Mechanics*, 75, 061015.

Copson, E., 1961. On certain dual integral equations. Paper presented at the Proc. Glasgow Math. Assoc.

Eringen, A. C., & Edelen, D., 1972. On nonlocal elasticity. *International Journal of Engineering Science*, 10, 233-248.

Exadaktylos, G. E. & Vardoulakis, I., 2001. Microstructure in linear elasticity and scale effects: a reconsideration of basic rock mechanics and rock fracture mechanics. *Tectonophysics*, 335**,** 81-109.

Exadaktylos, G., 1998. Gradient elasticity with surface energy: Mode-I crack problem. *International Journal of Solids and Structures*, 35**,** 421-456.

Fannjiang, A. C., Paulino, G. H., & Chan, Y. S., 2002. Strain gradient elasticity for antiplane shear cracks: a hypersingular integrodifferential equation approach. *SIAM Journal on Applied Mathematics*, 62, 1066-1091.

Fleck, N., & Hutchinson, J., 1997. Strain gradient plasticity. *Advances in Applied Mechanics*, 33, 296-361.

Sih, G. C., & Chen, E. P., 1981. Mechanics of fracture Cracks in composite materials. The Netherlands: Martinus Nijhoff Publishers.

Giannakopoulos, A., & Stamoulis, K., 2007. Structural analysis of gradient elastic components. *International Journal of Solids and Structures*, 44, 3440-3451.

Joseph, R. P., Wang, B., & Samali, B., 2017. Size effects on double cantilever beam fracture mechanics specimen based on strain gradient theory. *Engineering Fracture Mechanics*, 169, 309-320.

Karimipour, I., & Fotuhi, A. R., 2017. Anti-plane analysis of an infinite plane with multiple cracks based on strain gradient theory. *Acta Mechanica*, 228, 1793-1817.

Lam, D. C., Yang, F., Chong, A., Wang, J., & Tong, P., 2003. Experiments and theory in strain gradient elasticity. *Journal of the Mechanics and Physics of Solids*, 51, 1477-1508.

Li, X. F. (2001). Closed-form solution for a mode-III interface crack between two bonded dissimilar elastic layers. *International Journal of Fracture*, 109, 3-8.

Lindfield, G., & Penny, J., 2012. Numerical methods: using MATLAB: Academic Press.

McFarland, A. W., & Colton, J. S., 2005. Role of material microstructure in plate stiffness with relevance to microcantilever sensors. *Journal of Micromechanics and Microengineering*, 15, 1060.

Mindlin, R. D., 1964. Micro-structure in linear elasticity. *Archive for Rational Mechanics and Analysis*, 16, 51-78.

Mindlin, R. D., 1965. Second gradient of strain and surface-tension in linear elasticity. *International Journal of Solids and Structures*, 1, 417-438.

Mousavi, S. M., & Aifantis, E., 2015. A note on dislocation-based mode III gradient elastic fracture mechanics. *Journal of the Mechanical Behaviour of Materials*, 24, 115-119.

Paulino, G., Fannjiang, A., & Chan, Y. S., 2003. Gradient elasticity theory for mode III fracture in functionally graded materials—part I: crack perpendicular to the material gradation. *Journal of Applied Mechanics*, 70, 531-542.

Polizzotto, C., 2016. A note on the higher order strain and stress tensors within deformation gradient elasticity theories: Physical interpretations and comparisons. *International Journal of Solids and Structures*, 90, 116-121.

Singh, B., & Moodie, T. B., 1981. Closed-form solutions for finite length crack moving in a strip under anti-plane shear stress. *Acta Mechanica*, 38, 99-109.

Tait, R., & Moodie, T. B., 1981. On a problem in the dynamic theory of cracks. *Quarterly of Applied Mathematics*, 39, 419-423.

Vardoulakis, I., Exadaktylos, G., & Aifantis, E., 1996. Gradient elasticity with surface energy: mode-III crack problem. *International Journal of Solids and Structures*, 33, 4531-4559.

Vardoulakis, I., & Sulem, J. (1995). Bifurcation analysis in geomechanics Blackie Academic and Professional Glasgow Google Scholar.

Wang, B. L., & Mai, Y. W., 2006. Closed-form solution for an antiplane interface crack between two dissimilar magnetoelectroelastic layers. *Journal of Applied Mechanics*, 73, 281-290.

Yang, F., 1997. Exact solution for a finite length crack in a strip under general antiplane loading. *International Journal of Fracture*, 87, L57-L64.

Yang, F., Chong, A., Lam, D. C. C., & Tong, P., 2002. Couple stress based strain gradient theory for elasticity. *International Journal of Solids and Structures*, 39, 2731-2743.

Chapter 7

SCALE-DEPENDENT PIEZOELECTRIC ANTI-PLANE CRACKED MATERIAL LAYER: A THEORETICAL FRAMEWORK

Relevance to the thesis

The aim of this chapter is to extend the theoretical formulations, as mentioned in the previous chapter, to the scale-dependent piezoelectric anti-plane cracked material layer. The scope of this chapter is limited to mathematical framework only and numerical results are not evaluated. The work presented in this chapter is expected to give useful insights to conduct numerical analysis in our future research goals.

7.1 Introduction

As briefly described in chapter 2, the flexoelectricity has found great interest among the researchers working in the field of nanotechnology. Majdoub et al. (2008a, 2008b) provided the theoretical framework of flexoelectricity and determined the size-dependent elastic behaviour of piezoelectric nanostructures. Since flexoelectricity can even be induced in non-piezoelectric materials, Fousek et al. (1999) proposed the piezoelectric nanocomposite even without using the piezoelectric material. As far as the anti-plane crack problem is concerned, Yang (2004) was the first one considered the electric field gradient (without strain gradient effect) to provide an analytical solution for a semi-infinite crack. Karlis et al. (2007) developed a 2D boundary element method to analyze a fracture mechanics problem in gradient elastic solids, which was further extended to cater 3D mechanics as well (Karlis et al., 2008). Very recently, the constitutive equations and in-plane fracture mechanics analysis in piezoelectric material is provided by Sladek et al. (2017) in which both strain gradient effect and electric field-strain gradient coupling are included.

Since, in many practical engineering applications, the specimen boundaries are finite and hence contribute significantly to its fracture behaviour. One such case is the cracked material layer with finite height (as mentioned in chapter 6). Therefore, in this chapter, the constitutive and governing equations of a scale-dependent anti-plane cracked piezoelectric material layer are provided. The mathematical framework sketched in this chapter is expected to give useful insights to conduct numerical analysis in our future research goals.

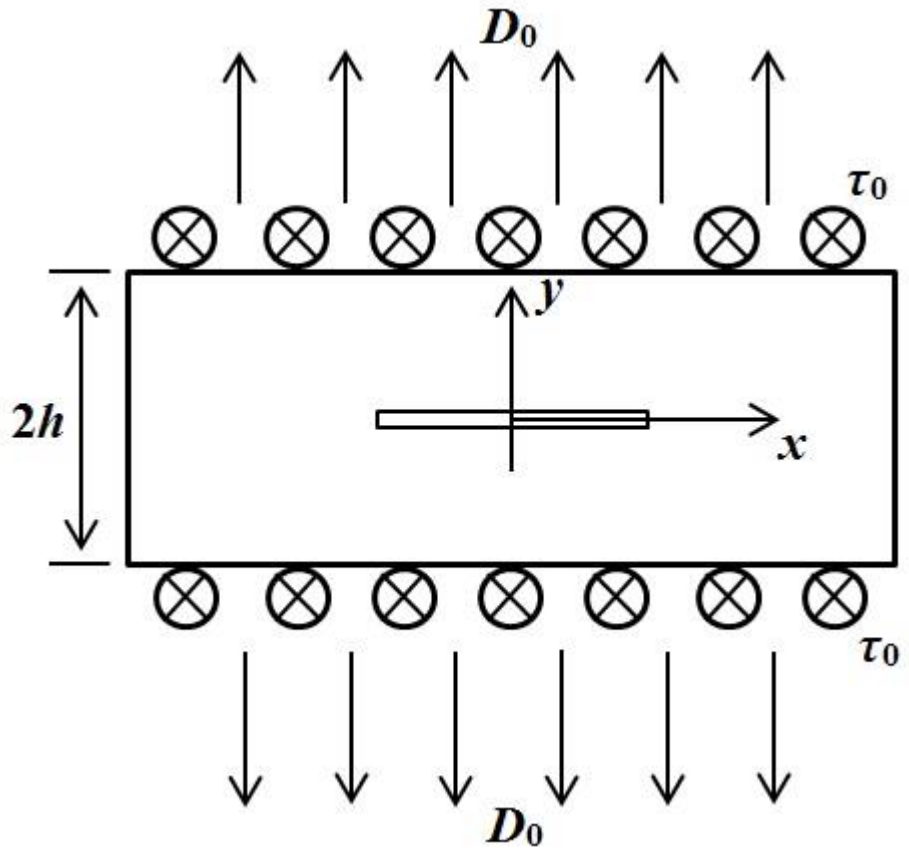

Figure 0.1 Schematic diagram of an anti-plane cracked piezoelectric material layer

7.2 Mathematical formulations (without surface gradient effect $l' = 0$)

The constitutive equations with the consideration of electric field-strain gradient coupling and pure non-local effect given as (Hu and Shen, 2009);

$$\tau_{ij} = c_{ijkl}\varepsilon_{kl} - e_{kij}E_k \tag{7.1}$$

$$\mu_{jkl} = -f_{ijkl}E_i + g_{jklmni}\kappa_{nmi} \tag{7.2}$$

$$D_k = a_{kl}E_l + e_{kij}\varepsilon_{ij} + f_{klmn}\kappa_{lmn} \tag{7.3}$$

Where c is the fourth order elastic constant tensor, e is the piezoelectric coefficient, f is the electric-field strain gradient coupling coefficient tensor, the tensor g represent the strain gradient elasticity effect and a is the material's permittivity second order tensor.

The symbols τ_{ij}, μ_{ijk} and D_i represent the Cauchy stress, higher order stress, and electric displacement component respectively. The indicial notation is employed in which the repeated indices represent summation and comma indicates differentiation with respect to the spatial variable. The strain ε_{ij} and strain gradient κ_{ijk} are related to the displacement u_i as; $\varepsilon_{ij} = (u_{i,j} + u_{j,i})/2$ and $\kappa_{ijk} = \varepsilon_{ij,k} = (u_{i,jk} + u_{j,ik})/2$ respectively. The schematic diagram of an anti-plane cracked piezoelectric material layer (τ_0 is the anti-plane shear stress) with in-plane electric displacement (D_0) is shown in Fig. 7.1; here subscript 0 represents the prescribed values. The constitutive equations in a compact form are given as;

$$\begin{bmatrix} \tau_{yz} \\ \tau_{xz} \end{bmatrix} = \begin{bmatrix} c_{44} & 0 \\ 0 & c_{44} \end{bmatrix} \begin{bmatrix} 2\varepsilon_{yz} \\ 2\varepsilon_{xz} \end{bmatrix} - \begin{bmatrix} 0 & e_{15} \\ e_{15} & 0 \end{bmatrix} \begin{bmatrix} E_x \\ E_y \end{bmatrix} \tag{7.4}$$

$$\begin{bmatrix} \mu_{yzx} \\ \mu_{xzx} \\ \mu_{yzy} \\ \mu_{xzy} \end{bmatrix} = -\begin{bmatrix} 0 & f_{15} \\ f_{15} & 0 \\ 0 & f_{15} \\ f_{15} & 0 \end{bmatrix} \begin{bmatrix} E_x \\ E_y \end{bmatrix} + \begin{bmatrix} g_{44} & 0 & 0 & 0 \\ 0 & g_{44} & 0 & 0 \\ 0 & 0 & g_{44} & 0 \\ 0 & 0 & 0 & g_{44} \end{bmatrix} \begin{bmatrix} 2\kappa_{yzx} \\ 2\kappa_{xzx} \\ 2\kappa_{yzy} \\ 2\kappa_{xzy} \end{bmatrix} \tag{7.5}$$

The higher order elastic parameter g_{11} is related to the conventional elastic stiffness coefficient c_{11} by a factor l which is known as internal length material parameter (Sladek et al., 2017; Xu and Shen, 2013). Similarly, the electric-field strain gradient coupling coefficient f_{31} is proportional to the conventional piezoelectric coefficient e_{31} by a scaling parameter m (Huang and Yu, 2006; Sladek et al., 2017). Following this, we can write Eq. (7.5) as follows;

$$\begin{bmatrix} \mu_{yzx} \\ \mu_{xzx} \\ \mu_{yzy} \\ \mu_{xzy} \end{bmatrix} = -m^2 \begin{bmatrix} 0 & e_{15} \\ e_{15} & 0 \\ 0 & e_{15} \\ e_{15} & 0 \end{bmatrix} \begin{bmatrix} E_x \\ E_y \end{bmatrix} + l^2 \begin{bmatrix} c_{44} & 0 & 0 & 0 \\ 0 & c_{44} & 0 & 0 \\ 0 & 0 & c_{44} & 0 \\ 0 & 0 & 0 & c_{44} \end{bmatrix} \begin{bmatrix} 2\kappa_{yzx} \\ 2\kappa_{xzx} \\ 2\kappa_{yzy} \\ 2\kappa_{xzy} \end{bmatrix} \tag{7.6}$$

On the other hand, the electric displacements in a compact form are;

$$\begin{bmatrix} D_x \\ D_y \end{bmatrix} = \begin{bmatrix} a_{11} & 0 \\ 0 & a_{22} \end{bmatrix} \begin{bmatrix} E_x \\ E_y \end{bmatrix} + \begin{bmatrix} 0 & e_{15} \\ e_{15} & 0 \end{bmatrix} \begin{bmatrix} 2\varepsilon_{yz} \\ 2\varepsilon_{xz} \end{bmatrix} + \begin{bmatrix} 0 & f_{15} & 0 & f_{15} \\ f_{15} & 0 & f_{15} & 0 \end{bmatrix} \begin{bmatrix} 2\kappa_{yzx} \\ 2\kappa_{xzx} \\ 2\kappa_{yzy} \\ 2\kappa_{xzy} \end{bmatrix} \quad (7.7)$$

Equation (7.7) may be written as;

$$\begin{bmatrix} D_x \\ D_y \end{bmatrix} = \begin{bmatrix} a_{11} & 0 \\ 0 & a_{22} \end{bmatrix} \begin{bmatrix} E_x \\ E_y \end{bmatrix} + \begin{bmatrix} 0 & e_{15} \\ e_{15} & 0 \end{bmatrix} \begin{bmatrix} 2\varepsilon_{yz} \\ 2\varepsilon_{xz} \end{bmatrix} + m^2 \begin{bmatrix} 0 & e_{15} & 0 & e_{15} \\ e_{15} & 0 & e_{15} & 0 \end{bmatrix} \begin{bmatrix} 2\kappa_{yzx} \\ 2\kappa_{xzx} \\ 2\kappa_{yzy} \\ 2\kappa_{xzy} \end{bmatrix} \quad (7.8)$$

Here $E_x = -\partial\varphi / dx$ and $E_y = -\partial\varphi / dy$. The total stresses σ_{xz} and σ_{yz}, considering a_{11}= a_{22} (Gao et al., 1997) are given as;

$$\sigma_{xz} = \tau_{xz} - \frac{\partial \mu_{xzx}}{\partial x} - \frac{\partial \mu_{xzy}}{\partial y},\ \sigma_{yz} = \tau_{yz} - \frac{\partial \mu_{yzx}}{\partial x} - \frac{\partial \mu_{yzy}}{\partial y} \quad (7.9)$$

Using Eqs. (7.4) and (7.5) we get;

$$\sigma_{xz} = c_{44}\frac{\partial w_z}{\partial x} + e_{15}\frac{\partial \varphi}{\partial x} - l^2 c_{44}\left[\frac{\partial^3 w_z}{\partial x^3} + \frac{\partial^3 w_z}{\partial x \partial y^2}\right] - m^2 e_{15}\left[\frac{\partial^2 \varphi}{\partial x^2} + \frac{\partial^2 \varphi}{\partial x \partial y}\right] \quad (7.10)$$

$$\sigma_{yz} = c_{44}\frac{\partial w_z}{\partial y} + e_{15}\frac{\partial \varphi}{\partial y} - l^2 c_{44}\left[\frac{\partial^3 w_z}{\partial x^2 \partial y} + \frac{\partial^3 w_z}{\partial y^3}\right] - m^2 e_{15}\left[\frac{\partial^2 \varphi}{\partial x \partial y} + \frac{\partial^2 \varphi}{\partial y^2}\right] \quad (7.11)$$

The equilibrium equation $(\partial\sigma_{xz} / \partial x) + (\partial\sigma_{yz} / \partial y) = 0$ with the aid of Eqs. (7.10) and (7.11) gives;

$$\begin{aligned} &c_{44}\left[\frac{\partial^2 w_z}{\partial x^2} + \frac{\partial^2 w_z}{\partial y^2}\right] - l^2 c_{44}\left[\frac{\partial^4 w_z}{\partial x^4} + \frac{\partial^4 w_z}{\partial y^4} + 2\frac{\partial^4 w_z}{\partial x^2 \partial y^2}\right] + e_{15}\left[\frac{\partial^2 \varphi}{\partial x^2} + \frac{\partial^2 \varphi}{\partial y^2}\right] - \\ &m^2 e_{15}\left[\frac{\partial^3 \varphi}{\partial x^3} + \frac{\partial^3 \varphi}{\partial x^2 \partial y} + \frac{\partial^3 \varphi}{\partial x \partial y^2} + \frac{\partial^3 \varphi}{\partial y^3}\right] = 0 \end{aligned} \quad (7.12)$$

or

$$c_{44}\nabla^2 w_z - l^2 c_{44}\nabla^4 w_z + e_{15}\left[1 - m^2\left[\frac{\partial}{\partial x} + \frac{\partial}{\partial y}\right]\right]\nabla^2\varphi = 0 \tag{7.13}$$

where $\nabla^2 = \partial^2/\partial x^2 + \partial^2/\partial y^2$

The second equilibrium equation $(\partial D_x/\partial x) + (\partial D_y/\partial y) = 0$ along with Eq. (7.7) gives;

$$-a_{11}\left[\frac{\partial^2\varphi}{\partial x^2} + \frac{\partial^2\varphi}{\partial y^2}\right] + e_{15}\left[\frac{\partial^2 w_z}{\partial x^2} + \frac{\partial^2 w_z}{\partial y^2}\right] + e_{15}m^2\left(\begin{array}{l}\dfrac{\partial^3 w_z}{\partial x^3} + \dfrac{\partial^3 w_z}{\partial y^3} + \\ \dfrac{\partial^3 w_z}{\partial x\partial y^2} + \dfrac{\partial^3 w_z}{\partial x^2\partial y}\end{array}\right) = 0 \tag{7.14}$$

or

$$\nabla^2\varphi = \frac{e_{15}}{a_{11}}\nabla^2 w_z\left[1 + m^2\left(\frac{\partial}{\partial x} + \frac{\partial}{\partial y}\right)\right] \tag{7.15}$$

Put (7.15) in (7.13) we get;

$$c_{44}\left[\nabla^2 w_z - l^2\nabla^4 w_z\right] + \frac{e_{15}^2}{a_{11}}\left[1 - m^2\left[\frac{\partial}{\partial x} + \frac{\partial}{\partial y}\right]\right]\nabla^2 w_z\left[1 + m^2\left(\frac{\partial}{\partial x} + \frac{\partial}{\partial y}\right)\right] = 0 \tag{7.16}$$

$$c_{44}\left[\nabla^2 w_z - l^2\nabla^4 w_z\right] + \frac{e_{15}^2}{a_{11}}\left[\begin{array}{l}\nabla^2 w_z + m^2\left(\dfrac{\partial}{\partial x} + \dfrac{\partial}{\partial y}\right)\nabla^2 w_z - \\ m^2\left(\dfrac{\partial}{\partial x} + \dfrac{\partial}{\partial y}\right)\nabla^2 w_z - m^4\left(\dfrac{\partial}{\partial x} + \dfrac{\partial}{\partial y}\right)^2\nabla^2 w_z\end{array}\right] = 0 \tag{7.17}$$

$$c_{44}\left[\nabla^2 w_z - l^2\nabla^4 w_z\right] + \frac{e_{15}^2}{a_{11}}\left[\nabla^2 w_z - m^4\left(\frac{\partial}{\partial x} + \frac{\partial}{\partial y}\right)^2\nabla^2 w_z\right] = 0 \tag{7.18}$$

$$c_{44}\left[\nabla^2 w_z - l^2\nabla^4 w_z\right] + \frac{e_{15}^2}{a_{11}}\left[\nabla^2 w_z - m^4\left(\frac{\partial^2}{\partial x^2} + \frac{\partial^2}{\partial y^2} + 2\left(\frac{\partial}{\partial x}\right)\left(\frac{\partial}{\partial y}\right)\right)\nabla^2 w_z\right] = 0 \tag{7.19}$$

$$c_{44}\left[\nabla^2 w_z - l^2\nabla^4 w_z\right] + \frac{e_{15}^2}{a_{11}}\left[\nabla^2 w_z - m^4\left(\nabla^4 w_z + 2\frac{\partial^4 w_z}{\partial x^3 \partial y} + 2\frac{\partial^4 w_z}{\partial x \partial y^3}\right)\right] = 0 \tag{7.20}$$

The Fourier transform in relation to Eq. (7.20) is defined as;

$$W(x,y) = \frac{1}{\sqrt{2\pi}}\int_{-\infty}^{\infty} w_z(s,y)e^{isx}ds \tag{7.21}$$

The inverse Fourier transform theorem gives;

$$w_z(x,y) = \frac{1}{\sqrt{2\pi}}\int_{-\infty}^{\infty} W(s,y)e^{-isx}ds \tag{7.22}$$

Considering each term in Eq. (7.20) and with the aid of Eq. (7.22) one gets;

$$\nabla^2 w_z = \frac{1}{\sqrt{2\pi}}\int_{-\infty}^{\infty}\left(-s^2 W(s,y) + \frac{\partial^2 W}{\partial y^2}\right)e^{-isx}ds \tag{7.23}$$

$$\nabla^4 w_z = \frac{1}{\sqrt{2\pi}}\int_{-\infty}^{\infty}\left(s^4 W(s,y) + \frac{\partial^4 W}{\partial y^4} - 2s^2\frac{\partial^2 W}{\partial y^2}\right)e^{-isx}ds \tag{7.24}$$

$$\frac{\partial^4 w_z}{\partial x^3 \partial y} = \frac{1}{\sqrt{2\pi}}\int_{-\infty}^{\infty} is^3 W(s,y)\frac{\partial W}{\partial y}e^{-isx}ds \tag{7.25}$$

$$\frac{\partial^4 w_z}{\partial x \partial y^3} = \frac{1}{\sqrt{2\pi}}\int_{-\infty}^{\infty} -is\frac{\partial^3 W}{\partial y^3}e^{-isx}ds \tag{7.26}$$

On putting Eq. (7.23) to (7.26) in Eq. (7.20) we get;

$$\begin{bmatrix} -\left(c_{44}l^2 + m^4 e_{15}^2/a_{11}\right)\dfrac{d^4}{dy^4} + i\left(2m^4 e_{15}^2/a_{11}\right)s\dfrac{d^3}{dy^3} + \\ \left(c_{44} + 2c_{44}s^2l^2 + e_{15}^2/a_{11} + 2s^2m^4 e_{15}^2/a_{11}\right)\dfrac{d^2}{dy^2} \\ -i\left(2m^4 e_{15}^2/a_{11}\right)s^3\dfrac{d}{dy} - \left(s^2c_{44} + c_{44}s^4l^2 + s^2 e_{15}^2/a_{11} + s^4m^4 e_{15}^2/a_{11}\right) \end{bmatrix} W = 0 \tag{7.27}$$

let $\lambda = d/dy$ so the characteristic equation from Eq. (7.27) can be written as;

$$\begin{aligned}&-\left(c_{44}l^2 + m^4 e_{15}^2/a_{11}\right)\lambda^4 + i\left(2m^4 e_{15}^2/a_{11}\right)s\lambda^3 + \\ &\left(c_{44} + 2c_{44}s^2l^2 + e_{15}^2/a_{11} + 2s^2m^4e_{15}^2/a_{11}\right)\lambda^2 - i\left(2m^4e_{15}^2/a_{11}\right)s^3\lambda - \\ &\left(s^2c_{44} + c_{44}s^4l^2 + s^2e_{15}^2/a_{11} + s^4m^4e_{15}^2/a_{11}\right) = 0\end{aligned} \tag{7.28}$$

if only the flexoelectric effect is considered, then Eq. (7.28) is reduced to;

$$\begin{aligned}&-m^4e_{15}^2/a_{11}\lambda^4 + i\left(2m^4e_{15}^2/a_{11}\right)s\lambda^3 + \left(c_{44} + e_{15}^2/a_{11} + 2s^2m^4e_{15}^2/a_{11}\right)\lambda^2 \\ &-i\left(2m^4e_{15}^2/a_{11}\right)s^3\lambda - \left(s^2c_{44} + s^2e_{15}^2/a_{11} + s^4m^4e_{15}^2/a_{11}\right) = 0\end{aligned} \tag{7.29}$$

In another case, if only the strain gradient effect is considered, the Eq. (7.28) is reduced as;

$$-c_{44}l^2\lambda^4 + \left(c_{44} + 2c_{44}s^2l^2 + e_{15}^2/a_{11}\right)\lambda^2 - \left(s^2c_{44} + c_{44}s^4l^2 + s^2e_{15}^2/a_{11}\right) = 0 \tag{7.30}$$

In order to simplify Eq. (7.30) let us assume $\sqrt{l} = m$, so Eq. (7.30) can be written as;

$$\begin{aligned}&-\left(c_{44} + e_{15}^2/a_{11}\right)l^2\lambda^4 + i\left(2l^2e_{15}^2/a_{11}\right)s\lambda^3 + \left(c_{44} + e_{15}^2/a_{11} + 2s^2l^2\left(c_{44} + e_{15}^2/a_{11}\right)\right)\lambda^2 \\ &-i\left(2l^2e_{15}^2/a_{11}\right)s^3\lambda - \left(s^2\left(c_{44} + e_{15}^2/a_{11}\right) + s^4l^2\left(c_{44} + e_{15}^2/a_{11}\right)\right) = 0\end{aligned} \tag{7.31}$$

Or

$$l^2\lambda^4 - 2i\gamma s\lambda^3 - \left(1 + 2s^2l^2\right)\lambda^2 + 2i\gamma s^3\lambda + \left(s^2 + s^4l^2\right) = 0 \tag{7.32}$$

where $\gamma = \dfrac{e_{15}^2}{a_{11}c_{44} + e_{15}^2}$

Roots of Eq. (7.32) i.e. λ_1, λ_2, $\lambda_3$andλ_4 would give the displacement w_z as following;

$$w_z(x, y) = \frac{2}{\pi}\int_0^\infty \left[A(s)e^{\lambda_1 y} + B(s)e^{\lambda_2 y} + C(s)e^{\lambda_3 y} + D(s)e^{\lambda_4 y}\right]\cos(sx)\mathrm{d}s \tag{7.33}$$

where$A(s)$, $B(s)$, $C(s)$ and $D(s)$ are the constants to be determined from the boundary conditions. The solution of Eq. (7.32) gives the following roots;

$$\lambda_1 = -s\,,\ \lambda_3 = s \tag{7.34a}$$

$$\lambda_2 = \frac{\sqrt{\begin{matrix}a_{11}^2c_{44}^2s^2l^4 + a_{11}^2c_{44}^2l^2 + 2a_{11}c_{44}e_{15}^2l^2m^4s^2 + \\ a_{11}c_{44}e_{15}^2l^2 + a_{11}c_{44}e_{15}^2m^4 + e_{15}^4m^4\end{matrix}} + e_{15}^2m^4si}{e_{15}^2m^4 + a_{11}c_{44}l^2} \tag{8.34b}$$

$$\lambda_4 = \frac{-\sqrt{\begin{matrix}a_{11}^2c_{44}^2s^2l^4 + a_{11}^2c_{44}^2l^2 + 2a_{11}c_{44}e_{15}^2l^2m^4s^2 + \\ a_{11}c_{44}e_{15}^2l^2 + a_{11}c_{44}e_{15}^2m^4 + e_{15}^4m^4\end{matrix}} + e_{15}^2m^4si}{e_{15}^2m^4 + a_{11}c_{44}l^2} \tag{7.34c}$$

It is to be noted that in case of non-flexoelectric material, the roots converge to that of typical isotropic material i.e. $\lambda_1 = -s\,,\ \lambda_3 = s\,, \lambda_2 = -\frac{\sqrt{1+s^2l^2}}{l}$ and $\lambda_4 = \frac{\sqrt{1+s^2l^2}}{l}$ as provided by (Vardoulakis et al., 1996). Also, let us assume the electric potential and displacement is correlated using the following function;

$$\psi = \varphi - \frac{e_{15}}{a_{11}}w_z - \frac{m^2e_{15}}{a_{11}}\left(\frac{\partial}{\partial x} + \frac{\partial}{\partial y}\right)w_z \tag{7.35}$$

The electric potential with the aid of Eq. (7.35) and Eq. (7.15) is given as;

$$\begin{aligned}\varphi(x,y) = {} & \frac{2}{\pi}\int_0^\infty \left[P_1(s)e^{-sy} + P_2(s)e^{sy}\right]\cos(sx)ds + \\ & \frac{2e_{15}}{\pi a_{11}}\int_0^\infty \left[A(s)e^{\lambda_1 y} + B(s)e^{\lambda_2 y} + C(s)e^{\lambda_3 y} + D(s)e^{\lambda_4 y}\right]\cos(\mathrm{sx})\mathrm{d}s - \\ & \frac{2m^2e_{15}}{\pi a_{11}}\left[\begin{matrix}\int_0^\infty \left[A(s)e^{\lambda_1 y} + B(s)e^{\lambda_2 y} + C(s)e^{\lambda_3 y} + D(s)e^{\lambda_4 y}\right]\sin(\mathrm{sx})\mathrm{d}s - \\ \int_0^\infty \left[\lambda_1 A(s)e^{\lambda_1 y} + \lambda_2 B(s)e^{\lambda_2 y} + \lambda_3 C(s)e^{\lambda_3 y} + \lambda_4 D(s)e^{\lambda_4 y}\right]\cos(\mathrm{sx})\mathrm{d}s\end{matrix}\right]\end{aligned} \tag{7.36}$$

7.3 Mathematical formulations (with surface gradient effect $l^{'} \neq 0$)

The tensor for the double stress with the consideration of surface gradient effect may be written as;

$$\begin{bmatrix} \mu_{yzx} \\ \mu_{xzx} \\ \mu_{yzy} \\ \mu_{xzy} \end{bmatrix} = -\begin{bmatrix} 0 & f_{15} \\ f_{15} & 0 \\ 0 & f_{15} \\ f_{15} & 0 \end{bmatrix} \begin{bmatrix} E_x \\ E_y \end{bmatrix} + \begin{bmatrix} g_{44} & 0 & 0 & 0 \\ 0 & g_{44} & 0 & 0 \\ 0 & 0 & g_{44} & 0 \\ 0 & 0 & 0 & g_{44} \end{bmatrix} \begin{bmatrix} 2\kappa_{yzx} \\ 2\kappa_{xzx} \\ 2\kappa_{yzy} \\ 2\kappa_{xzy} \end{bmatrix} - \begin{bmatrix} 0 & 0 \\ 0 & 0 \\ r_{44} & 0 \\ 0 & r_{44} \end{bmatrix} \begin{bmatrix} 2\varepsilon_{yz} \\ 2\varepsilon_{xz} \end{bmatrix} \quad (7.37)$$

The higher order elastic parameter r_{44} is related to the conventional elastic stiffness coefficient c_{11} by a factor $l^{'}$ which is known as the internal length material parameter for the surface. Equation (7.37) can then be written as;

$$\begin{bmatrix} \mu_{yzx} \\ \mu_{xzx} \\ \mu_{yzy} \\ \mu_{xzy} \end{bmatrix} = -m^2 \begin{bmatrix} 0 & e_{15} \\ e_{15} & 0 \\ 0 & e_{15} \\ e_{15} & 0 \end{bmatrix} \begin{bmatrix} E_x \\ E_y \end{bmatrix} + l^2 \begin{bmatrix} c_{44} & 0 & 0 & 0 \\ 0 & c_{44} & 0 & 0 \\ 0 & 0 & c_{44} & 0 \\ 0 & 0 & 0 & c_{44} \end{bmatrix} \begin{bmatrix} 2\kappa_{yzx} \\ 2\kappa_{xzx} \\ 2\kappa_{yzy} \\ 2\kappa_{xzy} \end{bmatrix} - l^{'} \begin{bmatrix} 0 & 0 \\ 0 & 0 \\ c_{44} & 0 \\ 0 & c_{44} \end{bmatrix} \begin{bmatrix} 2\varepsilon_{yz} \\ 2\varepsilon_{xz} \end{bmatrix} \quad (7.38)$$

Following the same method as in the previous section (7.2) we get the following equations for total stresses;

$$\sigma_{xz} = c_{44} \frac{\partial w_z}{\partial x} + e_{15} \frac{\partial \varphi}{\partial x} - l^2 c_{44} \left[\frac{\partial^3 w_z}{\partial x^3} + \frac{\partial^3 w_z}{\partial x \partial y^2} \right] - m^2 e_{15} \left[\frac{\partial^2 \varphi}{\partial x^2} + \frac{\partial^2 \varphi}{\partial x \partial y} \right] + l^{'} c_{44} \frac{\partial^2 w_z}{\partial x \partial y} \quad (7.39)$$

$$\sigma_{yz} = c_{44} \frac{\partial w_z}{\partial y} + e_{15} \frac{\partial \varphi}{\partial y} - l^2 c_{44} \left[\frac{\partial^3 w_z}{\partial x^2 \partial y} + \frac{\partial^3 w_z}{\partial y^3} \right] - m^2 e_{15} \left[\frac{\partial^2 \varphi}{\partial x \partial y} + \frac{\partial^2 \varphi}{\partial y^2} \right] + l^{'} c_{44} \frac{\partial^2 w_z}{\partial y^2} \quad (7.40)$$

The equilibrium equation $(\partial\sigma_{xz}/\partial x)+(\partial\sigma_{yz}/\partial y)=0$ gives;

$$c_{44}\nabla^2 w_z - l^2 c_{44}\nabla^4 w_z + e_{15}\nabla^2\varphi - m^2 e_{15}\left(\frac{\partial}{\partial x}+\frac{\partial}{\partial y}\right)\nabla^2\varphi + l' c_{44}\left(\frac{\partial}{\partial y}\right)\nabla^2 w_z = 0 \qquad (7.41)$$

From the second equilibrium equation $(\partial D_x/\partial x)+(\partial D_y/\partial y)=0$ we get

$$\begin{aligned} &-a_{11}\left[\frac{\partial^2\varphi}{\partial x^2}+\frac{\partial^2\varphi}{\partial y^2}\right]+e_{15}\left[\frac{\partial^2 w_z}{\partial x^2}+\frac{\partial^2 w_z}{\partial y^2}\right]+ \\ &e_{15}m^2\left(\frac{\partial^3 w_z}{\partial x^3}+\frac{\partial^3 w_z}{\partial y^3}+\frac{\partial^3 w_z}{\partial x\partial y^2}+\frac{\partial^3 w_z}{\partial x^2\partial y}\right)=0 \end{aligned} \qquad (7.42)$$

or

$$\nabla^2\varphi = \frac{e_{15}}{a_{11}}\nabla^2 w_z\left[1+m^2\left(\frac{\partial}{\partial x}+\frac{\partial}{\partial y}\right)\right] \qquad (7.43)$$

On Putting (7.43) in (7.41), we get

$$\begin{aligned} &c_{44}\left[\nabla^2 w_z - l^2\nabla^4 w_z + l'\frac{\partial}{\partial y}\nabla^2 w_z\right]+ \\ &\frac{e_{15}^2}{a_{11}}\left[\nabla^2 w_z - m^4\left(\nabla^4 w_z + 2\frac{\partial^4 w_z}{\partial x^3\partial y}+2\frac{\partial^4 w_z}{\partial x\partial y^3}\right)\right]=0 \end{aligned} \qquad (7.44)$$

Application of Fourier transform technique, similar to the one adopted in the previous section gives;

$$w_z(x,y) = \frac{1}{\sqrt{2\pi}}\int_{-\infty}^{\infty} W(s,y)e^{-isx}ds \qquad (7.45)$$

$$\nabla^2 w_z = \frac{1}{\sqrt{2\pi}}\int_{-\infty}^{\infty}\left(-s^2 W(s,y)+\frac{\partial^2 W}{\partial y^2}\right)e^{-isx}ds \qquad (7.46)$$

$$\frac{\partial}{\partial y}\nabla^2 w_z = \frac{1}{\sqrt{2\pi}}\int_{-\infty}^{\infty}\left(-s^2\frac{\partial W}{\partial y}+\frac{\partial^3 W}{\partial y^3}\right)e^{-isx}ds \qquad (7.47)$$

$$\nabla^4 w_z = \frac{1}{\sqrt{2\pi}} \int_{-\infty}^{\infty} \left(s^4 W(s,y) + \frac{\partial^4 W}{\partial y^4} - 2s^2 \frac{\partial^2 W}{\partial y^2} \right) e^{-isx} ds \tag{7.48}$$

$$\frac{\partial^4 w_z}{\partial x^3 \partial y} = \frac{1}{\sqrt{2\pi}} \int_{-\infty}^{\infty} is^3 W(s,y) \frac{\partial W}{\partial y} e^{-isx} ds \tag{7.49}$$

$$\frac{\partial^4 w_z}{\partial x \partial y^3} = \frac{1}{\sqrt{2\pi}} \int_{-\infty}^{\infty} -is \frac{\partial^3 W}{\partial y^3} e^{-isx} ds \tag{7.50}$$

On putting Eq. (7.46) to (7.50) in Eq. (7.44) we get

$$\left[\begin{array}{l} -\left(c_{44} l^2 + m^4 e_{15}^2 / a_{11}\right) \frac{d^4}{dy^4} + \left(c_{44} l' + 2ism^4 e_{15}^2 / a_{11}\right) \frac{d^3}{dy^3} + \\ \left(c_{44} + 2c_{44} s^2 l^2 + e_{15}^2 / a_{11} + 2s^2 m^4 e_{15}^2 / a_{11}\right) \frac{d^2}{dy^2} - \\ \left(s^2 c_{44} l' + 2is^3 m^4 e_{15}^2 / a_{11}\right) \frac{d}{dy} - \\ \left(s^2 c_{44} + c_{44} s^4 l^2 + s^2 e_{15}^2 / a_{11} + s^4 m^4 e_{15}^2 / a_{11}\right) \end{array} \right] W = 0 \tag{7.51}$$

So let $\lambda = d/dy$ so the characteristic equation from Eq. (7.51) is given as;

$$\begin{array}{l} -\left(c_{44} l^2 + m^4 e_{15}^2 / a_{11}\right) \lambda^4 + \left(c_{44} l' + 2ism^4 e_{15}^2 / a_{11}\right) \lambda^3 + \\ \left(c_{44} + 2c_{44} s^2 l^2 + e_{15}^2 / a_{11} + 2s^2 m^4 e_{15}^2 / a_{11}\right) \lambda^2 - \left(s^2 c_{44} l' + 2is^3 m^4 e_{15}^2 / a_{11}\right) \lambda - \\ \left(s^2 c_{44} + c_{44} s^4 l^2 + s^2 e_{15}^2 / a_{11} + s^4 m^4 e_{15}^2 / a_{11}\right) = 0 \end{array} \tag{7.52}$$

In order to simplify Eq. (7.52) let us assume $\sqrt{l} = m$, so Eq. (7.52) can be written as;

$$\begin{array}{l} -\left(c_{44} + e_{15}^2 / a_{11}\right) l^2 \lambda^4 + \left(c_{44} l' + 2isl^2 e_{15}^2 / a_{11}\right) \lambda^3 + \left(\begin{array}{l} c_{44} + e_{15}^2 / a_{11} + \\ 2s^2 l^2 \left(c_{44} + e_{15}^2 / a_{11}\right) \end{array} \right) \lambda^2 \\ -s^2 \left(c_{44} l' + 2isl^2 e_{15}^2 / a_{11}\right) \lambda - \left(s^2 \left(c_{44} + e_{15}^2 / a_{11}\right) + s^4 l^2 \left(c_{44} + e_{15}^2 / a_{11}\right)\right) = 0 \end{array} \tag{7.53}$$

Or

$$l^2 \lambda^4 - \gamma \lambda^3 - \left(1 + 2s^2 l^2\right) \lambda^2 + \gamma s^2 \lambda + \left(s^2 + s^4 l^2\right) = 0 \tag{7.54}$$

with $\gamma = \dfrac{c_{44}l^{'} + 2isl^2 e_{15}^2 / a_{11}}{a_{11}c_{44} + e_{15}^2}$

Roots of Eq. (7.32) i.e. λ_1, λ_2, λ_3 and λ_4 would give the displacement w_z as following;

$$w_z(x,y) = \frac{2}{\pi}\int_0^{\infty}\left[A(s)e^{\lambda_1 y} + B(s)e^{\lambda_2 y} + C(s)e^{\lambda_3 y} + D(s)e^{\lambda_4 y}\right]\cos(sx)\mathrm{d}s \qquad (7.55)$$

where$A(s)$, $B(s)$, $C(s)$ and $D(s)$ are the constants to be determined from the boundary conditions. The solution of Eq. (7.32) gives the following roots;

$$\lambda_1 = -s\,,\ \lambda_3 = s \qquad (7.56a)$$

$$\lambda_2 = \frac{\sqrt{\begin{matrix}4a_{11}^2c_{44}^2s^2l^4 + 4a_{11}^2c_{44}^2l^2 + a_{11}^2c_{44}^2l^{'2} + 8a_{11}c_{44}e_{15}^2l^2m^4s^2 + \\ 4a_{11}c_{44}e_{15}^2l^2 + 4a_{11}c_{44}e_{15}^2l^{'}m^4si + 4a_{11}c_{44}e_{15}^2m^4 + 4e_{15}^4m^4\end{matrix}} + (2e_{15}^2m^4si + a_{11}c_{44}l^{'})}{2(e_{15}^2m^4 + a_{11}c_{44}l^2)} \qquad (7.56b)$$

$$\lambda_4 = \frac{-\sqrt{\begin{matrix}4a_{11}^2c_{44}^2s^2l^4 + 4a_{11}^2c_{44}^2l^2 + a_{11}^2c_{44}^2l^{'2} + 8a_{11}c_{44}e_{15}^2l^2m^4s^2 + \\ 4a_{11}c_{44}e_{15}^2l^2 + 4a_{11}c_{44}e_{15}^2l^{'}m^4si + 4a_{11}c_{44}e_{15}^2m^4 + 4e_{15}^4m^4\end{matrix}} + (2e_{15}^2m^4si + a_{11}c_{44}l^{'})}{2(e_{15}^2m^4 + a_{11}c_{44}l^2)} \qquad (7.56c)$$

It is to be noted that in case of non-flexoelectric material, the roots converge to that of typical isotropic material i.e. $\lambda_1 = -s\,,\ \lambda_3 = s\,, \lambda_2 = -\dfrac{\sqrt{1+s^2l^2}}{l}$ and $\lambda_4 = \dfrac{\sqrt{1+s^2l^2}}{l}$ as provide by (Vardoulakis et al., 1996). Also, let us assume the electric potential and displacement is correlated using the following function;

$$\psi = \varphi - \frac{e_{15}}{a_{11}}w_z - \frac{m^2e_{15}}{a_{11}}\left(\frac{\partial}{\partial x} + \frac{\partial}{\partial y}\right)w_z \qquad (7.57)$$

The electric potential with the aid of Eq. (7.57) and Eq. (7.43) is given as;

$$\varphi(x,y)=\frac{2}{\pi}\int_0^{\infty}\left[P_1(s)e^{-sy}+P_2(s)e^{sy}\right]\cos(sx)ds+$$

$$\frac{2e_{15}}{\pi a_{11}}\int_0^{\infty}\left[A(s)e^{\lambda_1 y}+B(s)e^{\lambda_2 y}+C(s)e^{\lambda_3 y}+D(s)e^{\lambda_4 y}\right]\cos(sx)\mathrm{d}s- \tag{7.58}$$

$$\frac{2m^2e_{15}}{\pi a_{11}}\left[\begin{array}{l}\int_0^{\infty}\left[A(s)e^{\lambda_1 y}+B(s)e^{\lambda_2 y}+C(s)e^{\lambda_3 y}+D(s)e^{\lambda_4 y}\right]\sin(sx)\mathrm{d}s-\\ \int_0^{\infty}\left[\lambda_1 A(s)e^{\lambda_1 y}+\lambda_2 B(s)e^{\lambda_2 y}+\lambda_3 C(s)e^{\lambda_3 y}+\lambda_4 D(s)e^{\lambda_4 y}\right]\cos(sx)\mathrm{d}s\end{array}\right]$$

7.3.1 Boundary conditions:

In order to evaluate the coefficients of displacement i.e. $A(s)$, $B(s)$, $C(s)$ and $D(s)$, the general possible boundary conditions at the crack line ($y = 0$) are given as; $\tau_{yz}(x,0)=-\tau_1$ $|x|<a$ and $w_z(x,0)=0$ $|x|\geq a$, the specific boundary conditions are;

Stress-free boundaries i.e. $\tau_{yz}(x,\pm h)=0, \qquad |x|<\infty$

or clamped Boundaries i.e. $w_z(x,\pm h)=0, \qquad |x|<\infty$

For electrical boundary condition the material between the crack surface is considered to be impermeable (Sladek et al., 2011), so the electrical boundary condition is taken to be; $\psi(-h/2)=0$; $\psi(h/2)=V$, where V is the applied voltage. The constants $P_1(s)$ and $P_2(s)$ are evaluated with the aid of electrical boundary conditions.

7.4 Summary

The constitutive equations of the two-dimensional scale-dependent piezoelectric anti-plane cracked material layer of finite thickness are obtained. The displacement and electric potential are worked out using the Fourier transform technique via the roots of the resulting characteristic equation. Unlike the classical relation (Shin and Kim, 2016), the electric potential and crack displacement are assumed to be dependent on the flexoelectric coefficient m as well. The roots of a typical isotropic case as shown by

(Chan et al., 2008) and Vardoulakis et al. (1996) are recoved if one ignores the flexoelectric effect. The equations presented in this chapter are anticipated to give useful insights in defining the boundary value problem (either with stress-free or clamped boundaries) and to evaluate the numerical results.

CHAPTER 8

CONCLUSION AND FUTURE RECOMMENDATIONS

8.1 Conclusions

The thesis has presented the scale-dependent fracture in gradient elastic materials based on the simplest engineering type strain gradient theory (as briefly explained in section 2.3.2). This work deals with different types of one and two-dimensional fracture problems. In particular, one-dimensional problems are related to Mode I fracture in a double cantilever beam fracture mechanics specimen while the two-dimensional problems are limited to an anti-plane cracked material layer. The study is then extended to the piezoelectric materials in which the size-dependent piezoelectricity, also known as flexoelectricity, is also considered and its effects are thoroughly explained.

Initially, the non-linear large deformation behaviour of a cantilever beam is numerically evaluated using Euler beam model. In Chapter 2, the reason to consider large deformation at small scale is thoroughly explained and it is stated why the classical continuum theories are inadequate to deal with the scale-dependent fracture problems. In Chapter 3, the accuracy of the numerical results obtained through the Lobatto IIIa method, implemented via bvp4c program in Matlab, is checked with the available literature for small as well as the large deformation consideration. The bending behaviour of the cantilever beam is used to determine the Mode I fracture of the double cantilever beam. The results show that the strain gradient effect, in crack stiffening, is prominent when the height of the beam is comparable to microstructural

material characteristic length. It is also shown that the incorporation of the uncracked part of DCB also enhances the strain energy release rate at small scale and it must not be ignored when dealing with the scale-dependent problem. This observation is completely different from classical studies. Moreover, due to the massive surface area to volume ratio at small scale, the surface effects i.e. surface elasticity and surface residual stresses are also incorporated in the constitutive and governing equations. It is shown that the effect of surface residual stress is more prominent with the negative surface residual stress increase the crack stiffness while positive residual surface stress leads to a more compliant crack.

Next, the scale-dependent Mode I fracture study is extended to the piezoelectric material, in Chapters 4 and 5. A brief literature is reviewed in Chapter 2. First, the strain gradient elasticity theory is applied to obtain the constitutive equations for the bending behaviour of a piezoelectric cantilever beam with the aid of the variational principle. The strain energy release rate of a double cantilever beam is obtained using the methodology described in Chapter 3. However, the incorporation of strain gradient-Electromechanical coupling at small scale is incorporated in Chapter 5. In general, the models presented in Chapters 4 and 5 include the cumulative influence of strain gradient, surface effects and the uncracked part of the DCB. The results are presented and compared for two different electrical boundary conditions i.e. the short circuit and open circuit boundary condition. It is shown that the flexoelectric effect leads to crack stiffening and the strain energy release rate with the short circuit boundary condition is always higher than the open circuit boundary condition.

The implementation of the strain gradient theory was then extended to a two-dimensional anti-plane cracked material layer. Due to the potential research gap (as briefly mentioned in Chapters 2 and 6), the material layer is considered to be of finite height/thickness with two different boundary conditions i.e. stress-free boundaries and

clamped boundaries. In Chapter 6, the layer is considered of an isotropic material and both volumetric and surface strain gradient characteristics lengths are incorporated in the material's constitutive equations. The solution of each problem is discussed separately and reduced to the dual integral equations. Resulting Fredholm integral equation is solved numerically in which the kernel (an improper integral that ranges from 0 to infinity) of the second kind is solved by using Gauss-Laguerre quadrature to evaluate crack tip stress intensity factors. Incorporation of volumetric strain gradient effect increases crack stiffness by reducing the stress intensity factor. The positive surface gradient effect increases crack stiffness while negative surface gradient leads to a more compliant crack. In chapter 7, the electro-mechanical effects were added in order to model the scale-dependent piezoelectric material layer and the flexoelectric effects. However, the study is limited to theoretical modelling.

The research presented in this thesis has filled numerous research gaps associated with the scale-dependent modelling of materials. Furthermore, the analytical and numerical solutions developed in this study are expected to give more insights to those working on the empirical investigations and finite element simulations of the micro and nanoscale structures. Some of the recommendations for the future research that may be directed relation to this work are presented in the next section.

8.2 Future Recommendations

The following research directions are recommended based on the studies conducted in this thesis;

1) The results presented in this thesis are for homogenous materials, however, in many engineering practices, materials are nonhomogenous i.e composite and functionally graded materials. Additional investigations may be conducted to

capture the influence of material inhomogeneity on the scale-dependent material fracture.

2) To investigate the scale-dependent fracture toughness of a double cantilever beam fracture mechanics specimen (for both isotropic and piezoelectric materials) through experiments and comparing the results with those provided in Chapters,3, 4 and 5.
3) Potential extension of the work presented in Chapter 6 is to investigate the Mode III stress intensity factors for a cracked material layer with finite width.
4) To conduct the numerical analysis based on the theoretical modelling presented in Chapter 7 of this thesis.
5) The study conducted in Chapters 6 and 7 can be extended for Mode I and Mode II crack problems.

References (for Chapter 1,2,7 & 8)

Abdollahi, A., Peco, C., Millan, D., Arroyo, M. & Arias, I., 2014. Computational evaluation of the flexoelectric effect in dielectric solids. *Journal of Applied Physics,* 116**,** 093502.

Aifantis, E. C., 2016. Chapter One-Internal Length Gradient (ILG) Material Mechanics Across Scales and Disciplines. *Advances in Applied Mechanics,* 49**,** 1-110.

Aifantis, E. C., 1999. Strain gradient interpretation of size effects. *International Journal of Fracture,* 95**,** 299-314.

Aifantis, E. C., 2011. A note on gradient elasticity and nonsingular crack fields. *J. Mech. Behav. Mater,* 20**,** 103-105.

Baskaran, S., He, X., Chen, Q. & Fu, J. Y., 2011. Experimental studies on the direct flexoelectric effect in α-phase polyvinylidene fluoride films. *Applied Physics Letters,* 98**,** 242901.

Baskaran, S., He, X., Wang, Y. & Fu, J. Y., 2012. Strain gradient induced electric polarization in α-phase polyvinylidene fluoride films under bending conditions. *Journal of Applied Physics,* 111**,** 014109.

Batra, R., PorfirI, M. & Spinello, D., 2008. Reduced-order models for microelectromechanical rectangular and circular plates incorporating the Casimir force. *International Journal of Solids and Structures,* 45**,** 3558-3583.

Behzadi, S. & Rafii-Tabar, H., 2008. Atomistic modelling of crack propagation in a randomly rough nano-scale metallic surface. *Journal of Molecular Graphics and Modelling,* 27**,** 356-363.

Beléndez, T., Neipp, C. & Beléndez, A., 2002. Large and small deflections of a cantilever beam. *European Journal of Physics,* 23**,** 371.

Benvenuti, E. & Simone, A., 2013. One-dimensional nonlocal and gradient elasticity: closed-form solution and size effect. *Mechanics Research Communications,* 48**,** 46-51.

Besson, J., 2010. Continuum models of ductile fracture: a review. *International Journal of Damage Mechanics,* 19**,** 3-52.

Cady, W. G. 1946. Piezoelectricity: an introduction to the theory and applications of electromechanical phenomena in crystals.

Cahn, J. W., 1998. Thermodynamics of solid and fluid surfaces. *The Selected Works of John W. Cahn***,** 377-378.

Cammarata, R., 1997. Surface and interface stress effects on interfacial and nanostructured materials. *Materials Science and Engineering: A,* 237**,** 180-184.

Cammarata, R. C., 1994. Surface and interface stress effects in thin films. *Progress in Surface Science,* 46**,** 1-38.

Catalan, G., Lubk, A., Vlooswijk, A., Snoeck, E., Magen, C., Janssens, A., Rispens, G., Rijnders, G., Blank, D. & Noheda, B., 2011. Flexoelectric rotation of polarization in ferroelectric thin films. *Nature Materials,* 10**,** 963.

Chan, Y. S., Paulino, G. H. & Fannjiang, A. C., 2008. Gradient elasticity theory for mode III fracture in functionally graded materials—part II: crack parallel to the material gradation. *Journal of Applied Mechanics,* 75**,** 061015.

Chang, D., Muki, R. & Westmann, R., 1976. Double cantilever beam models in adhesive mechanics. *International Journal of Solids and Structures,* 12**,** 13-26.

Chen, S., Liu, L. & Wang, T., 2007. Small scale, grain size and substrate effects in nano-indentation experiment of film–substrate systems. *International journal of solids and structures,* 44**,** 4492-4504.

Cheng, M., Cheung, C., Lee, W., To, S. & Kong, L., 2008. Theoretical and experimental analysis of nano-surface generation in ultra-precision raster milling. *International Journal of Machine Tools and Manufacture,* 48**,** 1090-1102.

Chu, B. & Salem, D., 2012. Flexoelectricity in several thermoplastic and thermosetting polymers. *Applied Physics Letters,* 101**,** 103905.

Dingreville, R., Qu, J. & Cherkaoui, M., 2005. Surface free energy and its effect on the elastic behaviour of nano-sized particles, wires and films. *Journal of the Mechanics and Physics of Solids,* 53**,** 1827-1854.

Duan, H., Wang, J., Huang, Z. & Karihaloo, B., 2005. Size-dependent effective elastic constants of solids containing nano-inhomogeneities with interface stress. *Journal of the Mechanics and Physics of Solids,* 53**,** 1574-1596.

Eringen, A. C., 1972. Nonlocal polar elastic continua. *International Journal of Engineering Science,* 10**,** 1-16.

Eringen, A. C., 1983. On differential equations of nonlocal elasticity and solutions of screw dislocation and surface waves. *Journal of Applied Physics,* 54, 4703-4710.

Eringen, A. C., 2002. *Nonlocal continuum field theories,* Springer Science & Business Media.

Fermeglia, M., 2008. Multiscale molecular modeling: a tool for the design of nano structured materials. *Computer Aided Chemical Engineering,* 25**,** 725.

Fischer-Cripps, A. C., 2007. *Introduction to contact mechanics,* Springer.

Fischer, F., Waitz, T., Vollath, D. & Simha, N., 2008. On the role of surface energy and surface stress in phase-transforming nanoparticles. *Progress in Materials Science,* 53**,** 481-527.

Fleck, N. & Hutchinson, J., 1997. Strain gradient plasticity. *Advances in Applied Mechanics,* 33**,** 296-361.

Fleck, N. & Hutchinson, J., 2001. A reformulation of strain gradient plasticity. *Journal of the Mechanics and Physics of Solids,* 49**,** 2245-2271.

Fousek, J., Cross, L. & Litvin, D., 1999. Possible piezoelectric composites based on the flexoelectric effect. *Materials Letters,* 39**,** 287-291.

Fried, E. & Gurtin, M. E., 2003. The role of the configurational force balance in the nonequilibrium epitaxy of films. *Journal of the Mechanics and Physics of Solids,* 51**,** 487-517.

Gao, H., Zhang, T. Y. & Tong, P., 1997. Local and global energy release rates for an electrically yielded crack in a piezoelectric ceramic. *Journal of the Mechanics and Physics of Solids,* 45**,** 491-510.

Giannakopoulos, A., Amanatidou, E. & Aravas, N., 2006. A reciprocity theorem in linear gradient elasticity and the corresponding Saint-Venant principle. *International journal of solids and structures,* 43**,** 3875-3894.

Giannakopoulos, A. & Stamoulis, K., 2007. Structural analysis of gradient elastic components. *International journal of solids and structures,* 44**,** 3440-3451.

Griffith, A. A. 1921. *The phenomena of rupture and flow in solids.* .

Gurtin, M. E. & Murdoch, A. I., 1978. Surface stress in solids. *International Journal of Solids and Structures,* 14**,** 431-440.

He, J. & Lilley, C. M., 2008. Surface effect on the elastic behaviour of static bending nanowires. *Nano Letters,* 8**,** 1798-1802.

Heidelberg, A., Ngo, L. T., Wu, B., Phillips, M. A., Sharma, S., Kamins, T. I., Sader, J. E. & Boland, J. J., 2006. A generalized description of the elastic properties of nanowires. *Nano letters,* 6**,** 1101-1106.

Hsu, M. H., 2008. Electromechanical analysis of electrostatic nano-actuators using the differential quadrature method. *International Journal for Numerical Methods in Biomedical Engineering,* 24**,** 1445-1457.

Hu, S. & Shen, S., 2009. Electric field gradient theory with surface effect for nano-dielectrics. *Computers, Materials & Continua (CMC),* 13**,** 63.

Hu, S. & SheN, S., 2010. Variational principles and governing equations in nano-dielectrics with the flexoelectric effect. *Science China Physics, Mechanics and Astronomy,* 53**,** 1497-1504.

Huang, G. Y. & Yu, S. W., 2006. Effect of surface piezoelectricity on the electromechanical behaviour of a piezoelectric ring. *Physica Status solidi (b),* 243**,** R22-R24.

Jammes, M., Mogilevskaya, S. G. & Crouch, S. L., 2009. Multiple circular nano-inhomogeneities and/or nano-pores in one of two joined isotropic elastic half-planes. *Engineering Analysis with Boundary Elements,* 33**,** 233-248.

Jia, X., Yang, J., Kitipornchai, S. & Lim, C. W., 2010. Free vibration of geometrically nonlinear micro-switches under electrostatic and Casimir forces. *Smart Materials and Structures,* 19**,** 115028.

Jing, G., Duan, H. L., Sun, X., ZhanG, Z., Xu, J., Li, Y., Wang, J. & Yu, D., 2006. Surface effects on elastic properties of silver nanowires: contact atomic-force microscopy. *Physical Review B,* 73**,** 235409.

Kachanov, L., 1974. *Foundations of Fracture Mechanics,* Moscow:Nauka.

Kahrobaiyan, M., Asghari, M., Rahaeifard, M. & Ahmadian, M., 2011. A nonlinear strain gradient beam formulation. *International Journal of Engineering Science,* 49**,** 1256-1267.

Kang, Y. & Xie, H., 2010. Micro and nano metrology in experimental mechanics. *Optics and Lasers in Engineering,* 48**,** 1045.

Karlis, G., Tsinopoulos, S., Polyzos, D. & Beskos, D., 2007. Boundary element analysis of mode I and mixed mode (I and II) crack problems of 2-D gradient elasticity. *Computer Methods in Applied Mechanics and Engineering,* 196**,** 5092-5103.

Karlis, G., Tsinopoulos, S., Polyzos, D. & Beskos, D., 2008. 2D and 3D boundary element analysis of mode-I cracks in gradient elasticity. *Computer Modeling in Engineering and Sciences,* 26**,** 189.

Kiang, C. H., Endo, M., Ajayan, P., Dresselhaus, G. & Dresselhaus, M., 1998. Size effects in carbon nanotubes. *Physical Review Letters,* 81**,** 1869.

Kitamura, T., Hirakata, H., Sumigawa, T. & Shimada, T., 2016. *Fracture Nanomechanics,* CRC Press.

Koiter, W., 1964. Couple stresses in the theory of elasticity. *Proc. Koninklijke Nederl. Akaad. van Wetensch,* 67.

Lagowski, J., Gatos, H. & Sproles Jr, E., 1975. Surface stress and the normal mode of vibration of thin crystals: GaAs. *Applied Physics Letters,* 26**,** 493-495.

Lam, D., Yang, F., Chong, A., Wang, J. & Tong, P., 2003. Experiments and theory in strain gradient elasticity. *Journal of the Mechanics and Physics of Solids,* 51**,** 1477-1508.

Li, X. F., 2001. Closed-form solution for a mode-III interface crack between two bonded dissimilar elastic layers. *International Journal of Fracture,* 109**,** 3-8.

Li, X. F., Wang, B. L. & Mai, Y. W., 2008. Effects of a surrounding elastic medium on flexural waves propagating in carbon nanotubes via nonlocal elasticity. *Journal of Applied Physics,* 103**,** 074309.

Lim, C. & Wang, C., 2007. Exact variational nonlocal stress modeling with asymptotic higher-order strain gradients for nanobeams. *Journal of Applied Physics,* 101**,** 054312.

Lu, J., Lv, J., Liang, X., Xu, M. & Shen, S., 2016. Improved approach to measure the direct flexoelectric coefficient of bulk polyvinylidene fluoride. *Journal of Applied Physics,* 119**,** 094104.

Luo, J. & Wang, X., 2009. On the anti-plane shear of an elliptic nano inhomogeneity. *European Journal of Mechanics-A/Solids,* 28**,** 926-934.

Luo, J. & Xiao, Z., 2009. Analysis of a screw dislocation interacting with an elliptical nano inhomogeneity. *International Journal of Engineering Science,* 47**,** 883-893.

Ma, Q. & Clarke, D. R., 1995. Size dependent hardness of silver single crystals. *Journal of Materials Research,* 10**,** 853-863.

Majdoub, M., Sharma, P. & Cagin, T., 2008a. Enhanced size-dependent piezoelectricity and elasticity in nanostructures due to the flexoelectric effect. *Physical Review B,* 77**,** 125424.

Majdoub, M., Sharma, P. & Çağin, T., 2008b. Dramatic enhancement in energy harvesting for a narrow range of dimensions in piezoelectric nanostructures. *Physical Review B,* 78**,** 121407.

Mao, S. & Purohit, P. K., 2014. Insights into flexoelectric solids from strain-gradient elasticity. *Journal of Applied Mechanics,* 81**,** 081004.

Maranganti, R., Sharma, N. & Sharma, P., 2006. Electromechanical coupling in nonpiezoelectric materials due to nanoscale nonlocal size effects: Green's function solutions and embedded inclusions. *Physical Review B,* 74**,** 014110.

Mcfarland, A. W. & Colton, J. S., 2005. Role of material microstructure in plate stiffness with relevance to microcantilever sensors. *Journal of Micromechanics and Microengineering,* 15**,** 1060.

Mindlin, R. & Eshel, N., 1968. On first strain-gradient theories in linear elasticity. *International Journal of Solids and Structures,* 4**,** 109-124.

Mindlin, R. & Tiersten, H., 1962. Effects of couple-stresses in linear elasticity. *Archive for Rational Mechanics and Analysis,* 11**,** 415-448.

Mindlin, R. D., 1965. Second gradient of strain and surface-tension in linear elasticity. *International Journal of Solids and Structures,* 1**,** 417-438.

Mindlin, R. D., 1969. Continuum and lattice theories of influence of electromechanical coupling on capacitance of thin dielectric films. *International Journal of Solids and Structures,* 5**,** 1197-1208.

Mousavi, S. M. & Aifantis, E., 2015. A note on dislocation-based mode III gradient elastic fracture mechanics. *Journal of the Mechanical Behaviour of Materials,* 24**,** 115-119.

Mughrabi, H., 1987. A two-parameter description of heterogeneous dislocation distributions in deformed metal crystals. *Materials science and engineering,* 85**,** 15-31.

Nejad, M. Z. & Hadi, A., 2016. Eringen's non-local elasticity theory for bending analysis of bi-directional functionally graded Euler–Bernoulli nano-beams. *International Journal of Engineering Science,* 106**,** 1-9.

Nilsson, S., Sarwe, E. L. & Montelius, L., 2003. Fabrication and mechanical characterization of ultrashort nanocantilevers. *Applied physics letters,* 83**,** 990-992.

Papargyri-beskou, S., Tsepoura, K., Polyzos, D. & Beskos, D., 2003. Bending and stability analysis of gradient elastic beams. *International Journal of Solids and Structures,* 40**,** 385-400.

Pharr, G., Oliver, W. & Brotzen, F., 1992. On the generality of the relationship among contact stiffness, contact area, and elastic modulus during indentation. *Journal of materials research,* 7**,** 613-617.

Poddar, S. & Ducharme, S., 2013. Measurement of the flexoelectric response in ferroelectric and relaxor polymer thin films. *Applied Physics Letters,* 103**,** 202901.

Polizzotto, C., 2014. Stress gradient versus strain gradient constitutive models within elasticity. *International Journal of Solids and Structures,* 51**,** 1809-1818.

Polizzotto, C., 2015. A unifying variational framework for stress gradient and strain gradient elasticity theories. *European Journal of Mechanics-A/Solids,* 49**,** 430-440.

Popescu, M., 2007. The atomic scale modelling of nanomaterials. *Journal of Physics and Chemistry of Solids,* 68**,** 687-694.

Prasad, M. S., Venkatesha, C. & Jayaraju, T., 2011. Experimental methods of determining fracture toughness of fiber reinforced polymer composites under various loading conditions. *Journal of Minerals and Materials Characterization and Engineering,* 10**,** 1263.

Rabotnov, Y. N., 1987. *Introduction to fracture mechanics,* Moscow, Nauka.

Sapsathiarn, Y. & Rajapakse, R., 2012. A model for large deflections of nanobeams and experimental comparison. *IEEE Transactions on Nanotechnology,* 11**,** 247-254.

Sharma, N., Landis, C. & Sharma, P., 2010. Piezoelectric thin-film superlattices without using piezoelectric materials. *Journal of Applied Physics,* 108**,** 024304.

Sharma, P. & Ganti, S., 2004. Size-dependent Eshelby's tensor for embedded nano-inclusions incorporating surface/interface energies. *Journal of Applied Mechanics,* 71**,** 663-671.

Sharma, P., Ganti, S. & Bhate, N., 2003. Effect of surfaces on the size-dependent elastic state of nano-inhomogeneities. *Applied Physics Letters,* 82**,** 535-537.

Shen, S. & Hu, S., 2010. A theory of flexoelectricity with surface effect for elastic dielectrics. *Journal of the Mechanics and Physics of Solids,* 58**,** 665-677.

Shenoy, V. B., 2005. Atomistic calculations of elastic properties of metallic fcc crystal surfaces. *Physical Review B,* 71**,** 094104.

Shin, J. W. & Kim, T. U., 2016. Transient response of a Mode III interface crack between piezoelectric layer and functionally graded orthotropic layer. *International Journal of Solids and Structures,* 90**,** 122-128.

Sih, G. C. & Chen, E. P., 1981. *Mechanics of fracture Cracks in composite materials,* The Netherlands, Martinus Nijhoff Publishers.

Singh, B. & Moodie, T. B., 1981. Closed-form solutions for finite length crack moving in a strip under anti-plane shear stress. *Acta Mechanica,* 38**,** 99-109.

Sladek, J., Sladek, V., Stanak, P., Zhang, C. & Tan, C. L., 2017. Fracture mechanics analysis of size-dependent piezoelectric solids. *International Journal of Solids and Structures,* 113**,** 1-9.

Sladek, J., Sladek, V., Stanak, P., Zhang, C. & Wünsche, M., 2011. An interaction integral method for computing fracture parameters in functionally graded magnetoelectroelastic composites. *Computers Materials and Continua,* 23**,** 35.

Stamoulis, K. & Giannakopoulos, A., 2012a. A study of size effects and length scales in fracture and fatigue of metals by second gradient modelling. *Fatigue & Fracture of Engineering Materials & Structures,* 35**,** 852-860.

Stamoulis, K. & Giannakopoulos, A., 2012b. A study of size effects and length scales in fracture and fatigue of metals by second gradient modelling*. *Fatigue & Fracture of Engineering Materials & Structures,* 35**,** 852-860.

Streitz, F., Cammarata, R. & Sieradzki, K., 1994. Surface-stress effects on elastic properties. I. Thin metal films. *Physical Review B,* 49**,** 10699.

Toupin, R. A., 1962. Elastic materials with couple-stresses. *Archive for Rational Mechanics and Analysis,* 11**,** 385-414.

Trevelyan, J., 1992. The Effective Use and Accuracy of BEASY'S Discontinuous Boundary Elements for Fracture Mechanics Analysis. *Boundary Element Technology VII.* Springer.

Vardoulakis, I., Exadaktylos, G. & Aifantis, E., 1996. Gradient elasticity with surface energy: mode-III crack problem. *International Journal of Solids and Structures,* 33**,** 4531-4559.

Vardoulakis, I. & Sulem, J., 1995. *Bifurcation Analysis in Geomechanics,* London, Blackie/Chapman and Hall.

Volegov, P., Gribov, D. & TRUSOV, P., 2017. Damage and fracture: Classical continuum theories. *Physical Mesomechanics,* 20**,** 157-173.

Voyiadjis, G. Z., Almasri, A. H. & Park, T., 2010. Experimental nanoindentation of BCC metals. *Mechanics Research Communications,* 37**,** 307-314.

Wang, B., Hoffman, M. & Yu, A., 2012. Buckling analysis of embedded nanotubes using gradient continuum theory. *Mechanics of Materials,* 45**,** 52-60.

Wang, B. & Wang, K., 2013. Effect of surface residual stress on the fracture of double cantilever beam fracture toughness specimen. *Journal of Applied Physics,* 113**,** 153502.

Wang, K. & Wang, B., 2015. A general model for nano-cantilever switches with consideration of surface effects and nonlinear curvature. *Physica E: Low-dimensional Systems and Nanostructures,* 66**,** 197-208.

Wang, K. & Wang, B., 2016. Nonlinear fracture mechanics analysis of nano-scale piezoelectric double cantilever beam specimens with surface effect. *European Journal of Mechanics-A/Solids,* 56**,** 12-18.

Weissmüller, J. & Cahn, J., 1997. Mean stresses in microstructures due to interface stresses: A generalization of a capillary equation for solids. *Acta Materialia,* 45**,** 1899-1906.

Whitney, J., 1985. Stress analysis of the double cantilever beam specimen. *Composites Science and Technology,* 23**,** 201-219.

Wong, E. W., Sheehan, P. E. & Lieber, C. M., 1997. Nanobeam mechanics: elasticity, strength, and toughness of nanorods and nanotubes. *Science,* 277**,** 1971-1975.

Wu, B., Heidelberg, A., Boland, J. J., Sader, J. E., Sun, X. & LI, Y., 2006. Microstructure-hardened silver nanowires. *Nano letters,* 6**,** 468-472.

Xu, L. & Shen, S., 2013. Size-dependent piezoelectricity and elasticity due to the electric field-strain gradient coupling and strain gradient elasticity. *International Journal of Applied Mechanics,* 5**,** 1350015.

Yan, Z. & Jiang, L., 2011. The vibrational and buckling behaviours of piezoelectric nanobeams with surface effects. *Nanotechnology,* 22**,** 245703.

Yan, Z. & Jiang, L., 2013a. Flexoelectric effect on the electroelastic responses of bending piezoelectric nanobeams. *Journal of Applied Physics,* 113**,** 194102.

Yan, Z. & Jiang, L., 2013b. Size-dependent bending and vibration behaviour of piezoelectric nanobeams due to flexoelectricity. *Journal of Physics D: Applied Physics,* 46**,** 355502.

Yang, J., 2004. Effects of electric field gradient on an anti-plane crack in piezoelectric ceramics. *International journal of fracture,* 127**,** L111-L116.

Yu, M. F., Lourie, O., Dyer, M. J., Moloni, K., Kelly, T. F. & Ruoff, R. S., 2000. Strength and breaking mechanism of multiwalled carbon nanotubes under tensile load. *Science,* 287**,** 637-640.

Yue, Y., Xu, K., Chen, T. & Aifantis, E. C., 2015. Size effects on magnetoelectric response of multiferroic composite with inhomogeneities. *Physica B: Condensed Matter,* 478**,** 36-42.

Zhang, W.& Yuanqiang, C., 2010. Review of Damage Mechanics. *Continuum Damage Mechanics and Numerical Applications.* Berlin: Springer, Berlin, Heidelberg.

Zhang, Z. & Jiang, L., 2014. Size effects on electromechanical coupling fields of a bending piezoelectric nanoplate due to surface effects and flexoelectricity. *Journal of Applied Physics,* 116**,** 134308.

Zhang, Z., Yan, Z. & Jiang, L., 2014. Flexoelectric effect on the electroelastic responses and vibrational behaviours of a piezoelectric nanoplate. *Journal of Applied Physics,* 116**,** 014307.

APPENDIX A: PEER REVIEWED JOURNAL PAPERS

Paper 1:

Engineering Fracture Mechanics 169 (2017) 309–320

Contents lists available at ScienceDirect

Engineering Fracture Mechanics

journal homepage: www.elsevier.com/locate/engfracmech

Size effects on double cantilever beam fracture mechanics specimen based on strain gradient theory

R.P. Joseph *, B.L. Wang, B. Samali

Centre for Infrastructure Engineering, School of Computing, Engineering and Mathematics, Western Sydney University, Penrith, NSW 2751, Australia

ARTICLE INFO

Article history:
Received 20 April 2016
Received in revised form 20 October 2016
Accepted 24 October 2016
Available online 5 November 2016

Keywords:
Large deformation
Double cantilever beam
Strain gradient elasticity theory
Strain energy release rate

ABSTRACT

This paper investigates large deformation of a cantilever beam which is further employed to study the fracture behavior of double cantilever beam (DCB), based on strain gradient elasticity theory. Root effect of the DCB is also included for modelling and analyses. The numerical solutions of maximum tip deflection and strain energy release rate are presented. Results demonstrate that the consideration of large deformation is crucial at small scale, especially for more slender beams, as the bending behavior of the beam in that case is different from the classical results. The strain gradient and root effects of the DCB are more prominent when thickness of the beam is less than the material length scale parameter. The strain gradient model demonstrates significant stiffening behavior at the smaller scale. In general, the root effect may not be neglected if the length to thickness ratio of the beam is smaller. Overall, the strain energy release rate of the gradient model, even with the incorporation of root part, remains less than that of non-gradient model. This conclusion is entirely different from the classical method that neglects the uncracked part of the DCB.

1. Introduction

Mechanical structures, such as beams are often subjected to large deformation which tends to induce geometrical non linearity, such that the relation between applied force and the curvature becomes non-linear. This non-linear behavior will effectively change the stiffness of the structure. This response is shown to be dominant in literature for the case of clamped-clamped and simply supported beams. In contrast, the non-linear response of cantilever beam has received less attention comparatively [42]. Cantilever beams used in micro and nanoelectromechanical (MEMS & NEMS) switches often undergo geometrical non-linearity. Using linear theory, the error in strain energy release rate is found to be larger than 30%, as shown by mixed mode bending (MMB) tests. However, with the consideration of geometric nonlinearity, the redesigned MMB apparatus demonstrate the error to be less than 3% [36,46]. The conventional mathematical treatment of analysing a cantilever beam, that assumes small deformation does not hold many complexities and hence exact solution can be derived quite comfortably. Nevertheless, with the addition of large deformation (geometrical non linearity), the problem involves the non-linear term that are difficult to solve analytically. In the past, several efforts have been devoted to address this issue, for instance, the analysis of large deformation of cantilever beams may be found in work of Beléndez et al. [6] and Landau and Lifshitz [29]. It was shown that the results, with the consideration of large deformation, were in better agreement with

* Corresponding author.
E-mail addresses: r.joseph@westernsydney.edu.au, richardson.joseph77@gmail.com (R.P. Joseph).

http://dx.doi.org/10.1016/j.engfracmech.2016.10.013
0013-7944/

Nomenclature

A	cross-sectional area of the beam
a	length of the beam
b	width of the beam
DCB	double cantilever beam
E	Young's modulus
e_x	axial strain
F	applied force
G^s	shear modulus
G	strain energy release rate (large deformation)
G_o	classical strain energy release rate
G_g	strain energy release rate of a strain gradient model
h	height of the beam
I	moment of inertia of the beam
l	material length constant related to volumetric elastic strain energy
l'	material length constant related to surface elastic strain energy
M	bending moment of a beam
N	resultant force along the x-direction
$MEMS$	microelectromechanical systems
MMB	mixed mode bending
$NEMS$	nanoelectromechanical
p	normal stress on the $z = 0$ plane
Q	shear force on the beam cross-section
q	shear stress on the $z = 0$ plane
R	ratio of the strain energy release rate contributed by the uncracked part the cracked part of the DCB
s	arc length along the deformed beam
U	potential energy density
U_I	total strain energy
X	horizontal deflection
Y	vertical tip deflection (large deformation)
Y_o	classical tip vertical deflection
Y_g	vertical tip deflection of strain gradient model

Special symbols

u_o	displacement of the beam along the x direction
v	Poisson ratio
φ	angle of rotation of a beam
τ_x	Cauchy stresses
μ_x	double stresses
σ_x	total stresses

the experimental data upon comparison with the classical theory. Meanwhile different numerical techniques are also used to obtain large-deformation solutions for cantilever beam [35].

The bending behavior of cantilever beam in literature is often employed to study the fracture behavior of double cantilever beam (DCB) [16,39]. The DCB is typically considered to be consist of two cantilever beams attached with the root part (uncracked part) and is used broadly in experiments to determine the Mode I fracture toughness of the materials. In the tests of DCB, Devitt et al. [11] found that the effect of geometric nonlinearity on the mode I fracture toughness of composite materials is suffice for long cracks; similar findings are also mentioned in other reference [47]. Furthermore DCB is the most widely used test configuration for the study of crack propagation and arrest for composite materials and adhesives. Either in theoretical studies or experimental investigations, the DCB specimen has been found to be quite convenient to determine the mode I fracture toughness of homogenous, composite laminates and adhesively bonded materials. Sebaey et al. [37] used numerical methods to investigate the asymmetric crack growth in double cantilever beam tests of multidirectional composite laminates. The solution was the extension of the work previously conducted by Kanninen [24]. De Moura et al. [10] employed numerical and experimental methods to investigate the fracture characteristics of double cantilever wood beam specimen. De Morais [9] developed a new analytical method to compute mode I critical strain energy release rates unaffected by fibre bridging. Wang and Wang [45] derived the closed-form solutions of the strain energy release rate and stress inten-

sity factors, incorporating the effect of surface residual stresses at smaller scale, using Timoshenko beam theory for double cantilever beam specimen. Zhang et al. [49] presented the stress intensity factors of double cantilever nanobeams via gradient elasticity theory.

Classical continuum elasticity theories assume that the stresses in a material point depends only on the strain components at the same point. It does not account for contributions from the strain gradients. However, according to nonlocal theory of elasticity, the stress at a particular point not only depends on the strain at the same point but also on all the other points of the body [40,44]. This phenomenon is more evident when the dimensions of the structure are scaled down to the micro (MEMS) and nano-domains (NEMS). In this case, the material microstructural length scales become comparable to the length scale of deformation field which tends to cause non-homogenous and size dependent mechanical behavior [16]. Size dependent mechanical behavior in micro-scale elements have extensively been observed in experiments [13,26,27,28,30,31] and it has been understood that the non-classical continuum theories such as the higher-order gradient theories and couple stress theory can interpret this size depended behavior. The higher-order strain gradient theory was introduced by Mindlin [32] that includes the effect of the first and second derivatives of the strain tensor on the strain energy density. The physical interpretation of higher order strain tensor, employed in gradient elasticity theories are recently provided by Polizzotto [33]. The simple gradient theory employed by Vardoulakis and Sulem [41], combines the concepts of Form II of Mindlin theory, though it has fewer number of elastic constants comparatively. Consequently, the theory presented by Vardoulakis and Sulem [41] is much more convenient in applications [16] and therefore employed in this work. For one-dimensional case, the Cauchy (τ_x), double (μ_x) and total stresses (σ_x) are given for the beam bending in the following constitutive relations

$$\text{Cauchy stresses; } \tau_x = Ee_x + l'E\frac{de_x}{dx}, \text{ double stresses } \mu_x = l'Ee_x + l^2E\frac{de_x}{dx} \text{ and}$$

$$\text{Total stresses; } \sigma_x = \tau_x - \frac{d\mu_x}{dx} = E\left(e_x - l^2\frac{d^2e_x}{dx^2}\right)$$

In above equations, E is the Young's Modulus; e_x is the axial strain in the beam due to bending, l and l' are the material length constants related to volumetric and surface elastic strain energy. The use of simpler, engineering-type gradient theories [41] is much more convenient and valid as shown by Giannakopoulos et al. [15].

Nanoscale devices and structure demand accurate design and development. For this, it is vital to explore their characteristics thoroughly. The experimental investigation of the mechanical response, using modern scientific manipulations [7,20,23,43] and atomic/molecular modelling [5,12,34] are effective method to determine the size dependent behavior of the structure at micro/nano scale. However, the application of theoretical approaches for modelling nano structures is considered more attractive because of their lesser complexity and their capability to be implemented at all the possible length scales. Meanwhile, according to author's knowledge most of the works on micro and nano beam, based on nonlocal elasticity theories are limited to small deformation on the structures. In particular, the nonlinear analyses (large deformation) of micro and nano beams based on strain gradient theories still demand updates. Therefore, in this article, the influence of strain gradients, in terms of material length scale parameters, is introduced in Euler's model to investigate the non-linear deformation of cantilever beam. Next, the study is extended to explore the fracture behavior of double cantilever beam. The material properties of epoxy are used as an example. The schematic diagram of the DCB is shown in Fig. 1. Numerical results are obtained and presented for strain energy release rate for various beam configurations. Finally, the effect of root part (uncracked part) of double cantilever beam on strain energy release rate is further estimated to conclude the study.

2. Bending of cantilever beam

Generally, the geometrical non linearity may be divided into two main categories i.e. the geometrically non-linear strain (von Kármán strain) that induces the extension of mid-plane, and secondly, the non-linear relation between applied force and curvature. For a cantilever beam the contribution of von Kármán strain is insignificant for their structural analysis and hence can be neglected [19,18]. However, the effect of geometrically nonlinear curvature on the mechanical behavior of cantilever beams is substantial [2] and should be thoroughly assessed. As mentioned before, the solution for large deformation of a cantilever beam may not be obtained from classical beam theory. It is primarily due to the absence of the square of the first derivative in the curvature formulation that does not provide any correction for the shortening of the moment arm as the free end of the beam deflects. Therefore, for large finite loads, the deflection data deviates from the actual observation. The correction for the shortening of the moment arm becomes the major contribution to the solution of large deflection problems.

2.1. Theoretical formulations

The formulation is based on Euler-Bernoulli theorem, for which the moment–curvature relation of the beam along the x-axis is given as $EI\frac{d\varphi}{ds} = M$. Moment at any point $X_{(s)}$ along the beam may be written as $M = F.X_{(s)}$, upon differentiation and using $dX_{(s)}/ds = \cos\varphi$, we get

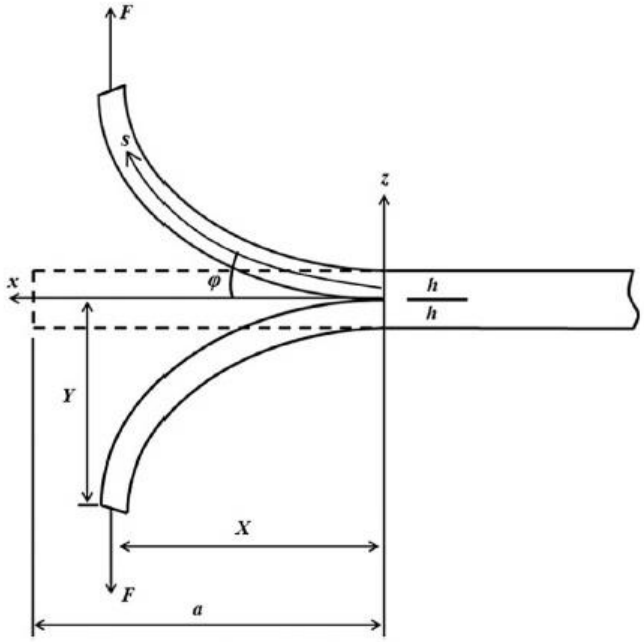

Fig. 1. Schematic diagram of double cantilever beam model.

$$EI\frac{d^2\varphi}{ds^2} + F\cos\varphi = 0 \tag{1}$$

Above equation is the non-linear differential equation that governs the deflection of a cantilever beam made of a linear elastic material subjected to vertical concentrated load at the free end. Eventually the arc length s (along the beam) and vertical deflection Y can be found as follows

$$s = \sqrt{\frac{EI}{2F}}\int_0^{\varphi}\frac{d\varphi}{\sqrt{\sin\varphi_o - \sin\varphi}}, \tag{2}$$

$$\frac{Y}{a} = \frac{1}{\sqrt{2}\alpha}\int_0^{\varphi_o}\frac{\sin\varphi d\varphi}{\sqrt{\sin\varphi_o - \sin\varphi}}, \quad \text{here } \alpha = \sqrt{\frac{Fa^2}{EI}}, a = \text{length of the beam} \tag{3}$$

Here φ_o is the unknown slope at the free end of the beam. Eqs. (2) and (3) can be split into complete and incomplete elliptic integrals of the first and second kinds that can be solved numerically. Alternatively Eq. (1) may be solved numerically to get φ, that may be used to get deflection by the following relation;

$$Y = \int_0^a \sin(\varphi)ds \tag{4}$$

Primarily, due to aforementioned size effects at micro/nano scale, the strain gradients must be incorporated in the formulations to accurately predict the structural behavior. In general, the higher order strain-gradient models, available in literature, are majorly concerned with second-order strain gradients. These models have been used in elasticity, plasticity and damage tolerance. As explained in the introduction, the theory presented by Vardoulakis and Sulem [41] is much more convenient in applications [16] and therefore employed in this work. For one-dimensional case, combined with linear elastic material behavior the constitutive equation can be written as [1,3];

$$\sigma = E(\varepsilon - l^2\nabla^2\varepsilon) \tag{5}$$

where σ is the axial stress, ϵ is the axial strain, E is the Young's modulus, l is the material parameter with the dimension of length that reflects the micromechanical properties of the material and $\nabla^2 = \partial^2/\partial x^2 + \partial^2/\partial y^2 + \partial^2/\partial z^2$ is the Laplacian operator. Eq. (5) is usually taken as a mean of smoothing of heterogeneity. On the other hand, strain gradient theory may also be

employed to introduce heterogeneity into the continuum. For latter case, the second order gradient model is of the type; $\sigma = E(\varepsilon + l^2\nabla^2\varepsilon)$. The sign of the higher-gradient term determines the character of the higher-gradient model. The gradient model with the negative sign has the better properties from the point of view of stability and uniqueness [3] and, therefore used in this study. The expression of strain for Euler-Bernoulli beam is given as, $\varepsilon = zk = z\frac{d\varphi}{ds}$,where k is the radius of curvature, φ is the deformed angle. Though a beam is defined in a 2D geometrical space, the xy-plane, the problem still remains in 1D as the resulting deflection is solely the function of "s" or "x". Therefore, the ∇^2 operator is reduced to cater only 1D gradient. The constitutive equation for a cantilever beam (provided length to height ratio $\geq$ 10 [8]) for 1D cases i.e. $\sigma_{yy} = \sigma_{zz} = \sigma_{yz} = \sigma_{xz} = \sigma_{xy} = 0$ according to Eq. (5) may be written as;

$$\sigma_{xx} = Ez\left[\frac{d\varphi}{ds} - l^2\frac{d^3\varphi}{ds^3}\right] \tag{6}$$

Bending moment at x is given as, $M = \int_A \sigma_{xx} z dA$. Using Eq. (6) in bending moment equation and upon integration over the cross section area A, one gets

$$M = EI\left[\frac{d\varphi}{ds} - l^2\frac{d^3\varphi}{ds^3}\right] \tag{7}$$

Eq. (7) gives the higher order, non-classical moment incorporating the effect of strain gradient. Here $I = \int_A z^2 dA$ is the second moment of cross-sectional area. Differentiating the above equation with respect to s, we get

$$\frac{dM}{ds} = EI\left[\frac{d^2\varphi}{ds^2} - l^2\frac{d^4\varphi}{ds^4}\right].$$

From Fig. 1, one can obtain

$$EI\left[\frac{d^2\varphi}{ds^2} - l^2\frac{d^4\varphi}{ds^4}\right] = -F\cos\varphi \tag{8}$$

Here we did not consider the dependence of E on size. In order to simplify the strain gradient model, EI was assumed to be constant as done by some other researches as well [22,25], our model applies to these materials without significant dependence of E on size.

Now, the boundary conditions of the DCB can be described as follows;

At clamped end i.e. $s = 0$, the slope or the boundary classical moments of the beam have to be specified [25] i.e. the rotation of the beam is zero $\varphi = 0$, and the trivial natural boundary conditions for the non-classical terms may be written as i.e. $\frac{d^3w}{dx^3} = 0$, where w is the deflection of the beam. However for large deformation it may estimate to be $\frac{d^2\varphi}{ds^2} = 0$ (since $\varphi = dw/ds$). Meanwhile, at free end i.e. $s = a$, $\frac{d\varphi}{ds} = 0$ [6] and the non-classical or higher order moment as depicted in Eq. (7) would also be zero at the free end that gives $\frac{d\varphi}{ds} - l^2\frac{d^3\varphi}{ds^3} = 0$. Overall, the boundary conditions may fairly be written as;

$$\text{At } s = 0 : \varphi = 0, \quad \frac{d^2\varphi}{ds^2} = 0$$

$$\text{At } s = a : \frac{d\varphi}{ds} = 0, \frac{d\varphi}{ds} - l^2\frac{d^3\varphi}{ds^3} \text{ or } \frac{d\varphi}{ds} = 0, \frac{d^3\varphi}{ds^3} = 0$$

The nonlinear boundary value problem as presented in Eq. (8) with respective boundary conditions is numerically solved using a finite difference method that implements a three-stage Lobatto IIIa collocation formula. Lobatto methods are the numerical integration methods to get the approximate solution of differential equations at the two end points t_n and t_{n+1} of each interval of integration $[t_n, t_{n+1}]$. These methods are based on trapezoidal quadrature rule. There are several types of Lobatto methods i.e. Lobatto IIIA, IIIB, IIIC and IIIC* that are usually characterized by coefficients being used in the approximated solution. Lobatto IIIA method is usually considered for boundary value problem due to their good stability properties. The Matlab code bvp4c for boundary value problems that have been used in this work is based on the 3 stage Lobatto IIIA method. Further details of this and other relevant methods are provided by Shampine et al. [38].

2.2. Results and Discussion

To illustrate the bending behavior of cantilever beam under large deformation, the material characteristic length (l) is taken to be 17.6 μm [25]. The values of force F (concentrated vertical force) and height h are chosen in such a way that the beam remains elastic everywhere. The static rotation of a cantilever beam, normalized by the classical result at the free end of the beam i.e. $Fa^2/(2EI)$ is presented in Fig. 2. The curves are depicted for $b/h = 2$, here b is the width of the beam. The normalized deformation curves are obtained for different h/l ratios ($a/h = 20$). It can be seen that, for smaller h/l ratios, the

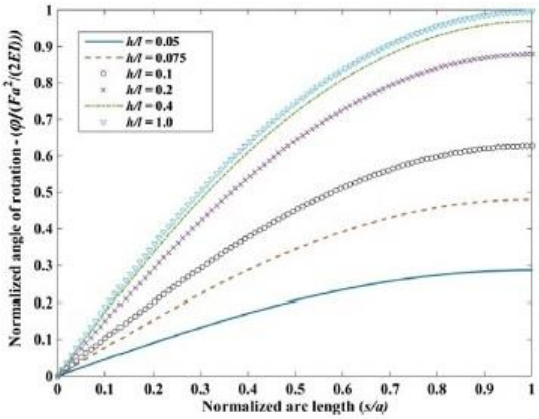

Fig. 2. Normalized angle of rotation along the beam for strain gradient model.

strain gradient beam models are stiffer than the classical models. The normalized deformations are shown to be increasing with increasing h/l, with the maximum deformation becoming almost comparable when $h/l \approx 1$. In order to further establish the negligence of strain gradient effect when $h \gg l$ and the effect of geometrical non-linearity with increased load factor F_o ($F_o = Fa^2/2(EI)$), the normalized maximum deflections for beams with various h/l ratios ($a/h = 20$) are numerically obtained using Eq. (4) and are shown in Fig. 3. Here Y_g and Y represent the deflection obtained with strain gradient and non-gradient model. Fig. 3 shows that the normalized tip deflection increases with the increasing load factor F_o, signifying greater effect of geometrical non-linearity (larger non-gradient deflection) at enhanced loads. Meanwhile, it may be seen that with higher h/l ratio, as high as 10, the maximum deflection of gradient and non-gradient model are equal, demonstrating negligible strain gradient effect. The comparison of Y_g with Y and Y_g with classical formulation (small deformation & without strain gradient effect) Y_o ($Y_o = Fa^3/(3EI)$) for various beam configurations is established in Fig. 4. The non-dimensional parameter as abscissa is defined for convenience, given as $3Fa^2/(Eh^4)$, also for comparison the h/l ratio is considered to be less than or equal to 1. This was done to precisely illustrate the effect of beam geometry on its mechanical behavior, particularly on smaller scale ($h \leqslant l$). The normalized maximum deflection Y_g/Y versus the non-dimensional parameter $3Fa^2/(Eh^4)$ is plotted in Fig. 4a. It is clear from Fig. 4a that the effect of strain gradient is more evident when the length to thickness ratio a/h is small, demonstrating small deflections for gradient structure and hence depicting stiffer response. The maximum deflection for strain gradient beam would approach as that of non-gradient beam, when the length of the beam is very large.

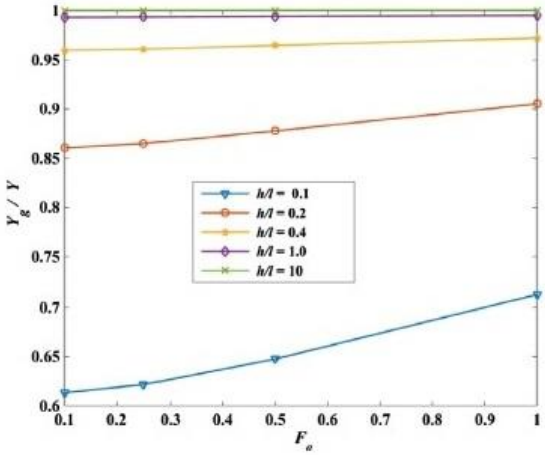

Fig. 3. Normalized tip deflection against the load factor F_o.

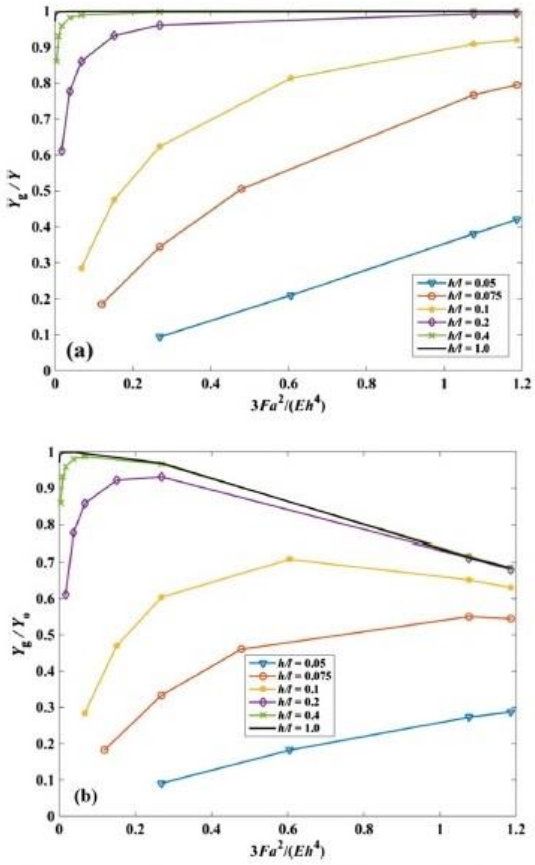

Fig. 4. Maximum tip deflection (large deformation), against the parameter $3Fa^2/(Eh^4)$, of gradient model normalized with: (a) non-gradient model (large deformation); (b) classical model.

It can also be seen that the difference between the results predicted by model with & without strain gradient effect (large deformation) is significant when h/l is low while the difference diminishes when h/l approaches 1(for the presented gradient model). The strain gradient effect is shown to be more prominent when $h/l \leqslant 0.2$. For instance when $h/l = 0.05$ and $3Fa^2/(Eh^4) = 1$, the strain gradient formulation predicts almost one-third of the deflection obtained from non-gradient formulation. Fig. 4b illustrates the comparison of results obtained from strain gradient model with the classical model (small deformation & without strain gradient effect). It is shown that for smaller beam lengths, the Y_g/Y and Y_g/Y_o are identical, indicating that the large deformation and classical model predict same results. However, with the increase of beam length (hence a/h ratio), the beam will undergo large deformation and hence the classical theory would overestimate the end point deflection. For each curve, the peak point is evident in Fig. 4b, which demonstrates the onset of a point at which deficiency of the classical model to accurately predict the large deformation becomes noticeable. Furthermore, it may fairly be concluded that when $h/l \geqslant 0.2$, the factor with which the classical model would overestimate the deflection converge to the same point. Next, the accurate tip deflections of a cantilever beam will be used to estimate the fracture behavior of double cantilever beam in the following section.

3. Fracture analysis of double cantilever beam

As illustrated in the previous section the size effect on the mechanical behavior of micro beam, the same influences may also be witnessed in fatigue and fracture properties as well. Since it has been demonstrated, in comparison with classical theories, the strain gradient theory predicts smaller strains [16] and hence longer life for small scale components according

to the approach introduced by Basquin [4]. Zhang et al. [48] experiments demonstrated a pronounced strengthening in the fatigue strength of small-scale metallic components. The results were credited to the fine grain size and small geometrical dimensions. Stamoulis and Giannakopoulos [39] adopted strain gradient elasticity formulations to study the size effect and length scale in fracture and fatigue of metals. They also employed SGE theory to analytically investigate the microstructural size effects in analysing cantilever bending and cracked bar uniaxial tension [16]. In recent times several attempts have been made to evaluate fracture analysis of complex geometries using advance numerical techniques [14,21] and to cater the size effect on the fracture properties at small scale as investigated by Giannakopoulos and Stamoulis [16,39] and Guha et al. [17], it is evident that this subject is still open for innovation and updates.

3.1. Numerical results and discussion

Strain energy release rate may be evaluated using $G = dU_I/bda$, where $U_1 = \frac{1}{2}\int_0^a U dx$ with U as the specific intrinsic energy [3]. Alternatively, taking the crack length to be the length of the beam as a and width b, the strain energy release rate of double cantilever beam is given by $G = F\,(dY_{max}/bda)$ [39]. Meanwhile, the classical Euler beam theory solution is given by $G_o = 12F^2a^2/(Eh^3b^2)$ [45]. The method adopted is based on the notion that the external work done ($F*Y_{max}$) will be stored in the body as potential energy.

Double cantilever beam may be assumed to consist of two cantilever beams with the configuration and loading as shown in the previous section (Fig. 1). Fig. 5 displays, the normalized energy release with respect to the non-dimensional parameter

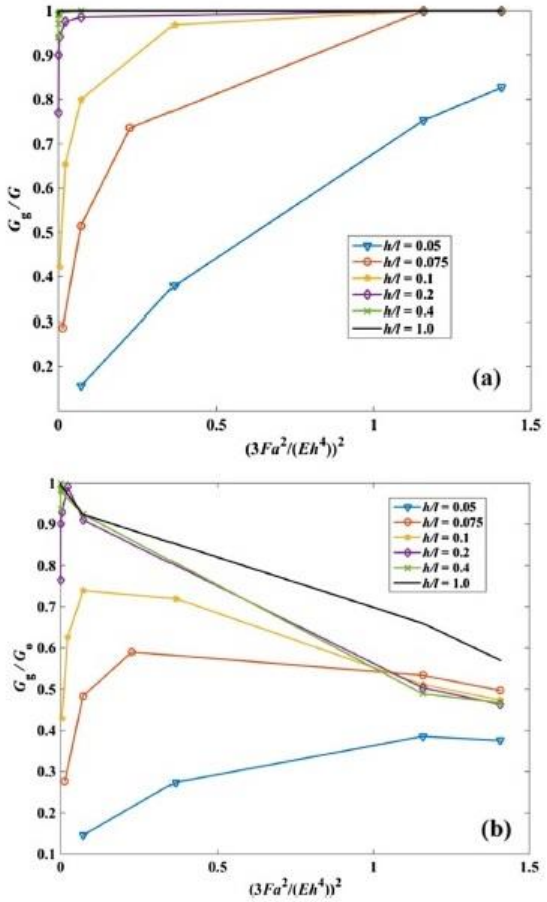

Fig. 5. Strain energy release rate (large deformation), against the parameter $(3Fa^2/(Eh^4))^2$, of gradient model normalized with: (a) non-gradient model (large deformation); (b) classical model.

$3Fa^2/(Eh^4)$. For comparison, as in the previous section, the results for strain gradient & non-gradient model (large deformation) and classical theory are given. Here the notations G_g, G and G_o are used to represent the energy release rate (G) for large deformation strain gradient model, large deformation non-gradient model and classical model (small deformation & without strain gradient effect) respectively. Evidently from Fig. 5a, the influence of strain gradient on the strain energy release becomes more prominent when h/l is low i.e. for thinner beams. In particular, the strain gradient effect cannot be neglected when $h/l \leqslant 0.2$, even when the ratio between the length to height of the beam is higher. Also, for $h/l \geqslant 0.2$, the strain gradient effect tends to diminish rapidly and eventually the strain energy release rate would be the same as predicted by large deformation formulation (without strain gradient). Meanwhile, the strain gradient effect diminishes when $h/l \approx 1$ (for the presented gradient model). Such observation is considerably different when the strain gradient results are compared with the classical ones for comparatively larger beams. From Fig. 5b, for larger a/h, the classical theory will tend to overestimate the strain energy release rate. This can be seen quite clearly as a peak point on each curve. For $h/l \leqslant 1$, this peak appeared quite early in the curve, depicting a particular a/h ratio, beyond which the classical model tends to overestimate the mechanical behavior.

3.2. Root Effect of the DCB

For the uncracked part of the DCB (Fig. 6), the strain gradient effect is much smaller as compare to that of the cracked part of DCB; therefore the strain gradient effect is neglected here. Thus, the governing equation and respective boundary conditions of the uncracked of the DCB due to its root effect, based on Timoshenko beam theory are shown in Appendix A;

The potential energy of the root part can be expressed as;

$$U_2 = 2\int_{-\infty}^{0} \frac{M^2}{2EI}\mathrm{d}x + 2\int_{-\infty}^{0} \frac{Q^2}{2G^sA}\mathrm{d}x \tag{9}$$

Here E is the Young's Modulus, G^s is the shear modulus, A is the area of cross section and I is the moment of inertia of the beam. It is interesting to note that, for root part, the integral varies from negative infinity to zero as per the coordinate system. From Appendix A (A.3) and using $M_{(a)} = F.X$ we get,

$$U_2 = \frac{F^2X^2_{(\varphi_a)}}{\sqrt{EIG^sA}}, \quad \text{here} \quad X_{(\varphi_a)} = \int_0^a \frac{\mathrm{d}X}{\mathrm{d}s}\mathrm{d}s = \int_0^a \cos\varphi(s)\mathrm{d}s \tag{10}$$

Here $X_{(\varphi_a)}$ is the horizontal tip position at deflection φ_a.

Now the effect of uncracked part of the DCB on its fracture behavior is numerically investigated. The ratio of the strain energy release rate contributed by the uncracked part to the strain energy release rate contributed by the cracked part of DCB is defined as R. Variations of R versus a/h for different h/l ratios are plotted in Fig. 7. It may be seen that for non-gradient model, R approaches 0.05 approximately, when the beam length to thickness ratio approaches 20, demonstrating a neglecting root effect of the DCB. However, when the dimensions of the DCB are very small i.e. for $h/l \leqslant 0.2$ & $a/h \leqslant 20$, the value of R may not be neglected even through the beam length to thickness ratio is higher. Interestingly, when $h/l \leqslant 0.1$ and the smaller a/h, the contribution of the root part is shown to be quite prominent and hence should be incorporated in the formulations when dealing with the strain gradient theory. For smaller h/l and a/h ratios, for instance $h/l = 0.05$ and $a/h = 10$, it can be seen that the energy release rate of uncracked part is 0.65 (approx.) times as that of cracked part but the overall response of the gradient model will remain stiffer. The comparison of gradient model with and without root effect with the non-gradient (large deformation) model is shown in Fig. 8. This observation clearly demonstrates the stiffening response of a structure at smaller scale (whether root effect are included or not) and is completely different from the classical results. Similarly, it has been observed that, for $h/l > 0.2$ when the length to thickness ratio of the beam exceeds 20 the energy release rate of uncracked part is small as compared to that of cracked part and hence may be neglected for the sake for model's simplicity.

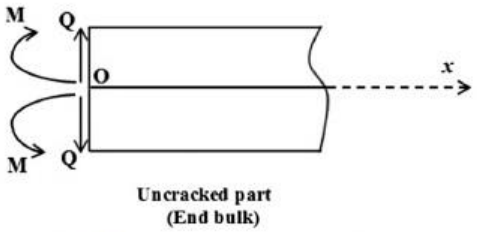

Fig. 6. Schematic diagram of root part of the DCB.

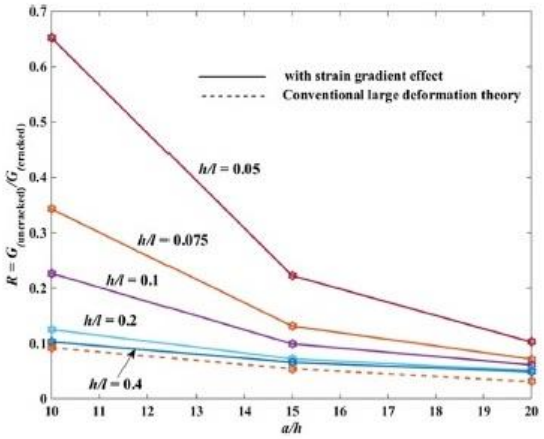

Fig. 7. Variation of R versus a/h.

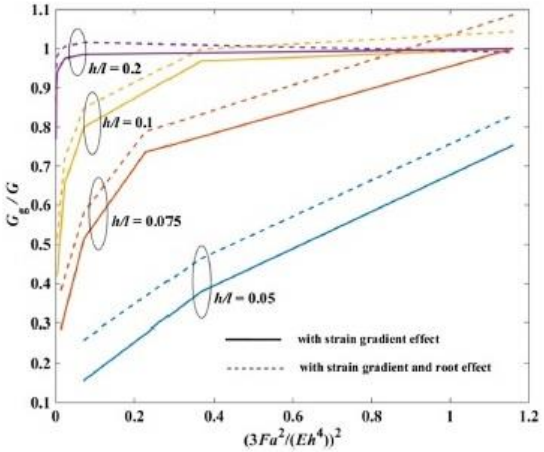

Fig. 8. Ratio of strain energy release rate with/without root effect against the parameter $(3Fa^2/(Eh^4))^2$.

4. Conclusions

Strain gradient contribution on the large deformation of cantilever beam is investigated and compared with the conventional large deformation (without strain gradient) and classical model. The gradient model is shown to enhance the stiffness of the beam. This size effect of cantilever beam is later employed to investigate the fracture behavior of double cantilever beam. The effect of strain gradient on the strain energy release rate is evaluated. Both the cracked and uncracked portions of the DCB are included. The strain energy release rate is numerically estimated by using Euler beam model. Due to small strains, the gradient effect is ignored for the uncracked part of the DCB. Results show that the strain gradient effect is prominent when $h/l \leqslant 0.2$, however the effect tends to diminish when the length to thickness ratio of the DCB increases. In particular, the strain gradient effect cannot be neglected when $h/l \leqslant 0.2$. Moreover, it is shown that the consideration of large deformation is essential for longer beams. The root effect also enhances the normalized strain energy release rate. It is observed that for $h/l \leqslant 0.2$, uncracked part plays a dominant role in the fracture behavior of the DCB and it must not be ignored. However, for $h/l > 0.2$, root effect may only be ignored provided $a/h \geqslant 20$. This observation is completely different from the classical result, which suggests that the root effect can be neglected if beam length to thickness ratio is higher [45]. The results of this paper are useful for the determination of the fracture toughness of micro/nanoscale materials and explanation of the test data of the DCBs.

Acknowledgement

The authors wish to express gratitude to Centre for Infrastructure Engineering, School of Computing, Engineering and Mathematics, Western Sydney University (Australia) for the support of the work. In particular, the authors are extremely thankful to the reviewers for their valuable suggestions in improving the quality of this paper.

Appendix A.

Governing equations of the root part of DCB

$$\frac{dN}{dx} = q, \quad \frac{dM}{dx} = Q + q\frac{h}{2}, \quad \frac{dQ}{dx} = p, \tag{A.1}$$

$$\frac{d^2u_0}{dx^2} = 0, \quad \frac{d^2\varphi}{dx^2} - \beta^2\varphi = 0, \quad p = G^sA\frac{d\varphi}{dx} \quad \text{here } \beta^2 = \frac{G^sA}{EI} \tag{A.2}$$

Boundary Conditions;

1. At $x = 0$, $N = 0$ and $M_{(0)} = FX_{(\varphi_0)}$
2. At $x = -\infty, N = 0, M = 0$

where p and q are, respectively the normal stress and the shear stress on the $z = 0$ plane and here q would be zero, u_0 is the displacement in x direction, N is the resultant force along the x direction, M is the bending moment, Q is the shear force on the beam cross-section, u_o is the displacement of the beam along the x direction. Using boundary conditions and Eq. (A.1), we obtain

$$N = 0, M(x) = M_{(0)}e^{\beta x}, Q(x) = \alpha M_{(0)}e^{\beta x} \tag{A.3}$$

References

[1] Aifantis EC. Strain gradient interpretation of size effects. Int J Fract 1999;95(1–4):299–314. http://dx.doi.org/10.1023/A:1018625006804.
[2] Anderson TJ, Nayfeh AH, Balachandran B. Experimental verification of the importance of the nonlinear curvature in the response of a cantilever beam. J Vib Acoust 1996;118(1):21–7. http://dx.doi.org/10.1115/1.2889630.
[3] Askes H, Suiker ASJ, Sluys LJ. A classification of higher-order strain-gradient models–linear analysis. Arch Appl Mech 2002;72(2–3):171–88. http://dx.doi.org/10.1007/s00419-002-0202-4.
[4] Basquin OH. The exponential law of endurance tests. Paper presented at the proc. ASTM; 1910.
[5] Behzadi SH, Rafii-Tabar H. Atomistic modelling of crack propagation in a randomly rough nano-scale metallic surface. J Mol Graph Model 2008;27(3):356–63. http://dx.doi.org/10.1016/j.jmgm.2008.06.005.
[6] Beléndez T, Neipp C, Beléndez A. Large and small deflections of a cantilever beam. Eur J Phys 2002;23(3):371. http://dx.doi.org/10.1088/0143-0807/23/3/317.
[7] Cheng MN, Cheung CF, Lee WB, To S, Kong LB. Theoretical and experimental analysis of nano-surface generation in ultra-precision raster milling. Int J Mach Tools Manuf 2008;48(10):1090–102. http://dx.doi.org/10.1016/j.ijmachtools.2008.02.006.
[8] Christensen J, Bastien C. Nonlinear optimization of vehicle safety structures: modeling of structures subjected to large deformations. USA: Butterworth-Heinemann; 2015.
[9] De Morais AB. A new fibre bridging based analysis of the Double Cantilever Beam (DCB) test. Compos A Appl Sci Manuf 2011;42(10):1361–8. http://dx.doi.org/10.1016/j.compositesa.2011.05.019.
[10] De Moura MFSF, Morais JJL, Dourado N. A new data reduction scheme for mode I wood fracture characterization using the double cantilever beam test. Eng Fract Mech 2008;75(13):3852–65. http://dx.doi.org/10.1016/j.engfracmech.2008.02.006.
[11] Devitt DF, Schapery RA, Bradley WL. A method for determining the mode I delamination fracture toughness of elastic and viscoelastic composite materials. J Compos Mater 1980;14:270–85. http://dx.doi.org/10.1177/002199838001400401.
[12] Fermeglia M. Multiscale molecular modeling: a tool for the design of nano structured materials. Comput Aided Chem Eng 2008;25:725. http://dx.doi.org/10.1016/S1570-7946(08)80126-5.
[13] Fleck NA, Hutchinson JW. Strain gradient plasticity. Adv Appl Mech 1997;33:296–361. http://dx.doi.org/10.1016/S0065-2156(15)00022-8.
[14] Fleming M, Chu YA, Moran B, Belytschko T, Lu YY, Gu L. Enriched element-free Galerkin methods for crack tip fields. Int J Numer Meth Eng 1997;40(8):1483–504. http://dx.doi.org/10.1002/(SICI)1097-0207(19970430)40:8.
[15] Giannakopoulos AE, Amanatidou E, Aravas N. A reciprocity theorem in linear gradient elasticity and the corresponding Saint-Venant principle. Int J Solids Struct 2006;43(13):3875–94. http://dx.doi.org/10.1016/j.ijsolstr.2005.05.048.
[16] Giannakopoulos AE, Stamoulis K. Structural analysis of gradient elastic components. Int J Solids Struct 2007;44(10):3440–51. http://dx.doi.org/10.1016/j.ijsolstr.2006.09.033.
[17] Guha S, Sangal S, Basu S. Finite element studies on indentation size effect using a higher order strain gradient theory. Int J Solids Struct 2013;50(6):863–75. http://dx.doi.org/10.1016/j.ijsolstr.2012.10.017.
[18] Jia XL, Yang J, Kitipornchai S. Pull-in instability of geometrically nonlinear micro-switches under electrostatic and Casimir forces. Acta Mech 2011;218(1–2):161–74. http://dx.doi.org/10.1007/s00707-010-0412-8.
[19] Jia XL, Yang J, Kitipornchai S, Lim CW. Free vibration of geometrically nonlinear micro-switches under electrostatic and Casimir forces. Smart Mater Struct 2010;19(11):115028. http://dx.doi.org/10.1088/0964-1726/19/11/115028.
[20] Jing GY, Duan HL, Sun XM, Zhang ZS, Xu J, Li YD, Yu DP. Surface effects on elastic properties of silver nanowires: contact atomic-force microscopy. Phys Rev B 2006;73(23):235409. http://dx.doi.org/10.1103/PhysRevB.73.235409.
[21] Joseph RP, Purbolaksono J, Liew HL, Ramesh S, Hamdi M. Stress intensity factors of a corner crack emanating from a pinhole of a solid cylinder. Eng Fract Mech 2014;128:1–7. http://dx.doi.org/10.1016/j.engfracmech.2014.07.021.
[22] Kahrobaiyan MH, Asghari M, Rahaeifard M, Ahmadian MT. A nonlinear strain gradient beam formulation. Int J Eng Sci 2011;49(11):1256–67. http://dx.doi.org/10.1016/j.ijengsci.2011.01.006.

[23] Kang Y, Xie H. Micro and nano metrology in experimental mechanics. Opt Lasers Eng 2010;48(11):1045. http://dx.doi.org/10.1016/j.optlaseng.2010.02.010.
[24] Kanninen MF. An augmented double cantilever beam model for studying crack propagation and arrest. Int J Fract 1973;9(1):83–92. http://dx.doi.org/10.1007/BF00035958.
[25] Kong S, Zhou S, Nie Z, Wang K. Static and dynamic analysis of micro beams based on strain gradient elasticity theory. Int J Eng Sci 2009;47(4):487–98. http://dx.doi.org/10.1016/j.ijengsci.2008.08.008.
[26] Lam DCC, Yang F, Chong ACM, Wang J, Tong P. Experiments and theory in strain gradient elasticity. J Mech Phys Solids 2003;51(8):1477–508. http://dx.doi.org/10.1016/S0022-5096(03)00053-X.
[27] Li XF, Wang BL. Vibrational modes of timoshenko beams at small scales. Appl Phys Lett 2009;94(10):101903. http://dx.doi.org/10.1063/1.3094130.
[28] Li XF, Wang BL, Lee KY. Size effects of the bending stiffness of nanowires. J Appl Phys 2009;105(7):074306. http://dx.doi.org/10.1063/1.3103322.
[29] Landau LD, Lifshitz EM. Theory of elasticity, vol. 7. Course of yhysics, 3, 109; 1986. [Identifier-ark:/13960/t6vx1gh69].
[30] Ma Q, Clarke DR. Size dependent hardness of silver single crystals. J Mater Res 1995;10(04):853–63. http://dx.doi.org/10.1557/JMR.1995.0853.
[31] McFarland AW, Colton JS. Role of material microstructure in plate stiffness with relevance to microcantilever sensors. J Micromech Microeng 2005;15(5):1060. http://dx.doi.org/10.1088/0960-1317/15/5/024.
[32] Mindlin RD. Second gradient of strain and surface-tension in linear elasticity. Int J Solids Struct 1965;1(4):417–38. http://dx.doi.org/10.1016/0020-7683(65)90006-5.
[33] Polizzotto C. A note on the higher order strain and stress tensors within deformation gradient elasticity theories: physical interpretations and comparisons. Int J Solids Struct 2016. http://dx.doi.org/10.1016/j.ijsolstr.2016.04.001.
[34] Popescu M. The atomic scale modelling of nanomaterials. J Phys Chem Solids 2007;68(5):687–94. http://dx.doi.org/10.1016/j.jpcs.2007.02.050.
[35] Rao GV, Raju KK. Variational formulation for the finite deflection analysis of slender cantilever beams and columns. Aeronaut Soc India, J 1977;29:133–5.
[36] Reeder JR, Crews Jr J. Nonlinear analysis and redesign of the mixed-mode bending delamination test; 1991.
[37] Sebaey TA, Blanco N, Lopes CS, Costa J. Numerical investigation to prevent crack jumping in Double Cantilever Beam tests of multidirectional composite laminates. Compos Sci Technol 2011;71(13):1587–92. http://dx.doi.org/10.1016/j.compscitech.2011.07.002.
[38] Shampine LF, Kierzenka J, Reichelt MW. Solving boundary value problems for ordinary differential equations in MATLAB with bvp4c; 2000. [Tutorial notes].
[39] Stamoulis K, Giannakopoulos AE. A study of size effects and length scales in fracture and fatigue of metals by second gradient modelling★. Fatigue Fract Eng Mater Struct 2012;35(9):852–60. http://dx.doi.org/10.1111/j.1460-2695.2012.01668.x.
[40] Togun N. Nonlocal beam theory for nonlinear vibrations of a nanobeam resting on elastic foundation. Boundary Value Probl 2016. http://dx.doi.org/10.1186/s13661-016-0561-3.
[41] Vardoulakis I, Sulem J. Bifurcation analysis in geomechanics. London: Blackie/Chapman and Hall; 1995.
[42] Villanueva LG, Karabalin RB, Matheny MH, Chi D, Sader JE, Roukes ML. Nonlinearity in nanomechanical cantilevers. Phys Rev B 2013;87(2):024304. http://dx.doi.org/10.1103/PhysRevB.87.024304.
[43] Voyiadjis GZ, Almasri AH, Park T. Experimental nanoindentation of BCC metals. Mech Res Commun 2010;37(3):307–14. http://dx.doi.org/10.1016/j.mechrescom.2010.02.001.
[44] Wang BL, Hoffman M, Yu AB. Buckling analysis of embedded nanotubes using gradient continuum theory. Mech Mater 2012;45:52–60. http://dx.doi.org/10.1016/j.mechmat.2011.10.003.
[45] Wang BL, Wang KF. Effect of surface residual stress on the fracture of double cantilever beam fracture toughness specimen. J Appl Phys 2013;113(15):153502. http://dx.doi.org/10.1063/1.4801875.
[46] Wang KF, Wang BL. Nonlinear fracture mechanics analysis of nano-scale piezoelectric double cantilever beam specimens with surface effect. Eur J Mech – A/Solids 2016;56:12–8. http://dx.doi.org/10.1016/j.euromechsol.2015.10.002.
[47] Williams JG. Large displacement and end block effects in the 'DCB' interlaminar test in modes I and II. J Compos Mater 1987;21(4):330–47. http://dx.doi.org/10.1177/002199838702100403.
[48] Zhang GP, Takashima K, Higo Y. Fatigue strength of small-scale type 304 stainless steel thin films. Mater Sci Eng, A 2006;426(1):95–100. http://dx.doi.org/10.1016/j.msea.2006.03.090.
[49] Zhang H, Li XB, Tang GJ, Shen ZB. Stress intensity factors of double cantilever nanobeams via gradient elasticity theory. Eng Fract Mech 2013;105(2013):58–64. http://dx.doi.org/10.1016/j.engfracmech.2013.03.005.

Paper 2:

Arch Appl Mech
https://doi.org/10.1007/s00419-018-1406-6

ORIGINAL

R. P. Joseph · B. Wang · B. Samali

Size-dependent stress intensity factors in a gradient elastic double cantilever beam with surface effects

Received: 5 April 2018 / Accepted: 30 May 2018

Abstract In this article, the size-dependent stress intensity factors in an elastic double cantilever beam (DCB) are obtained using strain gradient theory. The surface effects are included, while the DCB is assumed to undergo large deformation. Both cracked and uncracked parts (root effect) of the DCB are incorporated in modeling and analyses. The Variational principle is employed to obtain the governing equation and the corresponding boundary conditions. The deflections along the beam axis and stress intensity factors are obtained and plotted. Results exhibit large deformation to be influential for slender beams at small scale. Strain gradient effect tends to increase beam stiffness though reverse holds true for the root effect of the DCB. These effects on structure stiffness are conspicuous when the beam thickness is less than the material characteristic length. Due to positive surface residual stress, beam exhibits less stiff behavior in comparison with the negative surface residual stress. This softening behavior may be credited to the sign of curvature that causes an additional distributed load and alters beam stiffness. It is shown that even with the root effect, negative surface residual stress causes the DCB to display stiffer response by lowering the stress intensity factors and vice versa.

Keywords Stress intensity factors · Double cantilever beam · Strain gradient theory · Surface effects

1 Introduction

Redesigned mixed mode bending (MMB) apparatus, based on geometrical nonlinearity, reduces the error from 30 to 3% in determining its bending behavior [1,2]. The cantilever beam is one of the essential building blocks used in micro and nanoelectromechanical (MEMS and NEMS) devices and often undergoes geometrical nonlinearity. Generally, the geometrical nonlinearity associated with cantilever beam is due to the nonlinear curvature, effect of which is highly substantial [3] (due to the insignificance of Von Karman strain [4,5]). The DCB specimen is widely used to determine the critical stress intensity factors (or strain energy release rate) of homogenous, as well as non-homogenous materials under mode I loading configuration. Furthermore, a double cantilever beam is generally analyzed by examining the bending behavior of a cantilever beam [6,7], since it is considered to be made of two cantilevers attached with an uncracked part. Moreover, the consideration of geometric nonlinearity in the mode I fracture toughness of non-homogenous materials is sufficed for long cracks as shown by Devitt et al. [8] and Williams [9].

Contrary to the classical continuum elasticity theories, the non-classical theories assume that stress at a material point is not entirely depended on the strain at that point but also on all other points in the body [10,11]. This process in literature is referred as the strain gradient effect, and it is more evident when the external and the internal dimensions of the structure become comparable such as in micro-electromechanical

R. P. Joseph · B. Wang (✉) · B. Samali
Centre for Infrastructure Engineering, School of Computing, Engineering and Mathematics, Western Sydney University, Penrith, NSW 2751, Australia
E-mail: b.wang@westernsydney.edu.au

Published online: 07 June 2018

systems (MEMS) and nanoelectromechanical systems (NEMS). In that case, microstructural length scales of a particular material become comparable to the length scale of the deformation field that eventually leads to a non-homogenous and size-dependent structural behavior [6]. The strain gradient model employed in this work was introduced by Aifantis [12], Ru and Aifantis [13], and Vardoulakis & Sulem [14], which is considered more convenient in applications [6,15]. The Cauchy stress (τ_{xx}) and double stress (μ_{xxx}) for the 1-D case are given as: $\tau_{xx} = E\varepsilon_{xx}$ and $\mu_{xxx} = l^2 E\frac{d\varepsilon_{xx}}{dx}$ respectively [7]. Here, E is Young's Modulus; ε_{xx} is the axial strain in the beam due to bending, l is the material microstructural length constants related to the bulk strain energy. The total stresses (σ_{xx}) for the beam bending can be evaluated as: $\sigma_{xx} = \tau_{xx} - \frac{d\mu_{xxx}}{dx} = E(\varepsilon_{xx} - l^2\frac{d^2\varepsilon_{xx}}{dx^2})$. The application and validation of this simpler strain gradient theory are presented by Vardoulakis & Sulem [14] and Giannakopoulos et al. [6], respectively. A comprehensive review of this gradient theory along with the applications of internal length gradient across various scales is provided by Aifantis [16,17].

There are certain molecular effects that are fascinatingly obvious when the structural dimensions are in micro and nanometer range. Effect of the surface stresses is one of those effects that have thoroughly been explained [18,19]. The atoms on or near the free surface have different equilibrium requirements as compared to the ones in bulk. This difference causes an excess energy at the surface which is understood as a layer to which that energy is attached [20]. Accordingly, the thermodynamic theory of solid surface revealed that the relationship between the surface stress and surface free energy is obtainable [21–24]. Meanwhile, when the size of the structure is reduced to micro/nanoscale, the ratio of the surface area to bulk volume may become enormous. Therefore, the influence of surface effect on the mechanical behavior of the micro/nanomaterials becomes prominent and hence cannot be neglected [25]. Surface effects on micro/nanostructures may be characterized by two major types, i.e., the surface elasticity and the surface residual stress [26]. Gurtin and Murdoch [27] firstly considered the effect of surface stress in their theoretical framework based on continuum elasticity. In their work, the surface is considered as a mathematical layer of zero thickness with different material properties as compared to an underlying bulk. This theory has shown an excellent capability to successfully cater the surface effect on the mechanical behavior of the micro/nanostructures and is widely employed by the researchers throughout [28–33]. The general expression for the surface stress–strain relation is given as: $\sigma^s_{\alpha\beta} = \tau_o\delta_{\alpha\beta} + (\tau_o + \lambda^s)\varepsilon_{yy}\delta_{\alpha\beta} + 2(\mu^s - \tau^s)\varepsilon_{\alpha\beta} + \tau_o u^s_{\alpha,\beta}$, where λ^s and μ^s are the surface Lame constants, δ is Kronecker delta, and τ_o is the surface residual stress in the unconstrained condition. In general, the surface properties usually have anisotropic stress [34–36] depending upon the crystallographic direction of the surface. However, it is shown in the literature that a surface may assume anisotropic nature and it is still meaningful to use an appropriate average of the surface stresses [37–39].

The surface elastic model is effectively employed by the researchers with both surface residual stress and surface elasticity effects in the continuum model [34,40]. Moreover, the surface elastic model along with the generalized Young-Laplace equation has also been widely used to investigate the influence of surface effects on the mechanical response of nanostructures such as nanobeams/wires [26,41,42], nanoplates [43–45] and electrostatically actuated nanobeams [46–49]. However, the contribution of surface residual stress to the total surface stresses is considerably more noticeable than the surface elasticity [33,50]. As mentioned before that the DCB is a widely used specimen for the determination of fracture toughness of a particular material. However, very few efforts have been devoted to study its fracture behavior with the consideration of surface effect [25]. For precise fracture analysis, the future application of micro/nanomaterials demands an inclusion of surface effects in the crack tip field quantities such as strain energy release rate or stress intensity factor. This paper establishes the numerical analysis of a DCB specimen, subjected to large deformation, for the characterization of micro/nanomaterials, with the simultaneous consideration of surface effects and strain gradients. The schematic diagram of a DCB with surface residual stress is shown in Fig. 1a. Size-dependent fracture analysis of a DCB in terms of stress intensity factors with various beam configurations is presented. Finally, the role of uncracked part of the DCB (root effect) is elaborated to conclude this study.

2 Theoretical formulations of the size-dependent bending of a cantilever beam

Classical beam theory is inadequate to correctly evaluate the solution of a cantilever beam under large deformation (at enhanced loads in particular), primarily as it ignores the shortening of moment arm as the free end of the beam deflects. Due to this reason, the classical results deviate from the actual observations at elevated loads. The correction for this shortening of moment arm plays a key role in solving large deformation problems. For one dimension structure, the stress–strain relation for the bulk material (in case of large deformation) is

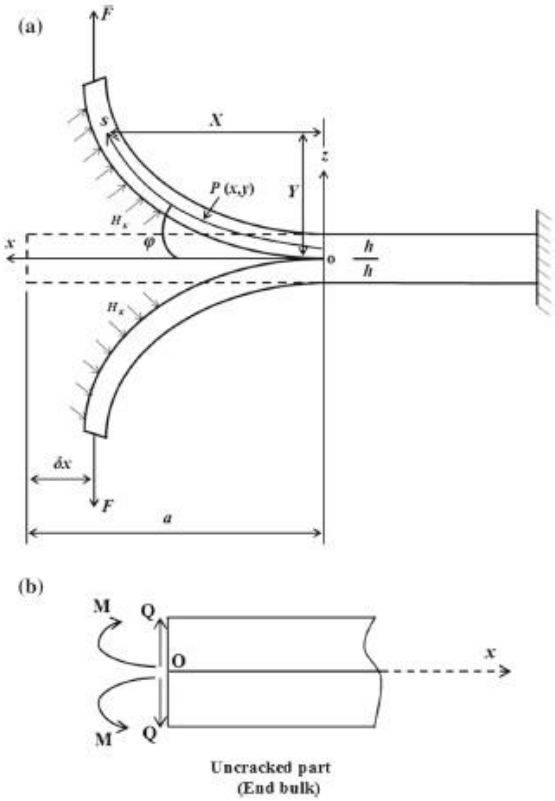

Fig. 1 Schematic diagram of **a** a double cantilever beam with surface residual stress; **b** the uncracked part

given as: $Ez\frac{d\varphi}{ds} = \sigma_{xx}$, where φ is the slope of beam and E is the Young's Modulus. For surface layer, the stress (τ^s) can be expressed as [51];

$$\tau^s = \tau_o + E_s\varepsilon^s_{xx} \tag{1}$$

where τ_o is the surface residual stress, E_s and ε^s_{xx} are Young's modulus and surface strain, respectively. Accordingly, the bending moment of a beam is given as:

$$M = \int_b z\sigma_{xx}dA + \int_C E_s\varepsilon^s_{xx}dC = EI_{eff}\frac{d\varphi}{ds} \tag{2}$$

where C is the perimeter of the beam's cross-section, $EI_{eff} = \frac{Ebh^3}{12} + \frac{E_sh^3}{6} + \frac{E_sbh^2}{2}$ [26,42]. At any specified point $P(x, y)$ along a curved beam, moment is given as: $M = F.(a - \delta x - x)$ (where a is the length of a beam and δx is the horizontal deflection), which if differentiated ($d(a - \delta x - x)/ds = -\cos\varphi$) gives;

$$EI_{eff}\frac{d^2\varphi}{ds^2} + F\cos\varphi = 0 \tag{3}$$

Vertical deflection Y and arc length s (along with the beam axis) may be evaluated as:

$$s = \sqrt{\frac{EI_{eff}}{2F}}\int_0^{\varphi}\frac{d\varphi}{\sqrt{\sin\varphi_o - \sin\varphi}} \tag{4}$$

$$\frac{Y}{a} = \frac{1}{\sqrt{2}\alpha} \int_0^{\varphi_o} \frac{\sin\varphi \mathrm{d}\varphi}{\sqrt{\sin\varphi_o - \sin\varphi}}; \text{ here } \alpha = \sqrt{\frac{Fa^2}{EI_{\text{eff}}}} \text{ and } a = \text{length of the beam} \tag{5}$$

Here, φ_o depicts an unknown slope at the free end. Eqs. (4) and (5) are usually solved numerically to evaluate Y. Alternatively, numerical techniques are applied to Eq. (3) to get φ and deflection Y by the following relation;

$$Y = \int_0^a \sin(\varphi) \mathrm{d}s \tag{6}$$

These straightforward formulations may not be precisely applied at micro/nanoscale due to the predominant size effect. In order to cater this, several strain gradient theories are available in the literature (mostly dealing with second-order strain gradients). The constitutive equation for the one-dimensional case in combination with the linear elastic material behavior is written as [15,52,53];

$$\sigma = E(\varepsilon - l^2 \nabla^2 \varepsilon) \tag{7}$$

where σ and ε are the axial stress and strain respectively, E is Young's modulus, l is the material characteristic length and $\nabla^2 = \partial^2/\partial x^2 + \partial^2/\partial y^2 + \partial^2/\partial z^2$ is the Laplacian operator. Strain for the Euler–Bernoulli beam is given as: $\varepsilon = z\kappa = z\frac{\mathrm{d}\varphi}{\mathrm{d}s}$, where κ is the curvature and φ is the deformed angle. The ∇^2 operator is reduced to cater only 1D gradient since the deformation is entirely the function of "s" (although a beam is defined in 2D geometrical space, i.e., xy-plane). For 1D cantilever beam, i.e., $\sigma_{yy} = \sigma_{zz} = \sigma_{yz} = \sigma_{xz} = \sigma_{xy} = 0$ (the beam length should at least 10 times of its height [54]), according to Eq. (7), the total stress (σ_{xx}) may be written as:

$$\sigma_{xx} = Ez\left[\frac{\mathrm{d}\varphi}{\mathrm{d}s} - l^2\frac{\mathrm{d}^3\varphi}{\mathrm{d}s^3}\right] \tag{8}$$

Bending moment at x is given as: $M = \int_A \sigma_{xx} z \mathrm{d}A$. Using Eq. (8) in the bending moment (for the bulk) equation and upon integration over the cross-section area A, one gets:

$$M = EI\left[\frac{\mathrm{d}\varphi}{\mathrm{d}s} - l^2\frac{\mathrm{d}^3\varphi}{\mathrm{d}s^3}\right] \tag{9}$$

here l is the material characteristics length. Here, $I = \int_A z^2 \mathrm{d}A$ is the second moment of cross-sectional area. Now, the governing equation and the corresponding boundary conditions of a strain gradient elastic cantilever beam are evaluated through a variational principle given as: $\delta(U_\mathrm{b} + U_\mathrm{s}) - \delta W = 0$, where W is the work done by the external forces, U_b and U_s are the strain energy of the bulk and surface, respectively. For one-dimensional case, the bulk strain energy U_b may be written as:

$$U_b = \frac{1}{2}\int_A \int_0^a [\tau_{xx}\varepsilon_{xx} + \mu_{xxx}.\nabla\varepsilon_{xx}] \mathrm{d}s\mathrm{d}A \tag{10}$$

where $\tau_{xx} = E\varepsilon_{xx}$ and $\mu_{xxx} = l^2 E(\mathrm{d}\varepsilon_{xx}/\mathrm{d}s)$ are the Cauchy and double stress, respectively, ε_{xx} is the axial strain and $\nabla\varepsilon_{xx} = \mathrm{d}\varepsilon_{xx}/\mathrm{d}s$ denotes the strain gradient. Accordingly, Eq. (10) may be written as: $U_b = (EI/2)\int [(\mathrm{d}\varphi/\mathrm{d}s)^2 + l^2(\mathrm{d}^2\varphi/\mathrm{d}s^2)^2]\mathrm{d}s$, where $\mathrm{I} = bh^3/12$ is the moment of inertia. The variation of the integral of the type $U = \int_0^a F(\varphi', \varphi'')\mathrm{d}s$ (where $\varphi' = \mathrm{d}\varphi/\mathrm{d}s$ and $\varphi'' = \mathrm{d}^2\varphi/\mathrm{d}s^2$) is given as:

$$\delta U = \int_0^a \left[\left\{-\frac{\mathrm{d}}{\mathrm{d}s}\left(\frac{\partial F}{\partial \varphi'}\right) + \frac{\mathrm{d}^2}{\mathrm{d}s^2}\left(\frac{\partial F}{\partial \varphi''}\right)\right\}\delta\varphi\right]\mathrm{d}s + \left[\left\{\left(\frac{\partial F}{\partial \varphi'}\right) - \frac{\mathrm{d}}{\mathrm{d}s}\left(\frac{\partial F}{\partial \varphi''}\right)\right\}\delta\varphi'\right]_0^a + \left[\left\{\left(\frac{\partial F}{\partial \varphi''}\right)\right\}\delta\varphi''\right]_0^a \tag{11}$$

From Eqs. (10) and (11) one gets:

$$\delta U_b = \int_0^a \left[-EI \left\{ \left(\frac{\partial^2 \varphi}{\partial s^2} - l^2 \frac{\partial^4 \varphi}{\partial s^4} \right) \right\} \delta\varphi \right] \mathrm{d}s + \left[\left\{ EI \left\{ \left(\frac{\partial \varphi}{\partial s} - l^2 \frac{\partial^3 \varphi}{\partial s^3} \right) \right\} \delta\varphi \right\} \delta\varphi' \right]_0^a + \left[EIl^2 \left\{ \frac{\partial^2 \varphi}{\partial s^2} \right\} \delta\varphi'' \right]_0^a \tag{12}$$

Similarly, the surface strain energy is written as:

$$U_s = \frac{1}{2} \int_A [\tau_{xx}^s \varepsilon_{xx}^s + \mu_{xxx}^s . \nabla \varepsilon_{xx}^s + \tau_o \varepsilon_{xx}^s] \mathrm{d}A \tag{13}$$

From Eqs. (11) and (13), one gets:

$$\delta U_s = \int_0^a \left[\left[-EI_s \left\{ \left(\frac{\partial^2 \varphi}{\partial s^2} - l^2 \frac{\partial^4 \varphi}{\partial s^4} \right) \right\} \right] \delta\varphi \right] \mathrm{d}s + \left[\left[EI_s \left\{ \left(\frac{\partial \varphi}{\partial s} - l^2 \frac{\partial^3 \varphi}{\partial s^3} \right) \right\} \right] \delta\varphi' \right]_0^a + \left[\left[EI_s l^2 \left\{ \frac{\partial^2 \varphi}{\partial s^2} \right\} \right] \delta\varphi'' \right]_0^a - \int_0^a T^s \delta\varphi \mathrm{d}s \tag{14}$$

where $I_s = (bh^2/2 + h^3/6)$ and $T^s = \int_0^a q \mathrm{d}s$, with $q(s)$ is the vertical load induced by the residual stress. According to the Young-Laplace equation [34,40], stress jump across each surface depends on the surface curvature that can be expressed as [34,40]; $\langle \sigma_{ij}^+ - \sigma_{ij}^- \rangle n_i n_j = \tau_{\alpha\beta}^s \kappa_{\alpha\beta}$, where n_i denotes the unit vector normal to the surface, σ_{ij}^+ and σ_{ij}^- are, respectively, the stresses above and below the surface, $\kappa_{\alpha\beta}$ is the surface curvature. Therefore, equivalent vertical load $q(x)$ induced by the residual stress is expressed as [26,42];

$$q = H\kappa = H \frac{\mathrm{d}\varphi}{\mathrm{d}s} \tag{15}$$

with $H = 2\tau_o b$ [26,42,55] where b is the width of the beam. The total force along the beam axis "s" is given as: $T^s = \int_0^a H \frac{\partial \varphi}{\partial s} \mathrm{d}s$. The variation of the work done by the external forces is written as: $\delta W = \int_0^a F \cos\varphi(s) \delta\varphi \mathrm{d}s$. So, the variational principle $\delta(U_b + U_s) - \delta W = 0$ gives:

$$\int_0^a \left[\left[-EI_{\mathrm{eff}} \left\{ \left(\frac{\partial^2 \varphi}{\partial s^2} - l^2 \frac{\partial^4 \varphi}{\partial s^4} \right) \right\} + H\varphi - H\varphi_{(a)} - F\cos\varphi \right] \delta\varphi \right] \mathrm{d}s - \left[\left[EI_{\mathrm{eff}} \left\{ \left(\frac{\partial \varphi}{\partial s} - l^2 \frac{\partial^3 \varphi}{\partial s^3} \right) \right\} \right] \delta\varphi' \right]_0^a + \left[\left[EI_{\mathrm{eff}} \left\{ \left(\frac{\partial^2 \varphi}{\partial s^2} \right) \right\} \right] \delta\varphi'' \right]_0^a = 0 \tag{16}$$

The governing equation can be written as:

$$EI_{\mathrm{eff}} \left[\frac{\mathrm{d}^2 \varphi}{\mathrm{d}s^2} - l^2 \frac{\mathrm{d}^4 \varphi}{\mathrm{d}s^4} \right] = -F\cos\varphi + H\varphi - H\varphi_{(a)} \tag{17}$$

where $EI_{\mathrm{eff}} = E\frac{bh^3}{12} + E_s(\frac{h^3}{6} + \frac{bh^2}{2})$. It is necessary to mention for simplification that the size dependence of E is not considered, as previously done in these references [56,57]. Our model applies to those materials that do not show the significant dependence of E on size. The boundary conditions evaluated from the variational principle require $EI_{\mathrm{eff}}[(\partial\varphi/\partial s) - l^2(\partial^3\varphi/\partial s^3)]$ (moment) and $EI_{\mathrm{eff}}(\partial^2\varphi/\partial s^2)$ (higher order moment) to be specified at $s = 0$ and $s = a$. So, one of the possible set of boundary conditions considered in this work is as follows; At clamped end, i.e., $s = 0$, slope, i.e., rotation of the beam is zero $\varphi = 0$, and the non-classical

terms (from variational principle) are written as: $\frac{d^2\varphi}{ds^2} = 0$. Meanwhile, at the free end, i.e., $s = a$, the classical moment (without strain gradient) would be zero which eventually gives; $\frac{d\varphi}{ds} = 0$. On the other hand, the moment (with strain gradient effect) would also be zero that further gives; $\frac{d\varphi}{ds} - l^2\frac{d^3\varphi}{ds^3} = 0$. In a nutshell, the boundary conditions considered in this work are written as:

$$\text{At } s = 0;\ \varphi = 0,\ \frac{d^2\varphi}{ds^2} = 0 \tag{18a}$$

$$\text{At } s = a;\ \frac{d\varphi}{ds} = 0,\ \frac{d\varphi}{ds} - l^2\frac{d^3\varphi}{ds^3} = 0 \text{ or} \frac{d\varphi}{ds} = 0,\ \frac{d^3\varphi}{ds^3} = 0 \tag{18b}$$

The nonlinear fourth-order differential equation (Eq. 17) with the respective boundary conditions (Eq. 18a) is solved using a three-stage Lobatto IIIa collocation formula. It is one of a widely used finite difference method to solve the boundary value problems. Details of this and some other relevant methods are provided by Shampine et al. [58].

3 Numerical results for the cantilever beam bending

For results, the material characteristic length (l) of epoxy, i.e., 17.6 μm [57] is taken to numerically evaluate the large deformation bending behavior of a cantilever beam. The concentrated vertical force F and height h are chosen in such a way that the beam remains elastic everywhere. In this study, the contribution of the surface residual stress toward the total surface stresses is found more noticeable than the surface elasticity, as shown by other researchers [33,50]. The end tip deflection for gradient model Y_g, non-gradient (large deformation) model Y_l and the classical model Y_o ($FL^3/3EI$) are plotted in Fig. 2. It is shown that when $t_l << h$, where t_l is the ratio of the layer's thickness to the height of the beam, the effect of surface elasticity is negligible and all three models give similar results. Surface elasticity modulus is taken to be as: $E_s = E_l t_l$ and $E_l = E = 1.44$ GPa [26,42]. The similar conclusion is drawn in the references [33,50]. Therefore, for further study, E_s and τ_o are assumed to be zero [59] and 0.2 μN/μm, respectively. The effect of the large deformation with increased load factor F_o ($F_o = Fa^2/2(EI)$) is shown by Joseph et al. [15], demonstrating its pronounced effect at the enhanced loads. The surface residual stress constant may be positive or negative [2]; therefore, results for both positive and negative residual stresses are presented. The vertical deflection of a cantilever beam along its axis, normalized with Y_o ($FL^3/3EI$) (classical endpoint vertical deflection), is presented in Fig. 3a. It can be seen, for smaller h/l ratios, that the gradient beam models are stiffer than the classical ones. The normalized deflections are shown to increase with increasing h/l, while the maximum deflection (at $s/a = 1$) of the strain gradient and classical model become comparable when $h/l \approx 1$ onwards. It is important to note that the effect of strain gradient is more prominent when $h/l \leq 0.2$; therefore, the subsequent results are primarily presented with $h/l \leq 0.2$. In Fig. 3b for $h/l \leq 0.2$, the results are obtained with strain gradient model with no surface effects, strain gradient model with positive surface residual stress and strain gradient model with negative surface residual stress. All effects have shown a significant contribution to the bending behavior of a cantilever beam. For instance, with the positive surface residual stress, the beam exhibits less stiff behavior and vice versa. This phenomenon is explained due to the sign of curvature associated with surface residual stress that causes an additional distributed load and change beam [26,51,59]. In the case of a positive surface residual stress, a positive curvature results in a positive distributed transverse force. This positive force increases the rotation of bending cantilever and thus beam behaves like a softer material. Meanwhile, this behavior is totally opposite when $\tau_o < 0$ and hence, the cantilever beam may exhibit a stiffer response comparatively.

The normalized maximum deflections (maximum tip deflection) for various beams configurations are numerically obtained using Eq. (6) and are shown in Fig. 4. Here, Y_g, Y_l and Y_o ($Fa^3/(3EI)$) represent the deflection obtained with strain gradient model, non-gradient model and using the classical formulations (small deformation). Additionally, for comparison, the maximum tip deflections for positive and negative residual stresses are also included. The non-dimensional parameter ($\alpha = 3Fa^2/(Eh^4)$) as abscissa is defined for convenience. The normalized maximum deflection Y_g/Y_l against α is plotted in Fig. 4a. From Fig. 4a, the strain gradient effect seems more pronounced for smaller (a/h), presenting smaller deflections and hence exhibiting stiffer response for the gradient beams. The effect of the surface residual stress on the tip deflections is shown to be more prominent for slender beams irrespective of h/l ratio. For a certain beam height, the effect of surface residual stress tends to increase with increasing beam length. Moreover, this behavior is also

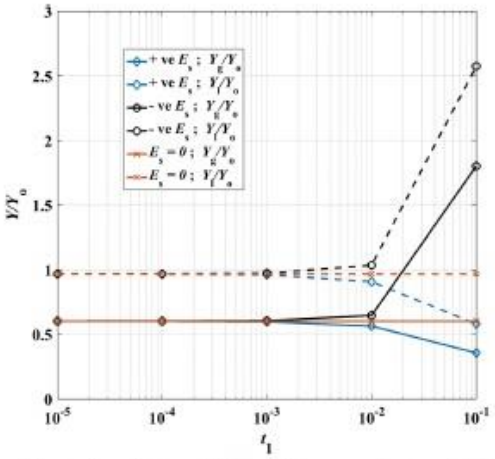

Fig. 2 Maximum tip deflection of the strain gradient model (Y_g) and the non-gradient model (Y_l), normalized with the classical results (Y_o) vs layer thickness to beam's height ratio ($t_1 = t/h$)

evident for increasing h/l ratio. It is clear that the positive surface residual stress induces larger tip transverse displacement while the opposite holds true for the negative surface residual stress. Figure 4b compares the strain gradient results with the classical model (without strain gradient & small deformation). It is shown for the smaller beam lengths that Y_g/Y_l and Y_g/Y_o are identical, indicating similar results for large as well as the small deformation theory. However, with an increase in beam slenderness (a/h ratio), the beam will undergo large deformation and hence the small deformation theory would over-estimate an endpoint vertical deflection. This is evident from a peak point (in each curve) in Fig. 4b, indicating classical model inadequacy to accurately predict the large deformation. Moreover, from Fig. 4b, it is quite evident that the pattern of maximum tip deflections, for the model with cumulative effects of strain gradient and surface residual stress, is similar to that of the model without surface residual stress (only strain gradient effect), apart from the fact that for positive surface residual stress the beam tends to exhibit softer behavior and vice versa. Nevertheless, from Fig. 4a, b, it may fairly be concluded that the effect of surface residual stress is more prominent for slender beams.

4 Fracture of a double cantilever beam with surface residual effect

Significant developments in the advance numerical methods have been made not only to accurately predict the fracture of various complex geometries [60,61] but also to cater the size effect on the fracture properties at smaller scale [6,7,62,63]. Adopting one of such numerical methods, in this section, the fracture property of a DCB, i.e., the stress intensity factor is evaluated numerically by taking the crack length to be the length of a beam as a and width b, the stress intensity factor (K) of a DCB may be written as $K = \sqrt{EG}$, where $G = F(\mathrm{d}Y_{\max}/b\mathrm{d}a)$ and it is defined as the strain energy release rate of a DCB. Meanwhile, the classical result is given by $G_o = 12F^2a^2/(Eh^3b^2)$ (Wang & Wang, 2013). Figure 5 displays the normalized stress intensity factors versus α. For comparison, as in Fig. 4, the results for the strain gradient model K_g, non-gradient model K_l and classical theory K_o are given. Additionally, for further illustration, the stress intensity factors for the model with the positive and negative residual stresses are also included. Evidently, from Fig. 5, the effect of the surface residual stress is more prominent when $h/l \geq 0.075$ and for slender beams. It is clear that the positive residual stress enhances the stress intensity factors and vice versa. Furthermore, the effect of the negative surface residual stress is more noticeable as compared to the positive residual stress. For instance, in Fig. 5a, for $h/l \geq 0.1$ beyond certain peak point the normalized stress intensity factor shows a swift decline, signifying a stiffer beam response. However, this prompt observation is completely absent in the case of positive surface residual stress. Moreover, the normalizations of strain gradient results with the classical ones are shown in Fig. 5b. From Fig. 5b, apart from the strain gradient effects, it may clearly be seen that effect of negative

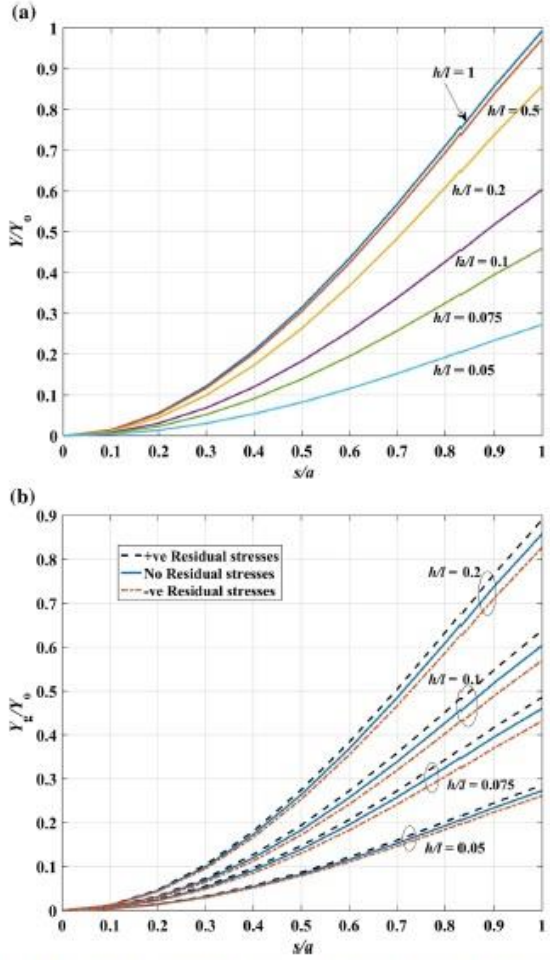

Fig. 3 **a** The vertical deflection along the beam axis (normalization with the classical result at the tip) for strain gradient models **b** The vertical deflection along the beam axis (normalization with the classical result at the tip) for the strain gradient models with surface residual effect

surface residual stress is more noticeable than that of the positive surface residual stress. On the other hand, the overestimation in the fracture characteristics is also evident following the trend as shown in Fig. 4.

5 Effect of the uncracked part

The strain gradient effect of the uncracked part of DCB is neglected (since strains in the uncracked part would be much lower than that in the cracked part). The schematic of uncracked part of a DCB is shown in Fig. 1b. The governing equation and respective boundary conditions of an uncracked part are provided by Wang & Wang [25] and Joseph et al. [15]. Here, it is necessary to mention the prominence of shear stresses at the uncracked part that must be incorporated in the constitutive equations. Therefore, Timoshenko beam model is more suitable to study the uncracked part of the DCB. Accordingly, the potential energy of an uncracked part

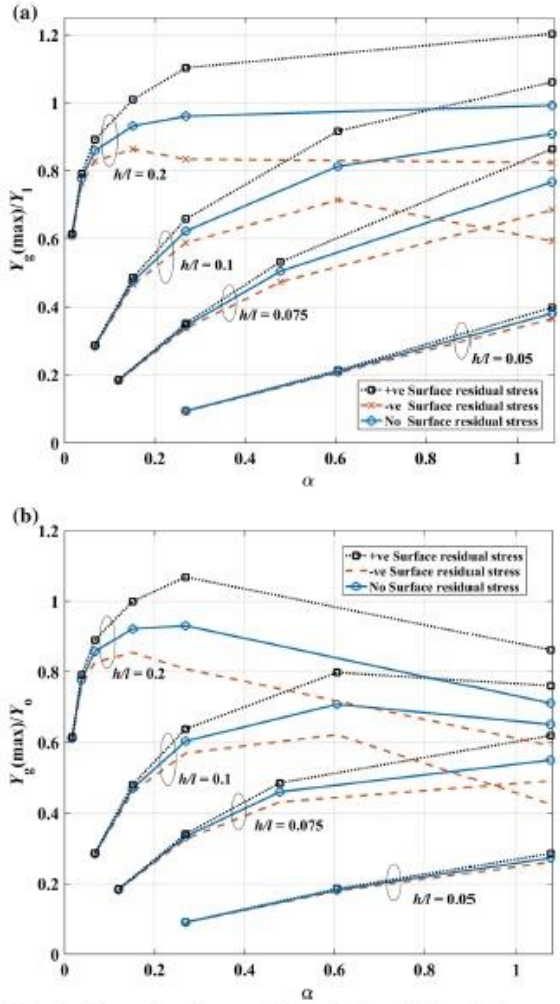

Fig. 4 **a** End point vertical deflection of the strain gradient model, normalization with the end point non-gradient vertical deflections (large deformation) **b** End point vertical deflection of the strain gradient model, normalization with the end point classical vertical deflections

(U_2) of DCB is given as:

$$U_2 = 2\int_{-\infty}^{0} \frac{M^2}{2EI_{\text{eff}}}\mathrm{d}x + 2\int_{-\infty}^{0} \frac{Q^2}{2G^s A}\mathrm{d}x \tag{19}$$

Here E is the Young's Modulus, G^s is the shear modulus, A is the area of cross-section and I_{eff} is the effective moment of inertia. Following the rectangular coordinate system, the integrals vary from negative

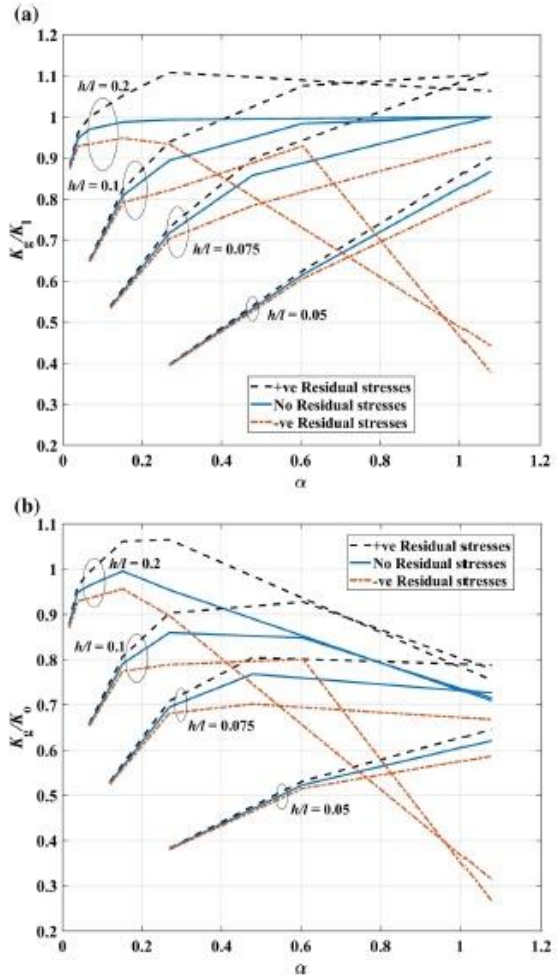

Fig. 5 **a** Stress intensity factors of the strain gradient model, normalization with the non-gradient stress intensity factors (large deformation) **b** Stress intensity factors of the strain gradient model, normalization with the classical stress intensity factors

infinity to zero. From the references [15,25] and using $M_{(o)} = F.X_{(\varphi_o)}$ we get:

$$U_2 = \frac{1}{\sqrt{EI_{\text{eff}}GA}}\left[F^2X^2_{(\varphi_o)} + \left[\int_0^a sH\frac{d\varphi}{ds}ds\right]^2\right] \tag{20}$$

Now, the influence of the root part of DCB is investigated numerically. Here, R_K and R_G are defined, where R_K is the ratio of the stress intensity factor associated with the uncracked part to that of the cracked part of DCB, while R_G is the ratio of the strain energy release rate of an uncracked part to the cracked part. Variations of R_K and R_G versus a/h for different h/l ratios are plotted in Fig. 6. The results are plotted for strain gradient model without surface residual stress, strain gradient model with positive surface residual stress and strain gradient model with negative surface residual stress. It can be seen in Fig. 6 that, for a particular

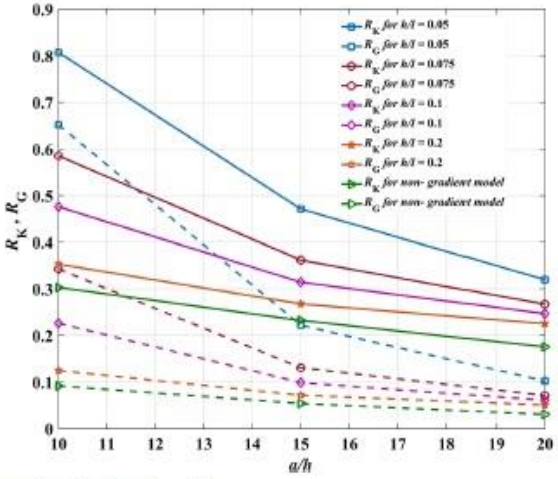

Fig. 6 Comparison of R_K and R_G plotted against a/h

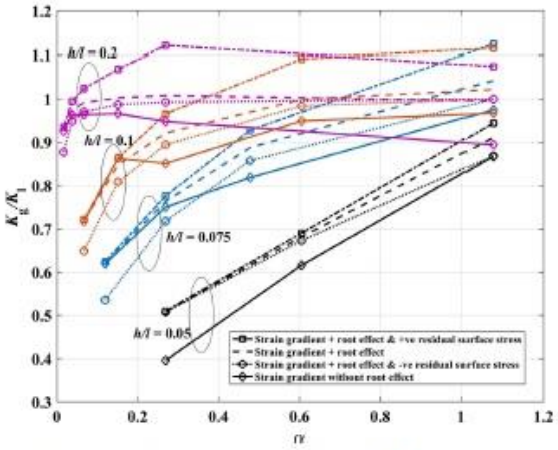

Fig. 7 Stress intensity factors with the consideration of uncracked part of DCB, normalization with the non-gradient stress intensity factors (large deformation)

h/l, all models show the identical results. Thus, it may be stated that ratios R_K and R_G depend on the DCB geometry and it is independent of the surface residual stress. Moreover, it may equally be concluded that for smaller DCBs, i.e., for $h/l \leq 0.2$, the value of R_K and R_G may not be neglected even though the beam length to thickness ratio is higher ($a/h \approx 20$) (which was the case in classical studies).

The comparison of two strain gradient models, i.e., with root effect and without root effect in terms of stress intensity factors is shown in Fig. 7. The results are plotted for models incorporating strain gradient effect without surface residual stress, strain gradient effect with positive surface residual stress and strain gradient effect with negative surface residual stress. In general, results show that even with the incorporation of root effect, the positive surface residual stress causes DCB to exhibit softer response by enhancing the normalized stress intensity factor and vice versa. Again, this phenomenon may be explained due to the sign of curvature associated with negative surface residual stress that causes an additional distributed load (opposite to the direction of endpoint force), which in return cause the DCB to exhibit stiffer response. Hence, the influence

of the root effect of DCB must be considered in mathematical modeling for accurate prediction of its fracture properties. It seems true even for the slender beams ($a/h > 20$), lest an underestimated fracture behavior would be expected.

6 Conclusion

The cumulative effects of the strain gradient and surface stress on the large deformation bending behavior of a cantilever beam are investigated. Both surface elasticity and surface residual stress are incorporated in the mathematical modeling. Due to the negligible influence of surface elasticity, most of the results are depicted only with the consideration of surface residual stress. The results are obtained for the strain gradient model with no surface effects, strain gradient model with positive surface residual stress and negative surface residual stress individually. Due to the positive surface residual stress, the beam exhibits less stiff behavior. This softening behavior may be attributed to the sign of curvature that causes an additional distributed load and change beam stiffness. Meanwhile, this behavior is totally opposite in the case when $\tau_0 < 0$; hence, a cantilever beam may exhibit a stiffer response comparatively. For the fracture property of DCB, i.e., stress intensity factor, the effect of the surface residual stress is shown to be increasing with increasing beam dimensions. In general, the influence of surface residual stress is more prominent when $h/l \geq 0.075$ and for slender beams. Moreover, the effect of negative surface residual stress was shown to be more noticeable than the positive surface residual stress. The root effect also enhances the normalized stress intensity factors. It was shown that the root effect on the ratios R_K and R_G for all three models remain same and thus it may be stated that R_K and R_G depend on the DCB geometry and are independent of the surface residual stress. It is observed for $h/l \leq 0.2$ that the significance of root effect must not be ignored.

References

1. Reeder, J.R., Crews Jr., J.: Nonlinear analysis and redesign of the mixed-mode bending delamination test (1991)
2. Wang, K., Wang, B.: Nonlinear fracture mechanics analysis of nano-scale piezoelectric double cantilever beam specimens with surface effect. Eur. J. Mech. A Solids **56**, 12–18 (2016)
3. Anderson, T., Nayfeh, A., Balachandran, B.: Experimental verification of the importance of the nonlinear curvature in the response of a cantilever beam. J. Vib. Acoust. **118**(1), 21–27 (1996)
4. Jia, X., Yang, J., Kitipornchai, S., Lim, C.W.: Free vibration of geometrically nonlinear micro-switches under electrostatic and Casimir forces. Smart Mater. Struct. **19**(11), 115028 (2010)
5. Jia, X.L., Yang, J., Kitipornchai, S.: Pull-in instability of geometrically nonlinear micro-switches under electrostatic and Casimir forces. Acta Mech. **218**(1–2), 161–174 (2011)
6. Giannakopoulos, A., Stamoulis, K.: Structural analysis of gradient elastic components. Int. J. Solids Struct. **44**(10), 3440–3451 (2007)
7. Stamoulis, K., Giannakopoulos, A.: A study of size effects and length scales in fracture and fatigue of metals by second gradient modelling. Fatigue Fract. Eng. Mater. Struct. **35**(9), 852–860 (2012)
8. Devitt, D., Schapery, R., Bradley, W.: A method for determining the mode I delamination fracture toughness of elastic and viscoelastic composite materials. J. Compos. Mater. **14**, 270–285 (1980)
9. Williams, J.: Large displacement and end block effects in the 'DCB' interlaminar test in modes I and II. J. Compos. Mater. **21**(4), 330–347 (1987)
10. Togun, N.: Nonlocal beam theory for nonlinear vibrations of a nanobeam resting on elastic foundation. Bound. Value Probl. **2016**(1), 1–14 (2016)
11. Wang, B., Hoffman, M., Yu, A.: Buckling analysis of embedded nanotubes using gradient continuum theory. Mech. Mater. **45**, 52–60 (2012)
12. Aifantis, E.C.: On the role of gradients in the localization of deformation and fracture. Int. J. Eng. Sci. **30**(10), 1279–1299 (1992)
13. Ru, C., Aifantis, E.: A simple approach to solve boundary-value problems in gradient elasticity. Acta Mech. **101**(1–4), 59–68 (1993)
14. Vardoulakis, I., Sulem, J.: Bifurcation Analysis in Geomechanics. Blackie Academic and Professional, Glasgow (1995)
15. Joseph, R.P., Wang, B., Samali, B.: Size effects on double cantilever beam fracture mechanics specimen based on strain gradient theory. Eng. Fract. Mech. **169**, 309–320 (2017)
16. Aifantis, E.C.: Update on a class of gradient theories. Mech. Mater. **35**(3), 259–280 (2003)
17. Aifantis, E.: Chapter one-internal length gradient (ILG) material mechanics across scales and disciplines. Adv. Appl. Math. **49**, 1–110 (2016)
18. Dingreville, R., Qu, J., Cherkaoui, M.: Surface free energy and its effect on the elastic behavior of nano-sized particles, wires and films. J. Mech. Phys. Solids **53**(8), 1827–1854 (2005)

19. Streitz, F., Cammarata, R., Sieradzki, K.: Surface-stress effects on elastic properties. I. Thin metal films. Phys. Rev. B **49**(15), 10699 (1994)
20. Fischer, F., Waitz, T., Vollath, D., Simha, N.: On the role of surface energy and surface stress in phase-transforming nanoparticles. Prog. Mater. Sci. **53**(3), 481–527 (2008)
21. Cahn, J.W.: Thermodynamics of Solid and Fluid Surfaces. In: Carter, W.C., Johnson, W.C. (eds.) The Selected Works of John W. Cahn, pp. 377–378. The Minerals, Metals & Materials Society, Pennsylvania (1998)
22. Cammarata, R.: Surface and interface stress effects on interfacial and nanostructured materials. Mater. Sci. Eng. A **237**(2), 180–184 (1997)
23. Cammarata, R.C.: Surface and interface stress effects in thin films. Prog. Surf. Sci. **46**(1), 1–38 (1994)
24. Fried, E., Gurtin, M.E.: The role of the configurational force balance in the nonequilibrium epitaxy of films. J. Mech. Phys. Solids **51**(3), 487–517 (2003)
25. Wang, B., Wang, K.: Effect of surface residual stress on the fracture of double cantilever beam fracture toughness specimen. J. Appl. Phys. **113**(15), 153502 (2013)
26. He, J., Lilley, C.M.: Surface effect on the elastic behavior of static bending nanowires. Nano Lett. **8**(7), 1798–1802 (2008)
27. Gurtin, M.E., Murdoch, A.I.: Surface stress in solids. Int. J. Solids Struct. **14**(6), 431–440 (1978)
28. Jammes, M., Mogilevskaya, S.G., Crouch, S.L.: Multiple circular nano-inhomogeneities and/or nano-pores in one of two joined isotropic elastic half-planes. Eng. Anal. Bound. Elem. **33**(2), 233–248 (2009)
29. Luo, J., Wang, X.: On the anti-plane shear of an elliptic nano inhomogeneity. Eur. J. Mech. A Solids **28**(5), 926–934 (2009)
30. Luo, J., Xiao, Z.: Analysis of a screw dislocation interacting with an elliptical nano inhomogeneity. Int. J. Eng. Sci. **47**(9), 883–893 (2009)
31. On, B.B., Altus, E., Tadmor, E.: Surface effects in non-uniform nanobeams: continuum vs. atomistic modeling. Int. J. Solids Struct. **47**(9), 1243–1252 (2010)
32. Wang, G.F., Feng, X.Q.: Effects of surface elasticity and residual surface tension on the natural frequency of microbeams. Appl. Phys. Lett. **90**(23), 231904 (2007)
33. Wang, G.F., Feng, X.Q.: Effect of surface stresses on the vibration and buckling of piezoelectric nanowires. Europhys. Lett. **91**(5), 56007 (2010)
34. Gurtin, M., Weissmüller, J., Larche, F.: A general theory of curved deformable interfaces in solids at equilibrium. Philos. Mag. A **78**(5), 1093–1109 (1998)
35. Shenoy, V.B.: Atomistic calculations of elastic properties of metallic fcc crystal surfaces. Phys. Rev. B **71**(9), 094104 (2005)
36. Weissmüller, J., Cahn, J.: Mean stresses in microstructures due to interface stresses: a generalization of a capillary equation for solids. Acta Mater. **45**(5), 1899–1906 (1997)
37. Duan, H., Wang, J., Huang, Z., Karihaloo, B.: Size-dependent effective elastic constants of solids containing nano-inhomogeneities with interface stress. J. Mech. Phys. Solids **53**(7), 1574–1596 (2005)
38. Sharma, P., Ganti, S.: Size-dependent Eshelby's tensor for embedded nano-inclusions incorporating surface/interface energies. J. Appl. Mech. **71**(5), 663–671 (2004)
39. Sharma, P., Ganti, S., Bhate, N.: Effect of surfaces on the size-dependent elastic state of nano-inhomogeneities. Appl. Phys. Lett. **82**(4), 535–537 (2003)
40. Chen, T., Chiu, M.S., Weng, C.N.: Derivation of the generalized Young–Laplace equation of curved interfaces in nanoscaled solids. J. Appl. Phys. **100**(7), 074308 (2006)
41. Ansari, R., Sahmani, S.: Bending behavior and buckling of nanobeams including surface stress effects corresponding to different beam theories. Int. J. Eng. Sci. **49**(11), 1244–1255 (2011)
42. He, J., Lilley, C.M.: Surface stress effect on bending resonance of nanowires with different boundary conditions. Appl. Phys. Lett. **93**(26), 263108 (2008)
43. Assadi, A., Farshi, B.: Vibration characteristics of circular nanoplates. J. Appl. Phys. **108**(7), 074312 (2010)
44. Assadi, A., Farshi, B., Alinia-Ziazi, A.: Size dependent dynamic analysis of nanoplates. J. Appl. Phys. **107**(12), 124310 (2010)
45. Zhang, L., Liu, J., Fang, X., Nie, G.: Size-dependent dispersion characteristics in piezoelectric nanoplates with surface effects. Physica E Low Dimens. Syst. Nanostruct. **57**, 169–174 (2014)
46. Fu, Y., Zhang, J.: Size-dependent pull-in phenomena in electrically actuated nanobeams incorporating surface energies. Appl. Math. Model. **35**(2), 941–951 (2011)
47. Koochi, A., Kazemi, A., Khandani, F., Abadyan, M.: Influence of surface effects on size-dependent instability of nano-actuators in the presence of quantum vacuum fluctuations. Phys. Scr. **85**(3), 035804 (2012)
48. Ma, J.B., Jiang, L., Asokanthan, S.F.: Influence of surface effects on the pull-in instability of NEMS electrostatic switches. Nanotechnology **21**(50), 505708 (2010)
49. Yang, F., Wang, G.F., Long, J.M., Wang, B.L.: Influence of surface energy on the pull-in instability of electrostatic nano-switches. J. Comput. Theor. Nanosci. **10**(5), 1273–1277 (2013)
50. Yan, Z., Jiang, L.: The vibrational and buckling behaviors of piezoelectric nanobeams with surface effects. Nanotechnology **22**(24), 245703 (2011)
51. Wang, K., Wang, B.: A general model for nano-cantilever switches with consideration of surface effects and nonlinear curvature. Physica E Low Dimens. Syst. Nanostruct. **66**, 197–208 (2015)
52. Aifantis, E.: Strain gradient interpretation of size effects. Int. J. Fract. **95**(1–4), 299–314 (1999)
53. Askes, H., Suiker, A., Sluys, L.: A classification of higher-order strain-gradient models-linear analysis. Arch. Appl. Mech. **72**(2–3), 171–188 (2002)
54. Christensen, J., Bastien, C.: Nonlinear Optimization of Vehicle Safety Structures: Modeling of Structures Subjected to Large Deformations. Butterworth–Heinemann, Oxford (2015)
55. Wang, G.F., Feng, X.Q.: Surface effects on buckling of nanowires under uniaxial compression. Appl. Phys. Lett. **94**(14), 141913 (2009)
56. Kahrobaiyan, M., Rahaeifard, M., Tajalli, S., Ahmadian, M.: A strain gradient functionally graded Euler–Bernoulli beam formulation. Int. J. Eng. Sci. **52**, 65–76 (2012)

57. Kong, S., Zhou, S., Nie, Z., Wang, K.: Static and dynamic analysis of micro beams based on strain gradient elasticity theory. Int. J. Eng. Sci. **47**(4), 487–498 (2009)
58. Shampine, L.F., Kierzenka, J., Reichelt, M.W.: Solving boundary value problems for ordinary differential equations in MATLAB with bvp4c. Tutorial notes (2000)
59. Wu, Q., Volinsky, A.A., Qiao, L., Su, Y.: Surface effects on static bending of nanowires based on non-local elasticity theory. Prog. Nat. Sci. Mater. Int. **25**(5), 520–524 (2015)
60. Fleming, M., Chu, Y., Moran, B., Belytschko, T., Lu, Y., Gu, L.: Enriched element-free Galerkin methods for crack tip fields. Int. J. Numer. Methods Eng. **40**(8), 1483–1504 (1997)
61. Joseph, R., Purbolaksono, J., Liew, H., Ramesh, S., Hamdi, M.: Stress intensity factors of a corner crack emanating from a pinhole of a solid cylinder. Eng. Fract. Mech. **128**, 1–7 (2014)
62. Guha, S., Sangal, S., Basu, S.: Finite element studies on indentation size effect using a higher order strain gradient theory. Int. J. Solids Struct. **50**(6), 863–875 (2013)
63. Joseph, R.P., Wang, B., Samali, B.: Strain gradient fracture in an anti-plane cracked material layer. Int. J. Solids Struct.(2018, in press)

Paper 3

Large Deformation and Strain Gradient Fracture Analysis of Double Cantilever Beams with Piezoelectric Effect

R. P. Joseph[1]; B. L. Wang[2]; and B. Samali[3]

Abstract: This paper examines the size-dependent fracture of a piezoelectric double cantilever beam (DCB) specimen based on large deformation–strain gradient theory. The governing equations with relevant boundary conditions for a piezoelectric cantilever beam with simultaneous consideration of surface piezoelectricity, surface elasticity, surface residual stress, and large deformation are obtained and solved numerically. These results are further utilized to investigate the fracture behavior of a DCB. Results show that the strain gradient effect is more pronounced when the beam height is less than the material length scale parameter. The strain gradient model anticipates significant stiffening behavior at micro/nanoscales. The effect of the surface residual stress is more substantial than that of surface elasticity and surface piezoelectricity. The study further established that the strain energy release rate of the short-circuit boundary condition is larger than that of open-circuit boundary condition. Using strain gradient model, the effect of the uncracked part of DCB is more noticeable on a smaller scale and should not be ignored even for slender beams. **DOI: 10.1061/(ASCE)EM.1943-7889.0001497.**

Author keywords: Size-dependent fracture; Piezoelectric double cantilever beam; Strain gradient theory; Surface residual stress; Strain energy release rate.

Introduction

Piezoelectric micro/nanomaterials are extensively used in small-scale devices such as nanoresonators (Gusso 2010) and nanogenerators (Yang et al. 2009). To fully establish their applications, detailed understanding of the fracture behavior of these micro/nanomaterials is essential. The fracture performance of macromaterials has been explored widely in the literature (Ma et al. 2005a, b; Shi et al. 2014; Zhou et al. 2005a, b). However, relevant studies related to micro/nanomaterials are uncommon. A comprehensive review of piezoelectric nanostructures and relevant achievements in this field is presented by Fang et al. (2013). Meanwhile, owing to the large surface area-to-volume ratio at the micro/nanoscale, the surface effect has been shown to contribute to determining the fracture properties of structures (Wang and Wang 2013). Nevertheless, for piezoelectric micro/nanomaterials, such an elasticity model may not accurately predict size-dependent fracture properties owing to the neglect of surface piezoelectricity (Zhang and Jiang 2014). Pioneering work on the development of the piezoelectric model with simultaneous incorporation of surface piezoelectricity, surface residual stress, and surface elasticity was done by Huang and Yu (2006). Some of the relevant findings may be seen in the works of Yue et al. (2015, 2014). Nan and Wang (2013) also found that the strain energy release rate, stress intensity factors, and electric field intensity factors are highly influenced by surface effects in nanomaterials. Very recently, Wang and Wang (2016) investigated the fracture toughness of nanoscale piezoelectric double cantilever beam (DCB) specimens incorporating large deformation, shear deformation, uncracked end bulk, surface residual stress, surface elasticity, and surface piezoelectricity.

A redesigned mixed-mode bending (MMB) apparatus that incorporates geometrical nonlinearity reduces error from 30 to 3% (Reeder and Crews Jr 1991; Wang and Wang 2016). In the context of geometrical nonlinearity, the contribution of Von Karman strain (midplane extension) in the case of a cantilever beam is insignificant and, hence, can be neglected (Jia et al. 2011, 2010). On the other hand, the effect of the nonlinear force/curvature relation in the static behavior of micro/nanocantilever beams (particularly in switches) is evident and therefore should be thoroughly assessed (Huang and Yu 2006; Jia et al. 2011). A typical DCB consists of two cantilever beams attached with an uncracked part, so its fracture analysis is often evaluated by studying the cantilever bending behavior (Joseph et al. 2017; Li and Lee 2016; Stamoulis and Giannakopoulos 2012; Giannakopoulos and Stamoulis 2007). For composite laminates and adhesively bonded materials, a DCB specimen has found to be quite suitable for the determination of Mode I fracture toughness. Moreover, consideration of geometric nonlinearity on the Mode I fracture toughness of nonhomogeneous materials is sufficient for long cracks, as shown by Devitt et al. (1980) and Williams (1987).

When the external dimensions of the structure become comparable to material length scale parameter (material microstructural length), this leads to nonhomogeneous and size-dependent mechanical behavior (Giannakopoulos and Stamoulis 2007). Strain gradient theory is one of the nonclassical continuum elasticity theories with the capacity to describe size-dependent behavior. Mindlin (1965) proposed three simplified versions of his strain gradient framework, that is, Forms I, II, and III. In Form I, the strain energy density is taken as a quadratic function of classical strains and

[1]Centre for Infrastructure Engineering, School of Computing, Engineering and Mathematics, Western Sydney Univ., Penrith, NSW 2751, Australia.

[2]Associate Professor, Centre for Infrastructure Engineering, School of Computing, Engineering and Mathematics, Western Sydney Univ., Penrith, NSW 2751, Australia (corresponding author). Email: B.Wang@westernsydney.edu.au

[3]Director, Centre for Infrastructure Engineering, School of Computing, Engineering and Mathematics, Western Sydney Univ., Penrith, NSW 2751, Australia.

Note. This manuscript was submitted on September 6, 2017; approved on February 21, 2018; published online on June 11, 2018. Discussion period open until November 11, 2018; separate discussions must be submitted for individual papers. This paper is part of the ***Journal of Engineering Mechanics***, © ASCE, ISSN 0733-9399.

second displacement gradient; in Form II, the gradient of strains is used in place of second displacement gradient and in Form III, the strain energy is taken as a function of strain, the rotation gradient, and the fully symmetric part of the strain gradient. Among these three forms, the problems of nonsymmetric stress tensor (in case of couple-stress theories) may only be avoided in Form II for which the total stresses are symmetric. Polizzotto (2016) recently explained the physical meaning of higher-order strain tensors used in gradient elasticity theories. The aforementioned strain gradient theories are primarily postulated to account for the quantitative estimation of the size effect, which is important in the design of micro- and nano-sized systems such as microelectromechanical systems and nanoelectromechanical systems (Liebold and Müller 2015).

It is evident that the incorporation of strain gradients in estimating the size effect at micro- and nanoscales yields stiffer elastic responses to external loads (Liebold and Müller 2015), such as an increase in the bending rigidity of microbeams made of epoxy, as shown by Lam et al. (2003). For piezoelectric materials, Ke et al. (2012) presented the nonlinear vibrations of Timoshenko nanobeams and the free vibration of piezoelectric nanoplates (Ke et al. 2015) using nonlocal elasticity theory. A DCB is an ideal specimen to determine Mode I fracture toughness and often undergoes large deformations (Devitt et al. 1980; Williams 1987). Therefore, the accurate design of micro/nanoscale piezoelectric structures demands thorough investigations of the fracture behavior of piezoelectric DCB specimens under large deformation. Moreover, theoretical modeling of micro/nanostructures is considered more relevant because of their capability of being implemented at all possible length scales.

In this article, a size-dependent fracture mechanics analysis of a piezoelectric DCB specimen with simultaneous consideration of large deformation, strain gradient effect, the uncracked bulk end part, surface residual stress, surface elasticity, and surface piezoelectricity is conducted. To the authors' knowledge, small-scale piezoelectric beam studies are mostly based either on continuum models or nonlocal elasticity theories considering small deformations. In this paper, the deformation behavior of a cantilever is studied first, and the findings of that examination is then used to study the fracture behavior of a piezoelectric DCB specimen. The results of the beam deformations, endpoint vertical deflections, and strain energy release rates are obtained numerically using the three-stage Lobatto IIIA collocation method.

Theoretical Background and Problem Formulation

The strain gradient model used in this work was introduced by Aifantis (1992) and Ru and Aifantis (1993) and is considered more convenient in practical applications (Giannakopoulos and Stamoulis 2007; Joseph et al. 2017). The Cauchy stress (τ_{xx}) and double stress (μ_{xx}) for the one-dimensional (1D) case are given as $\tau_{xx} = E\varepsilon_{xx}$ and $\mu_{xx} = l^2 E\frac{d\varepsilon_{xx}}{dx}$, respectively (Stamoulis and Giannakopoulos 2012). Here, E is Young's modulus, ε_{xx} is the axial strain in the beam due to bending, and l is the material length constant related to the bulk strain energy. The total stresses (σ_{xx}) for the beam bending can be evaluated as $\sigma_{xx} = \tau_{xx} - \frac{d\mu_{xx}}{dx} = E\left(\varepsilon_{xx} - l^2\frac{d^2\varepsilon_{xx}}{dx^2}\right)$. The application and validation of this simpler strain gradient theory are presented by Vardoulakis and Sulem (1995) and Giannakopoulos et al. (2006), respectively. A comprehensive review of this gradient theory and applications of the internal length gradient across various scales is provided by Aifantis (2003) and Aifantis (2016), respectively. The constitutive equation in the form of a Laplacian operator ($\nabla^2 = \partial^2/\partial x^2 + \partial^2/\partial y^2 + \partial^2/\partial z^2$) is given as (Aifantis 1999a, b)

$$\sigma = E(\varepsilon - l^2\nabla^2\varepsilon) \tag{1}$$

where σ, ε, E, and l are as defined earlier. Although the beam is defined in the x–y plane (a 2D geometrical space), the problem remains 1D since the deflection of the beam is exclusively the function of "s" or "x." Therefore, the operator ∇^2 is reduced to address only the 1D gradient effect (in the direction of the beam axis).

For piezoelectric material, the presence of a strain gradient affects not only the total stress but the electric displacement as well. For illustration purposes, a schematic diagram of a piezoelectric DCB specimen with the length of cracked part a, width b, and thickness h is shown in Fig. 1. The beam configuration is the same as that of Huang and Yu (2006), Shen and Hu (2010), Yan and Jiang (2011), and Zhang et al. (2008) and the "bulk + surface" model is used to model the DCB (Huang and Yu 2006). The constitutive equations of a piezoelectric cantilever beam (provided the length-to-height ratio ≥10 (Christensen and Bastien 2015) for the 1D case i.e., $\sigma_{yy} = \sigma_{zz} = \sigma_{yz} = \sigma_{xz} = \sigma_{xy} = 0$, along with the incorporation of strain gradient are written as

$$\sigma_{xx} = -c_{11}z\left(\frac{d\varphi}{ds} - l^2\frac{d^3\varphi}{ds^3}\right) - e_{31}E_Z \tag{2}$$

$$D_z = -e_{31}z\left(\frac{d\varphi}{ds} - l^2\frac{d^3\varphi}{ds^3}\right) + k_{33}E_Z \tag{3}$$

where φ = slope of the deformed beam; c_{11} = Young's modulus; D_z = electric displacement; E_z = electric-field component; l = material characteristic length; and k_{33} and e_{31} = bulk dielectric and piezoelectric constants, respectively.

Moreover, due to the enormous surface area to volume ratio at a smaller scale, the influence of surface effect on the mechanical behavior of micro/nanomaterials becomes prominent and must be considered (Fang et al. 2013; Wang and Wang 2013). Surface effects on micro/nanostructures may be divided into two distinct types i.e., the surface elasticity and the surface residual stress (He and Lilley 2008a). The effect of surface stress, based on continuum elasticity theory, was first considered by Gurtin and Murdoch (1978) in their theoretical framework. In their study, the surface layers of the structures have different material properties as compared to the underlying bulk material. Meanwhile, the surfaces are considered to be as mathematical layers of zero thickness. This theory has shown an excellent capability in successfully addressing the surface effect on the mechanical behavior of micro/nanostructures and has been thoroughly employed by many researchers. The stress of the surface layer (τ_x^s), using the results presented in reference (Huang and Yu 2006) along with strain gradient effects may be expressed as

$$\tau_{xx}^s = \tau_o + c_{11}^s(\varepsilon_{xx} - l^2\nabla^2\varepsilon_{xx}) - e_{31}^s E_z \tag{4}$$

where τ_o = surface residual stress; and c_{11}^s and e_{31}^s = Young's Modulus and piezoelectric constant of the surface, respectively. The electric field component can be expressed as $E_z = -\psi_{,z}$, here ψ is the electric potential and is taken to be constant along the beam span (x-axis) (Yan and Jiang 2011). It is known that $E_x \ll E_z$, so that $D_x \ll D_z$, therefore, only D_z and E_z will be considered for theoretical modeling. The equilibrium equation in the absence of electric charges is $D_{z,z} = 0$ (Wang and Wang 2016). Using the boundary conditions as follows:

$\psi(-h/2) = 0$; $\psi(h/2) = V$, E_z and ψ may be evaluated as following:

$$\psi = -\frac{e_{31}}{k_{33}}\left(\frac{d\varphi}{ds} - l^2\frac{d^3\varphi}{ds^3}\right)\left(\frac{z^2 - (h/2)^2}{2}\right) + V\frac{z}{h} + \frac{V}{2} \tag{5}$$

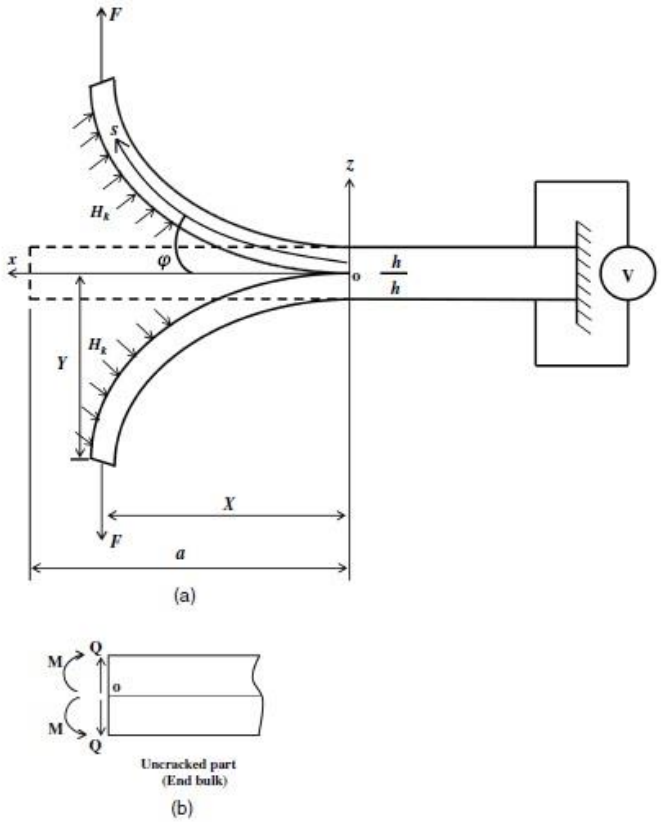

Fig. 1. Schematic diagrams: (a) piezoelectric double cantilever beam with surface residual stress; and (b) root part of DCB.

$$E_z = -\frac{\partial \psi}{\partial z} = z\frac{e_{31}}{k_{33}}\left(\frac{\mathrm{d}\varphi}{\mathrm{d}s} - l^2\frac{\mathrm{d}^3\varphi}{\mathrm{d}s^3}\right) - \frac{V}{h} \tag{6}$$

Therefore, bulk and surface stresses [at the upper $(h/2)$ and lower surfaces $(-h/2)$] are

$$\sigma_{xx} = -z\left(\frac{\mathrm{d}\varphi}{\mathrm{d}s} - l^2\frac{\mathrm{d}^3\varphi}{\mathrm{d}s^3}\right)\left(c_{11} + \frac{e_{31}^2}{k_{33}}\right) + \frac{e_{31}V}{h} \tag{7a}$$

$$\tau_{xx}^s = \tau_o - \left(\frac{h}{2}\right)\left(\frac{\mathrm{d}\varphi}{\mathrm{d}s} - l^2\frac{\mathrm{d}^3\varphi}{\mathrm{d}s^3}\right)\left(c_{11}^s + \frac{e_{31}^s e_{31}}{k_{33}}\right) + \frac{e_{31}^s V}{h} \tag{7b}$$

$$\tau_{xx}^s = \tau_o - \left(-\frac{h}{2}\right)\left(\frac{\mathrm{d}\varphi}{\mathrm{d}s} - l^2\frac{\mathrm{d}^3\varphi}{\mathrm{d}s^3}\right)\left(c_{11}^s + \frac{e_{31}^s e_{31}}{k_{33}}\right) + \frac{e_{31}^s V}{h} \tag{7c}$$

Therefore, the moment of cross section with the consideration of strain gradients, upper surface stress, lower surface stress as well as the surfaces in the thickness direction, is written as

$$M = EI_{\mathrm{eff}}\left[\frac{\mathrm{d}\varphi}{\mathrm{d}s} - l^2\frac{\mathrm{d}^3\varphi}{\mathrm{d}s^3}\right] \tag{8}$$

where $EI_{\mathrm{eff}} = \left(c_{11} + \frac{e_{31}^2}{k_{33}}\right)\frac{bh^3}{12} + \left(c_{11}^s + \frac{e_{31}^s e_{31}}{k_{33}}\right)\frac{h^3}{6} + \left(c_{11}^s + \frac{e_{31}^s e_{31}}{k_{33}}\right)\frac{bh^2}{2}$ (Huang and Yu 2006). Here c_{11} is assumed to be size-independent similar to the approach adopted by some other researchers (Joseph et al. 2017; Kahrobaiyan et al. 2011; Kong et al. 2009). Our model applies to those materials for which there isn't any significant size dependence of c_{11}. The electrical force of the cross section induced by the electrical components of σ_{xx} and τ_{xx}^s is given by (Wang and Wang 2016)

$$T = e_{31}Vb + 2bVe_{31}^s/h \tag{9}$$

The equivalent vertical load $q(s)$ induced by the surface residual stress is expressed as (He and Lilley 2008b; Wang and Feng 2009)

$$q(s) = H\kappa = H\frac{\mathrm{d}\varphi}{\mathrm{d}s} \tag{10}$$

with $H = 2\tau_o b$ is the effective lateral distribution load (He and Lilley 2008a, b; Wang and Feng 2009) here b is the beam width. Note that the effects of surface elasticity and surface piezoelectricity have been included in the effective bending stiffness, EI_{eff}. Therefore only τ_o is included in H. The equilibrium equations of the DCB give (Wang and Wang 2013); $\frac{\mathrm{d}Q}{\mathrm{d}s} = -H\frac{\mathrm{d}\varphi}{\mathrm{d}s}$, $\frac{\mathrm{d}M}{\mathrm{d}s} = Q$ (shear force). Bending moment at point any point "s" induced

by the equivalent distributed load $q(s)$, endpoint concentrated vertical force F and the electrical force of the cross-section T may be expressed as

$$M(s) = \int_0^a (\xi - s)(H + T)\frac{\partial \varphi}{\partial \xi} d\xi + F[x(a) - x(s)] \quad (11)$$

So, the governing equation of a Euler beam with the cumulative consideration of surface effects, piezoelectricity and strain gradient subjected to large deformation is written as

$$EI_{\text{eff}}\left[\frac{d^2\varphi}{ds^2} - l^2\frac{d^4\varphi}{ds^4}\right] = -F\cos\varphi + (H + T)\varphi - (H + T)\varphi_a \quad (12)$$

Here φ_a = unknown slope at the free end of the beam. Alternatively, the governing equation and respective boundary conditions may also be evaluated through a variational principle similar to the approach considered by Abdelkefi et al. (2011) for piezoelectric cantilever beams, Kong et al. (2009), Giannakopoulos and Stamoulis (2007), and Papargyri et al. (2003) for the strain gradient formulations using Euler beam model. The variational principle is given as $\delta(U_b + U_s) - \delta W = 0$, where W is the work done by the external forces, U_b and U_s are the strain energy of the bulk and surface respectively. In the 1D case, the bulk strain energy (U_b) is given as $U_b = \frac{1}{2}\int_A \int_0^a [\tau_{xx}\varepsilon_{xx} + \mu_{xxx} \cdot \nabla\varepsilon_{xx} + D_z E_z] ds dA$. On the other hand, the surface strain energy (U_s) is given as $U_s = \frac{1}{2}\int_A [\tau^s_{xx}\varepsilon^s_{xx} + \mu^s_{xxx} \cdot \nabla\varepsilon^s_{xx} + \tau_o\varepsilon^s_{xx}] dA$. Here ∇ denotes d/ds in the case of a large deformation. The variation of the work done by the external forces is written $\delta W = \int_0^a F\cos\varphi(s)\delta\varphi ds$. Thus, the variational principle $\delta(U_b + U_s) - \delta W = 0$ gives

$$\begin{aligned}\int_0^a \Bigg[\Bigg[-EI_{\text{eff}}\left\{\left(\frac{\partial^2\varphi}{\partial s^2} - l^2\frac{\partial^4\varphi}{\partial s^4}\right)\right\} + (H + T)\varphi \\ - (H + T)\varphi_{(a)} - F\cos\varphi\Bigg]\delta\varphi\Bigg] ds \\ - \left[\left[EI_{\text{eff}}\left\{\left(\frac{\partial\varphi}{\partial s} - l^2\frac{\partial^3\varphi}{\partial s^3}\right)\right\}\right]\delta\varphi'\right]_0^a \\ + \left[\left[EI_{\text{eff}}\left\{\left(\frac{\partial^2\varphi}{\partial s^2}\right)\right\}\right]\delta\varphi''\right]_0^a = 0 \end{aligned} \quad (13)$$

From Eq. (13) the governing equation similar to Eq. (12) is obtained. To solve the governing Eq. (12), we need four boundary conditions, that is, classical as well as nonclassical boundary conditions. The boundary conditions evaluated from the variational principle require $EI_{\text{eff}}[(\partial\varphi/\partial s) - l^2(\partial^3\varphi/\partial s^3)]$ (moment) and $EI_{\text{eff}}(\partial^2\varphi/\partial s^2)$ (higher-order moment) to be specified at $s = 0$ and $s = a$. Thus, one of the possible sets of boundary conditions considered in this work is as follows. At the clamped end, that is, $s = 0$, the rotation of the beam is zero ($\varphi = 0$). Meanwhile, for the nonclassical terms, the trivial natural boundary conditions (higher-order moment evaluated from the variational principle) is expressed as $\frac{d^2\varphi}{ds^2} = 0$. Moreover, at the free end, that is, $s = a$, the zero classical moment gives $\frac{d\varphi}{ds} = 0$ (Beléndez et al. 2002) and the nonclassical or higher-order moment (from variational principle) as depicted in Eq. (8) would also be zero, which gives $\frac{d\varphi}{ds} - l^2\frac{d^3\varphi}{ds^3} = 0$. Overall, the boundary conditions used in this paper are as follows:

$$\text{At } s = 0: \varphi = 0, \quad \frac{d^2\varphi}{ds^2} = 0 \quad (14a)$$

$$\text{At } s = a: \frac{d\varphi}{ds} = 0, \quad \frac{d\varphi}{ds} - l^2\frac{d^3\varphi}{ds^3} \quad \text{or} \quad \frac{d\varphi}{ds} = 0, \quad \frac{d^3\varphi}{ds^3} = 0 \quad (14b)$$

Eq. (12) with the boundary conditions described in Eq. (14) is solved numerically using MATLAB code bvp4c. This code is specifically designed for boundary value problems and is based on a finite-difference method that implements a three-stage Lobatto IIIA collocation formula. Lobatto methods (based on trapezoidal quadrature rule) are widely used in numerical integration for evaluating the approximate solution of differential equations at two endpoints, t_n and t_{n+1}, of the interval $[t_n, t_{n+1}]$. Out of several Lobatto methods, Lobatto IIIA is usually preferred for boundary value problems and therefore considered in this work. Further details about these methods are provided by Shampine et al. (2000), while the implementation of other methods such as dual boundary element method for the determination of fracture properties is provided by Joseph et al. (2014). Furthermore, the strain energy release rate G may be found by taking the beam length as a (crack length) and width b, and the strain energy release rate of the double cantilever beam can be written $G = F(dY_{\max}/bda)$ (Wang and Wang 2013; Stamoulis and Giannakopoulos 2012). For the uncracked part (root part) of the DCB, the governing equation [using Timoshenko beam theory (Wang and Wang 2013; Joseph et al. 2017)] is shown in the Appendix. It is necessary to mention the prominence of shear stresses at the uncracked part that must be incorporated into the constitutive equations. Therefore, the Timoshenko beam model is more suitable for studying the uncracked part of the DCB (Appendix). Accordingly, the potential energy of the uncracked part (U_r) is expressed as

$$U_r = 2\int_{-\infty}^{0} \frac{(M(x))^2}{2EI_{\text{eff}}} dx + 2\int_{-\infty}^{0} \frac{(Q(x))^2}{2G^s A} dx \quad (15)$$

Here, $M(x)$ and $Q(x)$ = bending moment and shear force on cross-sectional area A; G^s = effective shear modulus; and EI_{eff} = effective bending rigidity as defined in Eq. (8). As per the coordinate system, the integrals vary from negative infinity to zero. Using Eq. (15) and the Appendix, one obtains

$$U_r = \frac{1}{\sqrt{EI_{\text{eff}}G^s A}}\left[F^2X^2(\varphi_a) + \left[\int_0^a s(H + T)\frac{d\varphi}{ds} ds\right]^2\right] \quad (16)$$

where $X(\varphi_a)$ = endpoint horizontal deflection (as shown in Fig. 1); F = vertical concentrated force; φ_a = unknown slope at free end of beam; $H = 2\tau_o b$; and T = electrical force of cross section as given in Eq. (9).

Results and Discussion

To numerically solve Eq. (12), the material bulk properties of PZT-5H (Yan and Jiang 2012) are taken: $c_{11} = 102$ GPa, $e_{31} = -17.05$ cm^{-2}, $k_{33} = 1.76 \times 10^{-8}$ CV^{-1} m^{-1}, $G^s = c_{66} = 35.5$ GPa. For the surface, the properties are taken from Huang and Yu (2006) and Yan and Jiang (2011, 2012), that is, $E^s = 7.56$ Nm^{-1} and $e^s_{31} = -3 \times 10^{-8}$ cm^{-1}. The values of the surface residual stresses τ_o and material characteristic length (l) are assumed to be $+10$ Nm^{-1} (since it can be positive or negative) and 17.6 μm (Kong et al. 2009). To solve the bending problem of the piezoelectric DCB with strain gradient effects using the numerical method of the Lobatto IIIA collocation formula, the accuracy of this method is tested by comparing the large deformation (without strain gradient effect) results presented by Beléndez et al. (2002) and the results with the strain gradient effects (with and without surface effect and large deformation) presented by the authors (Joseph et al. 2017) against P_o [$P_o = Fa^2/2(EI)$]. The results are shown in Fig. 2 (here $\beta_y = Y/a$, where Y is the vertical endpoint deflection and a is the length of the beam) and are shown

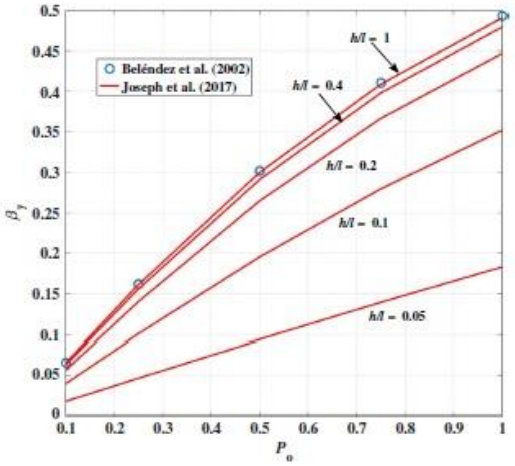

Fig. 2. Comparison of results obtained from current method with those by Beléndez et al. (2002) and Joseph et al. (2017).

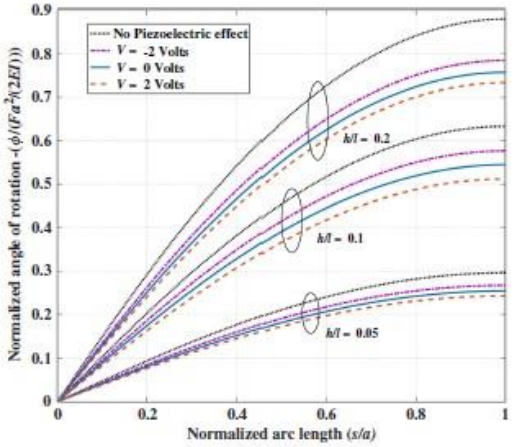

Fig. 4. Normalized angle of rotation along piezoelectric beam for strain gradient model.

to be in agreement. Nevertheless, it also vital to further elaborate the effect of the large deformation against the load factor P_o. The effect of a large deformation for gradient beams with increased load factor was recently shown by Joseph et al. (2017), demonstrating that the effect of a large deformation is more noticeable for a larger normalized endpoint force (gradient models are stiffer, but the plot is not a straight line, especially for $h/l < 0.2$). However, this effect shrinks when the height of the beam equals the material characteristic length. The results are shown in Fig. 3. Here, Y_g, Y_l, and Y_o are the endpoint vertical deflections for the strain gradient piezoelectric cantilever beam (large deformation theory), nongradient piezoelectric cantilever beam (large deformation theory), and classical beam Y_o $[Y_o = Fa^3/(3EI)]$, respectively. Meanwhile, contrary to classical theory, which assumes the endpoint deflection to be independent of the normalized endpoint force, this result

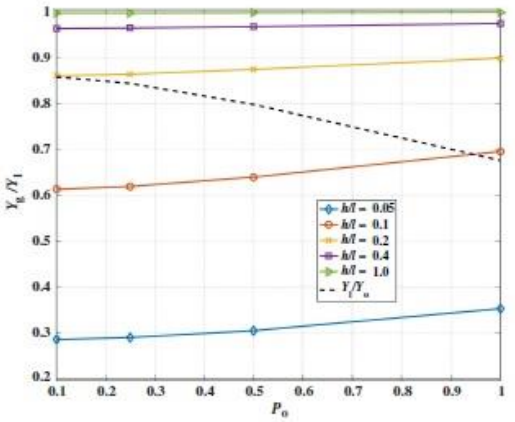

Fig. 3. Normalized tip deflection against load factor P_o (only bulk piezoelectric effect with $V = 0$ V).

demonstrates that a large deformation is more pronounced at a larger normalized endpoint force (curve for Y_l/Y_o).

For a piezoelectric cantilever bending under a large deformation, the force F (1 μN) and height h are chosen in such a manner that the beam remains elastic throughout. The static rotation of a cantilever beam (φ), normalized by, for example, $Fa^2/(2EI)$ (classical result at the free end of the beam), is presented in Fig. 4. Here a/h is taken as 20, and the only bulk piezoelectric effect is taken into account. It is shown that, for lower h/l ratios, the strain gradient beam models predict a stiffer behavior than the classical ones. The normalized deformations are shown to be increasing with a higher h/l ratio. A positive voltage tends to increase and a negative voltage tends to decrease the stiffness of the beam since a negative voltage will induce a compressive force that will make the beam behave softer (Wang and Wang 2016). Moreover, the results for a nonpiezoelectric beam are also shown representing relatively softer behavior. Hence, from Fig. 4 it is evident that the piezoelectric effect enhances beam stiffness.

For DCB, the rotation of the cantilever beam may be used to evaluate its strain energy release rate. This may be done by taking the length of the beam as crack length a and width b, and the strain energy release rate of the double cantilever beam is given by $G = F(dY_{max}/bda)$. Here, Y_{max} may be found using the relation $Y_{max} = \int_0^a \sin(\varphi_a)ds$, where φ_a is the unknown slope at the free end of the beam (as illustrated in the previous section). The effect of piezoelectricity on the strain energy release rate, normalized with the classical solution of a DCB $[G_o = 12F^2a^2/(c_{11}h^3b^2)]$, is plotted in Fig. 5. The results are plotted for different a/h and h/l ratios. Fig. 5 shows that the normalized strain energy release rate of the strain gradient piezoelectric DCB model (G_g) is lower for smaller h/l ratios. It is noted that the piezoelectric effect tends to increase the stiffness of the beam irrespective of the a/h ratio (but this effect decreases for more slender beams). The results are plotted for different voltage values (zero, positive, and negative). It may be seen that negative voltage increases and a positive voltage decreases the strain energy release rate. The effect of the applied voltage is more significant for slender beams. Moreover, it is necessary to evaluate the relationship between the gradient and nongradient piezoelectric DCB considering large deformation theory. For this, the ratio of the

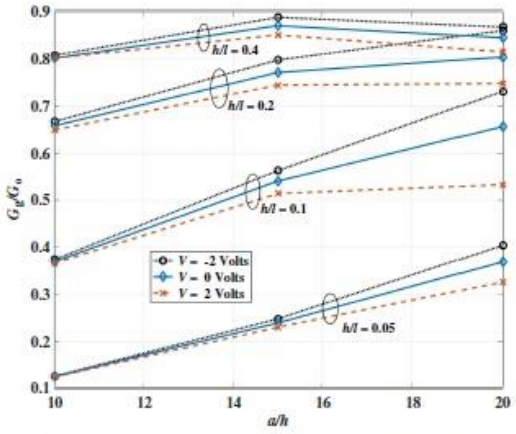

Fig. 5. Strain energy release rate for piezoelectric strain gradient DCB normalized with classical result: G_o.

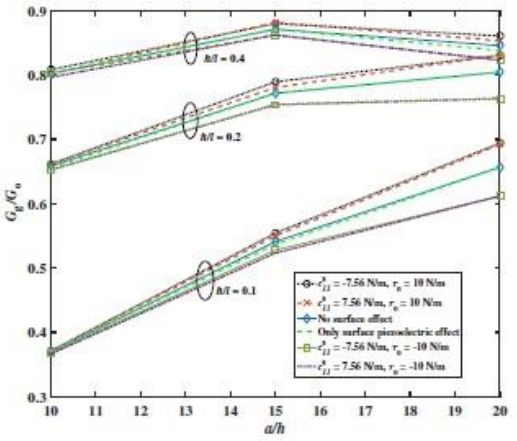

Fig. 7. Normalized strain energy release rate for piezoelectric strain gradient DCB with and without surface effects (surface elasticity, surface residual stress, and surface piezoelectricity; $V = 0$ V).

strain energy release rate for the strain gradient models (G_g) to the conventional large deformation (nongradient) piezoelectric DCB (G_l) is plotted in Fig. 6. The ratios are greater for positive voltages and smaller for negative voltages. Meanwhile, it may be clearly seen that the gradient effect is more prominent for smaller h/l and decreases as h/l increases. Like Fig. 5, Fig. 6 makes evident that the effect of the applied voltage is more significant for slender beams. Overall, it may fairly be concluded that the strain gradient effect must be incorporated into the formulation to accurately predict the fracture behavior of micro/nano piezoelectric DCB.

Next, the effect of surface effects, that is, surface elasticity and surface residual stress, on the fracture behavior of a piezoelectric DCB (here surface piezoelectricity is also considered) is evaluated and plotted in Fig. 7. Since surface elasticity and surface residual stress can be positive or negative, it is necessary to demonstrate the effect of both positive and negative surface parameters (surface

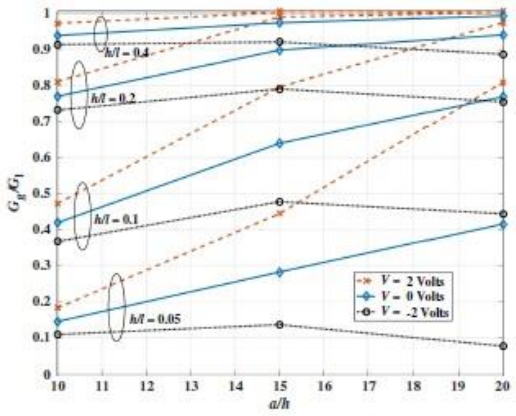

Fig. 6. Strain energy release rate for strain gradient piezoelectric DCB normalized with nongradient piezoelectric DCB.

residual stress and surface elasticity) on the strain energy release rate of the piezoelectric DCB. For this reason, the results are plotted with six different kinds of inputs, as shown in Fig. 7. Here voltage is taken as zero. The normalized strain energy release rate of the strain gradient models (different h/l ratios) of the piezoelectric DCB is evaluated and plotted. From Fig. 7 it is evident that the effect of surface elasticity and surface piezoelectricity is very small compared to that of surface residual stress, that is, the surface residual stress constitutes a major proportion of all the surface effects on the fracture behavior of the DCB (Wang and Wang 2013). Moreover, it can be seen that the surface effects are more prominent for higher a/h ratios, meaning for slender beams. The positive surface residual stress and negative surface elasticity enhance the normalized strain energy release rate, while the negative surface residual stress and positive surface elasticity reduce the normalized strain energy release rate. Owing to the prominent effect of surface residual stress, the results for the strain energy release rate are plotted separately in Fig. 8 with different applied voltages. Here the results are plotted only for $h/l = 0.05$ (under a higher strain gradient effect). Interestingly, under a positive applied voltage and negative surface residual stress ($V = 2$ V; $\tau_o = -10$ Nm^{-1}), the beam tends to behave much stiffer when $a/h > 15$. This stiffer behavior may be explained by the sign of the curvature and surface residual stress [using a Young–Laplace equation (Chen et al. 2006; Gurtin et al. 1998)], which cause an additional distributed load and change the beam stiffness (He and Lilley 2008a; Wang and Wang 2015; Wu et al. 2015). For instance, with a positive surface residual stress, a positive curvature results in a positive distributed transverse force. This positive force increases the rotation of the cantilever, so the beam behaves like a softer material. Meanwhile, this behavior is the complete opposite of that in the case where τ_o<0, so a cantilever beam may exhibit a comparatively stiffer response.

It is necessary to evaluate the fracture behavior of the piezoelectric DCB with different electrical boundary conditions, that is, the open- and short-circuit condition. For the short-circuit boundary condition, the electric field (E_z) would be zero, which would nullify the role of surface piezoelectricity. Here, the following

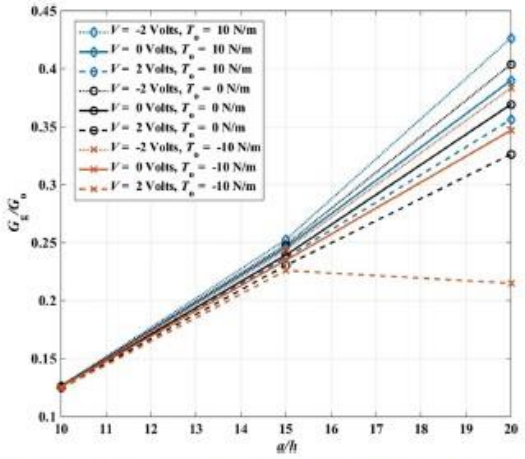

Fig. 8. Effect of surface residual stress on normalized strain energy release rate ($E^s = e^s_{31} = 0$).

parameters are considered: $V = 0$ V, $E^s = -7.56$ Nm^{-1}, and $\tau_o = -10$ Nm^{-1}. Fig. 9 shows the normalized strain energy release rate of the DCB with different electrical boundary conditions. From Fig. 9 it is evident that the normalized strain energy rate with a short-circuit boundary condition is larger than that of an open-circuit condition. This effect may be explained by comparing the bending rigidities of the beam with different electrical boundary conditions. For instance, in the case of a short circuit ($E_z = 0$), the bulk stress is given as $\sigma_{xx} = Ez\mathrm{d}\varphi/\mathrm{d}s$, which gives an effective bending rigidity of $EI_{\text{eff}} = c_{11}bh^3/12$. On the other hand, for an open-circuit boundary condition, the stress is $\sigma_{xx} = c_{11}z\mathrm{d}\varphi/\mathrm{d}s + e_{31}E_z$, which gives a bending rigidity of $EI_{\text{eff}} = (c_{11} + e^2_{31}/k_{33})bh^3/12$. It is evident, from a comparison of the two

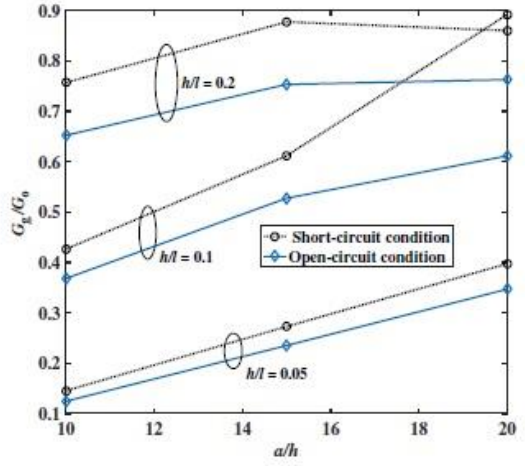

Fig. 9. Comparison of normalized strain energy release rate under different electrical boundary conditions ($E^s = -7.56$ N/m, $\tau_o = -10$ N/m, $V = 0$ V).

bending rigidities, that that of the short-circuit condition is smaller than that of the open-circuit condition. Therefore, the normalized energy release rate of the short circuit is larger than that of the open-circuit condition. This difference in normalized strain energy release rate is more evident when the height of the beam is increased.

Now the effect of the uncracked (root) part of the DCB is investigated numerically. Here all the surface effects are included, that is, $E^s = 7.56$ Nm^{-1}, $e^s_{31} = -3 \times 10^{-8}$ Nm^{-1}, and $\tau_o = -10$ Nm^{-1} ($V = 0$ V). First, the strain energy release rate of the uncracked part (G_2) is evaluated using $G_2 = dU_r/bda$ [U_r is defined in Eq. (16)]. Here R is defined as the ratio of the strain energy release rate contributed by the uncracked part to the cracked part of the DCB ($R = G_2/G_1$). The variations of R versus a/h for different h/l ratios are plotted in Fig. 10. The results are plotted for both piezoelectric DCB models (with and without the strain gradient effect). It can be seen from Fig. 10 in the case of strain gradient models that, for smaller DCBs, that is, $h/l \le 0.2$ and $a/h \le 20$, the value of R is huge and hence should not be neglected, even for slender beams (higher a/h ratios). Also when $h/l = 0.05$ and $a/h = 10$, the value of R is greater than 0.7 that establishes the contribution of the uncracked part of the DCB is approximately 70% of the cracked part. The shows the massive root effect at a smaller scale [which further elaborates the argument made by Wang and Wang (2013)]. The contribution of the uncracked part decreases as a/h is increased. The results presented in Fig. 10 further strengthen the argument presented by Wang and Wang (2013). However, for nongradient models, the contribution of the uncracked part is between 6 and 13% (depending on the height and a/h ratio). A comparison of the normalized strain energy release rate for the strain gradient model (with and without the root effect) as well as the nongradient (with and without the root effect) is shown in Fig. 11. It is evident that the incorporation of the uncracked part enhances the strain energy release rate of piezoelectric DCBs with different h/l and a/h ratios. In particular, for $h/l < 0.1$, it may fairly be stated that even with the fusion of the root effect [in either the strain gradient or nongradient (large deformation) model], the normalized strain energy release rate of the gradient model remains lower than that of the nongradient models (this highlights a massive strain gradient effect in lowering the strain energy release rate and, hence, stiffening the structure). Although the difference between the strain energy release rate of gradient and

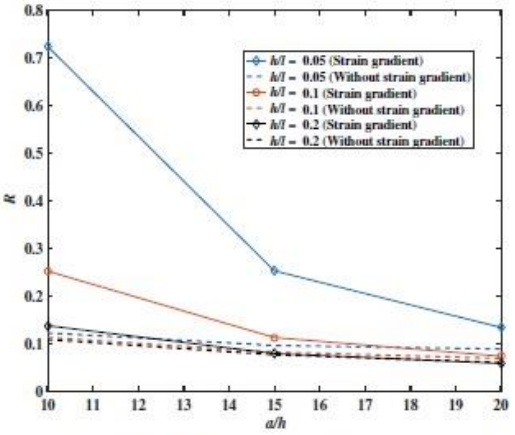

Fig. 10. Variation of R versus a/h.

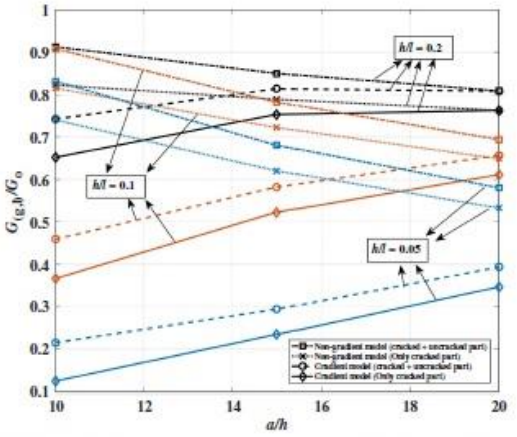

Fig. 11. Normalized strain energy release rate with/without root effect versus a/h (blue, $h/l = 0.05$; orange, $h/l = 0.1$; black, $h/l = 0.2$).

nongradient models decreases with a higher a/h ratio, but this statement may not be true when $h/l \geq 0.1$ since the strain energy release rate becomes more sensitive to beam slenderness (at higher h/l). Overall, from Figs. 10 and 11 it is evident that the incorporation of the root (uncracked) part is essential for making an accurate prediction of the fracture behavior of the DCB.

Conclusion

This paper investigates the influence of strain gradient on the fracture of piezoelectric a DCB fracture mechanics specimen subjected to a large deformation. The results demonstrate that the effect of a large deformation is dependent on the normalized endpoint force. As expected, the strain gradient model is shown to enhance the stiffness of a piezoelectric beam. The effects of strain gradient, surface piezoelectricity, surface elasticity, surface residual stress, applied voltage, and different electrical boundary conditions on the fracture behavior of a piezoelectric DCB are thoroughly studied. Both cracked and uncracked parts of the DCB are included in the modeling and analysis. Results show that the strain gradient effect tends to decrease the strain energy release rate, and this effect is more evident when $h/l < 0.4$. The effect of surface residual stress is more significant than surface elasticity and surface piezoelectricity. The strain energy release rate of a short-circuit model is higher than an open-circuit one. The root effect also enhances the normalized strain energy release rate and must not be ignored even for slender beams (this observation is completely different than in the case of classical results). The results of this paper will be useful not only for determining the fracture toughness of micro/nanoscale piezoelectric materials but also for explaining and validating the relevant test data.

Moreover, this paper studies a homogeneous DCB specimen; however, in many engineering practices, materials are nonhomogeneous, and their fracture has generated great interest among experts in the field of the mechanics of materials (Ma et al. 2007; Zhou et al. 2005b; Guo et al. 2004a, b). Additional investigations are clearly needed to gain further knowledge to capture the effect of material inhomogeneity on large deformations and strain gradient effects on the fracture of a DCB.

Appendix. Governing Equations of Root Part of DCB

$$\frac{dN}{dx} = q, \quad \frac{dM}{dx} = Q + q\frac{h}{2}, \quad \frac{dQ}{dx} = p \tag{17}$$

$$\frac{d^2u_0}{dx^2} = 0, \quad \frac{d^2\varphi}{dx^2} - \beta^2\varphi = 0, \quad p = G^s A\frac{d\varphi}{dx} \tag{18}$$

where $\beta^2 = \frac{G^s A}{EI_{eff}}$; and G^s = effective shear modulus.

The boundary conditions are as follows:

1. At $x = 0$, $N = 0$ and $M_{(0)} = FX_{(\varphi_a)}$
2. At $x = -\infty$, $N = 0$, $M = 0$

where p and q are, respectively, the normal stress and shear stress on the $z = 0$ plane; here q = zero; u_o and N = displacement and resultant force along x-direction, respectively; M = bending moment; Q = shear force on beam cross section; and φ_a = unknown slope at free end of beam. Using boundary conditions and Eq. (18), we obtain

$$N = 0, \quad M(x) = M_{(0)}e^{\beta x}, \quad Q(x) = \alpha M_{(0)}e^{\beta x} \tag{19}$$

References

Abdelkefi, A., F. Najar, A. Nayfeh, and S. B. Ayed. 2011. "An energy harvester using piezoelectric cantilever beams undergoing coupled bending–torsion vibrations." *Smart Mater. Struct.* 20 (11): 115007. https://doi.org/10.1088/0964-1726/20/11/115007.

Aifantis, E. C. 1992. "On the role of gradients in the localization of deformation and fracture." *Int. J. Eng. Sci.* 30 (10): 1279–1299. https://doi.org/10.1016/0020-7225(92)90141-3.

Aifantis, E. C. 1999a. "Gradient deformation models at nano, micro and macro scales." *J. Eng. Mater. Technol.* 121 (2): 189–202. https://doi.org/10.1115/1.2812366.

Aifantis, E. C. 1999b. "Strain gradient interpretation of size effects." *Int. J. Fract.* 95 (1–4): 299–314. https://doi.org/10.1023/A:1018625006804.

Aifantis, E. C. 2003. "Update on a class of gradient theories." *Mech. Mater.* 35 (3): 259–280. https://doi.org/10.1016/S0167-6636(02)00278-8.

Aifantis, E. C. 2016. "Chapter one-internal length gradient (ILG) material mechanics across scales and disciplines." *Adv. Appl. Mech.* 49: 1–110. https://doi.org/10.1016/bs.aams.2016.08.001.

Beléndez, T., C. Neipp, and A. Beléndez. 2002. "Large and small deflections of a cantilever beam." *Eur. J. Phys.* 23 (3): 371–379. https://doi.org/10.1088/0143-0807/23/3/317.

Chen, T., M. S. Chiu, and C. N. Weng. 2006. "Derivation of the generalized Young-Laplace equation of curved interfaces in nanoscaled solids." *J. Appl. Phys.* 100 (7): 074308. https://doi.org/10.1063/1.2356094.

Christensen, J., and C., Bastien 2015. *Nonlinear optimization of vehicle safety structures: Modelling of structures subjected to large deformations*. Oxford, UK: Butterworth-Heinemann.

Devitt, D., R. Schapery, and W. Bradley. 1980. "A method for determining the mode I delamination fracture toughness of elastic and viscoelastic composite materials." *J. Compos. Mater.* 14 (4): 270–285.

Fang, X. Q., J. X. Liu, and V. Gupta. 2013. "Fundamental formulations and recent achievements in piezoelectric nan-structures: A review." *Nanoscale* 5 (5): 1716–1726. https://doi.org/10.1039/c2nr33531j.

Giannakopoulos, A., E. Amanatidou, and N. Aravas. 2006. "A reciprocity theorem in linear gradient elasticity and the corresponding Saint-Venant principle." *Int. J. Solids Struct.* 43 (13): 3875–3894. https://doi.org/10.1016/j.ijsolstr.2005.05.048.

Giannakopoulos, A., and K. Stamoulis. 2007. "Structural analysis of gradient elastic components." *Int. J. Solids Struct.* 44 (10): 3440–3451. https://doi.org/10.1016/j.ijsolstr.2006.09.033.

Guo, L. C., L. Z. Wu, T. Zeng, and L. Ma. 2004a. "The dynamic fracture behavior of a functionally graded coating-substrate system." *Compos. Struct.* 64 (3–4): 433–441. https://doi.org/10.1016/j.compstruct.2003.09.044.

Guo, L.-C., L.-Z. Wu, T. Zeng, and L. Ma. 2004b. "Mode I crack problem for a functionally graded orthotropic strip." *Eur. J. Mech. A Solids* 23 (2): 219–234. https://doi.org/10.1016/j.euromechsol.2003.12.006.

Gurtin, M., J. Weissmuller, and F. Larche. 1998. "A general theory of curved deformable interfaces in solids at equilibrium." *Philos. Mag. A* 78 (5): 1093–1109. https://doi.org/10.1080/01418619808239977.

Gurtin, M. E., and A. I. Murdoch. 1978. "Surface stress in solids." *Int. J. Solids Struct.* 14 (6): 431–440. https://doi.org/10.1016/0020-7683(78)90008-2.

Gusso, A. 2010. "Acoustic electromechanical energy loss mechanism for suspended micro-and nanoelectromechanical resonators." *Appl. Phys. Lett.* 96 (19): 193504. https://doi.org/10.1063/1.3428786.

He, J., and C. M. Lilley. 2008a. "Surface effect on the elastic behavior of static bending nanowires." *Nano Lett.* 8 (7): 1798–1802. https://doi.org/10.1021/nl0733233.

He, J., and C. M. Lilley. 2008b. "Surface stress effect on bending resonance of nanowires with different boundary conditions." *Appl. Phys. Lett.* 93 (26): 263108. https://doi.org/10.1063/1.3050108.

Huang, G. Y., and S. W. Yu. 2006. "Effect of surface piezoelectricity on the electromechanical behaviour of a piezoelectric ring." *Phys. Status Solidi (b)* 243 (4): R22–R24. https://doi.org/10.1002/pssb.200541521.

Jia, X., J. Yang, S. Kitipornchai, and C. W. Lim. 2010. "Free vibration of geometrically linear micro-switches under electrostatic and Casimir forces." *Smart. Mater. Struct.* 19 (11): 115028. https://doi.org/10.1088/0964-1726/19/11/115028.

Jia, X. L., J. Yang, and S. Kitipornchai. 2011. "Pull-in instability of geometrically nonlinear micro-switches under electrostatic and Casimir forces." *Acta. Mech.* 218 (1–2): 161–174. https://doi.org/10.1007/s00707-010-0412-8.

Joseph, R. P., J. Purbolaksono, H. L. Liew, S. Ramesh, and M. Hamdi. 2014. "Stress Intensity factors of a corner crack emanating from a pinhole of a solid cylinder." *Eng. Fract. Mech.* 128: 1–7. https://doi.org/10.1016/j.engfracmech.2014.07.021.

Joseph, R. P., B. L. Wang, and B. Samali. 2017. "Size effects on double cantilever beam fracture mechanics specimen based on strain gradient theory." *Eng. Fract. Mech.* 169: 309–320. https://doi.org/10.1016/j.engfracmech.2016.10.013.

Kahrobaiyan, M. H., M. Rahaeifard, and M. T. Ahmadian. 2011. "A nonlinear strain gradient beam formulation." *Int. J. Eng. Sci.* 49 (11): 1256–1267. https://doi.org/10.1016/j.ijengsci.2011.01.006.

Ke, L. L., L. Chen, and Y. S. Wang. 2015. "Free vibration of nonlocal piezoelectric nanoplates under various boundary conditions." *Phys. E* 66: 93–106. https://doi.org/10.1016/j.physe.2014.10.002.

Ke, L. L., Y. S. Wang, and Z. D. Wang. 2012. "Nonlinear vibration of the piezoelectric nanobeams based on the nonlocal theory." *Compos. Struct.* 94 (6): 2038–2047. https://doi.org/10.1016/j.compstruct.2012.01.023.

Kong, S., S. Zhou, Z. Nie, and K. Wang. 2009. "Static and dynamic analysis of micro beams based on strain gradient elasticity theory." *Int. J. Eng. Sci.* 47 (4): 487–498. https://doi.org/10.1016/j.ijengsci.2008.08.008.

Lam, D. C. C., F. Yang, A. C. M. Chong, J. Wang, and P. Tong. 2003. "Experiments and theory in strain gradient elasticity." *J. Mech. Phys. Solids* 51 (8): 1477–1508. https://doi.org/10.1016/S0022-5096(03)00053-X.

Li, X. F., and K. Y. Lee. 2016. "Fracture of a thin power-law nonlinear material with a crack using the DCB model." *Int. J. Fract.* 201 (1): 119–125. https://doi.org/10.1007/s10704-016-0116-8.

Liebold, C., and W. F. Muller. 2015. "Applications of strain gradient theories to the size effect in submicro-structures incl. Experimental analysis of elastic material parameters." *Bull. TICMI* 19 (1): 45–55.

Ma, L., H. Li, R. Abdelmoula, and L. Wu. 2007. "Mode III crack problem in a functionally graded magneto-electro-elastic strip." *Int. J. Solids Struct.* 44 (17): 5518–5537. https://doi.org/10.1016/j.ijsolstr.2007.01.012.

Ma, L., L. Z. Wu, Z. G. Zhou, and L. C. Guo. 2005a. "Fracture analysis of a functionally graded piezoelectric strip." *Compos. Mater.* 69 (3): 294–300. https://doi.org/10.1016/j.compstruct.2004.07.007.

Ma, L., L. Z. Wu, Z. G. Zhou, and L. C. Guo. 2005b. "Scattering of the harmonic anti-plane shear waves by a crack in functionally graded piezoelectric materials." *Compos. Mater.* 69 (4): 436–441. https://doi.org/10.1016/j.compstruct.2004.08.001.

Mindlin, R. D. 1965. "Second gradient of strain and surface-tension in linear elasticity." *Int. J. Solids Struct.* 1 (4): 417–438. https://doi.org/10.1016/0020-7683(65)90006-5.

Nan, H., and B. Wang. 2013. "Effect of crack face residual surface stress on nanoscale fracture of piezoelectric materials." *Eng. Fract. Mech.* 110: 68–80. https://doi.org/10.1016/j.engfracmech.2013.08.002.

Papargyri-Beskou, S., K. Tsepoura, D. Polyzos, and D. Beskos. 2003. "Bending and stability analysis of gradient elastic beams." *Int. J. Solids Struct.* 40 (2): 385–400. https://doi.org/10.1016/S0020-7683(02)00522-X.

Polizzotto, C. 2016. "A note on the higher order strain and stress tensors within deformation gradient elasticity theories: Physical interpretations and comparisons." *Int. J. Solids Struct.* 90: 116–121. https://doi.org/10.1016/j.ijsolstr.2016.04.001.

Reeder, J. R., and J. Crews Jr. 1991. *Nonlinear analysis and redesign of the mixed-mode bending delamination test.* Hampton, VA: National Aeronautics and Space Administration, Langley Research Center.

Ru, C. Q., and E. C. Aifantis. 1993. "A simple approach to solve boundary-value problems in gradient elasticity." *Acta. Mech.* 101 (1–4): 59–68. https://doi.org/10.1007/BF01175597.

Shampine, L. F., J. Kierzenka, and M. W. Reichelt. 2000. "Solving boundary value problems for ordinary differential equations in MATLAB with BVP4C." Tutorial Notes. Accessed October 26, 2000. http://www.mathworks.com/bvp_tutorial.

Shen, S., and S. Hu. 2010. "A theory of flexoelectricity with surface effect for elastic dielectrics." *J. Mech. Phys. Solids* 58 (5): 665–677. https://doi.org/10.1016/j.jmps.2010.03.001.

Shi, M., H. P. Wu, L. Li, and G. H. Chai. 2014. "Calculation of stress intensity factors for functionally graded materials by using the weight functions derived by the virtual crack extension technique." *Int. J. Mech. Mater. Des.* 10 (1): 65–77. https://doi.org/10.1007/s10999-013-9231-0.

Stamoulis, K., and A. E. Giannakopoulos. 2012. "A study of size effects and length scales in fracture and fatigue of metals by second gradient modelling." *Fatigue Fract. Eng. Mater. Struct.* 35 (9): 852–860. https://doi.org/10.1111/j.1460-2695.2012.01668.x.

Vardoulakis, I., and J. Sulem. 1995. *Bifurcation analysis in geomechanics.* Glasgow, UK: Blackie/Chapman and Hall.

Wang, B. L., and K. F. Wang. 2013. "Effect of surface residual stress on the fracture of double cantilever beam fracture toughness specimen." *J. Appl. Phys.* 113 (15): 153502. https://doi.org/10.1063/1.4801875.

Wang, G. F., and X. Q. Feng. 2009. "Surface effects on buckling of nanowires under uniaxial compression." *Appl. Phys. Lett.* 94 (14): 141913. https://doi.org/10.1063/1.3117505.

Wang, K., and B. Wang. 2015. "A general model for nano-cantilever switches with consideration of surface effects and nonlinear curvature." *Phys. E* 66: 197–208. https://doi.org/10.1016/j.physe.2014.10.012.

Wang, K. F., and B. L. Wang. 2016. "Nonlinear fracture mechanics analysis of nano-scale piezoelectric double cantilever beam specimens with surface effect." *Eur. J. Mech. A-Solid* 56: 12–18. https://doi.org/10.1016/j.euromechsol.2015.10.002.

Williams, J. G. 1987. "Large displacement and end block effects in the 'DCB' interlaminar test in modes I and II." *J. Compos. Mater.* 21 (4): 330–347. https://doi.org/10.1177/002199838702100403.

Wu, Q., A. A. Volinsky, L. Qiao, and Y. Su. 2015. "Surface effects on static bending of nanowires based on non-local elasticity theory." *Prog. Nat. Sci.: Mater. Int.* 25 (5): 520–524. https://doi.org/10.1016/j.pnsc.2015.09.012.

Yan, Z., and L. Jiang. 2011. "The vibrational and buckling behaviors of piezoelectric nanobeams with surface effects." *Nanotechnology* 22 (24): 245703. https://doi.org/10.1088/0957-4484/22/24/245703.

Yan, Z., and L. Jiang. 2012. "Vibration and buckling analysis of a piezoelectric nanoplate considering surface effects and in-plane constraints." *Proc. R. Soc. A* 468 (2147): 3458–3475. https://doi.org/10.1098/rspa.2012.0214.

Yang, R., Y. Qin, C. Li, L. Dai, and Z. L. Wang. 2009. "Characteristics of output voltage and current of integrated nanogenerators." *Appl. Phys. Lett.* 94 (2): 022905. https://doi.org/10.1063/1.3072362.

Yue, Y. M., K. Y. Xu, and E. C. Aifantis. 2014. "Microscale size effects on the electromechanical coupling in piezoelectric material for anti-plane

problem." *Smart. Mater. Struct.* 23 (12): 125043. https://doi.org/10.1088/0964-1726/23/12/125043.

Yue, Y. M., K. Y. Xu, T. Chen, and E. C. Aifantis. 2015. "Size effects on magnetoelectric response of multiferroic composite with inhomogeneities." *Phys. B* 478: 36–42. https://doi.org/10.1016/j.physb.2015.08.056.

Zhang, W., T. Wang, and X. Chen. 2008. "Effect of surface stress on the asymmetric yield strength of nanowires." *Jpn. J. Appl. Phys.* 103 (12): 123527. https://doi.org/10.1063/1.2946447.

Zhang, Z., and L. Jiang. 2014. "Size effects on electromechanical coupling fields of a bending piezoelectric nanoplate due to surface effects and flexoelectricity." *Jpn. J. Appl. Phys.* 116 (13): 134308. https://doi.org/10.1063/1.4897367.

Zhou, Z. G., L. Z. Wu, and B. Wang. 2005a. "The behavior of a crack in functionally graded piezoelectric/piezomagnetic materials under anti-plane shear loading." *Arch. Appl. Mech.* 74 (8): 526–535. https://doi.org/10.1007/s00419-004-0369-y.

Zhou, Z. G., L. Z. Wu, and B. Wang. 2005b. "The dynamic behavior of two collinear interface cracks in magneto-electro-elastic materials." *Eur. J. Mech. A/Solids* 24 (2): 253–262. https://doi.org/10.1016/j.euromechsol.2004.10.006.

Paper 4:

International Journal of Solids and Structures 146 (2018) 214–223

Contents lists available at ScienceDirect

International Journal of Solids and Structures

journal homepage: www.elsevier.com/locate/ijsolstr

Strain gradient fracture in an anti-plane cracked material layer

R.P. Joseph, B.L. Wang*, B. Samali

Centre for Infrastructure Engineering, School of Computing, Engineering and Mathematics, Western Sydney University, Penrith, New South Wales 2751, Australia

ARTICLE INFO

Article history:
Received 25 November 2017
Revised 2 March 2018
Available online 4 April 2018

Keywords:
Stress intensity factors
Strain gradient elasticity theory
Material characteristic lengths
Dual integral equations

ABSTRACT

Fracture mechanics analysis in terms of evaluating stress intensity factors of an anti-plane isotropic cracked layer is carried out using strain gradient elasticity theory. The crack plane is assumed parallel to the layer edges. Both volumetric and surface strain gradient material characteristic lengths are considered in formulations and numerical solutions. Two boundary value problems corresponding to "stress-free" and "clamped" boundaries are considered in which each solution is reduced to the dual integral equations. The Fredholm integral equation, proceeding from the dual integral equations, is numerically solved to evaluate crack tip stress intensity factor. Stress intensity factors for stress-free boundary conditions are higher with smaller height (or with a longer crack) and vice versa for clamped boundaries. Volumetric strain gradient effect reduces stress intensity factor and demonstrates strong size effect on a smaller scale. Crack stiffness becomes more pronounced with positive surface strain gradient, while negative surface gradient leads to a more complaint crack. In general, the contribution of volumetric strain gradient is shown to be more dominant than that of surface strain gradient.

1. Introduction

Material discontinuities in micro and nanoscale structures promote its mechanical behavior to be size dependent. This size dependency (size effect) has been thoroughly observed in experimental studies (Fleck & Hutchinson, 1997; Lam et al., 2003; McFarland & Colton, 2005). The discrete nature of the material medium (at a smaller scale) is not considered in classical continuum theories where internal dimensions of the structure are assumed negligible in comparison to the external ones. Hence, material's elastic as well as the plastic behavior becomes scale-free and independent of an underlying microstructure. Over the years, several theories have been proposed incorporating intrinsic length scale in the continuum model to cater for size effect. Some of the well-known theories in this regard are non-local elasticity theory (Eringen and Edelen, 1972), couple stress theory (Yang et al., 2002) and strain gradient theory (Aifantis, 1992, 2003; Lam et al., 2003). Pioneer work related to strain gradient theory was first postulated by Mindlin (1964, 1965) and further re-established and updated by Aifantis in (1992) and (2003), respectively. The physical meaning of higher order strain tensor employed in gradient elasticity theories is recently provided by Polizzotto (2016). On the other hand, the strain gradient theory proposed by Vardoulakis et al. (1996), provides the simplest and most practical generalization of corresponding constitutive theory accounting for only two material characteristic lengths (with the units of length). These material constants are responsible for material volumetric and surface strain gradient terms, usually represented as l and l', respectively (Chan et al., 2008; Paulino et al., 2003; Vardoulakis et al., 1996). This theory has been successfully employed to observe size effects (Aifantis, 2011) in various engineering problems such as in twisted micro-wires and bent micro-cantilever beams (Aifantis, 1999). A comprehensive review of this gradient theory and applications of an internal length gradient across various scales is recently provided by Aifantis (2016). Further application and validation of this simpler strain gradient theory are confirmed by Vardoulakis and Sulem (1995) and Giannakopoulos and Stamoulis (2007). Very recently application can be found in the fracture study of double cantilever beam fracture mechanics specimen conducted by the authors (Joseph et al., 2017).

Quite a few studies related to the fracture problem in infinite medium (in which the geometric disturbance is only due to crack), based on gradient elasticity theories, are conducted over the years. For instance, one of the pioneering works in the field of gradient elasticity in Mode-III crack problem was conducted by Vardoulakis et al. (1996), Exadaktylos (1998) and subsequently by Exadaktylos and Vardoulakis (2001). In these papers, two material parameters l and l' related to volumetric and surface strain gradients were used to solve two boundary value problems i.e. traction boundary value problem and mixed boundary value problem. Paulino et al. (2003) and Chan et al. (2008) em-

* Corresponding author.
E-mail address: B.Wang@westernsydney.edu.au (B.L. Wang).

https://doi.org/10.1016/j.ijsolstr.2018.04.002
0020-7683/

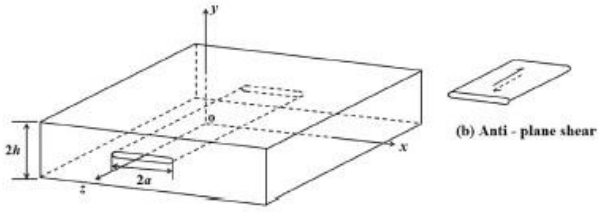

Fig. 1. Schematic diagrams.

ployed gradient elasticity theory to solve mode III crack problems in functionally graded materials. In the first case, crack is assumed perpendicular (Paulino et al., 2003), while in second case crack plane is parallel to the material gradation (Chan et al., 2008). Fannjiang et al. (2002) employed a hyper-singular integrodifferential equation approach to solve the anti-plane shear crack problem using strain gradient elasticity theory. Some interesting information related to dislocation based-gradient elastic fracture mechanics for the anti-plane crack problem is discussed by Mousavi and Aifantis (2015). A very comprehensive study related to an anti-plane analysis of an infinite plane with multiple cracks based on strain gradient theory is recently conducted by Karimipour and Fotuhi (2017).

Above studies are strictly related to the bodies whose edges are far away and any disturbance in the material medium is primarily due to crack initiation and propagation. However, in many practical engineering applications, the specimen boundaries are finite and hence contribute significantly to its fracture behavior. One such case is the crack initiation and propagation in elastic media of the form of layer/strip with finite height. Estimation of fracture properties in this case, such as stress intensity factor at the crack tip, is extremely vital to accurately predict crack growth rates. For classical case, several analytical models have been proposed by researchers using different approaches. For instance, closed form solutions of a crack at the mid-plane of elastic media subjected to anti-plane shear stress are obtained by (Yang, 1997). Singh et al. (1981) employed Fourier transform technique, while Tait and Moodie (1981) utilized the complex variable method to provide the closed form solution of mode-III crack moving along the center of an elastic strip. On the other hand, the solution of interface crack between two dissimilar materials in a closed form is provided by Li (2001). For an anti-plane interface crack between two dissimilar magneto-electroelastic layers, Wang and Mai (2006) evaluated closed-form solutions for stress intensity factors. Furthermore, thorough investigations of mode-III crack in multi-layered composites are provided by Sih and Chen (1981).

According to authors' knowledge, most of the models in literature may be divided into two groups; The first group relates to the evaluation of closed form solution of an anti-plane crack in an infinite medium based on gradient elasticity theories and the second group comprises those classical studies which are conducted to evaluate the closed form solution of cracked elastic strip/layer (finite boundaries). Therefore, in this article the simplest strain gradient theory (proposed by Vardoulakis et al. 1996, Exadaktylos, 1998 and subsequently elaborated by Exadaktylos and Vardoulakis, 2001) comprising two material parameters, related to volumetric and surface strain gradients, respectively, is applied to solve the mode III crack problem in an elastic isotropic layer. The objective here is to numerically estimate the crack tip stress intensity factors of a crack propagated at the middle plane of an elastic isotropic layer having finite height. Two types of boundary value problems are considered i.e. stress-free boundaries and clamped boundaries. The solution of each problem is reduced to dual integral equations. The kernel of the Fredholm integral equation (an improper integral that ranges from 0 to infinity) of the second kind, thus obtained (by applying the method of Copson (1961) on the dual integral equations) is numerically solved by using the collocation method of Gauss–Laguerre quadrature.

2. Theoretical formulations

This section introduces the constitutive equations and theoretical formulations of an isotropic elastic layer of finite thickness using strain gradient theory. Firstly, the constitutive equations are derived without incorporating surface strain gradient effect ($l' = 0$) followed by the detailed analysis of complete strain gradient model (with both volumetric and surface strain gradient effect). The approach considered in this paper is similar to one adopted by Vardoulakis et al. (1996) and Exadaktylos (1998).

Consider a crack of length $2a$ placed at the mid plane of an isotropic layer with thickness (height) $2h$. The boundaries of the layer are at $y = \pm h$ and reference axes are shown in Fig. 1a. The crack surfaces are subjected to the applied anti-plane shear stress (τ_1) as shown in Fig. 1b. The conditions at $y = 0$ are given as: $\tau_{yz}(x,0) = -\tau_1$ for $|x| < a$ and $w_z(x,0) = 0$ for $|x| \geq a$. For the upper half plane i.e. $y \geq 0$, the stresses and double stress derived from the constitutive equations of gradient elasticity with surface energy are given as (Chan et al., 2008; Vardoulakis et al., 1996)

$$\tau_{zx} = G\left[\frac{\partial w_z}{\partial x} - l^2\nabla^2\frac{\partial w_z}{\partial x}\right] \tag{1a}$$

$$\tau_{yz} = G\left[\frac{\partial w_z}{\partial y} - l^2\nabla^2\frac{\partial w_z}{\partial y}\right] \tag{1b}$$

$$\mu_{xxz} = Gl^2\frac{\partial^2 w_z}{\partial x^2} \tag{1c}$$

$$\mu_{xyz} = Gl^2\frac{\partial^2 w_z}{\partial x\partial y} \tag{1d}$$

$$\mu_{yxz} = G\left[-l'\frac{\partial w_z}{\partial x} + l^2\frac{\partial^2 w_z}{\partial x\partial y}\right] \tag{1e}$$

$$\mu_{yyz} = G\left[-l'\frac{\partial w_z}{\partial y} + l^2\frac{\partial^2 w_z}{\partial y^2}\right] \tag{1f}$$

Here $\nabla^2 = \partial^2/\partial x^2 + \partial^2/\partial y^2$, l and l' are the volumetric and surface material characteristic lengths, respectively. For an anti-plane shear crack problem as depicted in Fig. 1, we have $u_x = u_y = 0$, $u_z \neq 0$. Also $\sigma_{xx} = \sigma_{yy} = \sigma_{zz} = \tau_{xy} = 0$ while $\tau_{yz} \neq 0$ and $\tau_{xz} \neq 0$. The equilibrium equation i.e. $\partial\tau_{yz}/\partial y + \partial\tau_{xz}/\partial x = 0$ with the help of equations in (1) may be expanded as

$$\nabla^2 w_z - l^2\nabla^4 w_z = 0 \tag{2a}$$

Or

$$\left[\frac{\partial^2 w_z}{\partial x^2}+\frac{\partial^2 w_z}{\partial y^2}\right]-l^2\left[\frac{\partial^4 w_z}{\partial x^4}+\frac{\partial^4 w_z}{\partial y^4}+\frac{2\partial^4 w_z}{\partial x^2\partial y^2}\right]=0 \tag{2b}$$

The general solution of the fourth order differential Eq. (2) may be represented as; $w_z(x,y)=w_z^c(x,y)+w_z^g(x,y)$ (Vardoulakis et al., 1996), where w_z^c and w_z^g are the solutions of the harmonic ($\nabla^2 w_z^g=0$) and Helmholtz's equation ($w_z^g-l^2\nabla^2 w_z^g=0$). The application of Fourier transform gives the solution of harmonic function as

$$w_z^c(x,y)=\frac{2}{\pi}\int_0^\infty [A(s)e^{-sy}+C(s)e^{sy}]\cos(sx)ds,\quad y\geq 0 \tag{3}$$

while the solution of a Helmholtz's equation is given as

$$w_z^c(x,y)=\frac{2}{\pi}\int_0^\infty [B(s)e^{-y\sqrt{s^2+(1/l^2)}}+D(s)e^{y\sqrt{s^2+(1/l^2)}}]\cos(sx)ds,\quad y\geq 0 \tag{4}$$

combining Eqs. (3) and (4) gives

$$w_z(x,y)=\frac{2}{\pi}\int_0^\infty [A(s)e^{-sy}+B(s)e^{-y\sqrt{s^2+(1/l^2)}}+C(s)e^{sy}+D(s)e^{y\sqrt{s^2+(1/l^2)}}]\cos(sx)ds,\quad y\geq 0 \tag{5}$$

$A(s)$, $B(s)$, $C(s)$ and $D(s)$ are the constants to be determined from the boundary conditions.

2.1. Stress-free boundaries without surface gradient effect ($l'=0$)

The shear stress $\tau_{yz}(x,y)$ from Eqs. (1b) and (5) is written as

$$\tau_{yz}(x,y)=G\left[\begin{array}{l}\frac{2}{\pi}\int_0^\infty\left[\begin{array}{l}A(s)e^{-sy}(-s)+B(s)e^{-y\sqrt{s^2+(1/l^2)}}(-\sqrt{s^2+(1/l^2)})+\\ C(s)e^{sy}(s)+D(s)e^{y\sqrt{s^2+(1/l^2)}}(\sqrt{s^2+(1/l^2)})\end{array}\right]\cos(sx)ds\\ \frac{-2l^2}{\pi}\left[\begin{array}{l}-\int_0^\infty s^2\left[\begin{array}{l}A(s)e^{-sy}(-s)+B(s)e^{-y\sqrt{s^2+(1/l^2)}}(-\sqrt{s^2+(1/l^2)})+\\ C(s)e^{sy}(s)+D(s)e^{y\sqrt{s^2+(1/l^2)}}(\sqrt{s^2+(1/l^2)})\end{array}\right]\cos(sx)ds+\\ \int_0^\infty\left[\begin{array}{l}A(s)e^{-sy}(-s^3)+B(s)e^{-y\sqrt{s^2+(1/l^2)}}(-\sqrt{s^2+(1/l^2)})^3+\\ C(s)e^{sy}(s^3)+D(s)e^{y\sqrt{s^2+(1/l^2)}}(\sqrt{s^2+(1/l^2)})^3\end{array}\right]\cos(sx)ds\end{array}\right]\end{array}\right] \tag{6}$$

For stress free boundaries, similar to the classical case, the shear stress Eq. (6) at the upper and lower edge of the layer would be zero i.e. $\tau_{yz}(x,\pm h)=0$, $|x|<\infty$, that may further be reduced to

$$\tau_{yz}(x,h)=\frac{2G}{\pi}\int_0^\infty [A(s)e^{-sh}(-s)+C(s)e^{sh}(s)]\cos(sx)ds=0 \tag{7}$$

that gives $C(s)=e^{-2sh}A(s)$. The double stress $\mu_{yyz}(x,y)$ (with $l'=0$) from Eqs. (1f) and (5) is written as

$$\mu_{yyz}(x,y)=G\left[\frac{2l^2}{\pi}\int_0^\infty\left[\begin{array}{l}A(s)e^{-sy}(s^2)+B(s)e^{-y\sqrt{s^2+(1/l^2)}}\\ (s^2+(1/l^2))+C(s)e^{sy}(s^2)\\ +D(s)e^{y\sqrt{s^2+(1/l^2)}}(s^2+(1/l^2))\end{array}\right]\right]\times\cos(sx)ds \tag{8}$$

The double stress (Eq. (8)) at the upper edge is expressed as: $\mu_{yyz}(x,h)=0$, $|x|<\infty$ that is further reduced to

$$s^2l^2(A(s)e^{-sh}+C(s)e^{sh})+(s^2l^2+1)(B(s)e^{-h\sqrt{s^2+(1/l^2)}}+D(s)e^{h\sqrt{s^2+(1/l^2)}})=0 \tag{9}$$

By substituting $C(s)=e^{-2sh}A(s)$ in Eq. (9) one obtains

$$\frac{2}{a^{(1)}}A(s)e^{-sh}+(D(s)e^{h\sqrt{s^2+(1/l^2)}})=-B(s)e^{-h\sqrt{s^2+(1/l^2)}} \tag{10}$$

where $a^{(1)}=1+1/(s^2l^2)$. Similarly the second non-classical boundary condition at the crack surface is written as $\mu_{yyz}(x,0)=0$, $|x|<\infty$ that may further gives

$$s^2A(s)+(s^2+1/l^2)B(s)+s^2C(s)+(s^2+1/l^2)D(s)=0 \tag{11}$$

Again from $C(s)=e^{-2sh}A(s)$ and $a^{(1)}=1+1/(s^2l^2)$, Eq. (11) may be written as

$$D(s)=-(B(s)+(1+e^{-2sh})A(s)/a^{(1)}) \tag{12}$$

To obtain an expression for $B(s)$ in terms of $A(s)$, substituting Eq. (12) into Eq. (10) and after re-arrangement we get

$$\frac{2}{a^{(1)}}\left(e^{-sh}-\frac{(1+e^{-2sh})e^{h\sqrt{s^2+(1/l^2)}}}{2}\right)A(s)=B(s)\left(-e^{-h\sqrt{s^2+(1/l^2)}}+e^{h\sqrt{s^2+(1/l^2)}}\right) \tag{13}$$

Or $B(s)=2b^{(1)}A(s)/a^{(1)}$ with

$$b^{(1)}=\frac{e^{-sh}-(1+e^{-2sh})e^{h\sqrt{s^2+(1/l^2)}}/2a^{(1)}}{-e^{-h\sqrt{s^2+(1/l^2)}}+e^{h\sqrt{s^2+(1/l^2)}}} \tag{14}$$

And by substituting $B(s)=2b^{(1)}A(s)/a^{(1)}$ into Eq. (12) we get $D(s)$ in terms of $A(s)$

$$D(s)=-\frac{2}{a^{(1)}}\left(\frac{(1+e^{-2sh})}{2}+b^{(1)}\right)A(s) \tag{15}$$

Now in order to obtain the dual integral equations, Let $A(s)=G(s)/(1+e^{-2sh})$ so, $C(s)=e^{-2sh}A(s)$, $B(s)=2b^{(1)}A(s)/a^{(1)}$ and (15) provide expressions for $C(s)=e^{-2sh}G(s)/(1+e^{-2sh})$, $B(s)=2b^{(1)}G(s)/a^{(1)}(1+e^{-2sh})$ and $D(s)=-2((1+e^{-2sh})/2+b^{(1)})G(s)/(a^{(1)}(1+e^{-2sh}))$, respectively. Here $G(s)$ is an unknown function. From $w_z(x,0)=0$, $|x|\geq a$, we obtained

$$w_z=\frac{2}{\pi}\int_0^\infty [A(s)+B(s)+C(s)+D(s)]\cos(sx)ds=0,\quad |x|\geq a \tag{16}$$

By expressing $A(s)$, $B(s)$, $C(s)$ and $D(s)$ in terms of an unknown function $G(s)$ in Eq. (16) we obtain

$$\int_0^\infty E(s)\cos(sx)ds=0 \tag{17}$$

here $E(s)=P^{(1)}G(s)$ and

$$P^{(1)}=\frac{1}{1+e^{-2sh}}\left[1+e^{-2sh}-\frac{(1+e^{-2sh})}{a^{(1)}}\right]=1-\frac{1}{a^{(1)}}=\frac{1}{1+s^2l^2} \tag{18}$$

As l approaches 0, the term $(1+e^{-2sh})/a^{(1)}$ approaches zero as well and hence $P^{(1)}$ will reduce to 1. For second integral equation we have $\tau_{yz}(x,0)=-\tau_1$, $|x|<a$ which is expanded as

$$\tau_{yz}(x,0) = \frac{2G}{\pi}\left[\begin{array}{l}\int_0^\infty \left[\begin{array}{l}A(s)(-s)+B(s)(-\sqrt{s^2+(1/l^2)})+\\ C(s)(s)+D(s)(\sqrt{s^2+(1/l^2)})\end{array}\right]\cos(sx)ds \\ -l^2\left[\begin{array}{l}-\int_0^\infty s^2\left[\begin{array}{l}A(s)(-s)+B(s)(-\sqrt{s^2+(1/l^2)})+\\ C(s)(s)+D(s)(\sqrt{s^2+(1/l^2)})\end{array}\right] \\ \cos(sx)ds+ \\ \int_0^\infty \left[\begin{array}{l}A(s)(-s^3)+B(s)(-\sqrt{s^2+(1/l^2)})^3+\\ C(s)(s^3)+D(s)(\sqrt{s^2+(1/l^2)})^3\end{array}\right] \\ \cos(sx)ds\end{array}\right]\end{array}\right] = -\tau_1 \quad (19)$$

Eq. (19) can be reduced to

$$\frac{-2G}{\pi}\int_0^\infty [sA(s)-sC(s)]\cos(sx)ds = -\tau_1 \quad (20)$$

By substituting $C(s)=e^{-2sh}A(s)$ into Eq. (20) and after rearrangement we get $\int_0^\infty s[1-e^{-2sh}]A(s)\cos(sx)ds = \tau_1\pi/2G$, and since $A(s)=G(s)/(1+e^{-2sh})=E(s)/P^{(1)}(1+e^{-2sh})$, so

$$\int_0^\infty sF_{sg}(s)E(s)\cos(sx)ds = \frac{\tau_1\pi}{2G} \quad (21)$$

$$F_{sg}(s) = \frac{(1-e^{-2sh})}{P^{(1)}(1+e^{-2sh})} \quad (22)$$

here "sg" in subscript represents the "stress-free boundaries & gradient ($l'=0$)" case with $P^{(1)}$ given in Eq. (18). Eqs. (17) and (21) are the dual integral equations. When l approaches zero, $P^{(1)}$ approaches 1 and, hence, $F_{sg}(s)$ will reduce to the classical case (see Appendix).

2.2. Clamped boundaries without surface gradient effect ($l'=0$)

As with classical case (see appendix) for clamped boundaries i.e. $w_z(x,\pm h)=0$, $|x|<\infty$ and using Eq. (5) we get

$$A(s)e^{-sh}+B(s)e^{-h\sqrt{s^2+(1/l^2)}}+C(s)e^{sh}+D(s)e^{h\sqrt{s^2+(1/l^2)}}=0 \quad (23)$$

The non-classical trivial boundary condition for double stress at upper edge is $\mu_{yyz}(x,h)=0$, $|x|<\infty$ that yields (with $l'=0$)

$$s^2l^2A(s)e^{-sh}+(1+s^2l^2)B(s)e^{-h\sqrt{s^2+(1/l^2)}} + s^2l^2C(s)e^{sh}+(1+s^2l^2)D(s)e^{h\sqrt{s^2+(1/l^2)}}=0 \quad (24)$$

Also $\mu_{yyz}(x,0)=0$, $|x|<\infty$ further gives

$$A(s)+(1+1/(s^2l^2))B(s)+C(s)+(1+1/(s^2l^2))D(s)=0 \quad (25)$$

Eliminating $A(s)$ and $C(s)$ from Eqs. (23) and (24) we obtain

$$D(s) = \frac{-B(s)e^{-h\sqrt{s^2+(1/l^2)}}}{e^{h\sqrt{s^2+(1/l^2)}}} = -B(s)e^{-2h\sqrt{s^2+(1/l^2)}} = -B(s)a^{(2)} \quad \left(e^{-2h\sqrt{s^2+(1/l^2)}}=a^{(2)}\right) \quad (26)$$

Multiplying Eq. (25) by e^{sh} and subtracting Eq. (23) we get

$$\left(e^{sh}-e^{-sh}\right)A(s)+\left((1+1/(s^2l^2))e^{sh}-e^{-h\sqrt{s^2+(1/l^2)}}\right)B(s) + \left((1+1/(s^2l^2))e^{sh}-e^{h\sqrt{s^2+(1/l^2)}}\right)D(s)=0 \quad (27a)$$

or

$$b^{(2)}A(s)+c^{(2)}B(s)+d^{(2)}D(s)=0 \quad (27b)$$

where $b^{(2)}=(e^{sh}-e^{-sh})$, $c^{(2)}=((1+1/(s^2l^2))e^{sh}-e^{-h\sqrt{s^2+(1/l^2)}})$ and $d^{(2)}=((1+1/(s^2l^2))e^{sh}-e^{h\sqrt{s^2+(1/l^2)}})$. Substituting Eq. (26) into Eq. (27b) and after rearrangement we obtain

$$B(s) = \frac{b^{(2)}}{(a^{(2)}d^{(2)}-c^{(2)})}A(s) \quad (28)$$

And by substituting Eq. (28) into Eq. (26) we obtain $D(s)$ in terms of $A(s)$

$$D(s) = \frac{-b^{(2)}a^{(2)}}{(a^{(2)}d^{(2)}-c^{(2)})}A(s) \quad (29)$$

Now substituting Eqs. (28) and (29) into Eq. (23) we get $C(s)$ in terms of $A(s)$

$$C(s) = -A(s)\left[e^{-2sh}+\frac{b^{(2)}e^{-sh}}{(a^{(2)}d^{(2)}-c^{(2)})}\left(e^{-h\sqrt{s^2+(1/l^2)}}-a^{(2)}e^{h\sqrt{s^2+(1/l^2)}}\right)\right] = -A(s)e^{(2)} \quad (30)$$

where

$$\left[e^{-2sh}+\frac{b^{(2)}e^{-sh}}{(a^{(2)}d^{(2)}-c^{(2)})}\left(e^{-h\sqrt{s^2+(1/l^2)}}-a^{(2)}e^{h\sqrt{s^2+(1/l^2)}}\right)\right]=e^{(2)} \quad (31)$$

Now in order to obtain the dual integral equations, let $A(s)=G(s)/(1-e^{-2sh})$, so from Eqs. (28) to (30) we get $B(s)=b^{(2)}G(s)/((a^{(2)}d^{(2)}-c^{(2)})(1-e^{-2sh}))$, $D(s)=-b^{(2)}a^{(2)}G(s)/((a^{(2)}d^{(2)}-c^{(2)})(1-e^{-2sh}))$ and $C(s)=-e^{(2)}G(s)/(1-e^{-2sh})$, respectively. Here $G(s)$ is an unknown function. The dual integral equations may be obtained similar to the previous section (& from Eqs. (A.1) and (A.2))

$$\int_0^\infty E(s)\cos(sx)ds=0, \quad (32)$$

here $E(s)=P^{(2)}G(s)$ and

$$\int_0^\infty sF_{cg}(s)E(s)\cos(sx)ds=\frac{\tau_1\pi}{2G} \quad (33)$$

where

$$p^{(2)} = \frac{1}{1-e^{-2sh}}\left[\begin{array}{l}1-e^{-2sh}+\frac{b^{(2)}}{(a^{(2)}d^{(2)}-c^{(2)})}\left(1-a^{(2)}\right) \\ -\frac{b^{(2)}e^{-sh}}{(a^{(2)}d^{(2)}-c^{(2)})}\left(e^{-h\sqrt{s^2+(1/l^2)}}-a^{(2)}e^{h\sqrt{s^2+(1/l^2)}}\right)\end{array}\right] \quad (34)$$

$$F_{cg}(s) = \frac{(1+e^{-2sh}+e^{(2)}-e^{-2sh})}{p^{(2)}(1-e^{-2sh})} \quad (35)$$

As l approaches zero, the term $\frac{b^{(2)}}{(a^{(2)}d^{(2)}-c^{(2)})}(1-a^{(2)})-\frac{b^{(2)}e^{-sh}}{(a^{(2)}d^{(2)}-c^{(2)})}\left(e^{-h\sqrt{s^2+(1/l^2)}}-a^{(2)}e^{h\sqrt{s^2+(1/l^2)}}\right)$ in Eq. (34) approaches zero as well and hence $P^{(2)}$ will reduce to 1. Moreover, "cg" in subscript (Eq. (35)) represents the "clamped boundaries & gradient ($l'=0$)" case. When l approaches zero, $P^{(2)}$ given by Eq. (34) and $(e^{(2)}-e^{-2sh})$ in Eq. (35) approach to 1 and zero, respectively. Hence $F_{cg}(s)$ will reduce to the classical case (see appendix).

2.3. Stress-free boundaries with surface gradient effect ($l'\neq 0$)

The classical boundary condition, similar to the classical case (appendix) and strain gradient model ($l'=0$) gives $C(s)=e^{-2sh}A(s)$. The double stress (with l') from Eqs. (1f) and (5) is given as

$$\frac{-2l'}{\pi}\int_0^\infty \left[\begin{array}{l}A(s)e^{-sy}(-s)+B(s)e^{-y\sqrt{s^2+(1/l^2)}}(-\sqrt{s^2+(1/l^2)}) \\ +C(s)e^{sy}(s)+D(s)e^{y\sqrt{s^2+(1/l^2)}}(\sqrt{s^2+(1/l^2)})\end{array}\right] \times \cos(sx)ds + \left[\frac{2l^2}{\pi}\int_0^\infty \left[\begin{array}{l}A(s)e^{-sy}\left(s^2\right)+B(s)e^{-y\sqrt{s^2+(1/l^2)}}\left(s^2+(1/l^2)\right) \\ +C(s)e^{sy}\left(s^2\right)+D(s)e^{y\sqrt{s^2+(1/l^2)}}\left(s^2+(1/l^2)\right)\end{array}\right]\right] \times \cos(sx)ds = \mu_{yyz}(x,y) \quad (36)$$

The non-classical trivial boundary condition for double stress at the upper edge i.e. $\mu_{yyz}(x,h)=0$, $|x|<\infty$ is expanded as

$$(sl'+s^2l^2)A(s)e^{-sh}+(l'\sqrt{s^2+(1/l^2)}+l^2(s^2+(1/l^2)))\times B(s)e^{-h\sqrt{s^2+(1/l^2)}}+(-sl'+s^2l^2)C(s)e^{sh}+(-l'\sqrt{s^2+(1/l^2)}+l^2(s^2+(1/l^2)))D(s)e^{h\sqrt{s^2+(1/l^2)}}=0 \quad (37)$$

Substituting $C(s)=e^{-2sh}A(s)$ in Eq. (37) one obtains

$$(a^{(3)}+c^{(3)})e^{-sh}A(s)+(d^{(3)}e^{h\sqrt{s^2+(1/l^2)}})D(s)=(-b^{(3)}e^{-h\sqrt{s^2+(1/l^2)}})B(s) \quad (38a)$$

where

$$a^{(3)}=sl'+s^2l^2,\quad c^{(3)}=-sl'+s^2l^2,$$
$$b^{(3)}=l'\sqrt{s^2+(1/l^2)}+l^2(s^2+(1/l^2)),$$
$$d^{(3)}=-l'\sqrt{s^2+(1/l^2)}+l^2(s^2+(1/l^2)) \quad (38b)$$

Similarly the second non-classical boundary condition at the crack is written as; $\mu_{yyz}(x,0)=0$, $|x|<\infty$ that may further yields

$$a^{(3)}A(s)+b^{(3)}B(s)+c^{(3)}C(s)+d^{(3)}D(s)=0, \text{ or} \quad (39a)$$

$$D(s)=-(a^{(3)}+c^{(3)}e^{-2sh})A(s)-b^{(3)}B(s)/d^{(3)}. \quad (39b)$$

Since $C(s)=e^{-2sh}A(s)$, also let

$$D(s)=\alpha A(s)+\beta B(s) \quad (39c)$$

where

$$\alpha=-(a^{(3)}+c^{(3)}e^{-2sh})/d^{(3)},\quad \beta=-b^{(3)}/d^{(3)} \quad (39d)$$

Substituting Eq. (39c) in Eq. (38a) we get $B(s)$ in terms of $A(s)$

$$\gamma A(s)+\theta(\alpha A(s)+\beta B(s))=-\xi B(s) \quad (40)$$

where $\gamma=(a^{(3)}+c^{(3)})e^{-sh}$, $\theta=d^{(3)}e^{h\sqrt{s^2+(1/l^2)}}$, $\xi=b^{(3)}e^{-h\sqrt{s^2+(1/l^2)}}$ and after simplification we get

$$B(s)=-\frac{(\gamma+\theta\alpha)A(s)}{(\xi+\theta\beta)} \quad (41)$$

Substituting Eq. (41) into Eq. (39c) one obtains $D(s)$ in terms of $A(s)$

$$D(s)=\left[\alpha-\beta\frac{(\gamma+\theta\alpha)}{(\xi+\theta\beta)}\right]A(s) \quad (42)$$

To obtain dual integral Equations; Let $A(s)=G(s)/(1+e^{-2sh})$, so $C(s)=e^{-2sh}A(s)$, (41) and (42) give $C(s)=e^{-2sh}G(s)/(1+e^{-2sh})$, $B(s)=-(\gamma+\theta\alpha)G(s)/((\xi+\theta\beta)(1+e^{-2sh}))$ and $D(s)=[\alpha-\beta(\gamma+\theta\alpha)/(\xi+\theta\beta)]G(s)/(1+e^{-2sh})$ respectively. Here $G(s)$ is an unknown function. The dual integral equations may be obtained similar to the previous sections as

$$\int_0^\infty E(s)\cos(sx)ds=0 \quad (43)$$

here $E(s)=P^{(3)}G(s)$, and

$$\int_0^\infty sF_{sg'}(s)E(s)\cos(sx)ds=\frac{\tau_1\pi}{2G} \quad (44)$$

$$p^{(3)}=\frac{1}{1+e^{-2sh}}\left[1+e^{-2sh}-\frac{(\gamma+\theta\alpha)}{(\xi+\theta\beta)}+\alpha-\frac{\beta(\gamma+\theta\alpha)}{(\xi+\theta\beta)}\right] \quad (45)$$

$$F_{sg'}(s)=\frac{(1-e^{-2sh})}{p^{(3)}(1+e^{-2sh})} \quad (46)$$

As l and l' approach zero, the term $(\gamma+\theta\alpha)/(\xi+\theta\beta)+\alpha-\beta(\gamma+\theta\alpha)/(\xi+\theta\beta)$ in Eq. (45) also approaches zero and hence $P^{(3)}$ will reduce to 1. Moreover, "sg'" in subscript represents the "stress-free boundaries & gradient ($l'\neq 0$)" case and $P^{(3)}$ is given in Eq. (45). When l and l' approach zero, $P^{(3)}$ approaches 1 and, hence, $F_{sg'}(s)$ will reduce to the classical case (see appendix).

2.4. Clamped boundaries with surface gradient effect ($l'\neq 0$)

As done in Section 2.2 for clamped boundaries i.e. $w_z(x,\pm h)=0$, $|x|<\infty$ and using Eq. (5) we get

$$A(s)e^{-sh}+B(s)e^{-h\sqrt{s^2+(1/l^2)}}+C(s)e^{sh}+D(s)e^{h\sqrt{s^2+(1/l^2)}}=0 \quad (47)$$

The non-classical trivial boundary condition for double stress at upper edge is $\mu_{yyz}(x,h)=0$, $|x|<\infty$ that further gives

$$a^{(4)}A(s)e^{-sh}+b^{(4)}B(s)e^{-h\sqrt{s^2+(1/l^2)}}+c^{(4)}C(s)e^{sh}+d^{(4)}D(s)e^{h\sqrt{s^2+(1/l^2)}}=0 \quad (48)$$

Here $a^{(4)}=a^{(3)}$, $b^{(4)}=b^{(3)}$, $c^{(4)}=c^{(3)}$, $d^{(4)}=d^{(3)}$ Also $\mu_{yyz}(x,0)=0$, $|x|<\infty$ gives

$$a^{(4)}A(s)+b^{(4)}B(s)+c^{(4)}C(s)+d^{(4)}D(s)=0 \quad (49)$$

Multiplying Eq. (49) by e^{sh} and subtracting Eq. (48), we get

$$D(s)=\frac{(e^{-sh}-e^{sh})a^{(4)}A(s)+(e^{-h\sqrt{s^2+(1/l^2)}}-e^{sh})b^{(4)}B(S)}{(e^{sh}-e^{h\sqrt{s^2+(1/l^2)}})d^{(4)}}=\alpha^*A(s)+\beta^*B(s) \quad (50a)$$

where

$$\alpha^*=\frac{(e^{-sh}-e^{sh})a^{(4)}}{(e^{sh}-e^{h\sqrt{s^2+(1/l^2)}})d^{(4)}},\ \beta^*=\frac{(e^{-h\sqrt{s^2+(1/l^2)}}-e^{sh})b^{(4)}}{(e^{sh}-e^{h\sqrt{s^2+(1/l^2)}})d^{(4)}}B(s) \quad (50b)$$

Multiplying Eq. (49) by $e^{h\sqrt{s^2+(1/l^2)}}$ and subtracting Eq. (48) we get

$$B(s)=\frac{(e^{-sh}-e^{h\sqrt{s^2+(1/l^2)}})a^{(4)}A(s)-(e^{h\sqrt{s^2+(1/l^2)}}-e^{sh})c^{(4)}C(s)}{(e^{h\sqrt{s^2+(1/l^2)}}-e^{-h\sqrt{s^2+(1/l^2)}})b^{(4)}}=\gamma^*A(s)-\theta^*C(s) \quad (51a)$$

where

$$\gamma^*=\frac{(e^{-sh}-e^{h\sqrt{s^2+(1/l^2)}})a^{(4)}}{(e^{h\sqrt{s^2+(1/l^2)}}-e^{-h\sqrt{s^2+(1/l^2)}})b^{(4)}},$$
$$\theta^*=\frac{(e^{h\sqrt{s^2+(1/l^2)}}-e^{sh})c^{(4)}}{(e^{h\sqrt{s^2+(1/l^2)}}-e^{-h\sqrt{s^2+(1/l^2)}})b^{(4)}} \quad (51b)$$

Substituting Eq. (51a) in (50a) we get $D(s)$ in terms of $A(s)$ and $C(s)$

$$D(s)=\alpha^*A(s)+\beta^*B(s)=\alpha^*A(s)+\beta^*(\gamma^*A(s)-\theta^*C(s)) \quad (52a)$$

$$D(s)=(\alpha^*+\beta^*\gamma^*)A(s)-\theta^*\beta^*C(s) \quad (52b)$$

And substituting Eqs. (51a) and (52b) into Eq. (47) we get $C(s)$ in terms of $A(s)$

$$(e^{-sh}+\gamma^*e^{-h\sqrt{s^2+(1/l^2)}}+(\alpha^*+\beta^*\gamma^*)e^{h\sqrt{s^2+(1/l^2)}})A(s)+(e^{sh}-\theta^*e^{-h\sqrt{s^2+(1/l^2)}}-\theta^*\beta^*e^{h\sqrt{s^2+(1/l^2)}})C(s)=0 \quad (53)$$

After simplifying one obtains

$$C(s)=\frac{-(e^{-sh}+\gamma^*e^{-h\sqrt{s^2+(1/l^2)}}+(\alpha^*+\beta^*\gamma^*)e^{h\sqrt{s^2+(1/l^2)}})A(s)}{(e^{sh}-\theta^*e^{-h\sqrt{s^2+(1/l^2)}}-\theta^*\beta^*e^{h\sqrt{s^2+(1/l^2)}})}=-e^{(4)}A(s) \quad (54a)$$

where

$$\frac{(e^{-sh}+\gamma^*e^{-h\sqrt{s^2+(1/l^2)}}+(\alpha^*+\beta^*\gamma^*)e^{h\sqrt{s^2+(1/l^2)}})A(s)}{(e^{sh}-\theta^*e^{-h\sqrt{s^2+(1/l^2)}}-\theta^*\beta^*e^{h\sqrt{s^2+(1/l^2)}})}=e^{(4)} \quad (54b)$$

So, $B(s)$ and $D(s)$, in terms of $A(s)$ are written as

$$B(s) = \left(\gamma^* + \theta^* e^{(4)}\right)A(s) \tag{55}$$

$$D(s) = \left(\alpha^* + \beta^*\left(\gamma^* + \theta^* e^{(4)}\right)\right)A(s) \tag{56}$$

Now in order to get the dual integral equations let $A(s) = G(s)/(1 - e^{-2sh})$, so from Eqs. (54a), (55) and (56) we get $C(s) = -e^{(4)}G(s)/(1 - e^{-2sh})$, $B(s) = (\gamma^* + \theta^* e^{(4)})G(s)/(1 - e^{-2sh})$ and $D(s) = (\alpha^* + \beta^*(\gamma^* + \theta^* e^{(4)}))G(s)/(1 - e^{-2sh})$. Here $G(s)$ is an unknown function. The dual integral equations may be obtained similar to the previous sections as

$$\int_0^\infty E(s)\cos(sx)ds = 0, \quad \text{here } E(s) = P^{(4)}G(s) \tag{57}$$

here $E(s) = P^{(4)}G(s)$ and

$$\int_0^\infty sF_{cg}(s)E(s)\cos(sx)ds = \frac{\tau_1 \pi}{2G} \tag{58}$$

where

$$P^{(4)} = \frac{1}{1 - e^{-2sh}}(1 - e^{-2sh} + e^{-2sh} + \alpha^* + (1 + \beta^*)(\gamma^* + \theta^* e^{(4)}) - e^{(4)}) \tag{59}$$

$$F_{cg}(s) = \frac{(1 + e^{-2sh} + e^{(4)} - e^{-2sh})}{P^{(4)}(1 - e^{-2sh})} \tag{60}$$

As l and l' approach zero, the term $e^{-2sh} + \alpha^* + (1 + \beta^*)(\gamma^* + \theta^* e^{(4)}) - e^{(4)}$ also approaches zero and hence $P^{(4)}$ will reduce to 1. Moreover, "cg" in subscript represents the "clamped boundaries & gradient ($l' \neq 0$)" case. When l and l' approach zero, $P^{(4)}$ given by Eq. (59) and ($e^{(4)}$ - e^{-2sh}) approach to 1 and zero, respectively. Hence, $F_{cg}(s)$ will reduce to the classical case (see appendix).

3. Solution of dual integral equation

The dual integral equations presented in the previous section are treated with the method of Copson (1961) to give; $E(s) = (\pi \tau_1 a^2/2G)\int_0^1 \sqrt{\xi}\Omega(\xi)J_0(sa\xi)d\xi$ (Here J_0 is the Bessel function of the first kind of order zero), such that the Fredholm integral equation is obtained

$$\Omega(\xi) + \int_0^1 \Omega(\eta)L(\xi, \eta)d\eta = \sqrt{\xi}, \qquad 0 \le \xi \le 1. \tag{61}$$

Solving for $\Omega(\xi)$ (unknown function to be determined) and $L(\xi, \eta)$ (kernel) takes the form

$$L(\xi, \eta) = \sqrt{\xi\eta}\int_0^\infty s\left[F\left(\frac{s}{a}\right) - 1\right]J_0(s\xi)J_0(s\eta)ds, \quad 0 \le \xi, \eta \le 1, \tag{62}$$

The details of this method may be found in the work of Copson (1961) and Sih and Chen (1981). The Fredholm integral equation (Eq. (61)) is solved by the Matlab code Fie, in which the kernel is taken to be moderately smooth in [a, b] x [a, b] and also smooth on the diagonal. Here a and b are the lower and upper limits of the integral in Eq. (61) i.e. 0 and 1, respectively. More description related to different types of kernels with relevant examples can be seen in the work of Atkinson and Shampine (2007). For the kernel to be smooth it must be infinitely differentiable with respect to its variables i.e. ξ and η. Moreover, the term $\int_0^\infty s[F(s/a) - 1]J_0(s\xi)J_0(s\eta)ds$ in Eq. (62) is a smooth function of ξ and η but the multiplication of the term $\sqrt{\xi\eta}$ means the kernel function $L(\xi, \eta)$ will have a square root singularity. This effects the approximation of the integral at 1. Therefore, the change of variables in the integral equation is done as follows. Let $\xi = x^2$, $\eta = y^2$ such that $0 \le x, y \le 1$, introducing the new unknown function $W(x) = \Omega(x^2)$, Eq. (61) may be written as

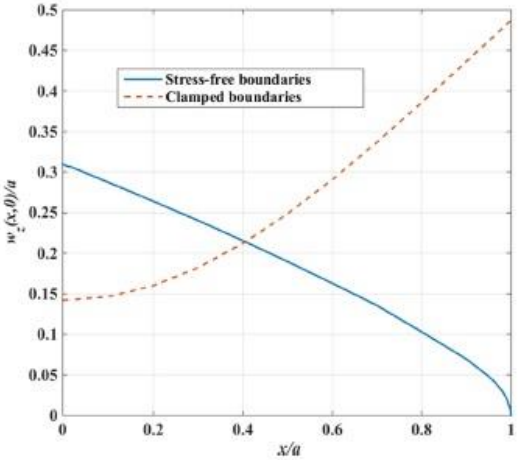

Fig. 2. Normalized quarter crack displacement profile for $h/a = 2$.

$$W(x) + \int_0^1 W(y)K(x, y)dy = x, \qquad 0 \le x \le 1 \tag{63}$$

The kernel now has the form

$$K(x, y) = 2yL_3(x^2, y^2), \qquad 0 \le x, y \le 1 \tag{64}$$

$$L_3(x^2, y^2) = xy\int_0^\infty s\left[F_3\left(\frac{s}{a}\right) - 1\right]J_0(sx^2)J_0(sy^2)ds, \qquad 0 \le x, y \le 1 \tag{65}$$

The kernel formula Eq. (64) is infinitely differentiable in terms of x and y. The integrand Eq. (63) is better behaved than in Eq. (61); it can be more easily approximated by numerical integration, which is at the heart of the program Fie. The evaluation of $W(1) = \Omega(1)$ is obtained, which is the normalized stress intensity factor at crack tip given by the following relation

$$K_{III} = \Omega(1)\tau_1\sqrt{a} \tag{66}$$

Where K_{III} is the mode III stress intensity factor at the crack tip, τ_1 and a are the applied stress on crack surface and half crack length respectively. Moreover, the Gauss–Laguerre quadrature method is used to solve the term $\int_0^\infty s[F(s/a) - 1]J_0(s\xi)J_0(s\eta)ds$ which is given as

$$\int_0^\infty f(x)dx = \sum_{i=1}^{n} A_i \exp(x_i)f(x_i) \tag{67}$$

Where x_i and $A_i \exp(x_i)$ are the nodes and weights, respectively. The parameters x_i and A_i are chosen such that for any n the rule is exact for polynomials up to and including degree 2n-1. More information on this method and the way it can be implemented in Matlab may be seen in the reference (Lindfield and Penny, 2012).

4. Results and discussion

Firstly, the quarter crack displacement profile with different types of boundary conditions i.e. stress-free boundaries and clamped boundaries are evaluated and compared in Fig. 2. Here h/a is taken as 2, where h and a are the half layer thickness and

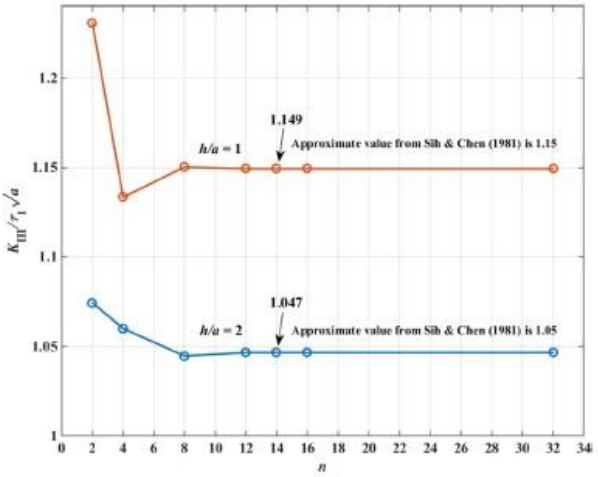

Fig. 3. Convergence study to get optimum n for Gauss–Laguerre quadrature method while comparison with the results provided by Sih and Chen (1981) is made.

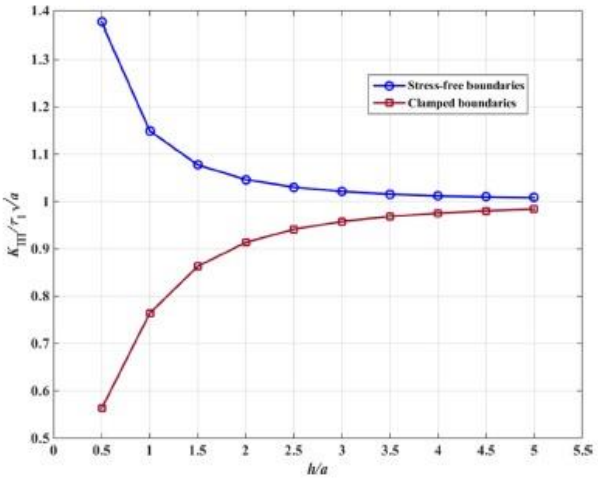

Fig. 4. Normalized stress intensity factor as a function of layer height to crack length ratio for classical models.

the half crack length respectively (see Fig. 1). With the stress-free boundaries, it may be seen from Fig. 2 that the displacement decreases along the crack and approaches zero near its tip. On the other hand, with clamped boundaries, the maximum displacement occurs at the crack tip. For further results, the value of n in Gauss–Laguerre quadrature method is chosen based on a convergence study conducted for the classical case subjected to stress-free boundaries. The plot of normalized stress intensity factor at the crack tip i.e. $W(1) = \Omega(1) = K_{III}/\tau_1\sqrt{a}$ versus n is plotted in Fig. 3. It is apparent from Fig. 3 that the value of $K_{III}/\tau_1\sqrt{a}$ is identical from $n = 12$ onwards. These results are compared with the results provided by Sih and Chen (1981) and they are both shown to be in good agreement. Therefore, in accordance with other numerical results $n = 14$ is taken throughout this study. In order to demonstrate the strain gradient effect, it is considered necessary to evaluate the classical results as a benchmark for both types of boundary conditions i.e. stress-free and clamped boundaries. Therefore, in Fig. 4, the normalized stress intensity factor at the crack tip is plotted as a function of "layer height to crack length" (h/a) ratio. It is clear from Fig. 4 $K_{III}/\tau_1\sqrt{a}$ to be decreasing with increasing h/a for stress-free boundaries, while this is completely the opposite in the case of clamped boundaries. This behavior is expected if one analyzes the $F(s)$ function for both cases (see appendix). The difference between the crack tip stress intensity factors for both types of boundary conditions is greater for smaller layer height and it diminishes as the height of the layer is increased. Moreover, the stress intensity factor is shown to approach 1 from $h/a = 5$ onwards for both types of boundary conditions.

Secondly, the results are evaluated for strain gradient models. Here, only the volumetric strain gradient effect, represented by the material parameter l (volumetric strain gradient material characteristic length), is considered (surface strain gradient is consid-

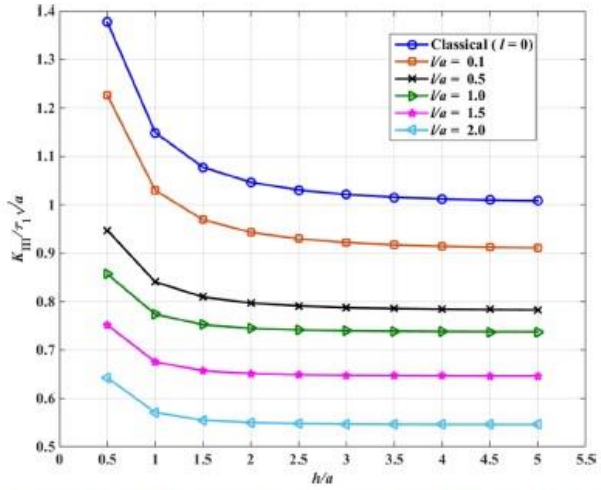

Fig. 5. Normalized stress intensity factor as a function of layer height to crack length ratio (h/a) for strain gradient models (without surface gradient effect) with stress-free boundaries.

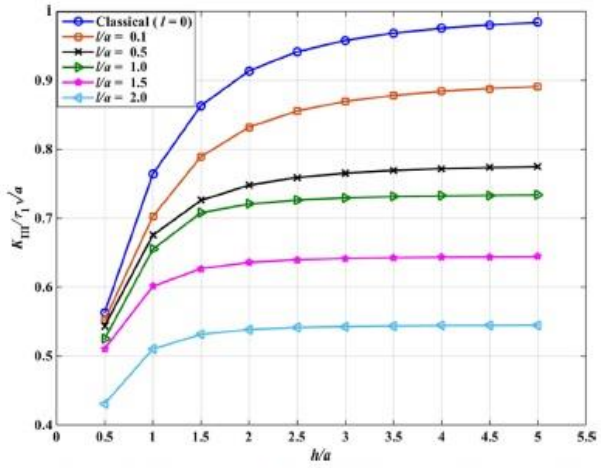

Fig. 6. Normalized stress intensity factor as a function of layer height to crack length ratio (h/a) for strain gradient elastic models (without surface gradient effect) with clamped boundaries.

ered as zero i.e. $l' = 0$). The stress intensity factors at the crack tip for different l/a versus h/a are plotted in Fig. 5 (for stress-free boundaries) and Fig. 6 (for clamped boundaries). It is clear from Figs. 5 and 6 that stress intensity factors decrease as l/a increases and vice versa. This may alternatively be defined as crack stiffening when compared with the classical case, with increasing l. The stiffening effect is evident for both stress-free and clamped boundary conditions. Moreover, it is apparent that results are closer to the classical ones when l leads to 0. This may also be explained if one examines $P^{(1)}$ given in (18) and $F_{sg}(s)$ given in Eq. (22) that if l approaches 0, $P^{(1)}$ approaches 1 and, hence, $F_{sg}(s)$ will reduce to the classical case. The same explanation applies to clamped boundaries from Eqs. (34) and (35).

Finally, stress intensity factors with both volumetric and surface strain gradient (represented as l and l') are presented in Figs. 7 and 8 for stress-free and clamped boundaries, respectively. It should be mentioned from the energy consideration that the material constant l' may assume positive as well as negative values (Vardoulakis et al., 1996). Therefore, the results are presented for both positive and negative surface strain gradient material parameter l' while maintaining the volumetric strain gradient material parameter l as constant. Results are plotted with $h/a = 1$ and 2 for comparison purposes. It may be seen from Figs. 7 and 8 that the crack stiffening effect becomes significant as l' increases in the domain $[0,l]$. On the other hand, negative l' leads to more "complaint" crack, which in general, in order to observe experimental data, is a desirable property of the mathematical model (Paulino et al., 2003; Vardoulakis et al., 1996). Overall, it may fairly be concluded that the effect of volumetric strain gradient is more prominent as compared to the surface strain gradient.

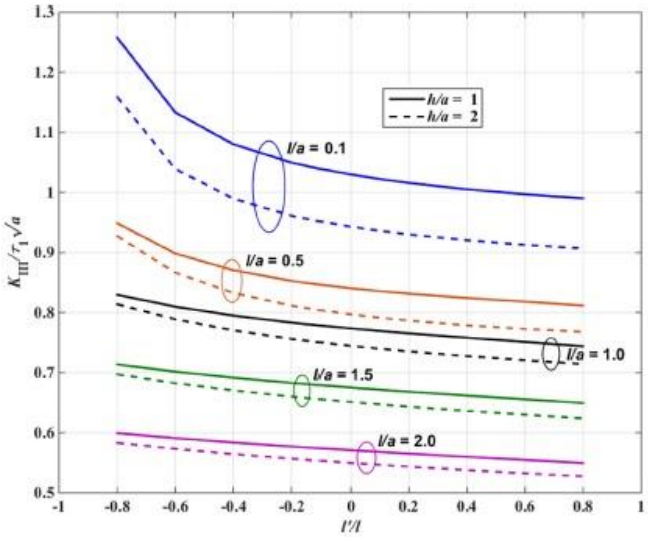

Fig. 7. Normalized stress intensity factor against different l'/l ratios for strain gradient elastic models (with surface gradient effect) with stress-free boundaries.

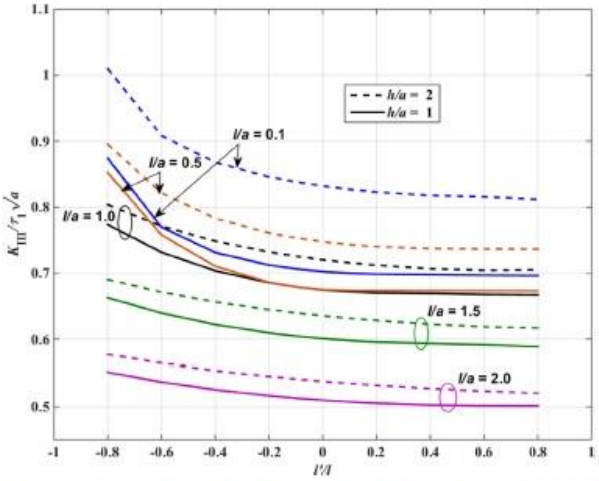

Fig. 8. Normalized stress intensity factor against different l'/l ratios for strain gradient elastic models (with surface gradient effect) with clamped boundaries.

5. Conclusion

Theoretical framework and corresponding computational strategy to solve anti-plane cracked material layer of finite height using strain gradient elasticity theory are presented in this paper. Both volumetric and surface gradient material parameters i.e. l and l' are considered in this article. Two types of boundary conditions i.e. stress-free and clamped boundaries are studied in this paper. The solution of each problem is discussed separately and reduced to the dual integral equations. Resulting Fredholm integral equation is solved numerically in which the kernel (an improper integral that ranges from 0 to infinity) of the second kind is solved by using Gauss–Laguerre quadrature to evaluate crack tip stress intensity factors. Classical results under stress-free boundary condition are obtained and compared with the available literature for benchmarking. Next, the results for strain gradient models are evaluated and plotted. Incorporation of volumetric strain gradient effect increases crack stiffness by reducing the stress intensity factor, demonstrating pronounced size effect at a smaller scale. Furthermore, from energy consideration, both positive and negative surface strain effects are considered in the following results by maintaining volumetric strain gradient material parameter as constant. Positive surface gradient effect stiffened crack while negative surface gradient leads to a more complaint crack. Potential extension of this work is investigating the stress intensity factors for finite width problem.

Appendix

Classical case

The conditions at crack line ($y = 0$) are given as

$$\tau_{yz}(x, 0) = -\tau_1 |x| < a \tag{A.1}$$

$$w_z(x, 0) = 0 |x| \geq a \tag{A.2}$$

The application of integral transform technique on the displacement solution that satisfies the non-trivial equilibrium equation in z- direction ($\partial^2 w_z/\partial x^2 + \partial^2 w_z/\partial y^2 = 0$) is written as

$$w_z(x, y) = \frac{2}{\pi} \int_0^\infty \left[A(s)e^{-sy} + B(s)e^{sy}\right] \cos(sx) ds \qquad y \geq 0 \tag{A.3}$$

with the aid of (A.3), $\tau_{yz} = G(\partial w_z/\partial y)$ may be expanded as

$$\tau_{yz}(x, y) = -\frac{2}{\pi} G \int_0^\infty s\left[A(s)e^{-sy} - B(s)e^{sy}\right] \cos(sx) ds \qquad y \geq 0 \tag{A.4}$$

Here G is the shear modulus of the material, $A(s)$ and $B(s)$ are constants to be determined from the boundary conditions.

Stress-free boundaries

For stress-free boundaries, the shear stresses at the upper and lower edge (i.e. $y = \pm h$) of the layer for all values of x would be zero. Mathematically, it may be written as

$$\tau_{yz}(x, \pm h) = 0, \quad |x| < \infty \tag{A.5}$$

Due to geometrical symmetry, only upper half of the layer is considered. From (A.4) and (A.5), it may be shown that $B(s) = e^{-2sh} A(s)$, so if $A(s) = E(s)/(1 + e^{-2sh})$ then $B(s) = e^{-2sh} E(s)/(1 + e^{-2sh})$, where $E(s)$ is an unknown function to be determined. The conditions in Eqs. (A.1) and (A.2) are satisfied if $E(s)$ is the solution of dual integral equations given as

$$\int_0^\infty E(s) \cos(sx) ds = 0, \qquad x \geq a \tag{A.6a}$$

$$\int_0^\infty s F_{sc}(s) E(s) \cos(sx) ds = \frac{\tau_1 \pi}{2G}, \qquad x < a \tag{A.6b}$$

With $F_{sc}(s) = (1 - e^{-2sh})/(1 + e^{-2sh})$, here "sc" in subscript represents the "stress-free boundaries & classical" case.

Clamped boundaries

The other practical situation that may be considered for analysis is the condition of clamped boundaries. For fixed boundaries the displacement in Eq. (A.3) must be zero at $y = \pm h$

$$w_z(x, \pm h) = 0, \quad |x| < \infty \tag{A.7}$$

With the assumption of symmetry (only upper half is considered) and using Eqs. (A.3) and (A.7) we get $B(s) = -e^{-2sh} A(s)$, so if $A(s) = E(s)/(1 - e^{-2sh})$, then $B(s) = -e^{-2sh} E(s)/(1 - e^{-2sh})$ and corresponding dual integral equations (A.6) may be obtained with $F_{sc}(s) = (1 + e^{-2sh})/(1 - e^{-2sh})$, here "cc" in subscript represents the "clamped boundaries & classical" case. It is evident that $F_{sc}(s)$ and $F_{cc}(s)$ are the inverses of each other.

References

Aifantis, E., 2016. Chapter one-internal length gradient (ILG) material mechanics across scales and disciplines. Adv. Appl. Mech. 49, 1–110.
Aifantis, E.C., 1992. On the role of gradients in the localization of deformation and fracture. Int. J. Eng. Sci. 30 (10), 1279–1299.
Aifantis, E.C., 1999. Strain gradient interpretation of size effects. Int. J. Fract. 95 (1), 299–314.
Aifantis, E.C., 2003. Update on a class of gradient theories. Mech. Mater. 35 (3), 259–280.
Aifantis, E.C., 2011. A note on gradient elasticity and nonsingular crack fields. J. Mech. Behav. Mater 20, 103–105.
Atkinson, K., Shampine, L., 2007. Solving Fredholm integral equations of the second kind in MATLAB. ACM Trans. Math. Software 34 (4).
Chan, Y.S., Paulino, G.H., Fannjiang, A.C., 2008. Gradient elasticity theory for mode III fracture in functionally graded materials-part II: crack parallel to the material gradation. J. Appl. Mech. 75 (6), 061015.
Copson, E., 1961. On certain dual integral equations. In: Paper Presented at the Proceedings of the Glasgow Mathematical Association.
Eringen, A.C., Edelen, D., 1972. On nonlocal elasticity. Int. J. Eng. Sci. 10 (3), 233–248.
Exadaktylos, G.E., Vardoulakis, I., 2001. Microstructure in linear elasticity and scale effects: a reconsideration of basic rock mechanics and rock fracture mechanics. Tectonophysics 335, 81–109.
Exadaktylos, G., 1998. Gradient elasticity with surface energy: Mode-I crack problem. Int. J. Solids Struct. 35, 421–456.
Fannjiang, A.C., Paulino, G.H., Chan, Y.S., 2002. Strain gradient elasticity for antiplane shear cracks: a hypersingular integrodifferential equation approach. SIAM J. Appl. Math. 62 (3), 1066–1091.
Fleck, N., Hutchinson, J., 1997. Strain gradient plasticity. Adv. Appl. Mech. 33, 296–361.
Sih, G.C., Chen, E.P., 1981. Mechanics of Fracture Cracks in Composite Materials. Martinus Nijhoff Publishers, The Netherlands.
Giannakopoulos, A., Stamoulis, K., 2007. Structural analysis of gradient elastic components. Int. J. Solids Struct. 44 (10), 3440–3451.
Joseph, R.P., Wang, B., Samali, B., 2017. Size effects on double cantilever beam fracture mechanics specimen based on strain gradient theory. Eng. Fract. Mech. 169, 309–320.
Karimipour, I., Fotuhi, A.R., 2017. Anti-plane analysis of an infinite plane with multiple cracks based on strain gradient theory. Acta Mech. 228 (5), 1793–1817.
Lam, D.C., Yang, F., Chong, A., Wang, J., Tong, P., 2003. Experiments and theory in strain gradient elasticity. J. Mech. Phys. Solids 51 (8), 1477–1508.
Li, X.F., 2001. Closed-form solution for a mode-III interface crack between two bonded dissimilar elastic layers. Int. J. Fract. 109 (2), 3–8.
Lindfield, G., Penny, J., 2012. Numerical Methods: Using MATLAB. Academic Press.
McFarland, A.W., Colton, J.S., 2005. Role of material microstructure in plate stiffness with relevance to microcantilever sensors. J. Micromech. Microeng. 15 (5), 1060.
Mindlin, R.D., 1964. Micro-structure in linear elasticity. Arch. Ration. Mech. Anal. 16 (1), 51–78.
Mindlin, R.D., 1965. Second gradient of strain and surface-tension in linear elasticity. Int. J. Solids Struct. 1 (4), 417–438.
Mousavi, S.M., Aifantis, E., 2015. A note on dislocation-based mode III gradient elastic fracture mechanics. J. Mech. Behav. Mater. 24 (3-4), 115–119.
Paulino, G., Fannjiang, A., Chan, Y.-S., 2003. Gradient elasticity theory for mode III fracture in functionally graded materials – part I: crack perpendicular to the material gradation. J. Appl. Mech. 70 (4), 531–542.
Polizzotto, C., 2016. A note on the higher order strain and stress tensors within deformation gradient elasticity theories: physical interpretations and comparisons. Int. J. Solids Struct. 90, 116–121.
Singh, B., Moodie, T.B., 1981. Closed-form solutions for finite length crack moving in a strip under anti-plane shear stress. Acta Mech. 38 (1-2), 99–109.
Tait, R., Moodie, T.B., 1981. On a problem in the dynamic theory of cracks. Q. Appl. Math. 39 (3), 419–423.
Vardoulakis, I., Exadaktylos, G., Aifantis, E., 1996. Gradient elasticity with surface energy: mode-III crack problem. Int. J. Solids Struct. 33 (30), 4531–4559.
Vardoulakis, I., & Sulem, J. (1995). Bifurcation analysis in geomechanics Blackie Academic and Professional Glasgow Google Scholar.
Wang, B.L., Mai, Y.W., 2006. Closed-form solution for an antiplane interface crack between two dissimilar magnetoelectroelastic layers. J. Appl. Mech. 73 (2), 281–290.
Yang, F., 1997. Exact solution for a finite length crack in a strip under general antiplane loading. Int. J. Fract. 87 (2), 157–164.
Yang, F., Chong, A., Lam, D.C.C., Tong, P., 2002. Couple stress based strain gradient theory for elasticity. Int. J. Solids Struct. 39 (10), 2731–2743.

Paper 5:

Composite Structures xxx (2018) xxx-xxx

Contents lists available at ScienceDirect

Composite Structures

journal homepage: www.elsevier.com

Fracture analysis of flexoelectric double cantilever beams based on the strain gradient theory

R.P. Joseph[a], Chunwei Zhang[b,*], B.L. Wang[a], B. Samali[a]

[a] Centre for Infrastructure Engineering, School of Computing, Engineering and Mathematics, Western Sydney University, Penrith, NSW 2751, Australia
[b] School of Civil Engineering, Qingdao University of Technology, Qingdao 266033, PR China

ARTICLE INFO

Keywords:
Fracture mechanics; Double cantilever beam
Strain gradient
Flexoelectricity
Large deformation
Energy release rate

ABSTRACT

In this article, the fracture behavior of a flexoelectric double cantilever beam (DCB) under large deformation is investigated using strain gradient theory. Incorporation of electric field-strain gradient coupling, known as flexoelectricity, in the constitutive equations of a 1D cantilever beam is studied. Moreover, due to the enormous surface area to volume ratio at micro/nanoscale, surface effects are also included in the theoretical formulations. The solutions of the cantilever beam deflections and strain energy release rates of the DCB with different configurations are numerically evaluated and compared. Numerical results anticipate significant size effect (higher structural stiffness) as the values of the material length scale parameter (l) and the material flexoelectric coefficient (f_{31}) are increased. DCB with the open circuit boundary condition demonstrates higher stiffness than the short circuit boundary condition. At micro/nanoscale, the effect of uncracked part of the DCB is found to be substantial in determining the strain energy release rate and it must not be ignored even for the slender beams.

1. Introduction

Ever increasing demand of piezoelectric micro/nanomaterials in small-scale devices such as Light emitting diodes (LEDs), nanoresonators and nanogenerators is evident as the technological advances toward the miniaturization of devices are being made [1]. Over the past several decades, numerous studies have been conducted to understand the fundamental physics behind the phenomenon of material polarization under the application of external mechanical stress. The classical relation between applied strain and electric polarization, known as piezoelectricity, is thoroughly defined [2] and has been widely used to investigate the fracture behavior of the piezoelectric materials at the macro scale. However, a number of experimental studies have demonstrated the size-dependent linear electro-mechanical coupling at micro/nanoscale [3,4]. This occurs when the structure dimensions become comparable to the material length scale and the state of stress at a point is not only depended on the strain but also on the strain gradient. The electromechanical coupling between polarization and strain gradient is termed as flexoelectricity [5,6]. Contrary to the piezoelectric effect, flexoelectricity is not just limited to non-centrosymmetric materials but it may induce electric polarization in the centrosymmetric material by breaking the material's symmetry [7]. Therefore, due to flexoelectric effect, non-piezoelectric materials may also be used to produce piezoelectric composites [8] and thus call out new challenges for researchers in the field of nanotechnology.

Due to an encounter of flexoelectricity in the modern era, detailed investigations relating to the fracture of micro/nano piezoelectric materials are essential in order to ensure their structural reliability for further establishing their applications. Traditionally, the amalgamation of classical continuum mechanics and electrostatics has been employed to study the electromechanical coupling phenomenon in piezoelectricity. However, in order to deal with the coupling of strain gradient and polarization, higher order gradient theories such as strain gradient theories must be employed. The pioneer work, extending the linear piezoelectric theory by incorporating the effect of polarization gradient was presented by Mindlin [9]. On the other hand, Maranganti and Sharma [10] included the polarization gradient as well as the strain gradient effect in their theoretical framework based on variational principle. Recently, Hu and Shen constructed a comprehensive model incorporating flexoelectricity, along with the electrostatic force [11] and the surface effects [12]. Mao and Purohit [5] presented detailed analysis for the flexoelectric solids using strain theory which is eventually used to derive the governing Navier equation for the isotropic materials. In recent

* Corresponding authors.
Email addresses: zhangchunwei@qut.edu.cn (C. Zhang); B.Wang@westernsydney.edu.au (B.L. Wang)

https://doi.org/10.1016/j.compstruct.2018.06.067
Received 19 February 2018; Received in revised form 12 May 2018; Accepted 16 June 2018
Available online xxx
0263-8223/

times Sladek [6] developed a finite element method (FEM) formulation to analyze the general 2D boundary value problem incorporating the electric-field strain gradient coupling in the constitutive equations. Some of the above-mentioned pioneer works have been thoroughly employed by researchers to investigate the electromechanical coupling behavior of piezoelectric nanobeams. For instance, Majdoub et al. [13] employed a modified Euler beam model and found that the electromechanical coupling coefficient in case of the piezoelectric nanowire is enhanced due to flexoelectric effect. Liang et al. [14] presented a modified Euler-Bernoulli beam model and highlighted some of its applications based on strain gradient theory. Yan and Jiang [15] evaluated the size-dependent electroelastic responses of piezoelectric nanobeams using Euler beam model along with the incorporation of flexoelectric effect. Moreover, this study was further extended to predict the size dependent bending and vibration behavior of Timoshenko beam model as well [7]. Li et al. [16] proposed a size dependent model for a layered micro beam incorporating the effect of electromechanical coupling. Some of the recent findings in this field can be found in the works of Qi et al. [17], Chu et al. [18], Yue et al. [19] and Qiu et al. [20].

The problem of evaluating the size-dependent electromechanical behavior of various beam models is mostly limited to small deformation consideration. However, several studies have shown that the incorporation of geometrical non-linearity can greatly reduce the error i.e. from 30% to 3% [21,22]. The geometrical non-linearity in case of the cantilever beam is primarily due to the non-linear force/curvature relation, and it must, therefore, be assessed thoroughly [23,24], particularly when it is associated with the fracture mechanics analysis of a double cantilever beam (DCB). Since DCB is considered to be made of two cantilever beams attached to the uncracked part, therefore, the bending behavior of cantilever beam is often employed to study the fracture toughness of DCB [25–29]. Moreover, the DCB specimen is an ideal choice for the determination of mode I fracture toughness of composite laminates and adhesively bonded materials in which the geometric non-linearity is sufficed for long cracks [30,31]. Furthermore, due to the enormous surface area to volume ratio at micro/nanoscale, the influence of surface effects becomes prominent and should not be ignored in order to accurately predict the mechanical behavior of the micro/nanostructures. Surface effects on micro/nanostructures may be characterized by two major types i.e. the surface elasticity and the surface residual stress [32]. Nevertheless, in case of piezoelectric nanomaterials, the effect of surface piezoelectricity must also be incorporated [33]. Huang and Yu [23] developed the pioneering work for the development of the piezoelectric model with simultaneous consideration of surface piezoelectricity, surface residual tress and surface elasticity.

In this paper, the fracture analysis of a flexoelectric (size-dependent piezoelectric) DCB is evaluated using modified Euler-Bernoulli beam model. In the constitutive equations, the effect of both strain gradient, as well as the electric field-strain gradient coupling, is considered. Moreover, the model also includes the simultaneous incorporation of large deformation, surface residual effects, surface elasticity, surface piezoelectricity and uncracked part of the DCB. The governing equation with respective boundary conditions, obtained through a variational principle, is solved numerically by using Lobatto IIIA collocation method. The description of the used numerical method and the application of some other numerical techniques are presented by various researchers [34–36]. The fracture mechanics results in this article are presented in terms of strain energy release rates.

2. Theoretical formulations

2.1. Bending of a flexoelectric cantilever beam

The constitutive equations with the consideration of electric field-strain gradient coupling are given as [11];

$$\tau_{ij} = c_{ijkl}\varepsilon_{kl} - e_{kij}E_k \tag{1}$$

$$\mu_{jkl} = -f_{ijkl}E_i + g_{jklmni}\kappa_{nmi} \tag{2}$$

$$D_k = a_{kl}E_l + e_{kij}\varepsilon_{ij} + f_{klmn}\kappa_{lmn} \tag{3}$$

where c is the fourth order elastic constant tensor, e is the piezoelectric coefficient, f is the electric-field strain gradient coupling (flexoelectric) coefficient tensor, the tensor g represent the strain gradient elasticity effect and a is the material's permittivity second order tensor. The symbols τ_{ij}, μ_{ijk} and D_i represent the Cauchy stress, higher order stress, and electric displacement component respectively. The indicial notation is employed in which the repeated indices represent summation and comma indicates differentiation with respect to the spatial variable. The strain ε_{ij} and strain gradient η_{ijk} are related to the displacement u_i as; $\varepsilon_{ij} = (u_{i,j} + u_{j,i})/2$ and $\eta_{ijk} = \varepsilon_{ij,k} = (u_{i,jk} + u_{j,ik})/2$ respectively. For illustration, the schematic diagram of a flexoelectric DCB specimen with the length of cracked part a, width b, thickness h is shown in Fig. 1. The beam configuration is same as that of the following Refs. [12,23,37] and the "bulk + surface" model [23] is used to modelled the DCB. For 1D mode I problem, the Cauchy and higher order stresses with the consideration of large deformation are written as;

$$\tau_{xx} = c_{11}z\frac{\mathrm{d}\varphi}{\mathrm{d}s} - e_{31}E_z \tag{4}$$

$$\mu_{xxx} = -f_{31}E_z + g_{11}\kappa_{xxx} = -f_{31}E_z + l^2c_{11}z\frac{\mathrm{d}^2\varphi}{\mathrm{d}s^2} \tag{5}$$

where φ is the slope of the deformed beam, c_{11} is the Young's modulus. The higher order elastic parameter g_{11} is related to the conventional elastic stiffness coefficient c_{11} by a factor l which is known as internal length material parameter [6,38]. The total stress is given as;

$$\sigma_{xx} = \tau_{xx} - \frac{\mathrm{d}\mu_{xxx}}{\mathrm{d}s} \tag{6}$$

The electric field component can be expressed as; $E_z = -\psi_{,z}$, here ψ is the electric potential and taken to be constant along the beam span (x-axis) [37]. The electrical displacement in the z-direction is written as;

$$D_z = a_{33}E_z + e_{31}\varepsilon_{xx} + f_{31}\kappa_{xxx} = -a_{33}\frac{\mathrm{d}\psi}{\mathrm{d}z} + e_{31}z\frac{\mathrm{d}\varphi}{\mathrm{d}s} + f_{31}z\frac{\mathrm{d}^2\varphi}{\mathrm{d}s^2} \tag{7}$$

Due to the massive surface area to volume ratio at the nanoscale, the influence of surface effects must be considered in the theoretical modeling [39]. As previously mentioned that the surface effects of micro/nanostructures may be divided into two distinct types i.e. the surface elasticity and the surface residual stress [32]. However, the effect of surface residual stress is always prominent [39]. The surface stress σ^s_{xx} and electric displacement D^s_x in x-direction including the effects of surface piezoelectricity is given as [22];

$$\sigma^s_{xx} = \tau_o + c^s_{11}\varepsilon_{xx} - e^s_{31}E_z \tag{8}$$

$$D^s_x = D^0_x + e^s_{15}\gamma_{xy} + a^s_{11}E_x \tag{9}$$

where τ_o in Eq. (8) is the surface residual stress, c^s_{11} is the Young's Modulus of the surface, e^s_{31} is the piezoelectric constant of the surface, γ_{xy} is

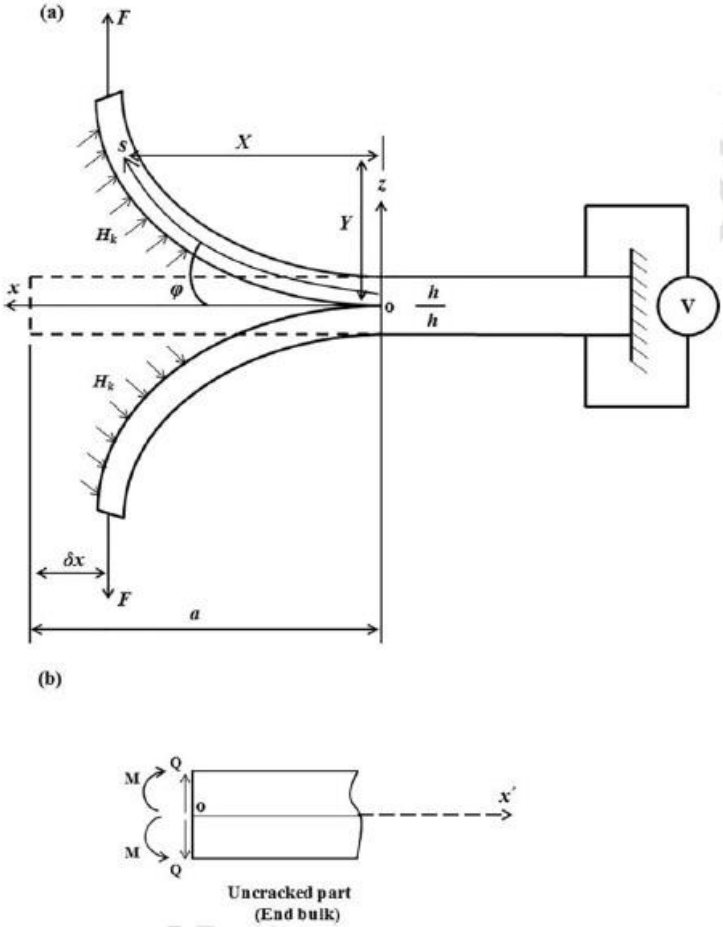

Fig. 1. Schematic diagrams: (a) flexoelectric double cantilever beam with surface residual stress; (b) root part of DCB.

the shear stress, a_{11}^{s} is the surface material permittivity. Electric energy, electric displacement and the strain gradient effect of the surfaces is neglecting since its value is negligible as compared to the bulk. Moreover, it is known that $E_x \ll E_z$, so that $D_x \ll D_z$, therefore, only D_z and E_z will be considered for theoretical modeling. The equilibrium equation in the absence of electric charges is $D_{z,z} = 0$ [22] that gives;

$$\psi(z) = \frac{1}{a_{33}}\frac{\mathrm{d}}{\mathrm{d}s}\left[e_{31}\varphi + f_{31}\frac{\mathrm{d}\varphi}{\mathrm{d}s}\right]\frac{(z)^2}{2} + C_1 z + C_2 \tag{10}$$

here C_1 and C_2 are the constants to be determined. Using the boundary conditions i.e. $\psi(-h/2) = 0$; $\psi(h/2) = V$, where V is the applied voltage, E_z and ψ may be evaluated as follows;

$$\begin{aligned}\psi(-h/2) = {} & \frac{e_{31}}{a_{33}}\frac{\mathrm{d}}{\mathrm{d}s}\left[\varphi + m^2\frac{\mathrm{d}\varphi}{\mathrm{d}s}\right]\frac{(-h/2)^2}{2} \\ & - C_1(h/2) + C_2 \\ = {} & 0\end{aligned} \tag{11}$$

$$\begin{aligned}\psi(h/2) = {} & \frac{e_{31}}{a_{33}}\frac{\mathrm{d}}{\mathrm{d}s}\left[\varphi + m^2\frac{\mathrm{d}\varphi}{\mathrm{d}s}\right]\frac{(h/2)^2}{2} + C_1(h/2) + C_2 \\ = {} & V\end{aligned} \tag{12}$$

solving Eqs. (11) and (12) gives;

$$\begin{aligned}C_1 = {} & V/h, C_2 \\ = {} & \frac{V}{2} - \frac{1}{a_{33}}\frac{\mathrm{d}}{\mathrm{d}s}\left[e_{31}\varphi + f_{31}\frac{\mathrm{d}\varphi}{\mathrm{d}s}\right]\frac{(h/2)^2}{2}\end{aligned} \tag{13}$$

so, the electric potential from Eq. (10) is given as;

$$\begin{aligned}\psi(z) = {} & \frac{1}{a_{33}}\frac{\mathrm{d}}{\mathrm{d}s}\left[e_{31}\varphi + f_{31}\frac{\mathrm{d}\varphi}{\mathrm{d}s}\right]\frac{(z^2 - (h/2)^2)}{2} \\ & + \frac{V}{h}z + \frac{V}{2}\end{aligned} \tag{14}$$

The corresponding electric field in z-direction may be written as;

$$E_z = -\frac{\mathrm{d}\psi}{\mathrm{d}z} = -\frac{1}{a_{33}}\frac{\mathrm{d}}{\mathrm{d}s}\left[e_{31}\varphi + f_{31}\frac{\mathrm{d}\varphi}{\mathrm{d}s}\right]z - \frac{V}{h} \tag{15}$$

with the aid of Eq. (15), bulk and surface stress from Eqs. (6) and (8) are written as;

$$\sigma_{xx} = c_{11}z\left[\frac{\mathrm{d}\varphi}{\mathrm{d}s} - l^2\frac{\mathrm{d}^3\varphi}{\mathrm{d}s^3}\right] + \frac{z}{a_{33}}\left[e_{31}^2\frac{\mathrm{d}\varphi}{\mathrm{d}s} - f_{31}^2\frac{\mathrm{d}^3\varphi}{\mathrm{d}s^3}\right] + e_{31}\frac{V}{h} \tag{16}$$

$$\sigma_{xx}^s = \tau_0 + c_{11}^s\left(\int_C z^2 dC\right)\frac{\mathrm{d}\varphi}{\mathrm{d}s} + \frac{e_{31}^s}{a_{33}}\left(\int_C z^2 dC\right)\frac{\mathrm{d}}{\mathrm{d}s}\left[e_{31}\varphi + f_{31}\frac{\mathrm{d}\varphi}{\mathrm{d}s}\right] + e_{31}^s\frac{V}{h} \tag{17}$$

where C is the perimeter of the cross-section. Therefore, the moment of the cross section ($M = \int_A \sigma_{xx} z dA + \int_S \sigma_s z dS$) with the consideration of strain gradients and flexoelectricity is;

$$M = \overbrace{\frac{\mathrm{d}\varphi}{\mathrm{d}s}\left[\left(c_{11} + \frac{e_{31}^2}{a_{33}}\right)\frac{bh^3}{12} + \left(c_{11}^s + \frac{e_{31}e_{31}^s}{a_{33}}\right)\left(\frac{bh^2}{2} + \frac{h^3}{6}\right)\right]}^{\text{Classical Piezoelectricity}} - \overbrace{l^2\frac{\mathrm{d}^3\varphi}{\mathrm{d}s^3}\left[c_{11}\frac{bh^3}{12}\right]}^{\text{Strain gradient effect}} + \underbrace{\frac{\mathrm{d}^2\varphi}{\mathrm{d}s^2}\left[\frac{f_{31}e_{31}^s}{a_{33}}\left(\frac{bh^2}{2} + \frac{h^3}{6}\right)\right] - \frac{\mathrm{d}^3\varphi}{\mathrm{d}s^3}\left[\frac{f_{31}^2}{a_{33}}\frac{bh^3}{12}\right]}_{\text{Electricfield–Strain gradient coupling effect}} \tag{18}$$

The electrical force at the cross-section is given as;

$$T = \int_A \sigma_x dA + \int_s \tau_x ds = e_{31}Vb + 2be_{31}^s\frac{V}{h} \tag{19}$$

The equivalent vertical load $q(s)$ induced by the surface residual stress is expressed as [39,40];

$$q(s) = H\kappa = H\frac{\mathrm{d}\varphi}{\mathrm{d}s} \tag{20}$$

with $H = 2\tau_o b$ is the effective lateral distribution load [32,40,41], τ_o is the surface residual stress and b is the beam width. Note that the effects of surface elasticity and surface piezoelectricity have been included in the effective bending stiffness as expressed in Eq. (18), therefore only τ_o is included in H. The equilibrium equations of the DCB give [39]; $\frac{dQ}{ds} = -H\frac{d\varphi}{ds}$, $\frac{dM}{ds} = Q$ (shear force). Bending moment at any point "s" induced by the equivalent distributed load $q(s)$, endpoint concentrated vertical force F and the electrical force of the cross-section T may be expressed as;

$$M_{(o)} = \int_0^a (\xi - s)(H + T)\frac{\partial\varphi}{\partial\xi}\mathrm{d}\xi + F[x(a) - x(s)] \tag{21}$$

It is important to note at any specified point $P(x,y)$ along a curved beam, bending moment induced by the external force F is given as; $M = F.(a - \delta x - X)$ (where a is the length of a beam and δx is the horizontal deflection), which if differentiated ($\mathrm{d}(a - \delta x - X)/\mathrm{d}s = -\cos\varphi$). So, the following governing equation of a Euler beam with the cumulative effects of surface, piezoelectricity and strain gradient subjected to large deformation is written as;

$$\overbrace{\frac{\mathrm{d}^2\varphi}{\mathrm{d}s^2}\left[\left(c_{11} + \frac{e_{31}^2}{a_{33}}\right)\frac{bh^3}{12} + \left(c_{11}^s + \frac{e_{31}e_{31}^s}{a_{33}}\right)\left(\frac{bh^2}{2} + \frac{h^3}{6}\right)\right]}^{\text{Classical Piezoelectricity}} - \overbrace{l^2\frac{\mathrm{d}^4\varphi}{\mathrm{d}s^4}\left[c_{11}\frac{bh^3}{12}\right]}^{\text{Strain gradient effect}} + \underbrace{\frac{\mathrm{d}^3\varphi}{\mathrm{d}s^3}\left[\frac{f_{31}e_{31}^s}{a_{33}}\left(\frac{bh^2}{2} + \frac{h^3}{6}\right)\right] - \frac{\mathrm{d}^4\varphi}{\mathrm{d}s^4}\left[\frac{f_{31}^2}{a_{33}}\frac{bh^3}{12}\right]}_{\text{Electricfield–Strain gradient coupling effect}} = -F\cos\varphi + (H + T)\varphi - (H + T)\varphi_a \tag{22}$$

here φ_a is the unknown slope at the free end of the beam. Alternatively, the governing equation and respective boundary conditions may also be evaluated through a variational principle. The variational principle is given as; $\delta(U_b + U_s) - \delta W = 0$, where W is the work done by the external forces, U_b and U_s are the strain energy of the bulk and surface respectively. For one-dimensional case, the bulk strain energy (U_b) is given as; $U_b = \frac{1}{2}\int_A\int_0^a [\tau_{xx}\varepsilon_{xx} + \mu_{xxx}\nabla.\varepsilon_{xx} + D_z E_z]\mathrm{d}s\mathrm{d}A$. As previously mentioned that the equilibrium equation in the absence of electric charges is $D_{z,z} = 0$ (by means of the Gaussian theorem [42]). So, the electric Gibbs energy of the bulk is written as; $U_b = \frac{1}{2}\int_A\int_0^a [\tau_{xx}\varepsilon_{xx} + \mu_{xxx}\nabla.\varepsilon_{xx}]\mathrm{d}s\mathrm{d}A$. On the other hand, the surface strain energy (U_s) is given as; $U_s = \frac{1}{2}\int_A [\tau_{xx}^s\varepsilon_{xx}^s + \tau_o\varepsilon_{xx}^s]\mathrm{d}A$. Here ∇ denotes (d/ds) in the case of large deformation. The variation of the work done by the external forces is written as; $\delta W = -\int_0^a F\cos\varphi(s)\delta\varphi\mathrm{d}s$. So, the variational principle $\delta(U_b + U_s) - \delta W = 0$ gives;

$$\int_0^a \left[\frac{\mathrm{d}}{\mathrm{d}s}\left(M - \frac{\mathrm{d}M^h}{\mathrm{d}s} + M^s\right) + F\cos\varphi - (H + T)\varphi + (H + T)\varphi_a\right]\delta\varphi ds + \left[-\left(M - \frac{\mathrm{d}M^h}{\mathrm{d}s} + M^s\right)\delta\varphi'\right]_0^a + [M^h\delta\varphi'']_0^a = 0 \tag{23}$$

where M, M^h and M^s are the classical bending moment, higher-order bending moment and bending moment due to surface stress respectively, which are defined as;

$$M = \int_A \tau_{xx} z\mathrm{d}A,\ M^h = \int_A \mu_{xxx}\mathrm{d}A,\ M^s = \int_A \tau_{xx}^s z\mathrm{d}A \tag{24}$$

Using above equations M, M^h and M^s are evaluated as;

$$M = c_{11}\left(\frac{bh^3}{12}\right)\frac{d\varphi}{ds} + \frac{e_{31}}{a_{33}}\frac{d}{ds}\left[e_{31}\varphi + f_{31}\frac{d\varphi}{ds}\right]\left(\frac{bh^3}{12}\right) \tag{25}$$

$$M^s = c_{11}^s\left(\frac{bh^2}{2}+\frac{h^3}{6}\right)\frac{d\varphi}{ds} + \frac{e_{31}^s}{a_{33}}\frac{d}{ds}\left[e_{31}\varphi + f_{31}\frac{d\varphi}{ds}\right]\left(\frac{bh^2}{2}+\frac{h^3}{6}\right) \tag{26}$$

$$M^h = l^2 c_{11}\left(\frac{bh^3}{12}\right)\frac{d^2\varphi}{ds^2} + \frac{f_{31}}{a_{33}}\frac{d}{ds}\left[e_{31}\varphi + f_{31}\frac{d\varphi}{ds}\right]\left(\frac{bh^3}{12}\right) \tag{27}$$

The governing equation from Eq. (23) is given as;

$$\frac{d}{ds}\left(M - \frac{dM^h}{ds} + M^s\right) + F\cos\varphi - (H+T)\varphi + (H+T)\varphi_a = 0 \tag{28}$$

with the aid of Eqs. (25-27) and from Eq. (28), one may get the governing equation (Eq. (22)). The boundary conditions evaluated from the variational principle require $\left(M - \frac{dM^h}{ds} + M^s\right)$ (total moment) and M^h (higher-order moment) to be specified at $s = 0$ and $s = a$.

2.2. Boundary conditions

In order to solve the governing Eq. (22), we need four boundary conditions to be specified at $s = 0$ and $s = a$ (classical as well as non-classical). With the consideration of classical and non-classical boundary conditions evaluated from the variational principle, it is evident that more than one set of boundary conditions may be obtained. However, in our case, the classical boundary condition at the fixed end of the beam i.e. $s = 0$ is expressed as; $\varphi = 0$ [43], which indicates zero rotation. Meanwhile at the free end i.e. $s = a$, the classical moment for the piezoelectric beam from Eq. (18) gives; $d\varphi/ds = 0$. The higher order boundary conditions from the variational principle give;

At $s = 0$, $M^h = 0$ namely;

$$\frac{bh^3}{12}\left(l^2 c_{11} + \frac{f_{31}^2}{a_{33}}\right)\frac{d^2\varphi}{ds^2} + \left(\frac{e_{31}f_{31}}{a_{33}}\frac{bh^3}{12}\right)\frac{d\varphi}{ds} = 0 \tag{29a}$$

At $s = a$, with $d\varphi/ds = 0$ (classical one) and with zero higher order moment ($d^2\varphi/ds^2 = 0$), from $\left(M - \frac{dM^h}{ds} + M^s = 0\right)$ we get;

$$\frac{d^3\varphi}{ds^3}\left[l^2 c_{11} + c_{11}\frac{f_{31}^2}{a_{33}}\right]\frac{bh^3}{12} = 0, \text{ namely } \frac{d^3\varphi}{ds^3} = 0 \tag{29b}$$

so, the set of boundary conditions considered in this work is given as;

$$\text{At } s = 0;\ \varphi = 0 \text{ and } \frac{bh^3}{12}\left(l^2 c_{11} + \frac{f_{31}^2}{a_{33}}\right)\frac{d^2\varphi}{ds^2} + \left(\frac{e_{31}f_{31}}{a_{33}}\frac{bh^3}{12}\right)\frac{d\varphi}{ds} = 0 \tag{30a}$$

$$\text{At } s = a;\ d\varphi/ds = 0 \text{ and } \frac{d^3\varphi}{ds^3} = 0 \tag{30b}$$

2.3. Strain energy release rate of the cracked and uncracked part of DCB

The strain energy release rate G may be found by taking the beam length as a (crack length) and width b, the strain energy release rate of a double cantilever beam is given as; $G = F\,(dY_{max}/bda)$. Here $Y_{max} = \int_0^a \sin(\varphi)ds$ [26,39]. On the other hand, for the uncracked part of the DCB, the influence of the shear stresses must not be ignored. Therefore the governing equations of the uncracked part of the DCB are usually evaluated using Timoshenko beam theory [22]. According to which the potential energy of the uncracked or root part (U_r) is expressed as;

$$U_r = 2\int_{-\infty}^{0}\frac{M_{(x)}^2}{2EI_{\text{eff}}}dx + 2\int_{-\infty}^{0}\frac{Q_{(x)}^2}{2G^s A}dx \tag{31a}$$

$$EI_{\text{eff}} = \left(c_{11} + \frac{e_{31}^2}{a_{33}}\right)\frac{bh^3}{12} + \left(c_{11}^s + \frac{e_{31}e_{31}^s}{a_{33}}\right)\left(\frac{bh^2}{2}+\frac{h^3}{6}\right) \tag{31b}$$

where $M_{(x)}$ and $Q_{(x)}$ are the bending moment and shear force on the cross-section area A respectively, G^s is an effective shear modulus and EI_{eff} is the effective bending rigidity as defined in Eq. (31b). As per the coordinate system, the integrals vary from negative infinity to zero. Using Eq. (31a) and the results provided by Joseph et al. [26] one gets;

$$U_r = \frac{1}{\sqrt{EI_{\text{eff}}G^s A}}\left[F^2X^2(\varphi_a) + \left[\int_0^a s(H+T)\frac{d\varphi}{ds}ds\right]^2\right] \tag{32a}$$

$$\int_0^a s(H+T)\frac{d\varphi}{ds}ds = (H+T)\left[s.\varphi(s)\Big|_0^a - \int_0^a \varphi ds\right] \tag{32b}$$

where $X(\varphi_a)$ is the endpoint horizontal deflection (as shown in Fig. 1), F is the vertical concentrated force, φ_a is the unknown slope at the free end of the beam, $H = 2\tau_o b$ and T is the electrical force of cross-section (Eq. (19)).

2.4. Electrical boundary conditions

2.4.1. Short-circuit boundary condition

Here the governing equations of two electrical boundary conditions i.e. short circuit and open circuit boundary conditions are evaluated.

For short circuit boundary condition, the electric field would be zero i.e. $E_z = 0$. Therefore the total stress of the bulk and surface are written as;

$$\sigma_{xx} = c_{11} z \left[\frac{d\varphi}{ds} - l^2 \frac{d^3\varphi}{ds^3}\right] \tag{33}$$

$$\sigma^s_{xx} = \tau_0 + c^s_{11} z \frac{d\varphi}{ds} \tag{34}$$

Eq. (33) depicts only mechanical gradient to be effective, so the piezoelectric material properties and strain field-strain gradient coupling effect would vanish. The moment is found to be;

$$M = \left[\frac{d\varphi}{ds} - l^2 \frac{d^3\varphi}{ds^3}\right] c_{11} \frac{bh^3}{12} + \frac{d\varphi}{ds}\left[c^s_{11}\left(\frac{bh^2}{2} + \frac{h^3}{6}\right)\right] \tag{35}$$

Moreover, due to diminishing potential difference across the boundaries, the governing Eq. (22) would reduce to;

$$\left[\frac{d^2\varphi}{ds^2} - l^2 \frac{d^4\varphi}{ds^4}\right] c_{11} \frac{bh^3}{12} + \frac{d^2\varphi}{ds^2}\left[c^s_{11}\left(\frac{bh^2}{2} + \frac{h^3}{6}\right)\right] = -F\cos\varphi + H\varphi - H\varphi_a \tag{36}$$

The classical and non-classical boundary conditions (evaluated from variational principle) are as follows;

$$\text{At } s = 0 : \varphi = 0, M^h = 0 \text{ gives; } \frac{d^2\varphi}{ds^2} = 0 \tag{37a}$$

$$\begin{aligned} \text{At } s = a \\ : \left(M - \frac{dM^h}{ds} + M^s\right. \\ \left. = 0\right) \text{ gives; } \frac{d\varphi}{ds} \\ = 0, \frac{d\varphi}{ds} - l^2 \frac{d^3\varphi}{ds^3} \\ = 0 \text{ or } \frac{d\varphi}{ds} \\ = 0, \frac{d^3\varphi}{ds^3} \\ = 0 \end{aligned} \tag{37b}$$

2.4.2. Open-circuit boundary conditions

Similarly, for an open circuit, the electrical displacement would be zero i.e. $D_z = 0$ [22] that gives;

$$\begin{aligned} D_z &= a_{33}E_z + e_{31}\varepsilon_{xx} + f_{31}\kappa_{xxx} \\ &= a_{33}E_z + e_{31} z \frac{d\varphi}{ds} + f_{31} z \frac{d^2\varphi}{ds^2} \\ &= 0 \end{aligned} \tag{38}$$

or

$$E_z = -\frac{e_{31}}{a_{33}} z \frac{d\varphi}{ds} - \frac{f_{31}}{a_{33}} z \frac{d^2\varphi}{ds^2} \tag{39}$$

with the aid of Eq. (39), the total moment is given in Eq. (18) is recovered. Meanwhile, the electrical force T would be zero. So, the resulting governing Eq. (22) is reduced to;

$$\begin{aligned} &\frac{d^2\varphi}{ds^2}\left[\left(c_{11} + \frac{e^2_{31}}{a_{33}}\right)\frac{bh^3}{12} + \left(c^s_{11} + \frac{e_{31}e^s_{31}}{a_{33}}\right)\left(\frac{bh^2}{2} + \frac{h^3}{6}\right)\right] \\ &- l^2 \frac{d^4\varphi}{ds^4}\left[c_{11}\frac{bh^3}{12}\right] + \frac{d^3\varphi}{ds^3}\left[\frac{f_{31}e^s_{31}}{a_{33}}\left(\frac{bh^2}{2} + \frac{h^3}{6}\right)\right] \\ &- \frac{d^4\varphi}{ds^4}\left[\frac{f^2_{31}}{a_{33}}\frac{bh^3}{12}\right] = -F\cos\varphi + H\varphi - H\varphi_a \end{aligned} \tag{40}$$

Along with the classical boundary conditions, the higher-order boundary conditions are also similar to those in Eq. (30). The governing Eqs. (22), (36) and (40) with the mechanical boundary conditions are solved numerically using a Matlab function bvp4c. This function solves the boundary value problem with the aid of three-stage Lobatto IIIa collocation formula (which is a preferred method in the case of boundary value problems). Detailed literature about this method and its implement in bvp4c is provided by Shampine et al. [35].

3. Numerical results

In order to evaluate the numerical solution of Eq. (22), the material bulk properties of $BaTiO_3$ are taken [33,44,45] i.e. $c_{11} = 131\,\text{GPa}$, $e_{31} = -4.4\,\text{Cm}^{-2}$, $a_{33} = 1.2658\times10^{-8}\,\text{CV}^{-1}\text{m}^{-1}$, $G^s = c_{66} = 44.7\,\text{GPa}$. For the surface, the properties are taken as $E^s = 9.72\,\text{Nm}^{-1}$ [18,45] and $e^s_{31} = 0.7\times10^{-9}\,\text{Cm}^{-1}$ [46]. The value of surface residual stresses τ_0 is assumed to be $\pm10\,\text{Nm}^{-1}$ (since it can be positive or negative) and it may range from 1 to $10\,\text{Nm}^{-1}$[47]. In order to investigate the effect of strain gradient, the material length scale parameter (l) and the flexoelectricity coefficient (f_{31}) are related to an introduced factor q as;

$$l^2 = q.l^2_o,\ f_{31} = q.f_{(31)o} \tag{41}$$

and the numerical values of l^2_o and $f_{(31)o}$ are assumed to be $4\times10^{-9}\text{m}^2$ and 1×10^{-6}C/m (as the flexoelectric coefficient may range from 1 to 10μC/m [48]). Since the effect of large deformation is more pronounced at elevated load, therefore, bending behavior of a cantilever beam is not independent of the normalized endpoint force as elaborated by the authors in their previous article [26]. Here, the endpoint vertical force F (1 μN) and height h (10 μm) are chosen in a manner such that the beam remains elastic throughout. The results of the vertical deflections along a flexoelectric cantilever beam (Y_f), normalized by the end-point vertical deflection (under large deflection) of the classical piezoelectric beam ($Y_{p(max)}$) are presented in Fig. 2. With the consideration of only bulk piezoelectricity and $a/h = 20$, the normalized beam deflections are evaluated for different values of q. It is shown that for higher q (greater flexoelectric effect), the strain gradient model predicts stiffer behavior. Effect of flexoelectricity and beam slenderness on its bending behavior is further elaborated in Fig. 3, where the end-point flexoelectric beam deflection is normalized with that of classical piezoelectric cantilever beam Y_p (with large deformation). The results are also obtained for positive as well as the negative voltage (for $q = 1$ only). From Fig. 3, the stiffening effect is shown to be more prominent for smaller (a/h) (apart from the stiffening effect with increasing q). Positive voltage tends to increase the stiffness of the beam and vice versa since the negative voltage will induce a compressive force which makes the beam to behave softer [22]. Moreover, the results for the

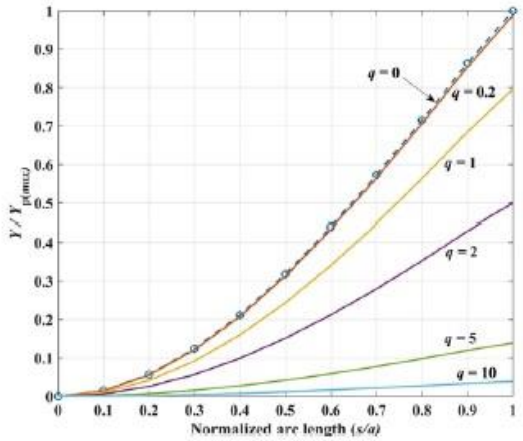

Fig. 2. Deflection along the beam axis.

classical piezoelectric beam (with large deformation) may be recovered as the value of q is reduced to zero.

In order to investigate the fracture behavior of DCB, the endpoint vertical deflection of a cantilever beam is used to evaluate its strain energy release rate given as; $G = F\,(\mathrm{d}Y_{max}/b\mathrm{d}a)$, where b and a are the width and length of the beam respectively. The strain release rate of a flexoelectric DCB G_f normalized with the strain energy release rate of the classical piezoelectric DCB G_p (with large deformation) against different a/h ratios is plotted in Fig. 4. Here the applied external voltage is set to 5 V. As expected, the strain energy release rate of the flexoelectric DCB increases as q is decreased and eventually, the results of classical piezoelectric DCB are recovered as q approaches zero. Next, the effect of surface stresses is evaluated and presented. Since the effect of surface residual stress is found to be more pronounced as compared to the effect of surface elasticity (as shown by Wang and Wang [39] and Yan and Jiang [37]) and surface piezoelectricity, therefore only the effect of surface residual stress for $q = 1$ is presented in Fig. 5 (the normalization factor G_p is same as defined before). It is shown that the flexoelectric DCB exhibit stiffer response by lowering the normalized strain energy release rate with negative surface residual stress and vice versa. The stiffer or softer response may be attributed to the signs of curvature during the bending of a cantilever beam as thoroughly explained by He and Lilley [32].

Meanwhile, it is also important to present the results with different electrical boundary conditions. Therefore, the strain energy release rate of the flexoelectric DCBs with the short circuit and open circuits boundary conditions are evaluated (as described in Section 2.4) and compared in Fig. 6. From Fig. 6, it is evident that the strain energy release rate with the short circuit boundary condition is higher than those with the open circuit boundary condition. It is clear from the governing equations of short and open circuit boundary conditions as presented in Eqs. (36) and (40) respectively that the effective bending rigidity components associated with the higher order strain gradient ($\mathrm{d}^2\varphi/\mathrm{d}s^2$) and ($\mathrm{d}^4\varphi/\mathrm{d}s^4$) are greater for open circuit boundary condition. Moreover, the piezoelectric (e_{31} and e^s_{31}) and flexoelectric (f_{31}) coefficients also play a significant part in the open circuit model, which on the other hand is absent for the short circuit model. This indicates that larger force is required to deform the beam under open circuit and hence higher stiffness and lower strain release rate is expected. The results shown here are similar to the one shown by Wang and Wang [22] but those were the results of the classical piezoelectric DCB (with the large deformation consideration).

The effect of uncracked part of the DCB on its fracture analysis is crucial as demonstrated by the authors in their previous article (Joseph et al. [26]). Therefore, the effect of the uncracked/root part is established with the help of a variable $R = G_{uc}/G_c$ which is defined as the ratio of the strain energy release rate of the uncracked part (G_{uc}) to the cracked part (G_c). The plot of R vs a/h is shown in Fig. 7. Here all the surface effects are included i.e. $E^s = 9.72\,\mathrm{Nm}^{-1}$, $e^s_{31} = 0.7 \times 10^{-9}\,\mathrm{Cm}^{-1}$,

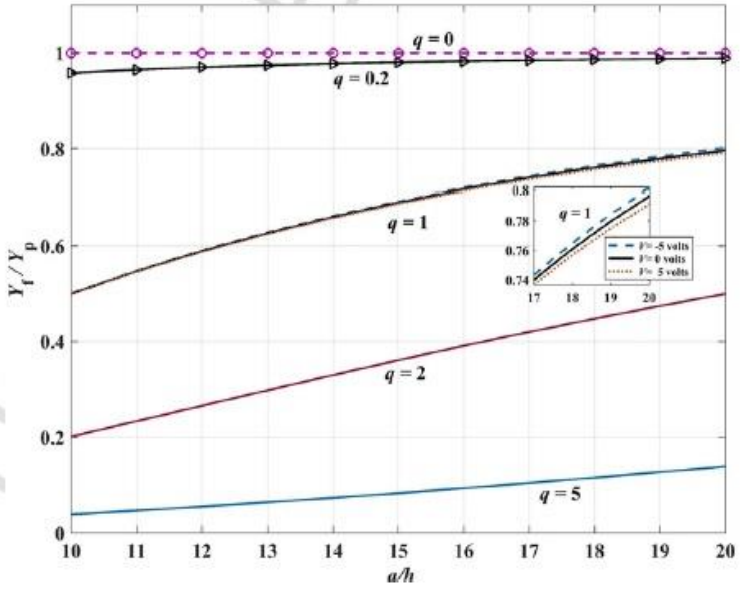

Fig. 3. Maximum tip deflection of a cantilever beam vs a/h.

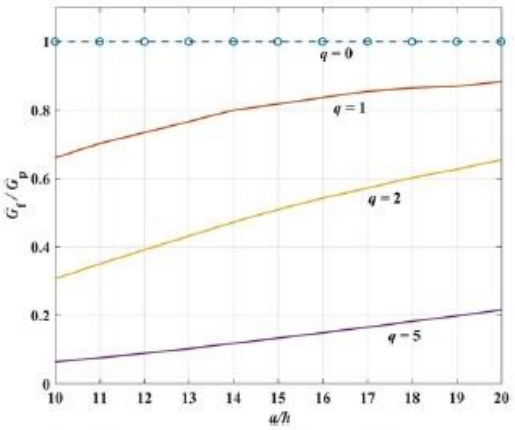

Fig. 4. Strain energy release rate of the flexoelectric DCB vs a/h.

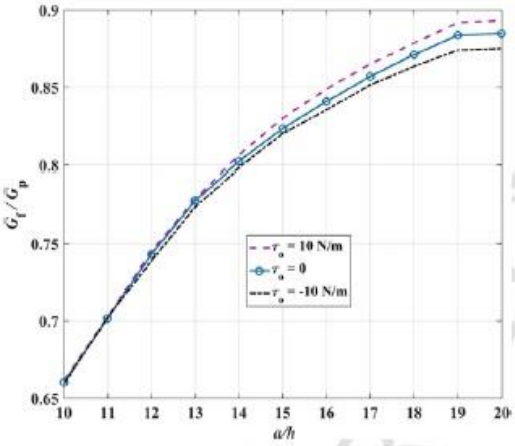

Fig. 5. Effect of surface residual stress (for $q = 1$).

$\tau_o = -10\ \mathrm{Nm}^{-1}$ and voltage is taken as 5 V. It may be seen from Fig. 7 that for flexoelectric DCB, the contribution of the uncracked part to characterize its fracture behavior is more noticeable as q is increased. For instance, at $q = 5$ and $a/h = 10$, the strain energy release rate uncracked part is more than that of the cracked part, hence demonstrating stronger size effect. However, as q approaches zero, R is usually less than 10% and it may be neglected for the sake of model simplicity. Next, the comparison between the total strain energy release rate G_T ($G_T = G_c + G_{uc}$) and the strain energy release rate of the cracked G_c is made for the flexoelectric as well as the classical piezoelectric DCB ($q = 0$). The results in Fig. 8 further established the argument presented in Fig. 7 that for higher q such as $q = 5$, the contribution of the strain energy release rate of the uncracked part is very significant in the total strain energy release rate of the DCB. The contribution of the uncracked part reduces as q is decreased and as a/h is increased. By examining Figs. 7 and 8 one may say that the effect of the uncracked part must not be ignored in case of flexoelectric DCB even when the beam is slender (higher a/h).

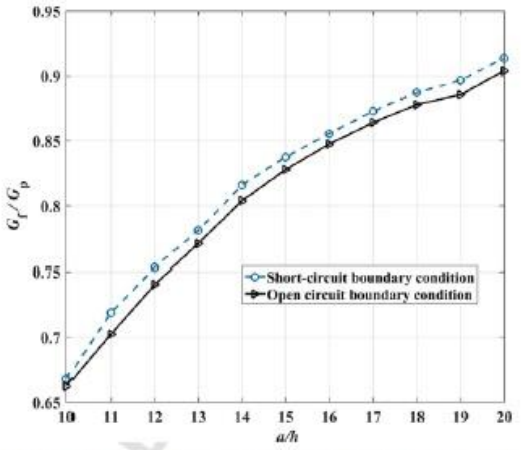

Fig. 6. Comparison of the strain energy release rate of the short circuit with the open circuit boundary condition.

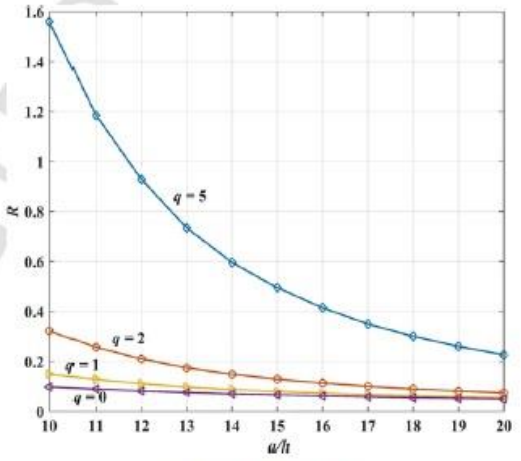

Fig. 7. Variation of R vs a/h.

4. Conclusion

In this paper, the fracture analysis of a flexoelectric DCB (size dependent piezoelectric DCB) is investigated using the strain gradient elasticity theory. Contrary to the classical approach, this work is based on the consideration of large deformation which is a common phenomenon at the nanoscale. The governing equation and the relevant boundary conditions are obtained by means of a variational principle. The surface effects are also incorporated in the theoretical framework as well as the numerical results. The flexoelectric DCB is shown to exhibit stiffer response than the classical piezoelectric DCB. Meanwhile, the strain energy release rate of the flexoelectric DCBs with different electrical boundary conditions i.e. short circuit and open circuit boundary conditions are evaluated and compared. It is demonstrated that the effect of the uncracked part of a flexoelectric DCB is very prominent in determining its fracture behavior and it must not be ignored even for the slender beams. The findings of this research paper are not only

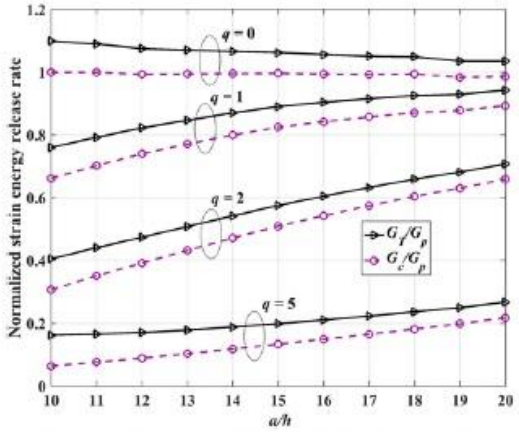

Fig. 8. Comparison of the strain energy release rate of the DCB with and without the uncracked part.

beneficial for the relevant experimental design but also in testing the available real time data.

References

[1] L.L. Ke, C. Liu, Y.S. Wang, Free vibration of nonlocal piezoelectric nanoplates under various boundary conditions, Physica E 66 (2015) 93–106.
[2] W.G. Cady, Piezoelectricity: An introduction to the theory and applications of electromechanical phenomena in crystals, Mcgraw-Hill, 1946.
[3] S. Baskaran, X. He, Q. Chen, J.Y. Fu, Experimental studies on the direct flexoelectric effect in α-phase polyvinylidene fluoride films, Appl Phys Lett 98 (24) (2011) 242901.
[4] G. Catalan, A. Lubk, A. Vlooswijk, E. Snoeck, C. Magen, A. Janssens, et al., Flexoelectric rotation of polarization in ferroelectric thin films, Nat Mater 10 (12) (2011) 963–967.
[5] S. Mao, P.K. Purohit, Insights into flexoelectric solids from strain-gradient elasticity, J Appl Mech 81 (8) (2014) 081004.
[6] J. Sladek, V. Sladek, P. Stanak, C. Zhang, C.L. Tan, Fracture mechanics analysis of size-dependent piezoelectric solids, Int J Solids Struct 113 (2017) 1–9.
[7] Z. Yan, L. Jiang, Size-dependent bending and vibration behaviour of piezoelectric nanobeams due to flexoelectricity, J Phys D Appl Phys 46 (35) (2013) 355502.
[8] N. Sharma, C. Landis, P. Sharma, Piezoelectric thin-film superlattices without using piezoelectric materials, J Appl Phys 108 (2) (2010) 024304.
[9] R.D. Mindlin, Continuum and lattice theories of influence of electromechanical coupling on capacitance of thin dielectric films, Int J Solids Struct 5 (11) (1969) 1197–1208.
[10] R. Maranganti, N. Sharma, P. Sharma, Electromechanical coupling in nonpiezoelectric materials due to nanoscale nonlocal size effects: Green's function solutions and embedded inclusions, Phys Rev B 74 (1) (2006) 014110.
[11] S. Hu, S. Shen, Variational principles and governing equations in nano-dielectrics with the flexoelectric effect, Sci China Phys Mech Astron 53 (8) (2010) 1497–1504.
[12] S. Shen, S. Hu, A theory of flexoelectricity with surface effect for elastic dielectrics, J Mech Phys Solids 58 (5) (2010) 665–677.
[13] M. Majdoub, P. Sharma, T. Cagin, Enhanced size-dependent piezoelectricity and elasticity in nanostructures due to the flexoelectric effect, Phys Rev B 77 (12) (2008) 125424.
[14] X. Liang, S. Hu, S. Shen, A new Bernoulli-Euler beam model based on a simplified strain gradient elasticity theory and its applications, Compos Struct 111 (2014) 317–323.
[15] Z. Yan, L. Jiang, Flexoelectric effect on the electroelastic responses of bending piezoelectric nanobeams, J Appl Phys 113 (19) (2013) 194102.
[16] A. Li, S. Zhou, S. Zhou, B. Wang, Size-dependent analysis of a three-layer microbeam including electromechanical coupling, Compos Struct 116 (2014) 120–127.
[17] L. Qi, S. Zhou, A. Li, Size-dependent bending of an electro-elastic bilayer nanobeam due to flexoelectricity and strain gradient elastic effect, Compos Struct 135 (2016) 167–175.
[18] L. Chu, G. Dui, C. Ju, Flexoelectric effect on the bending and vibration responses of functionally graded piezoelectric nanobeams based on general modified strain gradient theory, Compos Struct 186 (2018) 39–49.
[19] Y. Yue, K. Xu, E. Aifantis, Microscale size effects on the electromechanical coupling in piezoelectric material for anti-plane problem, Smart Mater Struct 23 (12) (2014) 125043.
[20] Y. Qiu, H. Wu, J. Wang, J. Lou, Z. Zhang, A. Liu, et al., The enhanced piezoelectricity in compositionally graded ferroelectric thin films under electric field: a role of flexoelectric effect, J Appl Phys 123 (8) (2018) 084103.
[21] Reeder JR, Crews J Jr. Nonlinear analysis and redesign of the mixed-mode bending delamination test. Technical Report; 1991.
[22] K. Wang, B. Wang, Nonlinear fracture mechanics analysis of nano-scale piezoelectric double cantilever beam specimens with surface effect, European Journal of Mechanics-A/Solids 56 (2016) 12–18.
[23] G.Y. Huang, S.W. Yu, Effect of surface piezoelectricity on the electromechanical behaviour of a piezoelectric ring, Phys Status Solidi (b) 243 (4) (2006).
[24] X.L. Jia, J. Yang, S. Kitipornchai, Pull-in instability of geometrically nonlinear micro-switches under electrostatic and Casimir forces, Acta Mech 218 (1–2) (2011) 161–174.
[25] A. Giannakopoulos, K. Stamoulis, Structural analysis of gradient elastic components, Int J Solids Struct 44 (10) (2007) 3440–3451.
[26] R.P. Joseph, B. Wang, B. Samali, Size effects on double cantilever beam fracture mechanics specimen based on strain gradient theory, Eng Fract Mech 169 (2017) 309–320.
[27] Joseph RP, Wang BL. Large deformation of the double cantilever beam fracture mechanics specimen with surface effects based on strain gradient theory. In: Journal of Material Sciences & Engineering, Proceedings of the 3rd International Conference on Smart Materials and Structures, Orlando, USA, 20–22 March 2017. p. 80.
[28] X.F. Li, K.Y. Lee, Fracture of a thin power-law nonlinear material with a crack using the DCB model, Int J Fract 201 (1) (2016) 119–125.
[29] K. Stamoulis, A. Giannakopoulos, A study of size effects and length scales in fracture and fatigue of metals by second gradient modelling, Fatigue Fract Eng Mater Struct 35 (9) (2012) 852–860.
[30] D. Devitt, R. Schapery, W. Bradley, A method for determining the mode I delamination fracture toughness of elastic and viscoelastic composite materials, J Compos Mater 14 (1980) 270–285.
[31] J. Williams, Large displacement and end block effects in the 'DCB' interlaminar test in modes I and II, J Compos Mater 21 (4) (1987) 330–347.
[32] J. He, C.M. Lilley, Surface effect on the elastic behavior of static bending nanowires, Nano Lett 8 (7) (2008) 1798–1802.
[33] Z. Zhang, L. Jiang, Size effects on electromechanical coupling fields of a bending piezoelectric nanoplate due to surface effects and flexoelectricity, J Appl Phys 116 (13) (2014) 134308.
[34] R. Joseph, J. Purbolaksono, H.L. Liew, S. Ramesh, M. Hamdi, Stress intensity factors of a corner crack emanating from a pinhole of a solid cylinder, Eng Fract Mech 128 (2014) 1–7.
[35] L.F. Shampine, J. Kierzenka, M.W. Reichelt, Solving boundary value problems for ordinary differential equations in MATLAB with bvp4c, Tutorial Notes (2000) 1–27.
[36] H. Wu, L. Li, G. Chai, F. Song, T. Kitamura, Three-dimensional thermal weight function method for the interface crack problems in bimaterial structures under a transient thermal loading, J Therm Stresses 39 (4) (2016) 371–385.
[37] Z. Yan, L. Jiang, The vibrational and buckling behaviors of piezoelectric nanobeams with surface effects, Nanotechnology 22 (24) (2011) 245703.
[38] L. Xu, S. Shen, Size-dependent piezoelectricity and elasticity due to the electric field-strain gradient coupling and strain gradient elasticity, Int J Appl Mech 5 (02) (2013) 1350015.
[39] B. Wang, K. Wang, Effect of surface residual stress on the fracture of double cantilever beam fracture toughness specimen, J Appl Phys 113 (15) (2013) 153502.
[40] J. He, C.M. Lilley, Surface stress effect on bending resonance of nanowires with different boundary conditions, Appl Phys Lett 93 (26) (2008) 263108.
[41] G.F. Wang, X.Q. Feng, Surface effects on buckling of nanowires under uniaxial compression, Appl Phys Lett 94 (14) (2009) 141913.
[42] X. Liang, S. Hu, S. Shen, Effects of surface and flexoelectricity on a piezoelectric nanobeam, Smart Mater Struct 23 (3) (2014) 035020.
[43] S. Kong, S. Zhou, Z. Nie, K. Wang, Static and dynamic analysis of micro beams based on strain gradient elasticity theory, Int J Eng Sci 47 (4) (2009) 487–498.
[44] A.E. Giannakopoulos, S. Suresh, Theory of indentation of piezoelectric materials, Acta Mater 47 (7) (1999) 2153–2164.
[45] Y. Yue, K. Xu, T. Chen, A micro scale Timoshenko beam model for piezoelectricity with flexoelectricity and surface effects, Compos Struct 136 (2016) 278–286.
[46] S. Dal, M. Gharbi, P. Sharma, H.S. Park, Surface piezoelectricity: size effects in nanostructures and the emergence of piezoelectricity in non-piezoelectric materials, J Appl Phys 110 (10) (2011) 104305.
[47] R.C. Cammarata, Surface and interface stress effects in thin films, Prog Surf Sci 46 (1) (1994) 1–38.
[48] A.N. Morozovska, E.A. Eliseev, A.K. Tagantsev, S.L. Bravina, L.Q. Chen, S.V. Kalinin, Thermodynamics of electromechanically coupled mixed ionic-electronic conductors: Deformation potential, Vegard strains, and flexoelectric effect, Phys Rev B 83 (19) (2011) 195313.